# Charge transport in monolayer protected Au and Ag clusters in electrolyte environment and transport properties of a redox-active ionic liquid

Inauguraldissertation
der Philosophisch-naturwissenschaftlichen Fakultät
der Universität Bern

vorgelegt von
**Nataraju Bodappa**
von Indien

Leiter der Arbeit:
Prof. Dr. Thomas Wandlowski
Departement für Chemie und Biochemie
Universität Bern

# Charge transport in monolayer protected Au and Ag clusters in electrolyte environment and transport properties of a redox-active ionic liquid

Inauguraldissertation
der Philosophisch-naturwissenschaftlichen Fakultät
der Universität Bern

vorgelegt von
**Nataraju Bodappa**
von Indien

Leiter der Arbeit:
Prof. Dr. Thomas Wandlowski
Departement für Chemie und Biochemie
Universität Bern

Von der Philosophisch-naturwissenschaftlichen Fakultät angenommen.

Der Dekan:
Bern, 07.11.2014                                        Prof. Dr. Gilberto Colangelo

# Table of contents

# Abstract

This dissertation compiles interdisciplinary topics broadly in Raman spectroscopy, nanoparticle synthesis, nanoparticle electrochemistry and ionic liquids. Chapter one describes the overview on the two topics Monolayer protected gold and silver cluster synthesis and investigation of their electrochemical and electrical studies and, secondly, physico-chemical and charge transport studies of ionic liquids (ILs) ranging from conventional (redox-inactive) to redox-active ILs. At the end of the chapter the scope of this thesis is described in a problem solving based approach.

Chapter two describes the principles and techniques which rationalize in the designed problems and the experiments. In chapter three, the general procedures used in preparing the experiments and the sample preparation for the voltammetric, electrochemical Raman, and Scanning Tunneling Microscopy/ Spectroscopy (STM/STS) experiments are discussed.

In chapter four, results are presented in the form of the three publications and one chapter of first results. In the first publication, we have studied Au(55 nm)@SiO$_2$ nanoparticles (NPs) on two low-index phases of gold and platinum single crystal electrodes in ClO$_4^-$ and SO$_4^{2-}$ ion-containing electrolytes by both electrochemical methods and in-situ shell-isolated nanoparticle enhanced Raman spectroscopy (SHINERS). The blocking of the electrode with surfactants originating from the synthesis of as-prepared SHINERS NPs is shown and an efficient procedure to overcome this problem is introduced, which provides a fundamental platform for the application of SHINERS in surface electrochemistry and beyond. The method is based on a hydrogen evolution treatment of the SHINERS-NP-modified single-crystal surfaces. The reliability of our preparation strategy is demonstrated in electrochemical SHINERS experiments on the potential-controlled adsorption and phase formation of pyridine on Au(hkl) and Pt(hkl). High-quality Raman spectra on these well-defined and structurally carefully characterized single-crystal surfaces were obtained. The analysis of the characteristic A1 vibrational modes revealed perfect agreement with the interpretation of single-crystal voltammetric and chronoamperometric experiments. The study demonstrates that the SHINERS protocol developed in this work qualifies this Raman method as a pioneering approach with unique opportunities for in situ structure and reactivity studies at well-defined electrochemical solid/liquid interfaces.

In the second publication, a proof-of-concept study is presented by electrochemically controlled scanning probe experiments performed on tailor-made Au particles of narrow dispersity. In particular the charge transport characteristics through chemically synthesized hexane-1-thiol and 4-pyridylbenzene-1-thiol mixed monolayer protected $Au_{144}$ clusters (MPCs) by differential pulse voltammetry (DPV) and electrochemical scanning tunneling spectroscopy (EC-STS) are reported. The pyridyl groups exposed by the Au-MPCs enable their immobilization on Pt(111) substrates. By varying the humidity during their deposition, samples coated by stacks of compact monolayers of Au-MPCs or decorated with individual, laterally separated Au-MPCs are obtained. DPV experiments with stacked monolayers of $Au_{144}$-MPCs and EC-STS experiments with laterally separated individual $Au_{144}$-MPCs are performed both in aqueous and ionic liquid electrolytes. Lower capacitance values were observed for individual clusters compared to ensemble clusters. This trend remains the same irrespective of the composition of the electrolyte surrounding to the $Au_{144}$-MPC. The resolution of the energy level spacing of single clusters however, is strongly affected by the proximity of neighboring particles.

In the third publication, a redox-active ionic liquid (IL), 1-butyl-1'-heptyl-4,4'-bipyridinium bis(trifluoromethanesulfonyl) imide has been synthesized and its transport processes were investigated. The conductivity and viscosity of the IL, as well as the diffusion coefficients of its components were studied over a 50 °C wide temperature range: for the diffusivity studies, both the pulsed-gradient spin-echo (PGSE)–NMR technique and voltammetric measurements have been applied. The measured data are presented in the paper and are compared to each other. It was found that the diffusion coefficients determined by means of NMR and chronoamperometry measurements are, within the range of experimental error, equal — and they are (in accordance with other ionic liquid studies) higher than what the conductivity or viscosity measurements indicate. The results are interpreted in the light of the existing theories. The measured diffusion coefficients and bulk conductivities can be well interrelated based on the "ionicity" concept (that is, by treating the ionic liquid as a weak electrolyte). In agreement with the empirical Walden rule, a direct comparison between the measured conductivities and viscosities is also possible, for which a hole conduction model is utilized. Based on the fact that both the electrochemical and the NMR measurements yield practically the same diffusion coefficients in the system, there is no evidence that interpretations based in other redox-active IL systems on "homogeneous electron transfer" apply to the system studied here.

In chapter 4.4, first results are presented on stabilization of monolayer protected silver clusters ("$Ag_9MSA_7$", MSA= Mercpatosuccinic acid) and their electrochemical and electrospray ionisation mass spectrometry (ESI-MS) investigations. Here, it has been shown that an enhanced stability of "$Ag_9MSA_7$" MPCs can be achieved by submitting them to phase transfer into an organic solvent in the presence of sterically bulky counterions. The resulting phase transferred clusters, "$Ag_9MSA_7(TOA)_x$" show a very high stability in ambient conditions that has enabled for the first time to perform voltammetric investigations. Size exclusion chromatography reveals also a minor yield of clusters with a smaller size during the synthesis of "$Ag_9MSA_7$" clusters. The electrochemical studies of the "$Ag_9MSA_7(TOA^+)_x$" (1.63 nm) clusters show an electrochemical gap of 1.19 V with a HOMO-LUMO gap of 0.87 eV. However, as an important result, the combination of the MS investigations with the electrochemically determined HOMO-LUMO gap strongly suggest that the real cluster sizes are larger than the empirically used formula "$Ag_9MSA_7(TOA^+)_x$".

In chapter five, the findings are summarized and an outlook is given of the investigated problems in the view of broader range.

# వియుక్త (shortened abstract in Telugu)

ఈ సిద్ధాంత వ్యాసానికి విస్తారంగా రామస్ స్పెక్ట్రోస్కోపీ, నానోపార్టికల్ సంశ్లేషణ, నానోపార్టికల్ విద్యుత్ రసాయన శాస్త్రం మరియు అయాను ద్రవాలు బహుళశాస్త్ర విషయాలు కూర్చింది . అధ్యయము ఒకటి, రెండు అంశాలపై పర్యవలోకనం వివరిస్తుంది. మొదట ఏకపొర రక్షిత బంగారు మరియు వెండి క్లస్టర్ సంశ్లేషణ మరియు వాటి విద్యుత్ రసాయన మరియు విద్యుత్ పరిశోధనలు మరియు రెండవది, సంప్రదాయ (రెడాక్స్ క్రియారహితంగా) అయాను ద్రవాలు  నుండి మొదలుకొని క్రియాశీల రెడాక్స్ అయాను ద్రవాలు యొక్క భౌతిక రసాయన మరియు ఛార్జ్ రవాణా అధ్యయనాలు చర్చించబడ్డాయి. అధ్యయం చివర, ఈ థీసిస్ యొక్క పరిధిని సమస్య పరిష్కార ఆధారిత విధానం ద్వారా వివరించబడింది .

చాప్టర్ రెండులా, రూపొందించిన సమస్యలు మరియు ప్రయోగాలు యొక్క హేతుబద్ధ సూత్రాలు మరియు పద్ధతులు గురించి వివరిస్తుంది .చాప్టర్ మూడు, సాధారణ విధానాలు ప్రయోగాలు మరియు వోల్టమట్రీ, విద్యుత్ రసాయన రామస్, మరియు స్కానింగ్ టన్నెలింగ్ సూక్ష్మదర్శిని / స్పెక్ట్రోస్కోపీ కోసం నమూనా తయారీ సిద్ధం ఉపయోగించే ప్రయోగాలతో చర్చించడం జరిగింది .

అధ్యయం నాలుగు, మూడు ప్రచురణలు రూపంలో ఫలితాలు ఇంకా మొదటి ఫలితాలు ఒకటి అధ్యయం రూపంలో ఇవ్వడం జరిగింది. మొదటి ప్రచురణలో, షెల్ ఐసోలేటెడ్ నానోపార్టికల్ రామస్ స్పెక్ట్రోస్కోపీ చేయడంలో జరుగుతున్న సమస్యలు మరియు పరిష్కారాలు గురించి చర్చించాను. రెండవ ప్రచురణలో, వోల్టమట్రీ మరియు స్కానింగ్ టన్నెలింగ్ సూక్ష్మదర్శిని/స్పెక్ట్రోస్కోపీ పద్ధతులను ఉపయోగించి $Au_{144}$ ఏకపొర రక్షిత సమూహాలు ద్వారా జరిగే ఛార్జ్ రవాణా ప్రక్రియలు, సమస్యలు మరియు వాటి పరిష్కారాలు గురించి చర్చించాను. మూడవ ప్రచురణలో, ఒక క్రియాశీల రెడాక్స్ అయాను ద్రవము, 1-butyl-1'-heptyl-4,4'-bipyridinium bis(trifluoromethanesulfonyl)imide యొక్క భౌతిక రసాయన మరియు ఛార్జ్ రవాణా అధ్యయనాలు గురించి పరిశోధించడం జరిగింది. అధ్యయం  4.4 లో, ఏకపొర రక్షిత వెండి సమూహాలు ("$Ag_9MSA_7$"), MSA=Mercaptosuccinic acid మరియు వాటి విద్యుత్ మరియు electrospray అయనీకరణ మాస్ స్పెక్ట్రోమెట్రీ పరిశోధనలు, స్థిరీకరణ మొదటి ఫలితాల గురించి పరిశోధింపబడింది.

 అధ్యయం ఐదు, మేము కనుగొన్న సంగ్రహంగా మరియు విస్తృత పరిధి దృష్ట్యా దర్యాప్తు సమస్యలు ఒక క్లుప్తంగ ఇవ్వడం జరిగింది.

# Acronyms

| | |
|---|---|
| $[C_4VC_7][Tf_2N]_2$ | 1-butyl-1'-heptyl-4,4'-bipyridinium bis(trifluoromethanesulfonyl) imdie |
| $[C_6C_1Im][FEP]$ | 1-hexyl-3-methylimidazolium-tris(pentafluoroethyl)trifluorophosphate |
| $[HMI][Tf_2N]$ | 1-hexyl-3-methylimidazolium bis(trifluoromethanesulfonyl)imide |
| AES | Auger electron spectroscopy |
| AFM | Atomic force microscopy |
| ATR | Attenuated total reflection configuration |
| $Au@SiO_2$ | $SiO_2$ shell isolated gold core nanoparticle |
| BTPPA-TPFB | Bis(triphenylphosphoranylidene) ammonium tetrakis(penta-fluorophenyl)borate |
| $C_6S$ | Hexane-1-thiolate |
| $C_{MPC}$ | Monolayer protected cluster capacitance |
| CV | Cyclic voltammetry |
| $D_-$ | Anionic diffusion coefficient |
| $D_+$ | Cationic diffusion coefficient |
| $D_{APP}$ | Apparent diffusion coefficient |
| $D_E$ | Electron diffusion coefficient |
| $D_{PHYS}$ | Self-diffusion (physical diffusion) coefficient |
| DPV | Differential pulse voltammetry |
| DSC | Differential scanning calorimetry |
| *e* | Elementary charge |
| $E_C$ | Coulomb repulsion energy |
| EC-STS | Electrochemical Scanning tunneling spectroscopy |

| | |
|---|---|
| EELS | Electron energy loss spectroscopy |
| $E_s$ | Substrate potential |
| ESI-MS | Electrospray ionization mass spectrometry |
| $E_t$ | Tip potential |
| $f_{--}$, $f_{++}$ | Like-ion velocity cross correlation parameters |
| $f_{+-}$ | Unlike-ion velocity cross correlation parameters |
| FAB-MS | Fast atom bombardment mass spectrometry |
| Fc | Ferrocene |
| GSH | Glutathione |
| $h$ | Plank constant |
| $H_2MSA$ | Mercaptosuccinic acid |
| HER-SHINERS | Hydrogen-evolution-range shell isolated nanoparticle Raman spectroscopy |
| $I_L$ | Limiting current |
| ILs | Ionic liquids |
| $I_{set}$ | Set point current |
| $I_{soln}$ | Integrated Raman intensities for solution species |
| $I_{surface}$ | Integrated Raman intensities for surface species |
| $k_B$ | Boltzmann constant |
| $k_{Ex}$ | Electron self-exchange rate constant |
| $k_{meas}$ | Measured electrical bulk conductivity (specific conductance) |
| $k_{NMR}$ | Bulk conductivity calculated from the diffusion coefficients measured by NMR |
| $k_{visc}$ | Bulk conductivity calculated from the measured viscosities |
| MALDI-TOF | Matrix assisted laser desorption ionization-time of flight |
| $m_e$ | Mass of the electron |

| | |
|---|---|
| MI | Molecular imaging |
| MPCs | Monolayer protected clusters |
| MSA | Mercpatosuccinic acid (in deprotanated form) |
| $N_A$ | Avogadro constant |
| NALC | N-acetyl-L-cysteine |
| NMBA | 5-mercapto 2-nitrobenzoic acid |
| NPs | Nanoparticles |
| $N_{soln}$ | Amount of solution molecules in the laser beam |
| $N_{surface}$ | Amount of surface molecules in the laser beam |
| PAGE | Poly acrylamide gel electrophoresis |
| PET | Phenyl ethane thiol |
| PGSE-NMR | Pulsed-gradient spin-echo NMR |
| p-MBA | Para mercaptobenzoic acid |
| PTFE | Polytetrafluoroethylene |
| PZC | Potential of zero charge |
| $R_-$ | Hydrodynamic radius of anion |
| $R_+$ | Hydrodynamic radius of cation |
| RTIL | Room temperature ionic liquid |
| SAM | Self assembled monolayer |
| SBB | 4(tertbutyl)-benzyl-mercaptan |
| SEC | Size exclusion chromatography |
| SEF | Surface enhancement factor |
| SEM | Scanning electron microscopy |
| SERS | Surface enhanced Raman spectroscopy |
| SET | Single electron tunneling |

| | |
|---|---|
| SHINERS | Shell isolated nanoparticle enhanced Raman spectroscopy |
| SHINPs | Shell isolated nanoparticles |
| SPR | Surface plasmon resonance |
| SR | Arenethiolate/Alkanethiolate |
| STM | Scanning tunneling microscopy |
| STS | Scanning tunneling spectroscopy |
| $TBAPF_6$ | Tetrabutyl ammonium hexafluorophospahete |
| TEM | Transmission electron microscopy |
| TERS | Tip-enhanced Raman spectroscopy |
| TOABr | Tetraoctyl ammonium bromide |
| $V_{bias}$ | Bias voltage |
| VFT | Vogel-Fulcher-Tammann |
| $z_i$ | Charge number |
| α | Degree of dissociation |
| ΔV | Peak-to-peak voltage spacing |
| $λ_-$ | Molar ionic conductivity of anion |
| $λ_+$ | Molar ionic conductivity of cation |
| ν | Sweep rate |
| $\boldsymbol{\Phi}$ | barrier height |
| $\boldsymbol{\varepsilon_m}$ | Relative permittivity of the monolayer |
| $\boldsymbol{\varepsilon_s}$ | Dielectric constant of the solvent |
| $\boldsymbol{\varepsilon_0}$ | Permittivity of the free space |

# 1. Introduction

## 1.1. Monolayer protected gold and silver clusters

### 1.1.1. Synthesis

Metal clusters comprising up to several hundreds of atoms protected by organic molecules such as aliphatic and aromatic thiols, acetylene, phosphines, amines, are called monolayer protected metal clusters (MPCs). These MPCs are bridges between molecules and larger nanoparticles, **Figure 1**[1]. The synthesis and fundamental studies on nobel metal MPCs have been the subject of intense research over the past decade[1-6]. Whereas especially gold MPCs have been synthesized with high atomistic precision, and their electrochermical properties have been investigated, very little is still known about the synthesis and the electrochemical propertiesof analogous silver MPCs.

Gold MPCs were first synthesized by Brust et.al[7], using a two phase liquid-liquid system. These colloidal particles show very high stability with time. Then further synthesis methods of MPCs were explored by several groups using different kinds of ligands and metals over the past two decades[1, 8]. Afterwards, as a challenging task, the synthesis was more focused on preparing  uniformly sized MPCs and to find out their exact molecular compositions.
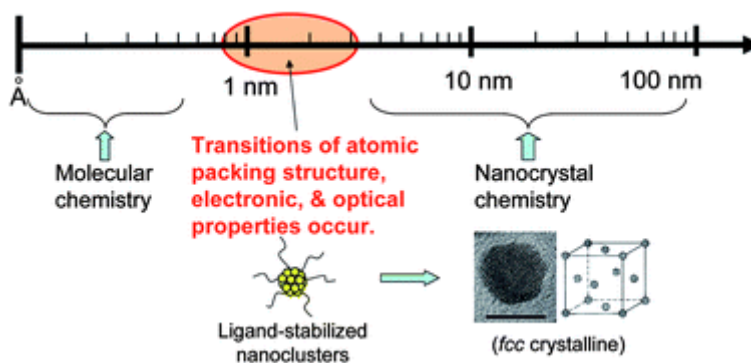


**Figure 1:** Metal nanoclusters as bridges between organometallic complexes and nanocrystals. From[1].

Several analytical techniques were applied to reveal the precise molecular formulas of such MPCs and to understand their structure, size and composition. For example, mass spectrometry[9] has been widely used to investigate the composition of the cluster entities. The first crystallization of the compound $Au_{102}(p\text{-}MBA)_{44}$[10] has boosted the further synthesis and understanding of the cluster properties and has then risen profound interest to the researchers by applying crystallization to clusters such as $Au_{102}(p\text{-}MBA)_{44}$[10], $[N(C_8H_{17})_4][Au_{25}(SC_2H_4Ph)_{18}]$[11], $Au_{38}(SC_2H_4Ph)_{18}$[12], $Au_{36}(SPh\text{-}tBu)_{24}$[13], and $Au_{28}(SPh\text{-}tBu)20$[14]. Ligand exchange reactions, involving an exchange of the monolayer ligands of the MPCs with other ligands of interest have also been studied[15].

In comparison to the gold cluster synthesis, the synthesis of silver clusters is quite challenging due to the surface oxidation of silver by atmospheric oxygen. However, the synthesis of arenethiolate protected silver clusters (soluble in organic solvents) $Ag_{152}(PET)_{60}$[16] (PET=Phenylethanethiol), $Ag_{280}(SBB)_{120}$[17] (SBB=4-(tert-butyl)benzyl mercaptan), has been reported recently and their composition was successfully investigated with electrospray ionization mass-spectrometry (ESI-MS). But in most cases the silver clusters need to be water soluble to be used in biological applications. Therefore, research focused on the preparation of stable water soluble Ag clusters with precisely defined composition has a large impact. In contrast to silver clusters stabilized with aromatic thiols that are soluble in organic solvents, water soluble silver clusters are very difficult to synthesize due to their easy oxidation in presence of water and oxygen. Nevertheless, several groups made efforts in this direction to find out the causes affecting the stability and to stabilize such clusters.[18, 19] Udaya et al, reported the synthesis of water soluble Ag clusters such as $Ag_{7,8}(H_2MSA)_{7,8}$[20], $Ag_9(H_2MSA)_7$,[21] $Ag_{32}(GSH)_{19}$[22, 23] by interfacial etching and solid state methods. Farrag et al, reported that $Ag_x(NALC)_y$[24] (NALC=N-acetyl-L-cysteine) and $Ag_x(L\text{-}GSH)_y$,[24] (L-GSH= L-glutathione) clusters were synthesized. Magic compositions of $Ag_x(GSH)_y$ clusters were separated by using polyacrylamide gel electrophoresis (PAGE) by the Bigioni group[18]. Also the synthesis of $Ag_{44}(p\text{-}NMBA)_{30}$[19], $Ag_{25}(capt)_{18}$[25], $Ag_7(DMSA)_4$[26] and $Ag_{32}(GSH)_{24}$[22, 27] clusters has been reported.

A breakthrough was achieved recently by solving the crystal structure of the $Ag_{44}(SR)_{30}$ clusters independently by the groups of Bigioni[28] and of Zheng[29]. Interestingly, the interfacial

structure observed on the thiol to the silver surface is drastically different than the well-known RS(Au-SR-)$_x$,(x =1, 2) oligomeric unit found in thiolated Au MPCs and self-

## Surface motif structures
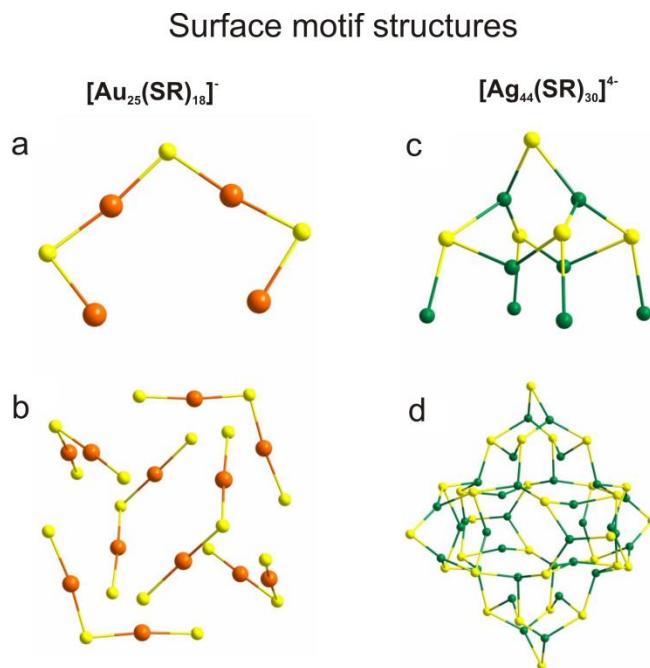


**Figure 2.** The surface Au-SR coordination structure (a) and the surface protected layer structure (b) of [Au$_{25}$(SR)$_{18}$]$^-$. The surface Ag-SR coordination structure (c) and the surface protected layer structure (d) of [Ag$_{44}$(SR)30]$^{4-}$. Color legend: orange spheres Au; green spheres Ag; yellow spheres S. All carbon atoms are omitted for clarity. From[29].

assembled monolayers on Au(111)[30]. In thiolate capped Au MPCs, Au(I) cations are linearly coordinated to two thiolate ligands that are also bound to two core Au atoms, **Figure 2**. However, in case of the surface layer of the [M$_{12}$Ag$_{32}$(SR)$_{30}$]$^{4-}$ (M=Au/Ag), the cluster consists of six three-dimensional Ag$_2$(SR)$_5$ units in which Ag cations bind to three thiolate ligands in a planar Ag(SR)$_3$ configuration. The five thiolate ligands in each surface Ag$_2$(SR)$_5$ motif are classified into two groups[29]. Although the four thiolates directly bonded to the Ag atoms on the M$_{12}$@Ag$_{20}$ core are threefold coordinated, the one thiolate joining the outmost Ag(I) cations is twofold coordinated.[28, 29]

## 1.1.2. Electrical properties of MPCs

Metal Nanoparticles (NPs) have been well investigated and used in biosensing and light scattering. In general, the larger NPs exhibit surface plasmonic resonance (SPR), i.e. oscillation of the surface (conductive) electrons induced by light. For example, this can be visualized as

characteristic surface plasmon peak in the absorption spectrum at ~ 400, 520 and 650 nm for Ag, Au and Cu NPs respectively. However if the NP size decreases to the order of magnitude of MPCs, the energy levels break down from continuous to discrete states due to the quantum size effect. This means that surface plasmonic peaks are observed only with nanoparticles and not with nanoclusters. Therefore, by looking at the absorption spectra it is possible to differentiate smaller nanoclusters of the size of MPCs from bigger NPs. From **Figure 3**, it can be clearly seen that SPR is observed for $Au_{2406}$, but the lack of SPR for $Au_{25}$, $Au_{55}$, and $Au_{140}$ confirms that these samples are nanoclusters.[31]
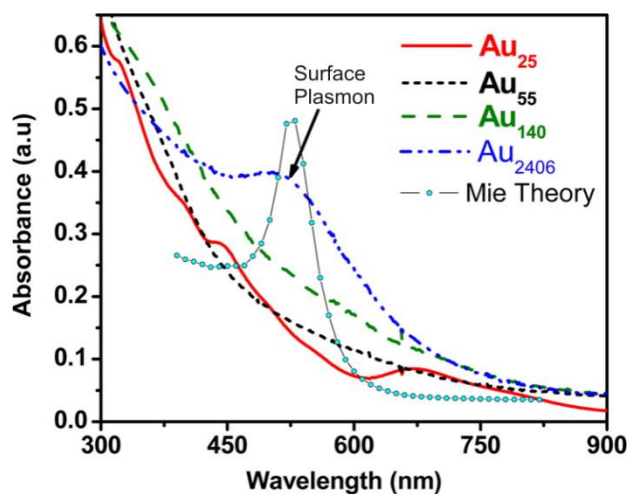


**Figure 3.** Optical absorption for $Au_{25}$, $Au_{55}$, $Au_{140}$, $Au_{140}$ and $Au_{2406}$ and the Mie theory calculation using parameters similar to $Au_{25}$. From[31].

The further miniaturization of the current microelectronics and the physical size limits imposed in integrated circuits requires new concepts and technologies. For this, molecules, metal complexes, and hybrid inorganic metal clusters (such as MPCs) can be used as new building block units for molecular electronics. Charging effects arising from metallic clusters can be used as promising concepts in developing single electron transistors, sensors, data storage[32] and switching devices.[33, 34] The electrical properties of nanoparticles have been addressed by using three methods namely *electrochemical methods*, *nanometer spaced electrodes* (nanogaps) and *scanning tunneling microcopy and spectroscopy*.[33, 35]

The observation of single electron (quantized) charging is possible for noble metal MPCs in classical electrochemical experiments at room temperature. The particles that are either dissolved in the electrolyte solution or are immobilized on an electrode surface act as a tiny

capacitor accepting and donating the electrons from/to the electrode surface. First such observations were made by the group of Murray[36, 37] who reports that the quantized charging current peaks in *voltammtery* are due to the electrochemical double layer charging of the metal-electrolyte interface. Furthermore it is reported that the quantized charging peaks of gold MPCs break down into a molecular redox-like behavior when the core size reduces from 28 to 8 kDa. In addition to this, they have used a simple concentric sphere capacitor model to calculate the capacitance values of MPCs at each charge state. Based on this, the experimentally measured dependence of the cluster capacitance on the chain length of the monolayer agrees with the theoretical model[38]. As the cluster capacitance varies with the core size and is related with peak spacing, monodispersity in size is a critical aspect in observing the quantized charging phenomena. If the sample is polydisperse, the charging peaks of different sizes present will overlap.[39, 40] As each cluster has its own characteristic charging patterns, *voltammetric methods* give a direct measure of size and dispersity. Besides these results, also the electrochemical behavior of $Au_{25}$, $Au_{38}$, $Au_{144}$ clusters have been studied.[41, 42]

Similar to synthetic studies of silver clusters, their electrochemical properties have also only been investigated to a limited extent. Branham et al,[43] reported the first electrochemical studies of silver clusters, $Ag_{140}BBT_{53}$ (BBT=4-tert-butylbenzyl mercaptan). It has been shown that the charging of these silver MPCs also behaves similarly to gold MPCs. However in some silver MPCs, oxide layer formation occurs on the MPC surface during its synthesis with the consequence of absence of electrochemical charging features on these MPC surfaces[43]. The same phenomena have been observed by several other groups[44].

As we discussed the available methods to address the electrical properties of the MPCs, each of the methods has its own advantages and disadvantageous. For example electrochemical methods cannot provide device information upto the single particle level, but they can be used to make an ambient large scale stable device[45]. Nanogap setups are relatively good methods in terms of the device fabrication for larger size NPs (5-20 nm), but not for a size less of than 2 nm.[33] Nanogaps have also the drawback in making a contact in a reproducible way difficult, and the control of nanoparticles in such gap is a difficult task. Nevertheless reserachers use mechanical breaking and also electromigration techniques to prepare such nanogaps.[34] Klein et al[46] succeeded to make a single NP nanogap of a few nanoameters. Even though electrochemical scanning tunneling microscopy and spectroscopy (EC-STM/STS) configurations

have a limitation for nanoparticle device fabrication, they are quite useful to understand the working principle of the device upto the level of single NPs. The electrical properties of NPs are sensitive to both the chemical nature of the ligand shell and the geometry of the contacts.[33]

Some of the examples concerning the sensitivity for the ligand shell are discussed below. Recently, Xu et al[47] have investigated the change in the STM/STS tunneling characteristics of hexanethiolate protected Au NPs (3.2-6.3 and 11.8 nm) upon the exposure of the NP/SAM/Au structure to organic vapors. It has been shown that for particles with a size of ~6 nm an enlargement of the Coulomb gap is observed in the *I-V* curves by increasing the vapor concentration and decreasing the vapor polarity. Gittins et al,[48] have studied the STM/STS characteristics of an Au NP (6 nm) containing a viologen redox molecule in the ligand shell. It has shown that by reducing and oxidizing the viologen molecule the transparency of the insulating barrier could be modified. Brousseau et al[49] reported a pH dependence of the *I-V* characteristics of an Au NP coated with galvinol and octanethiol. The changes were observed in the single electron tunneling (SET) staircase upon inducing charges on the galvinol by changing the pH of the surrounding solution. Albrecht et al[50] described that dielectric saturation effects alter the SET characterizes of $Au_{144}$ nanoclusters coated with mixed ligands of hexanethiol and 4-mercaptopyridine.

The results obtained from all the above mentioned methods give an essential information in many applications to understand the fundamental aspects of more complicated processes in the fields of solar cells,[51] catalysis,[52] biology[53], sensing[54] and electronics[55].

## 1.2. Physico-chemical and charge transport studies of Ionic Liquids

### 1.2.1 Conventional redox-inactive ILs

Research on Ionic liquids (ILs) takes great attention in chemistry and the chemical industry due to their interesting properties in comparison with conventional organic solvents for chemical reactions, calatalyic processes, separation and purification procedures[56-59]. This can be recognized from the growth of the the annual number of publications[60] in this field. ILs can be defined as salts with melting points near room temperature composed of cations and anions[4]

and can therefore also be used as electrolytes in power sources and electrochemical devices[61]. The growing interest for ILs for many applications is due to their unusual properties, in particular 1) a highly concentrated ionic atmosphere, 2) a low vapour pressure and flammability, 3) a wide liquid temperature range in conjunction with thermal stability, 4) fast ion transport, 5) a wide potential range for electrochemical applications, 5) structure-forming properties on the nanoscale and 6) significant flexibility in material design due to the availability of wide varieties of cations and anions[4]. Significant progress has been made to understand the synthesis and properties of ILs. Several reviews were published on the electrochemical reactivity[62], the thermal stability[63], and the use as solvents for the sysnthesis and catalysis[64].

The ionic liquids are designed according to the need of the practical applications. However the understanding of the properties and synthesis of the ILs are complementary. Physicochemical properties and charge transport studies are a major subject investigated by many research groups[4, 65-68]. To understand the chemical reactivity and the physicochemical properties of conventional molecular solvents, empirical solvent polarity scales have been proposed.[69]. Similar to molecular solvents, the dielectric constant[70] and the solubility parameters[71] have been considered to explain the ionic structure of the ILs. However, ILs are more complex than conventional molecular solvents, because both cations and anions have their own ion characteristics in addition to Coulomb, Van-der-Waals, hydrogen bonding and $\pi$-$\pi$ interactions[4]. Even though ideal ILs are considered to consist of non-associated ions, in reality they can form to some extent aggregates or clusters. Such IL association has experimentally been observed[72, 73]. Therefore it is also important to correlate the ionicity concept with the ionic structure of the ILs.

## 1.2.2 Redox-active ILs

Similar to conventional (redox-inactive) ILs, redox ILs have been synthesized. Redox ILs are room-temperature molten salts where an electro active (redox) component is either directly attached to the cation or anion by means of an alkyl chain bridge, or where the cation or anion itself has an intrinsic electro-active nature. Examples are shown in **Figure 3**. Redox ILs are very good model systems to study both physicochemical and charge transport properties in absence of any other electrolyte solvents. However, up to now studies of the redox ILs are rather limited.

It has been well known that charge transfer can occur by charge hopping between adjacent redox sites in redox-active polymeric films.[74] The group of Murray has suggested in several studies a similar hypothesis for some redox-active ILs[75-77] based on charge electron transfer between adjacent redox groups to explain apparent differences between the self-diffusion coefficients of the ionic IL entities and an electrochemically determined "apparent" diffusion coefficient. However, direct experimental evidence for this proposed hypothesis has not been provided in this work. This questions therefore remains an interesting topic for further investigation that is also the subject of part of the present thesis.



A   Fc—LINKER—[imidazolium ring, N⊕N] —SIDECHAIN
X⁻

Fc-Ferrocenyl, Linker & Sidechain = R

B   Fc—(CH₂ chain)—$\overset{\oplus}{P}(nBu)_3$
$\overset{\ominus}{PF_6}$

C   $H_3C(OC_2H_4)_3$—$\overset{\oplus}{N}$—(bipyridinium)—$\overset{\oplus}{N}$—$(C_2H_4O)_3CH_3$
$\overset{\ominus}{BF_4}$          $\overset{\ominus}{BF_4}$
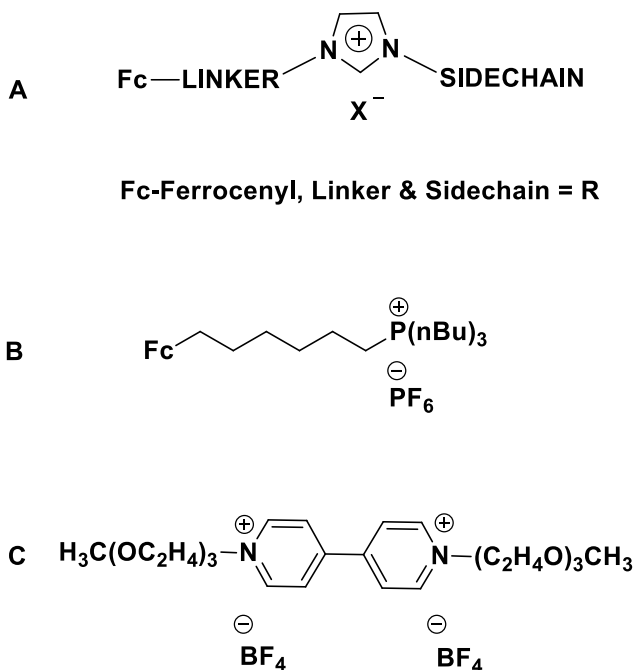
**Figure 4.** Some of the studied redox ionic-liquids systems. From[77]

In addition to all of the above mentioned aspects, redox ILs are also used as electrolytes in the Graetzel type dye sensitized solar cell[78, 79]. It is therefore essential to understand the charge and mass transport of the redox ILs.

## 1.3. Scope of this thesis

This thesis work is an interdisciplinary work focused on 1. Protocols for efficient usage of $SiO_2$ shell isolated Au NPs ($Au@SiO_2$) in electrochemical Raman experiments 2. addressing the quantized charging properties of *single* $Au_{144}$ mixed MPCs, 3. Charge and mass transport studies of a viologen based ionic liquid, and 4. The enhancement of the stability and first electrochemical and ESI-MS studies of mercaptosuccinic acid protected Ag clusters "($Ag_9MSA_7$)".

Shell Isolated Nanoparticle Enhanced Raman Spectroscopy (SHINERS)[80] is an effective technique to study the electrochemical solid-liquid interface from polycrystalline to single crystal electrode surfaces. However, *additional* current and spectroscopic features appear in voltammetric and Raman experiments, and therefore cause *disturbances* in the data interpretation and assignment. Here, we introduce an efficient procedure to overcome this problem, which provides a fundamental platform for the application of SHINERS in surface electrochemistry and beyond. The solution of this problem is presented in **publication 4.1**.

Voltammetric methods were used to map the energy level information (charging studies) of MPCs. However, these techniques are limited for studies of en ensemble of particles. For the first time Albrecht et al[50] investigated the quantized charging properties for an array of $Au_{144}$ mixed MPCs. However, they could not achieve to control the particle assembly onto the level of a submonolayer or single particles, and therefore the investigation of the quantized charging of single $Au_{144}$ mixed MPCs was still an open question. A successful approach to this topic is presented in **publication 4.2**.

The group of Murray et al.[76, 81] has investigated the mass and charge transport properties of some redox-active ILs with electrochemical methods and conductivity investigations and have proposed an electron hopping process between adjacent redox centers involving also the counterions to explain apparent deviations of the electrochemically determined diffusion coefficients from the self diffusion coefficients. However, there is not a sufficient evidence based on fully conclusive experimental techniques to support this hypothesis. In this thesis, we have chosen for the first time a combined investigation of the diffusion properties of a redox-active IL by electrochemical techniques and by pulsed-gradient spin-echo (PGSE)-NMR and show that in

our redoy-active IL system there is no evidence for such electron hopping transfer. This investigation is presented in **publication 4.3**.

In a recent publication, we have reported the synthesis of water soluble silver clusters, whose composition has been assigned to the formula "$Ag_9(H_2MSA)_7$" ($H_2MSA$ = mercaptosuccinic acid)[33] based on its fragmentation products. These clusters decompose slowly in water within one day to silver(I) thiolate. In this thesis, we discuss the approaches to stabilize the clusters and show first investigations of the cluster composition based on size separation, TEM, electrochemical and mass spectrometric techniques. These first results are presented in **Chapter 4.4.**

## 1.4. References

[1]     R. Jin, *Nanoscale* **2010**, *2*, 343.
[2]     H. Qian, M. Zhu, Z. Wu, R. Jin, *Acc. Chem. Res.* **2012**, *45*, 1470.
[3]     G. Li, R. Jin, *Acc. Chem. Res.* **2013**, *46*, 1749.
[4]     K. Ueno, H. Tokuda, M. Watanabe, *PCCP* **2010**, *12*, 1649.
[5]     L. C. Branco, J. N. Rosa, J. J. Moura Ramos, C. A. M. Afonso, *Chemistry – A European Journal* **2002**, *8*, 3671.
[6]     J. S. Wilkes, J. A. Levisky, R. A. Wilson, C. L. Hussey, *Inorg. Chem.* **1982**, *21*, 1263.
[7]     M. Brust, M. Walker, D. Bethell, D. J. Schiffrin, R. Whyman, *Journal of the Chemical Society, Chemical Communications* **1994**, 801.
[8]     H. Qian, M. Zhu, Z. Wu, R. Jin, *Acc. Chem. Res.* **2012**, *45*, 1470.
[9]     A. Dass, A. Stevenson, G. R. Dubay, J. B. Tracy, R. W. Murray, *J. Am. Chem. Soc.* **2008**, *130*, 5940.
[10]    P. D. Jadzinsky, G. Calero, C. J. Ackerson, D. A. Bushnell, R. D. Kornberg, *Science* **2007**, *318*, 430.
[11]    M. W. Heaven, A. Dass, P. S. White, K. M. Holt, R. W. Murray, *J. Am. Chem. Soc.* **2008**, *130*, 3754.
[12]    H. Qian, W. T. Eckenhoff, Y. Zhu, T. Pintauer, R. Jin, *J. Am. Chem. Soc.* **2010**, *132*, 8280.
[13]    C. Zeng, H. Qian, T. Li, G. Li, N. L. Rosi, B. Yoon, R. N. Barnett, R. L. Whetten, U. Landman, R. Jin, *Angewandte Chemie-International Edition* **2012**, *51*, 13114.
[14]    C. Zeng, T. Li, A. Das, N. L. Rosi, R. Jin, *J. Am. Chem. Soc.* **2013**, *135*, 10011.
[15]    M. J. Hostetler, A. C. Templeton, R. W. Murray, *Langmuir* **1999**, *15*, 3782.
[16]    I. Chakraborty, A. Govindarajan, J. Erusappan, A. Ghosh, T. Pradeep, B. Yoon, R. L. Whetten, U. Landman, *Nano Lett.* **2012**, *12*, 5861.
[17]    Y. Negishi, R. Arai, Y. Niihori, T. Tsukuda, *Chem. Commun.* **2011**, *47*, 5693.
[18]    S. Kumar, M. D. Bolan, T. P. Bigioni, *J. Am. Chem. Soc.* **2010**, *132*, 13141.
[19]    L. G. AbdulHalim, S. Ashraf, K. Katsiev, A. R. Kirmani, N. Kothalawala, D. H. Anjum, S. Abbas, A. Amassian, F. Stellacci, A. Dass, I. Hussain, O. M. Bakr, *Journal of Materials Chemistry A* **2013**.
[20]    T. Udaya Bhaskara Rao, T. Pradeep, *Angew. Chem. Int. Ed.* **2010**, *49*, 3925.
[21]    T. U. B. Rao, B. Nataraju, T. Pradeep, *J. Am. Chem. Soc.* **2010**, *132*, 16304.
[22]    T. Udayabhaskararao, M. S. Bootharaju, T. Pradeep, *Nanoscale* **2013**, *5*, 9404.

[23]  F. Bertorelle, R. Hamouda, D. Rayane, M. Broyer, R. Antoine, P. Dugourd, L. Gell, A. Kulesza, R. Mitrić, V. Bonačić-Koutecký, *Nanoscale* **2013**, *5*, 5637.
[24]  M. Farrag, M. Tschurl, U. Heiz, *Chem. Mater.* **2013**, *25*, 862.
[25]  N. Cathcart, P. Mistry, C. Makra, B. Pietrobon, N. Coombs, M. Jelokhani-Niaraki, V. Kitaev, *Langmuir* **2009**, *25*, 5840.
[26]  Z. Wu, E. Lanni, W. Chen, M. E. Bier, D. Ly, R. Jin, *J. Am. Chem. Soc.* **2009**, *131*, 16672.
[27]  J. Guo, S. Kumar, M. Bolan, A. Desireddy, T. P. Bigioni, W. P. Griffith, *Anal. Chem.* **2012**, *84*, 5304.
[28]  A. Desireddy, B. E. Conn, J. Guo, B. Yoon, R. N. Barnett, B. M. Monahan, K. Kirschbaum, W. P. Griffith, R. L. Whetten, U. Landman, T. P. Bigioni, *Nature* **2013**, *501*, 399.
[29]  H. Yang, Y. Wang, H. Huang, L. Gell, L. Lehtovaara, S. Malola, H. Häkkinen, N. Zheng, *Nat Commun* **2013**, *4*.
[30]  H. Hakkinen, *Nat Chem* **2012**, *4*, 443.
[31]  S. H. Yau, O. Varnavski, J. D. Gilbertson, B. Chandler, G. Ramakrishna, T. Goodson, *The Journal of Physical Chemistry C* **2010**, *114*, 15979.
[32]  R. J. Tseng, C. Tsai, L. Ma, J. Ouyang, C. S. Ozkan, Y. Yang, *Nat Nano* **2006**, *1*, 72.
[33]  M. Homberger, U. Simon, *Philosophical Transactions of the Royal Society A: Mathematical, Physical and Engineering Sciences* **2010**, *368*, 1405.
[34]  A. Zabet-Khosousi, A. A. Dhirani, *Chem. Rev.* **2008**, *108*, 4072.
[35]  T. Laaksonen, V. Ruiz, P. Liljeroth, B. M. Quinn, *Chem. Soc. Rev.* **2008**, *37*, 1836.
[36]  S. Chen, R. S. Ingram, M. J. Hostetler, J. J. Pietron, R. W. Murray, T. G. Schaaff, J. T. Khoury, M. M. Alvarez, R. L. Whetten, *Science* **1998**, *280*, 2098.
[37]  S. Chen, R. W. Murray, S. W. Feldberg, *The Journal of Physical Chemistry B* **1998**, *102*, 9898.
[38]  J. F. Hicks, A. C. Templeton, S. Chen, K. M. Sheran, R. Jasti, R. W. Murray, J. Debord, T. G. Schaaff, R. L. Whetten, *Anal. Chem.* **1999**, *71*, 3703.
[39]  J. F. Hicks, D. T. Miles, R. W. Murray, *J. Am. Chem. Soc.* **2002**, *124*, 13322.
[40]  O. Toikkanen, Vol. Doctoral, School of Chemical Technology, Aalto University publication series DOCTORAL DISSERTATIONS 19/2011 **2011**, 136.
[41]  B. M. Quinn, P. Liljeroth, V. Ruiz, T. Laaksonen, K. Kontturi, *J. Am. Chem. Soc.* **2003**, *125*, 6644.
[42]  D. Lee, R. L. Donkers, G. Wang, A. S. Harper, R. W. Murray, *J. Am. Chem. Soc.* **2004**, *126*, 6193.
[43]  M. R. Branham, A. D. Douglas, A. J. Mills, J. B. Tracy, P. S. White, R. W. Murray, *Langmuir* **2006**, *22*, 11376.
[44]  V. R. Chaudhari, P. A. Hassan, S. K. Haram, *New J. Chem.* **2014**, *38*, 1761.
[45]  A. N. Shipway, M. Lahav, I. Willner, *Adv. Mater.* **2000**, *12*, 993.
[46]  D. L. Klein, P. L. McEuen, J. E. B. Katari, R. Roth, A. P. Alivisatos, *Appl. Phys. Lett.* **1996**, *68*, 2574.
[47]  L.-P. Xu, S. Chen, *Chem. Phys. Lett.* **2009**, *468*, 222.
[48]  D. I. Gittins, D. Bethell, D. J. Schiffrin, R. J. Nichols, *Nature* **2000**, *408*, 67.
[49]  L. C. Brousseau, Q. Zhao, D. A. Shultz, D. L. Feldheim, *J. Am. Chem. Soc.* **1998**, *120*, 7645.
[50]  T. Albrecht, S. F. L. Mertens, J. Ulstrup, *J. Am. Chem. Soc.* **2007**, *129*, 9162.
[51]  R. S. Selinsky, Q. Ding, M. S. Faber, J. C. Wright, S. Jin, *Chem. Soc. Rev.* **2013**, *42*, 2963.
[52]  D. R. Kauffman, D. Alfonso, C. Matranga, P. Ohodnicki, X. Deng, R. C. Siva, C. Zeng, R. Jin, *Chemical Science* **2014**.
[53]  W. H. De Jong, P. J. Borm, *Int. J. Nanomedicine* **2008**, *3*, 133.
[54]  K. Saha, S. S. Agasti, C. Kim, X. Li, V. M. Rotello, *Chem. Rev.* **2012**, *112*, 2739.
[55]  A. N. Shipway, E. Katz, I. Willner, *ChemPhysChem* **2000**, *1*, 18.
[56]  T. Welton, *Chem. Rev.* **1999**, *99*, 2071.
[57]  J. D. Holbrey, K. R. Seddon, *Clean Products and Processes* **1999**, *1*, 223.
[58]  P. Wasserscheid, W. Keim, *Angew. Chem. Int. Ed.* **2000**, *39*, 3772.

[59]    Z. Fei, T. J. Geldbach, D. Zhao, P. J. Dyson, *Chemistry – A European Journal* **2006**, *12*, 2122.

[60]    E. Visser Ann, J. Bridges Nicholas, D. Rogers Robin, Eds., *Ionic Liquids: Science and Applications*, Vol. 1117, American Chemical Society, 2012.

[61]    M. Galiński, A. Lewandowski, I. Stępniak, *Electrochim. Acta* **2006**, *51*, 5567.

[62]    P. Hapiot, C. Lagrost, *Chem. Rev.* **2008**, *108*, 2238.

[63]    C. Maton, N. De Vos, C. V. Stevens, *Chem. Soc. Rev.* **2013**, *42*, 5963.

[64]    J. P. Hallett, T. Welton, *Chemical Reviews (Washington, DC, United States)* **2011**, *111*, 3508.

[65]    R. Seddon Kenneth, A. Stark, M.-J. Torres, in *Pure Appl. Chem.*, Vol. 72, **2000**, 2275.

[66]    H. Tokuda, K. Hayamizu, K. Ishii, M. A. B. H. Susan, M. Watanabe, *The Journal of Physical Chemistry B* **2004**, *108*, 16593.

[67]    H. Tokuda, K. Hayamizu, K. Ishii, M. A. B. H. Susan, M. Watanabe, *The Journal of Physical Chemistry B* **2005**, *109*, 6103.

[68]    H. Tokuda, K. Ishii, M. A. B. H. Susan, S. Tsuzuki, K. Hayamizu, M. Watanabe, *The Journal of Physical Chemistry B* **2006**, *110*, 2833.

[69]    C. Reichardt, *Chem. Rev.* **1994**, *94*, 2319.

[70]    C. Daguenet, P. J. Dyson, I. Krossing, A. Oleinikova, J. Slattery, C. Wakai, H. Weingärtner, *The Journal of Physical Chemistry B* **2006**, *110*, 12682.

[71]    S. H. Lee, S. B. Lee, *Chem. Commun.* **2005**, 3469.

[72]    A. Triolo, O. Russina, H.-J. Bleif, E. Di Cola, *The Journal of Physical Chemistry B* **2007**, *111*, 4641.

[73]    J. N. A. Canongia Lopes, A. A. H. Pádua, *The Journal of Physical Chemistry B* **2006**, *110*, 3330.

[74]    G. Inzelt, *Conducting Polymers*, Springer, 2012.

[75]    W. Wang, R. Balasubramanian, R. W. Murray, *The Journal of Physical Chemistry C* **2008**, *112*, 18207.

[76]    R. Balasubramanian, W. Wang, R. W. Murray, *J. Am. Chem. Soc.* **2006**, *128*, 9994.

[77]    J. E. F. Weaver, D. Breadner, F. Deng, B. Ramjee, P. J. Ragogna, R. W. Murray, *The Journal of Physical Chemistry C* **2011**, *115*, 19379.

[78]    V. K. Thorsmølle, G. Rothenberger, D. Topgaard, J. C. Brauer, D.-B. Kuang, S. M. Zakeeruddin, B. Lindman, M. Grätzel, J.-E. Moser, *ChemPhysChem* **2011**, *12*, 145.

[79]    V. K. Thorsmølle, D. Topgaard, J. C. Brauer, S. M. Zakeeruddin, B. Lindman, M. Grätzel, J.-E. Moser, *Advanced Materials (Weinheim, Germany)* **2012**, *24*, 781.

[80]    J. F. Li, Y. F. Huang, Y. Ding, Z. L. Yang, S. B. Li, X. S. Zhou, F. R. Fan, W. Zhang, Z. Y. Zhou, Y. WuDe, B. Ren, Z. L. Wang, Z. Q. Tian, *Nature* **2010**, *464*, 392.

[81]    T. Hatazawa, R. H. Terrill, R. W. Murray, *Anal. Chem.* **1996**, *68*, 597.

# 2. Principles and Techniques

## 2.1 Electrochemical properties of monolayer protected metal clusters (MPCs)

If we compare the electrochemical properties of a metal with macroscopic dimensions with those of the metal with nanometer scale dimensions, the electrochemical properties change drastically due to size-dependent quantization effects. For example, the energy levels in the bulk metal systems are continuous, and upon size reduction to the 10-100 nm range, surface plasmonic resonance appears. If the size is further reduced below ca. 5 nm, surface plasmonic resonance disappears, and the discrete nature of the energy levels appears. Electrochemical techniques are therefore very suitable to investigate the size and the dispersity in size from macroscopic to sub-nanometer range particles. For example, the electrochemical properties of thiol protected noble metal clusters have been intensely investigated[1, 2]. Depending on the size of the particles, the


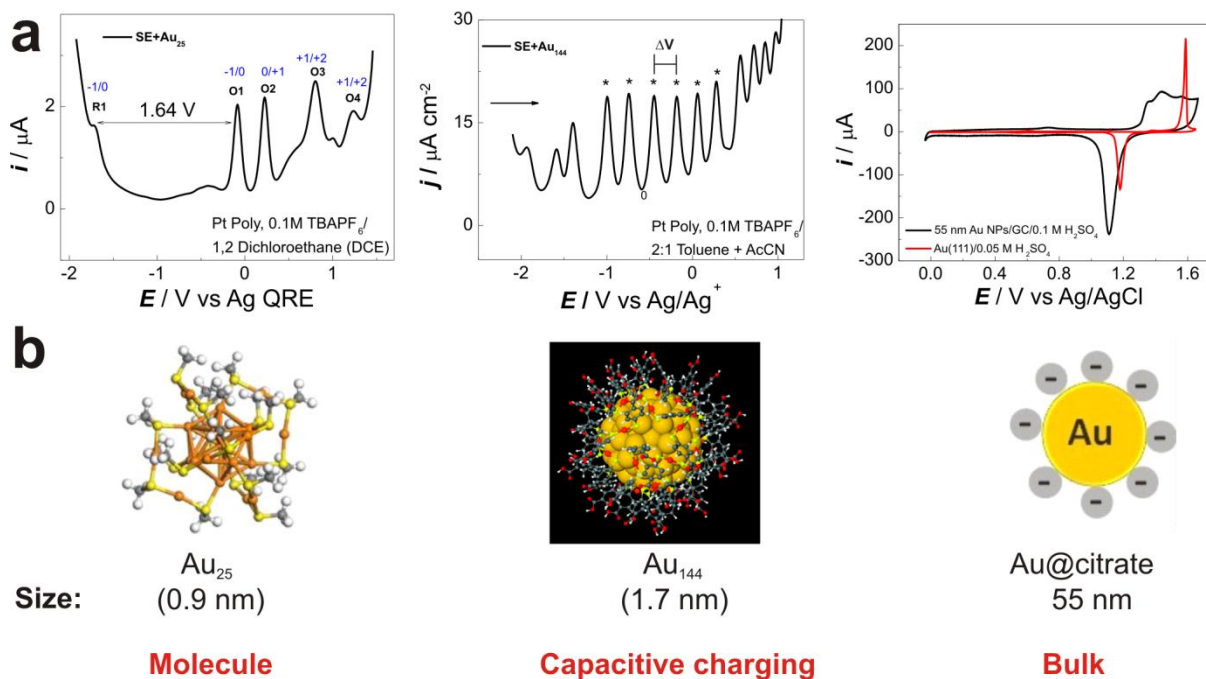
**Figure 1.** (a) Overview of the core size dependent voltammetric behavior of MPCs [$Au_{25}(C_6S)_{18}$, $Au_{38}(C_6S)_{24}$, $Au_{144}(C_6S)_{60}$, Au@citrate measured in our lab and (b) the corresponding simplified structures from refs[3-5].

voltammetry can be classified into three categories: Molecule-like voltammetry (size <1nm), quantized double layer charging (size 2-3nm) and bulk continuum voltammetry (size >3nm)[1], An example for these different categories is shown in **Figure 1** for the voltammograms of gold MPCs ranging from sub-nanometer to 100 nm size.

In the two examples of Figure 1 showing the quantum effects ("Molecule" and "Capacitive charging"), each peak corresponds to an addition or removal of an electron, and the peak spacing $\Delta V$ is connected to the MPC capacitance $C_{MPC}$ by the formula $\Delta V = e/C_{MPC}$ .[6, 7] For the experimental observation of quantized charging, $\Delta V$ should be greater than $6k_BT/e$ (~150 mV at room temperature) to enable to resolve individual peaks[2]. For metallic clusters (size 2-3 nm), the charging is purely a capacitive phenomenon and the successive addition and the removal of electrons is separated by the charging energy only. This capacitive charging arises from the nanometer size core and sub-attofarad capacitance associated with the protected ligand monolayer shell. The addition or removal of an electron to the MPCs (acting as a tiny capacitor) alters the energy barrier of the MPCs. This associated energy barrier must be overcome before a second electron is added or removed to/from the MPC[8], and this additional energy barrier results in the voltage separation between the adjacent charging events. These phenomena can be anticipated as waves in linear sweep or cyclic voltammetry (CV) of dispersed clusters in solution or of immobilized clusters on a metal electrode, and as peaks in differential pulse voltammetry (DPV)[8]. However, the voltammetric features of clusters depend also on the size of the cluster. As the size of the cluster decreases, the evolution of the HOMO-LUMO gap is noticed, similar to the case of molecules[9]. The first two added or removed electrons occupy the same energy level, and the spacing between them is the capacitive charging. Therefore, for small clusters the charging is a combination of capacitive and molecule-like behavior[8]. The electrochemical energy gaps and the HOMO-LUMO gaps of Au MPCs with different size are listed in **Figure 2**.
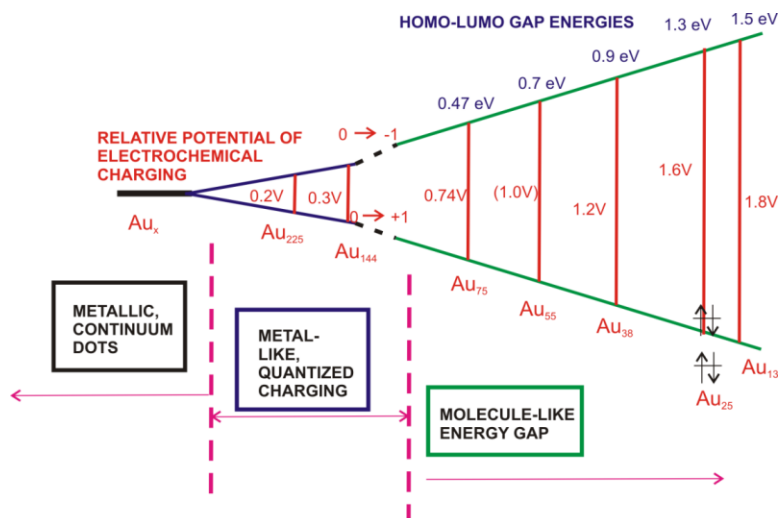
**Figure 2.** Energy level gaps for different size Au MPCs. From[1].

**Cluster capacitance models:**

The cluster capacitance determines the charging energy related with the peak separation ΔV. Therefore it is important to determine factors that affect the cluster capacitance. An electrostatic model for the clusters predicts how the capacitance value changes with the cluster core size and the ligand shell property, as shown in **Figure 3**[9, 10].



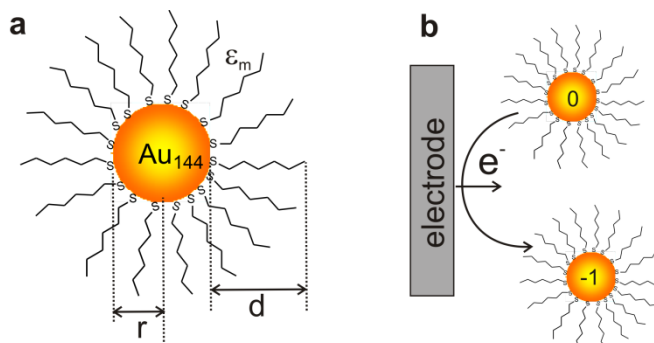**Figure 3.** Schematics of hexane-1-thiol protected gold MPCs (a) and the single electron transfer process in a freely diffusing MPC at the electrode/ electrolyte interface.

The first model used for calculating the cluster capacitance is a purely electrostatic, concentric sphere capacitor model[11].

$$C = 4\pi\varepsilon_m\varepsilon_0 \left(\frac{r}{d}\right)(r + d) \qquad\qquad \text{Equation (1)}$$

where $C$ is the cluster capacitance, $\varepsilon_m$ is the relative permitivitiy of the thiol monolayer (ligand shell), $\varepsilon_0$ is the permittivity of the free space. $r$ is the radius of the cluster core and $d$ is thethickness of the monolayer shell. Even though the concentric sphere capacitor model predicts the capacitance values and explains the experimentally observed increase of capacitance values using shorter ligands and larger cores, it fails to explain the increase of capacitance values at higher charge states, and the decrease of the capacitance value at a close to zero charge state[10, 12, 13]. The above model does not take into account of electrical double layer formation between the charged particle and the ions of electrolyte. It also assumes the potential drop across the core and bulk phase happens in the protective monolayer. Finally, it has also not been included the effect of solvent on the capacitance values of the clusters.[11]

Later, a concentric sphere model has been developed by Girault *et al.*,[14] who introduced the solvent medium effect.

$$\Delta V = \frac{e}{4\pi\varepsilon_0(r_0+d)}\left(\frac{d}{\varepsilon_m r_0} + \frac{1}{\varepsilon_s}\right) \qquad \text{Equation (2)}$$

Where, $e$ is the elementary charge of electron and $\varepsilon_s$ is the dielectric constant of the solvent. This model predicts solvent dependent capacitances and ignores the double layer formation. Later, Quinn *et al*,[2, 15] introduced a more complex model, which takes into account the formation of the electrical double layer around the MPCs and ion penetration into the monolayer to explain the increase of the capacitance values at higher charge states.

## 2.2 Charge transport through individual nanoparticles in an Electrochemical Scanning Tunneling Microscopy and Scanning Tunneling Spectroscopy (EC-STM/STS) configuration

The charging phenomena seen in voltammetric experiments are described in analogy to classical Coulomb stair-case experiments.[16] Whereas classical voltammetric experiments describe electron transfer processes in an ensemble of particles, an electrochemical STM/STS configuration enables to study the electrical transport properties up to a single particle level, as shown schematically in **Figure 4a**. The charge transport in MPCs is mainly affected by three energy factors, namely the energy level spacing $\Delta E$, the coulomb repulsion energy $E_c$ and the

thermal energy $k_BT$[2]. In order to observe single electron charging phenomena at room temperature experimentally, the following conditions must be fulfilled.

1. The two barrier resistance values (tip to MPC and MPC to substrate) should be higher than the quantum resistance, $h/e^2 = 25.8$ kΩ.

2. The single electron charging energy $E_C$ should be higher than the thermal energy $k_BT$ at room temperature.

The above two conditions are fulfilled by the intrinsic nature of the MPC core size and structure of the monolayer ligand shell. Therefore we can do the STM/STS studies for the single electron transfer events through the MPCs.
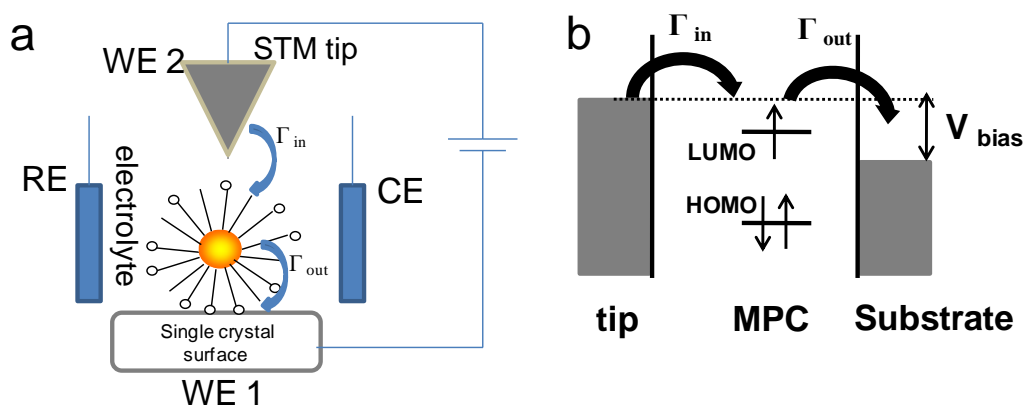


**Figure 4. (a)** Schematics of double tunneling barriers in the case of the electrochemical scanning tunneling spectroscopy of assembled monolayer protected Au clusters. **(b)** Schematics of the energy level alignment of the tip and substrate with an MPC showing the possible electron transport process.

The principle of the electrochemical STS experiments is based on the situation when the Fermi levels of the tip and the substrate come into resonance with the Fermi level of the nanoparticle, whereby the charge transport occurs through the tip-particle-substrate junction, as shown in **Figure 4b**. The process can therefore be described as two consecutive molecular reduction and re-oxidation sequence[17].

The advantage of tunneling spectroscopy is that it enables both the injection/withdrawal of electrons into/from the MPCs, as well as a simple shuttle transfer of the electrons through the MPCs. In contrast to this, voltammetric techniques are limited to only injection/withdrawal of electrons into/from MPCs. Therefore Electrochemical tunneling spectroscopy is a good tool to understand the energy level information of the given cluster entity.

If the tunneling rate into the cluster ($\Gamma_{in}$) is faster than the tunneling out of the cluster ($\Gamma_{out}$), then the electrons accumulate in the cluster. If, however, the tunneling rate into the cluster is slower than the tunneling out of the cluster, the electrons just shuttle through the cluster. The first case is called shell filling spectroscopy, whereas the second case is called shell tunneling spectroscopy.[2] Therefore, the charge transport through a single cluster can be tuned by adjusting the distance between the STM tip and the cluster. In most of the STM configurations the asymmetric nature of the junction has a significant effect on the charge transport through the system. Experimentally the above discussed principles have been tested very well at cryogenic temperatures in the case of semiconductor quantum dots[18-21] whereas only very limited studies have been done on metal MPCs[16, 22].

## 2.3 Charge and mass transport studies in ionic liquids

Kaufman[23] and Engler[24, 25] proposed that electrons provide conductivity of thick films of a pyrrolizin electroactive polymer by hopping between the redox sites. They argued that the process of electron transfer occurs only if the electroactive sites are enough mobile and the film matrix is sufficiently porous to allow the penetration of ions by supporting electrolyte to maintain electroneutrality.[26] It has been then shown that this mechanism **may also** be valid for charge propagation when ionic redox species are bound electrostatically within polyelectrolyte films.[27-31] These studies discussed the diffusion limited current in the context of the Dahm-Ruffs relation[32, 33], who proposed the following relation for the *experimentally*[34] found diffusion coefficient of a redox couple in homogeneous solution ($D_{APP}$) in terms of the second order self-exchange rate constant for the redox couple, ($k_{EX}$) and the diffusion coefficient that measured in the absence of the electron self-exchange ($D_{PHYS}$), **Figure 5**.[31]
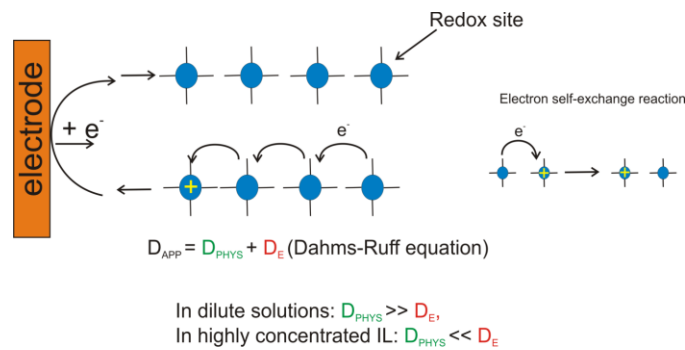


**Figure 5.** Schematics of charge transport in highly concentrated redox ILs. From[35]

$$D_{App} = D_{PHYS} + D_E$$

From cubic lattice model, $D_E = \frac{K_{ex}\,\delta^2 C}{6}$

$$\therefore D_{App} = D_{PHYS} + \frac{K_{ex}\,\delta^2 C}{6} \qquad (1)$$

Where, $k_{Ex}$ is electron self-exchange rate constant, $\delta$ is the distance between the redox sites where the electron transfer occurs, $C$ is the total concentration of the redox species. $6$ is the number of direction electron can exchange.[35]

Murray et al.[36, 37] applied the above mentioned concept also in the discussion of charge transport mechanism of redox ILs. However, there is no *direct* experimental evidence to-date to support this hypothesis. In addition to charge transport studies involving also conductivity, mass transport properties such as diffusion coefficients and viscosity are also important quantities for the understanding of the structure-related properties of ILs. In this field, the consideration of concepts such as ionicity, that may affect the modelling and interpretation of transport equations, remains a challenging task. To gain a further insight in both the charge and mass transport properties of ILs more detailed studies are still required.

In view of the possible future increased application of ILs as electrolyte systems for nanoscale studies at the electrode/electrolyte interface, a redox IL has been chosen in this thesis for detailed studies, allowing both the investigation of charge transfer and of mass transfer in the same system.

## 2.4 Linear Sweep and Cyclic Voltammetry (CV)

Linear sweep and cyclic voltammetry are amongst the most important techniques employed by electrochemists to investigate the mechanisms of electrochemical reactions. In the case of cyclic voltammetry, the potential is swept linearly with constant sweep rate (v) first in one direction, then reversed and scanned in the opposite direction at the same sweep rate (v) within a certain potential range, as shown in **Figure 6** (left side). A typical reversible current-voltage response for the case of a soluble redox compound dissolved in the electrolyte has the form shown in

**Figure 6** (right side). The current response when sweeping the potential to negative values is called cathodic current ($I_{pc}$), and the positive counterpart is called anodic current ($I_{pa}$). The corresponding peak potentials are named $E_{pc}$ and $E_{pa}$, respectively. The height and width of the peaks, the separation between the peak potentials $E_{pc}$ and $E_{pa}$, and the correlation between peak height and sweep rate strongly depend on the kinetics of the electrochemical process. The formal potential of the redox system is given as $E_0 = (E_{pc} + E_{pa})/2$[38] and can then be used to identify the involved redox compounds.
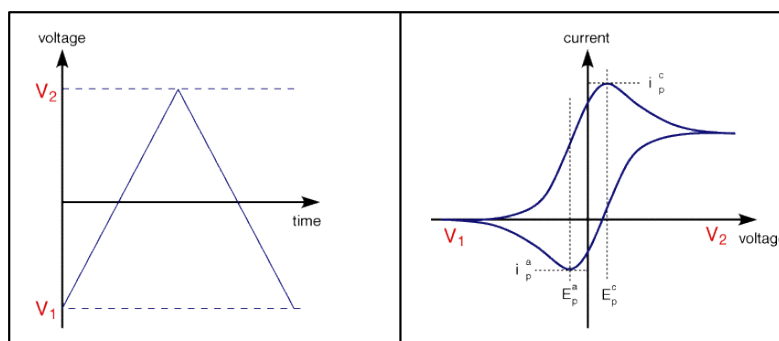


**Figure 6.** Cyclic voltammetry: Potential-time signal (left side) and typical current-voltage curve for a redox system in solution (right side). From[39]

Experiments are usually carried out in a solution containing a large excess of inert electrolyte in order to increase the conductivity of the solution, to eliminate effects of migration of any charged analyte and to compress the size of the double layer adjacent to the working electrode to the nm range or below. For a diffusion-controlled, reversible electrochemical redox reaction the voltammogram recorded has certain well defined characteristics.[38]

i) The potential separation between the current peaks is $\Delta E_p = E_{pc} - E_{pa} = 59/n$ mV; n = the number of electrons.

ii) The ratio of the peak currents amounts to ($I_{pc}/I_{pa}$) = 1 at different scan rates.

iii) The peak current $I_p$ is proportional to the square root of the sweep rate ($v^{1/2}$) and to the bulk concentration ($C_b$).

Conditions (ii) and (iii) are necessary but not sufficient criteria that a reaction is diffusion controlled. Besides them, condition (i) has to be fulfilled to prove unambiguously the diffusion controlled kinetics of the reaction.

In case of a surface-confined reversible redox reaction (adsorbed state), a linear relation between the scan rate and the heights of the corresponding current peaks is observed.[38]

## 2.5 Differential pulse voltammetry (DPV)

All electrochemical pulse modulation techniques have been developed to minimize the contribution and overlap of charging and adsorption currents over faradaic currents involving an electron transfer with the compound to be investigated. DPV is an example of such a pulse modulated technique, where a potential pulse of constant amplitude and width is modulated on top of a linear potential scan, as shown in **Figure 7**. The current is sampled just before and at the end of the modulation pulse, recording the current difference as the result. The obtained difference current – voltage curves resemble approximately the first derivative of a sampled normal linear voltage scan, resulting in sharper peaks instead of waves.
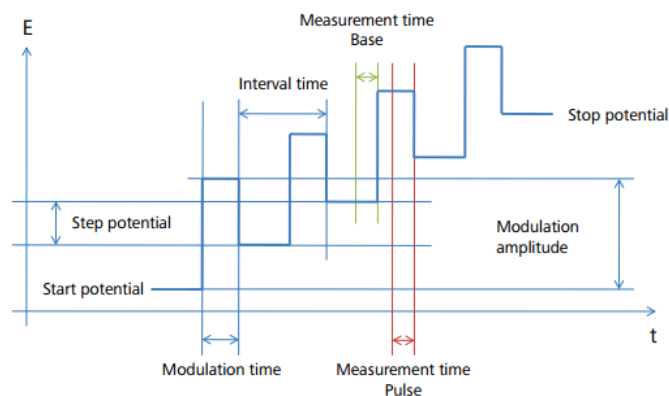


**Figure 7.** The potential-time program for differential pulse voltammetry. From[39]

Compared to the normal pulse technique, Faradaic signals can be discriminated better from background signals related with double layer charging and adsorption, due to the larger 2nd derivative of the current/potential relation for faradaic processes. In this way, the sensitivity is increased and the measured current represents almost exclusively a faradaic reaction involving a direct electron exchange with the compound. To avoid distortion and broadening of the DPV peaks, the modulation amplitude should preferably be used in the range of 5-100 mV.[40]

## 2.6 Electrochemical STM/STS

Scanning tunneling microscopy (STM) was invented in 1981 at the IBM Zurich Research Laboratory by G. Binnig and H. Rohrer.[41] This technique is widely used in the fields such as surface and interfacial science, biochemistry and nano-electronics.

When an atomically sharp conductive tip is brought close to a conductive surface with a bias voltage, electrons tunnel from one side to the other side. The tunneling current follows the exponential dependence on the tunneling distance (gap width) as shown below.[42]

$$i \propto E_{bias} \, . \, exp\left(-\frac{4\pi}{h}\sqrt{2m_e\Phi}.s\right)$$

Here, $E_{bias}$ represents the bias voltage, $m_e$ is mass of the electron, $h$ is the Plank constant, $\Phi$ is barrier height and $s$ is gap width.

Later, the STM was extended to solid-liquid interfaces at electrochemical conditions independently by the groups of Bard et al.[43], Siegenthaler et al.[44], Itaya et al.[45], and Behm et al.[46]. All 4 groups employed the same concept, presented schematically in **Figure 8,** whereby the potential of the working (substrate) electrode $E_S$ and of the tunneling tip $E_T$ are independently controlled versus a reference electrode by means of a bipotentiostat. This allows to adjust the potential of the tip to a value where only a vanishing faradaic current flows, whereas the potential of the working electrode is set to a value where the electrochemical process to be investigated occurs. The tunneling bias voltage is then given by $E_{bias} = E_T - E_S$. The independent control of the tip potential at an appropriately chosen value where faradaic reactions are absent is the most important measure to prevent the superposition of the tunneling current by unwanted faradaic currents at the tip, which can be a principal problem in electrolytic STM. An equally important disturbance of the tunneling current can occur from capacitive current contributions at the tip, as the double layer capacitance of the substrate-electrolyte-tip configuration can give rise to charging current signals due to small fluctuations in the tip-substrate distance. To reduce this effect, the substrate-electrolyte-tip double layer capacitance has to be lowered by decreasing drastically the tip surface exposed to the electrolyte with rigorous tip insulation except for the foremost protruding tip part.

Electrochemical STM (EC-STM) offers great advantages not only to image electrode surfaces and processes in contact with the electrolyte at atomic scale, but also to study the charge transport through systems up to single molecule level, as shown in the previous subchapter in the STM-break junction method. In combination with high-resolution imaging, STM-based charge transport studies are powerful tools for enhanced insight into correlations between structure and functional properties of nanoscale systems. In addition to the STM imaging, three possible STM-based spectroscopic modes

i)      tunneling current-distance ($i_t$-s) mode,

ii)     tunneling current-overpotential ($i_t$-$\eta$, fixed $E_{bias}$) mode, and

iii)    current-variable bias ($i_t$-$E_{bias}$) mode

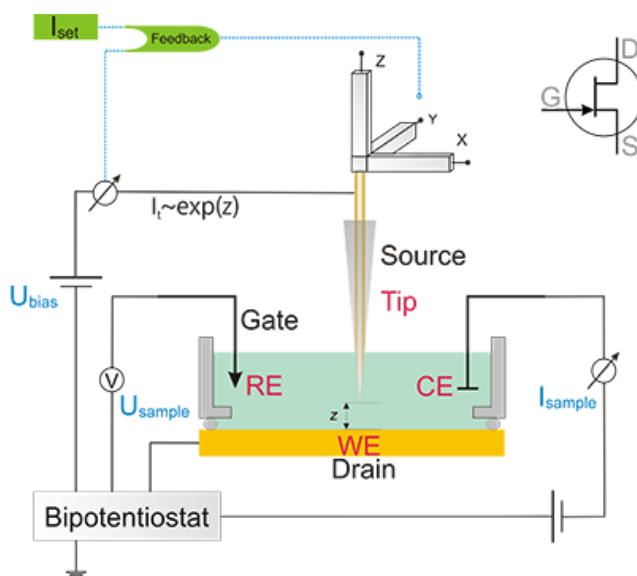can be performed.



**Figure 8.** Schematics of an electrochemical STM set-up.[47]

## 2.7 References

[1]     R. W. Murray, *Chem. Rev.* **2008**, *108*, 2688.
[2]     T. Laaksonen, V. Ruiz, P. Liljeroth, B. M. Quinn, *Chem. Soc. Rev.* **2008**, *37*, 1836.
[3]     O. Lopez-Acevedo, J. Akola, R. L. Whetten, H. Grönbeck, H. Häkkinen, *The Journal of Physical Chemistry C* **2009**, *113*, 5035.

[4]     J. Akola, M. Walter, R. L. Whetten, H. Häkkinen, H. Grönbeck, *J. Am. Chem. Soc.* **2008**, *130*, 3756.
[5]     yuchinhuang, Vol. 2012, http://yuchinhuang.wordpress.com/,  **2012**.
[6]     A. C. Templeton, W. P. Wuelfing, R. W. Murray, *Acc. Chem. Res.* **2000**, *33*, 27.
[7]     R. W. Murray, *Chemical Reviews (Washington, DC, United States)* **2008**, *108*, 2688.
[8]     O. Toikkanen, Vol. Doctoral, School of Chemical Technology, Aalto University publication series DOCTORAL DISSERTATIONS 19/2011 **2011**, 136.
[9]     S. Chen, *Science* **1998**, *280*, 2098.
[10]    J. F. Hicks, A. C. Templeton, S. Chen, K. M. Sheran, R. Jasti, R. W. Murray, J. Debord, T. G. Schaaff, R. L. Whetten, *Anal. Chem.* **1999**, *71*, 3703.
[11]    S. Chen, R. W. Murray, S. W. Feldberg, *The Journal of Physical Chemistry B* **1998**, *102*, 9898.
[12]    J. F. Hicks, D. T. Miles, R. W. Murray, *J. Am. Chem. Soc.* **2002**, *124*, 13322.
[13]    R. Guo, D. Georganopoulou, S. W. Feldberg, R. Donkers, R. W. Murray, *Anal. Chem.* **2005**, *77*, 2662.
[14]    B. Su, H. H. Girault, *The Journal of Physical Chemistry B* **2005**, *109*, 11427.
[15]    B. M. Quinn, P. Liljeroth, V. Ruiz, T. Laaksonen, K. Kontturi, *J. Am. Chem. Soc.* **2003**, *125*, 6644.
[16]    R. S. Ingram, M. J. Hostetler, R. W. Murray, T. G. Schaaff, J. T. Khoury, R. L. Whetten, T. P. Bigioni, D. K. Guthrie, P. N. First, *J. Am. Chem. Soc.* **1997**, *119*, 9279.
[17]    A. M. Kuznetsov, J. Ulstrup, *The Journal of Physical Chemistry A* **2000**, *104*, 11531.
[18]    E. P. A. M. Bakkers, D. Vanmaekelbergh, *Physical Review B* **2000**, *62*, R7743.
[19]    E. P. A. M. Bakkers, A. W. Marsman, L. W. Jenneskens, D. Vanmaekelbergh, *Angew. Chem. Int. Ed.* **2000**, *39*, 2297.
[20]    E. Bakkers, D. Vanmaekelbergh, *Physical Review B* **2000**, *62*, R7743.
[21]    E. P. A. M. Bakkers, Z. Hens, A. Zunger, A. Franceschetti, L. P. Kouwenhoven, L. Gurevich, D. Vanmaekelbergh, *Nano Lett.* **2001**, *1*, 551.
[22]    P. Yang, I. Arfaoui, T. Cren, N. Goubet, M.-P. Pileni, *Nano Lett.* **2012**, *12*, 2051.
[23]    A. Taleb, F. Silly, A. O. Gusev, F. Charra, M. P. Pileni, *Advanced Materials (Weinheim, Germany)* **2000**, *12*, 633.
[24]    F. B. Kaufman, E. M. Engler, *J. Am. Chem. Soc.* **1979**, *101*, 547.
[25]    A. H. Schroeder, F. B. Kaufman, V. Patel, E. M. Engler, *J. Electroanal. Chem. Interfacial Electrochem.* **1980**, *113*, 193.
[26]    N. Oyama, F. C. Anson, *J. Electrochem. Soc.* **1980**, *127*, 640.
[27]    D. A. Buttry, F. C. Anson, *J. Electroanal. Chem. Interfacial Electrochem.* **1981**, *130*, 333.
[28]    H. S. White, J. Leddy, A. J. Bard, *J. Am. Chem. Soc.* **1982**, *104*, 4811.
[29]    C. R. Martin, I. Rubinstein, A. J. Bard, *J. Am. Chem. Soc.* **1982**, *104*, 4817.
[30]    J. S. Facci, R. H. Schmehl, R. W. Murray, *J. Am. Chem. Soc.* **1982**, *104*, 4959.
[31]    D. A. Buttry, F. C. Anson, *J. Am. Chem. Soc.* **1983**, *105*, 685.
[32]    H. Dahms, *The Journal of Physical Chemistry* **1968**, *72*, 362.
[33]    I. Ruff, V. J. Friedrich, *The Journal of Physical Chemistry* **1971**, *75*, 3297.
[34]    I. Ruff, *Electrochim. Acta* **1970**, *15*, 1059.
[35]    J. E. F. Weaver, in *Chemistry*, Vol. Ph. D., University of North Carolina at Chapel Hill, UNC Electronic Theses and Dissertations **2010**.
[36]    T. Hatazawa, R. H. Terrill, R. W. Murray, *Anal. Chem.* **1996**, *68*, 597.
[37]    R. Balasubramanian, W. Wang, R. W. Murray, *J. Am. Chem. Soc.* **2006**, *128*, 9994.
[38]    Z. Li, *Dissertation* **2007**, *16*.
[39]    A.J. Bard, L.R. Faulkner, *Electrochemical Methods*, John Wiley&Sons,  2001.
[40]    NOVA, user, mannual, *http://www.ecochemie.nl/download/NovaTutorials/VA_tutorial.pdf*.
[41]    G. Binnig, H. Rohrer, C. Gerber, E. Weibel, *Appl. Phys. Lett.* **1982**, *40*, 178.
[42]    J. G. Simmons, *J. Appl. Phys.* **1963**, *34*, 1793.
[43]    Ovadia Lev, Fu-Ren Fan, A. J. Bard, *J. Electrochem. Soc.* **1988**, *135*, 783.

[44]    P. Lustenberger, H. Rohrer, R. Christoph, H. Siegenthaler, *J. Electroanal. Chem. Interfacial Electrochem.* **1988**, *243*, 225.

[45]    K. Itaya, E. Tomita, *Surf. Sci.* **1988**, *201*, L507.

[46]    J. Wiechers, T. Twomey, D. M. Kolb, R. J. Behm, *J. Electroanal. Chem. Interfacial Electrochem.* **1988**, *248*, 451.

[47]    W. Thomas, http://wandlowski.dcb.unibe.ch/research/equipment/stm.html,  **2005-2007**.

# 3. Experimental procedures and instrumentations

## 3.1 Chemicals and materials

All the chemicals and materials used in this thesis can be found in the corresponding result chapters under the sections *chemicals and materials*.

## 3.2 General procedures of cleaning cells

For synthesis purpose the glassware was first cleaned with aqua regia to remove any trace amount of metal ions and rinsed well with Milli-Q water and was then dried in an oven. In the case of conventional electrochemical experiments the glass ware were boiled in a 25 % HNO₃ solution and rinsed thoroughly with Milli-Q water, followed by a boiling process in Milli Q water for three to four times to completely remove the acid from the surfaces. In the case of EC-STM experiments, cell and O ring were soaked in a piranha solution and repeated as above to remove all the acid.

## 3.3 Sample preparation for electrochemical, EC-STM and Raman experiments

### 3.3.1 Electrode fabrication

The below mentioned single crystal half bead and "bead-on-a-sheet" electrodes have been fabricated in our research group according to the procedure described in the Supplementary Information of the publication by Kolivoska et al[1]:  Here we describe the fabrication of Pt(111) (i) half-bead and (ii) "bead-on-a-sheet" electrodes. Using the similar procedure corresponding gold electrodes could be prepared. Adapted from[1]

**Fabrication of bead electrodes**. A Pt wire (0.50 mm in diameter, 99,999%, Goodfellow) was first cleaned by immersion into an aqua regia mixture for ≈ 10 s. Afterwards, the wire was rinsed with Milli-Q water and vertically positioned by the aid of a lab clamp. The lower part of the Pt wire was melted by a hydrogen flame, forming a progressively growing Pt bead. The melting of the wire was stopped when the bead size reached approximately 2 mm in diameter.

Subsequently, the bead was heated up and melted again. After letting it solidify without cooling down completely, the bead was quickly immersed into the aqua regia mixture for 10 s and copiously rinsed with Millipore water. This melting/immersing/rinsing cycle is known to gradually remove impurities driven to the surface of the Pt bead. The cycles were repeated until no impurities could be observed on the surface upon heating the bead in the flame. The Pt bead prepared in this way was melted again and left to solidify *very slowly* using the hydrogen flame from a nozzle positioned on a slowly moving lab jack. The resulting Pt bead electrode **(Figure 1a)** was immediately placed in a glass test-tube to avoid contamination. The bead electrode was further processed either (i) to form a half-bead Pt(111) electrode (for hanging meniscus-type of measurements, **(Figure 1b)** or alternatively (ii) was fixed on a platinum sheet (10 mm x 10 mm x 1.0 mm, 99.95% Goodfellow (**Figure 1c**) equipped with a 0.50 mm (diameter) Pt wire for electrical connection. The half- bead Pt(111) electrode **(Figure 1b)** was used to study the shell
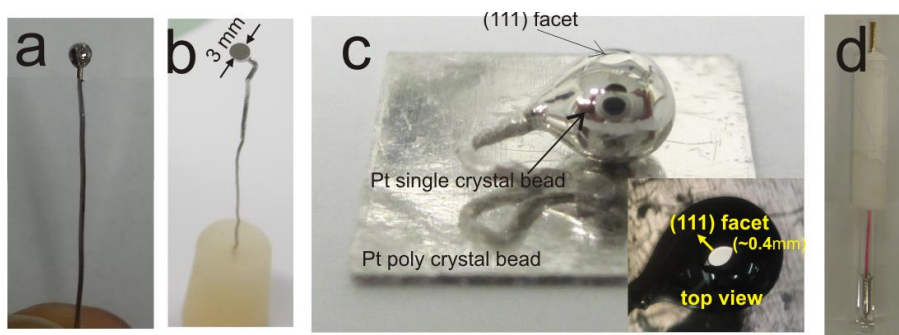


**Figure 1.** Photographs of a lab-made half-bead Pt(111) electrode (b), and a lab-made "bead-on-a-sheet" Pt(111) electrode (c). The inset shows the top view of the "bead-on-a-sheet" electrode. Commercial polycrystalline Pt microelectrode (d).

isolated nanoparticle Raman experiments and for voltammetric experiments with $Au_{144}$ mixed MPCs assemblies. The Pt "bead-on-a-sheet" electrode **(Figure 1c)** was fabricated so that one of the (111) facets (naturally grown on the bead and with an area of several $\mu m^2$) pointed upwards **(Figure 1c, inset)**. The facet was used as a substrate for all electrochemical STM/STS experiments. A commercial gold microdisk electrode (Bioanalytical Systems), shown in **Figure 1d,** was used for all chronoamperometric measurements, as well as cyclic voltammetry and electrochemical impedance measurements in the study of the viologen redox-active Ionic Liquid.

**Fabrication of half-bead (hanging-meniscus type) Pt(111) electrodes.** A Pt wire attached to a bead electrode **(Figure 1a)** was glued to an aluminum cylinder. The bead was oriented so that

one of the naturally grown (111) facets was parallel to the cylinder surface. A proper alignment was ensured by inspecting the direction of a laser beam reflected off the (111) facet. The aluminum cylinder with the bead electrode was placed into a steel drum of a matching size. A quickly solidifying two-component dispersion (Technowitz 4004, Heraeus Kulzer GmbH) was poured on the Pt bead in the steel drum until the bead was entirely immersed. The assembly was left to harden overnight. The entire assembly was then polished by an emery paper (coarseness P100) in the direction parallel to the electrode surface until approximately half of the bead was removed. The newly exposed surface was subsequently polished by a series of emery papers with decreasing coarseness (P100 to P1200) and then with an aqueous colloidal dispersion of alumina with gradually decreasing particle sizes (from 1 μm through 0.3 μm to 50 nm). Finally, the Technowitz dispersion was removed by dissolving by a repetitive boiling in acetone. The released half-bead electrode **(Figure 1b)** was subsequently cleaned by an immersion into the concentrated $H_2SO_4$ (Sigma Aldrich) overnight, to remove the Technowitz dispersion and alumina residues. The electrode was then extensively rinsed with Milli-Q water, tempered in an electromagnetic induction oven at orange heat (≈1500 °C) in an argon atmosphere overnight, cooled down to room temperature and immediately placed in a clean glass test-tube under the argon atmosphere for storage. The electrode surface was inspected by cyclic voltammetry in the aqueous 0.1 M $H_2SO_4$ (Merck, Suprapure). Only electrodes showing characteristic features of the Pt(111) surface were employed further in this study.

### 3.3.2. Preparation of electrode surfaces modified with $SiO_2$ shell-isolated NPs

A detailed description for the synthesis of silica shell-isolated Au core NPs (Au@$SiO_2$) is given in the subchapter of the publication presented in chapter 4.1 in the methods section. **Figure 2** shows a schematic representation for the sample preparation for the Raman experiments.
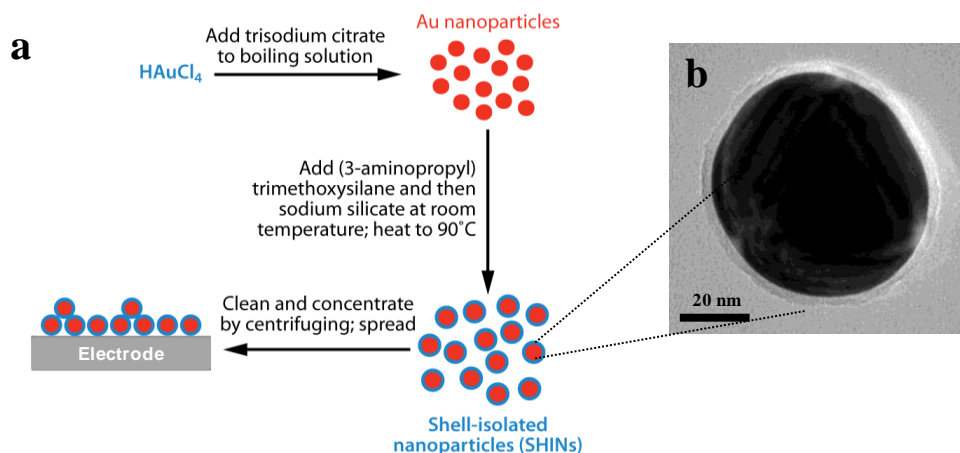
**Figure 2**. (a) Schematic presentation of the electrode surface preparation modified with shell-isolated Au NPs. From[2] (b) High-resolution transmission electron microscopy (HR-TEM) image of a single Au@SiO$_2$ NP (from chapter 4.1).

### 3.3.3. Preparation of electrode surfaces modified with Au$_{144}$ monolayer protected clusters (MPCs)

The Au$_{144}$(C$_6$S)$_{60}$(C$_{11}$H$_8$NS)$_6$ MPCs (m = 2.1 mg, M = 36 520 g/mol, n = 57 nmol) were dissolved in CH$_2$Cl$_2$ (3 mL), forming a solution with the concentration of 19 μM. Lab-made Pt (111) electrodes **(Figure 1a, 1c)** were flame-annealed with a butane flame, shown in **Figure 3a,**
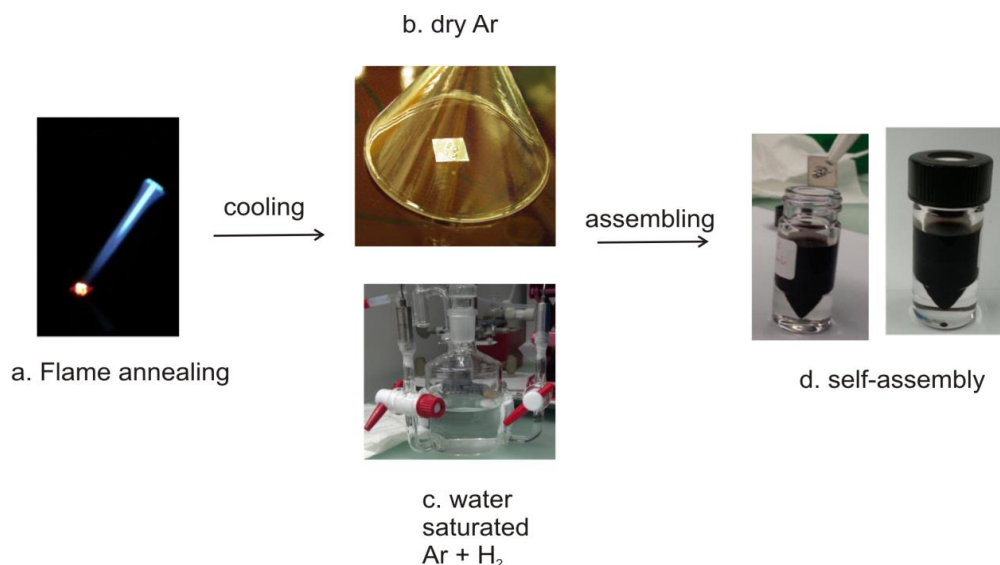


**Figure 3.** Photographs for the self-assembling procedure of Au$_{144}$ mixed monolayer MPCs onto the Pt(111) surface. Details are given in the text.

for 1 minute to red-glow temperature and subsequently cooled down in two different ways: (1) under a dry Ar stream for about 10 min, shown in **Figure 3b,** and (2) by cooling in a closed flask containing a water-saturated mixture of Ar/H$_2$ (4:1 v/v), shown in **Figure 3c**. After that, the electrode was immersed into the above cluster solution (**Figure 3d**) for 1 hour and rinsed with 10 ml of CH$_2$Cl$_2$ to remove all physisorbed MPC layers. The electrode was then immediately transferred into the deareated electrochemical cell.

## 3.4. Electrochemistry

All electrochemical experiments were carried out by either using a commercial μ-Autolab type-III potentiostat/galvanostat (PGSTAT-30; Metrohm Autolab) system or using a homemade potentiostat/controlling system.[3] Before each measurement, the single crystal electrodes were first cleaned by an electrochemical polishing method followed by annealing with a butane flame. In particular, the Au and Pt single-crystal electrodes were anodically oxidized at +5 V in 1 M H$_2$SO$_4$ for 30 seconds and then chemically reduced by keeping the electrode in 1 M HCl solution about 1 minute followed by extensive washing with Milli-Q water to remove all the adsorbed chloride ions on the electrode surface. The above procedure was repeated three to four times. As a result of this procedure, surface layers were removed and a fresh surface was obtained for each experiment. The resulting electrode was then flame-annealed. After flame-annealing, the electrode was cooled in Ar environment to avoid the surface contamination. The above mentioned electrochemical polishing method was also used to remove the nanoparticles from the surface.

A lab-made large volume glass cell with a typical volume of working solution of 50-150 mL, shown in **Figure 4a**, was used for the measurements in the aqueous solutions. For the experiments in organic electrolytes and in ionic liquids a single compartment small-volume cell with a working volume as small as 200 µL, shown in **Figure 2b.** An Ag/AgCl- or a Pt or Ag wire were used as reference electrodes, and a Pt wire served as counter electrode. The electrolyte solutions were de-oxygenated by Ar bubbling for 15-20 minutes before each experiment. The
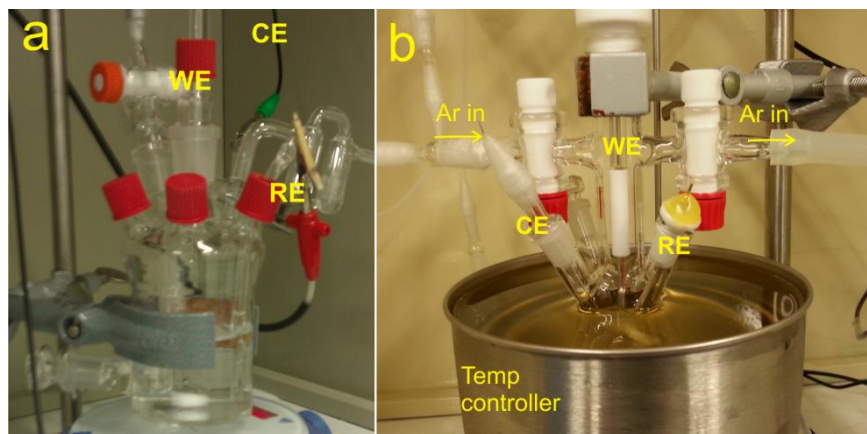
**Figure 4.** Photographs of the large volume and small volume electrochemical cells. Further explanations in the text.

space over the electrolyte in the electrochemical cell was continuously purged with Ar to avoid any further oxygen contamination during the measurement. The cleaned working electrodes were fixed into the glass capillary holder and contacted with the electrolyte solutions under a preset precise potential control. All electrochemical measurements were carried out in a Faraday cage to shield the experimental set-up from electronic noise.

## 3.5 Electrochemical STM (EC-STM)

STM tips were prepared by either mechanically cutting or electrochemically etching of a Pt/Ir (80/20) wire ($\Phi = 0.25$ mm, 99.999%; Goodfellow). In case of etching, the clamped Pt/Ir wire was immersed into a solution of 1 M $CaCl_2$ + 0.25 M HCl with an applied AC voltage amplitude of 80 V vs. a glassy carbon electrode. The cut/etched tips were then coated by a thin layer of polyethylene as shown in **Figure 5a**. For that, a small piece of polyethylene was melted on a thin Pt sheet with a small hole in its center. The cut/etched tip was then passed through the hole from the bottom part of the sheet. With this procedure, the tip was coated with polyethylene except for its outermost apex, as shown in **Figure 5b**. However, there are several materials and methods in use for coating the STM tip such as polyethylene, Apiezon wax, nail coat, or electrophoretic paint coating. Appropriate coating materials have to be selected according to the experimental electrolytic environment.
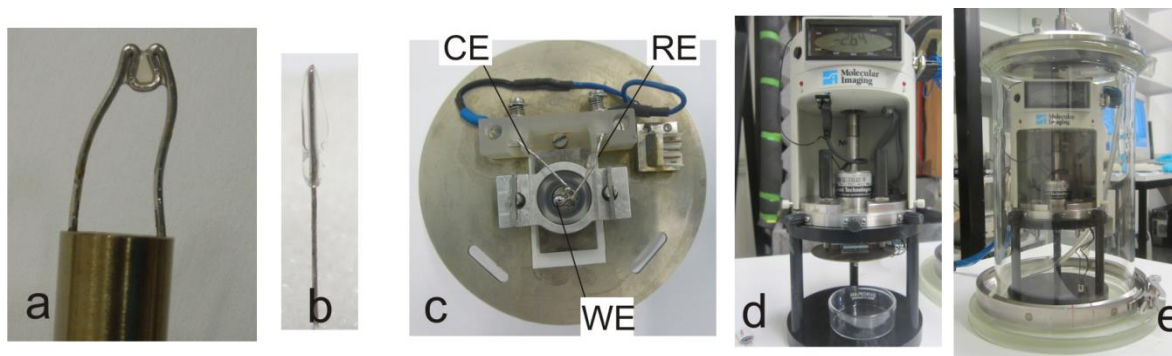
**Figure 5.** Photographs of the tip coating set-up (a), a polyethylene coated Pt/Ir tip (b), the STM cell assembled base plate (c), the Molecular imaging, MI-STM head installed with scanner (d), and the entire MI-STM together with the glass chamber (e).

**Figure 5c** shows the *assembled STM sample base plate*. The Pt single crystal surfaces were fixed on the metal holder of the STM cell by using an O-ring. Two platinum wires served as counter and quasi-reference electrode, respectively. The Pt quasi-reference electrode is stable in a ionic liquid electrolyte. An Au/AuO wire was used as quasireference electrode in 0.1 M $NaClO_4$ solution. The electrolyte was then filled into the cell after connecting the microscope setup under potential control. All EC-STM experiments were conducted using a molecular imaging indtrument (MI, Agilent technologies, Inc.), as shown in **Figure 5d**. All STM experiments were performed under Ar atmosphere (**Figure 5e**). The tip potential $E_T$ must be controlled at a proper potential range where the tip material is stable and neither oxidation of the tip nor hydrogen evolution take place. This is crucial in the case for a tungsten tip. The alternatives of the tip material are Pt-Ir and Au, which have a more extended potential window, but are usually less sharp than the tungsten tip. At an appropriately chosen potential, a well-coated tip should typically show a remaining faradaic current of less than 5 pA.

# 3.6 References

[1]    V. Kolivoska, M. Mohos, I. V. Pobelov, S. Rohrbach, K. Yoshida, W. J. Hong, Y. C. Fu, P. Moreno-Garcia, G. Meszaros, P. Broekmann, M. Hromadova, R. Sokolova, M. Valasek, T. Wandlowski, *Chem. Commun.* **2014**, *50*, 11757.
[2]    J. R. Anema, J.-F. Li, Z.-L. Yang, B. Ren, Z.-Q. Tian, *Annual Review of Analytical Chemistry* **2011**, *4*, 129.
[3]    M. Gábor, L. Chen, P. Ilya, W. Thomas, *Nanotechnology* **2007**, *18*, 424004.

# 4. Results

## 4.1    Publication 1:

**In Situ SHINERS at Electrochemical Single-Crystal Electrode/Electrolyte Interfaces:
Tuning Preparation Strategies and Selected Applications**

Authors: Jian-Feng Li, Alexander Rudnev, Yongchun Fu, **Nataraju Bodappa**, Thomas Wandlowski

Status: Published

N. Bodappa's contribution in this publication:

• Synthesis of silica ($SiO_2$) shell-isolated gold core nanoparticles and preparation of electrode surfaces modified with nanoparticles for voltammetric and Raman experiments.

# *In Situ* SHINERS at Electrochemical Single-Crystal Electrode/Electrolyte Interfaces: Tuning Preparation Strategies and Selected Applications

Jian-Feng Li,[†,§] Alexander Rudnev,[†,‡,§] Yongchun Fu,[†] Nataraju Bodappa,[†] and Thomas Wandlowski[†,*]

[†]Department of Chemistry and Biochemistry, University of Bern, Freiestrasse 3, Bern, Bern CH-3012, Switzerland and [‡]Frumkin Institute of Physical Chemistry and Electrochemistry, Russian Academy of Sciences, Leninskii pr. 31, Moscow, Moscow Oblast 119991, Russia. [§]J.-F. Li and A. Rudnev contributed equally to this work

**ABSTRACT**   We have studied Au(55 nm)@SiO$_2$ nanoparticles (NPs) on two low-index phases of gold and platinum single crystal electrodes in ClO$_4^-$ and SO$_4^{2-}$ ion-containing electrolytes by both electrochemical methods and *in-situ* shell-isolated nanoparticle enhanced Raman spectroscopy (SHINERS). We showed the blocking of the electrode with surfactants originating from the synthesis of as-prepared SHINERS NPs. We introduce an efficient procedure to overcome this problem, which provides a fundamental platform for the application of SHINERS in surface electrochemistry and beyond. Our method is based on a hydrogen evolution treatment of the SHINERS-NP-modified single-crystal surfaces. The reliability of our preparation strategy is demonstrated in electrochemical SHINERS experiments on the potential-controlled adsorption and phase formation of pyridine on Au(hkl) and Pt(hkl). We obtained high-quality Raman spectra on these well-defined and structurally carefully characterized single-crystal surfaces. The analysis of the characteristic A$_1$ vibrational modes revealed perfect agreement with the interpretation of single-crystal voltammetric and chronoamperometric experiments. Our study demonstrates that the SHINERS protocol developed in this work qualifies this Raman method as a pioneering approach with unique opportunities for *in situ* structure and reactivity studies at well-defined electrochemical solid/liquid interfaces.
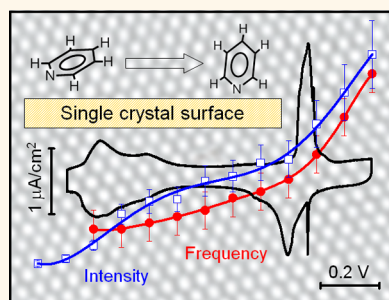
**KEYWORDS:** single-crystal electrodes · surface-enhanced Raman · SHINERS · Au@SiO$_2$ · nanoparticles · cyclic voltammetry · pyridine

Surface enhanced Raman spectroscopy is a powerful spectroscopic technique to study molecular adsorption and mechanisms of electrochemical reactions at metal/electrolyte interfaces.[1−3] The method was initially limited to rough and/or nanostructured surfaces of coinage metals and subsequently extended toward transition metals by exploiting various concepts of "borrowing" SERS activity.[4−6] During the past decade, template and nanoparticle-based fabrication strategies led to various SERS-active plasmonic nanostructures of controlled size, shape and composition to approach single molecule sensitivity and to overcome the problem of ill-defined surface morphologies of roughened samples.[7,8] Examples for applications at electrochemical solid/liquid interfaces are gold and silver nanoclusters,[9−11] nanorods[12] and template-based or nanosphere lithography.[13,14]

The extension of SERS to well-defined single-crystal metal/electrolyte interfaces was pioneered by Otto *et al.*, who studied the adsorption of pyridine molecules on Cu(hkl) surfaces.[15] Ikeda *et al.*[16] and Cui *et al.*[17] reported high quality, potential-dependent Raman spectra of aromatic thiols on gold single-crystal electrodes using gap-mode plasmon excitation in a sandwich structure Au(hkl)/organic monolayer/Au(55 nm) nanoparticles (NPs). A particular unique approach for expanding SERS to electrified single-crystal electrode/electrolyte interfaces, termed shell-isolated nanoparticle enhanced Raman spectroscopy (SHINERS), was developed by Tian *et al.*[18−21] The principle of the method is based on the assembly of a sphere-plane gap mode system composed of gold or silver NPs surrounded by a chemically inert, ultrathin and pinhole-free coating of SiO$_2$ or Al$_2$O$_3$, dispersed on electrode surfaces, such as metals, oxides or silicon. The NPs act as plasmonic antennas and provide the electromagnetic
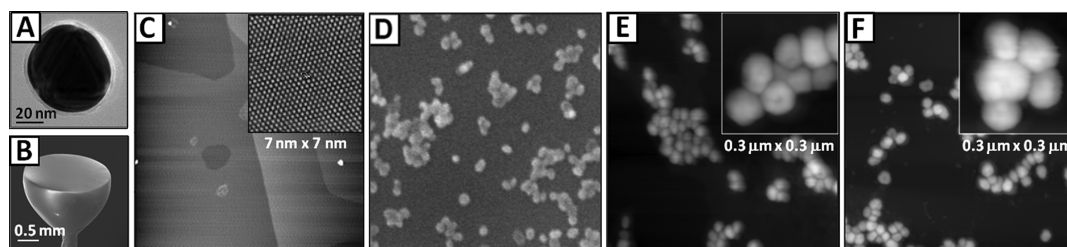
**Figure 1.** (A) HRTEM image of 55 nm Au@SiO$_2$ NPs with ∼3 nm shell thickness. (B) SEM image of a Au(111) half-bead single-crystal electrode. (C) Large-scale AFM and high-resolution (7 nm × 7 nm) STM images of an island-free Au(111)-(1 × 1) surface. (D) SEM image and (E,F) AFM images of a Au(111)-(1 × 1) single-crystal surfaces modified with Au@SiO$_2$ SHINERS NPs (E) before and (F) after HER cleaning procedure. The corresponding insets represent magnifications (0.3 $\mu$m × 0.3 $\mu$m) of SHINERS NP islands. The large scale images in panels (C) to (F) represent frames of (2 $\mu$m × 2 $\mu$m) in size.

enhancement of Raman scattering, while the SiO$_2$ or Al$_2$O$_3$ shells prevent the core from interacting with the electrochemical system under study. Three-dimensional finite-difference-time-domain (3D FTDT) simulations demonstrated that most of the enhancement occurs between the SHINERS NPs and the substrate.[18]

The overall SHINERS signal is substantially greater than for tip-enhanced Raman spectroscopy (TERS), an alternative plasmon-based approach for Raman spectroscopy at single-crystal surfaces with potential for applications in an electrochemical environment.[22,23] The latter is based on a single TERS tip, while the laser in the former approach probes a significantly larger number of plasmonic antennas.[18,19] SHINERS has been demonstrated to give high quality Raman spectra of adsorbates at various atomically flat surfaces, such as Au(hkl), Pt(hkl), Rh(hkl) and Cu(hkl). Examples include hydrogen on Pt(111)[18] and Rh(111),[19] CO on Pt(111),[19] SCN$^-$ on Au(hkl),[18] pyridine on Au(hkl) and Pt(hkl),[20] viologen on Au(111),[24] 2,2'-bipyridine on Au(hkl),[25] benzotriazole on Cu(hkl)[26] and two very recent studies of Au(111) surface oxidation in H$_2$SO$_4$[27] respective alkynes on Pt(111).[28] These pioneering studies demonstrate convincingly the ability of SHINERS to obtain high-quality face-dependent Raman spectra of adsorbates at single-crystal surfaces. The method bears a great potential in exploring correlations between structure and reactivity as well as in monitoring intermediates and pathways for a wide range of fundamental and applied processes at electrochemical interfaces.

However, the more general application of SHINERS in surface electrochemistry requires several important issues to be addressed. These include (1) the modeling of the spectroscopic response, the role of adsorbates and nearby solution species, (2) exploring SHINERS NPs as plasmonic antennas "only" and minimizing their role on the spatial occupation (blocking) of surface sites, (3) the chemical inertness of the NP-shell as well as (4) their effect on the potential distribution at the modified electrode/electrolyte interface. The preparation of chemically inert and "clean" single-crystal surfaces modified with SHINERS NPs for subsequent structure and reactivity studies is rather difficult. Reagents used in the synthesis of the NPs may interfere severely with

Raman signals of adsorbates under investigation. Attempts to improve the inertness of NPs involve iodine displacement,[29] chemical polishing with cyanide,[30,31] ozone cleaning,[32] argon ion sputtering[31] or the deposition of ligand-free NPs on suitable substrates in a vacuum.[13] However, none of these methods are applicable to single-crystal surfaces modified with SHINERS NPs because of surface roughening and damaging of the isolation shell.

In this paper we explore the influence of submonolayer coverages of Au(55 nm)@SiO$_2$ (∼3 nm) NPs on the electrochemical response of low-index gold and platinum single-crystal electrodes (Figure 1A−C) in ClO$_4^-$ and SO$_4^{2-}$ ion-containing electrolytes. We address the blocking of surface sites and introduce cathodic polarization as a unique strategy to prepare electrochemically rather inert NP-modified electrode surfaces. The quality of this preparation strategy is illustrated in electrochemical SHINERS experiments on the potential-controlled adsorption and phase formation of pyridine on Au(hkl) and Pt(hkl).

## RESULTS AND DISCUSSION

**Electrochemical Conditioning of the Au(111)-Au(55 nm)@SiO$_2$ Electrodes.** Figure 1D,E shows typical SEM and AFM images of a Au(111)-(1 × 1) surface modified with Au(55 nm)@SiO$_2$ SHINERS NPs. The sample was prepared by drop-casting a dilute NP solution followed by gentle drying in a stream of argon and subsequent extended rinsing with Mill-Q water to dissolve unbound particles. Following this protocol, we obtained submonolayers of NPs with coverages ranging between 20 to 30%. Typically, the NPs are assembled in evenly distributed small islands containing from 4 up to 30 NPs. These islands are rather uniformly distributed on the substrate surface under our experimental conditions. The statistical analysis demonstrates that the islands contain typically 15−20 NPs (see Supporting Information for details). Isolated NPs or three-dimensional clusters are rarely observed after HER treatment.

Cyclic voltammograms (CVs) recorded in the double layer regions as well as upon extension to surface oxidation and reduction demonstrate a distinct influence of
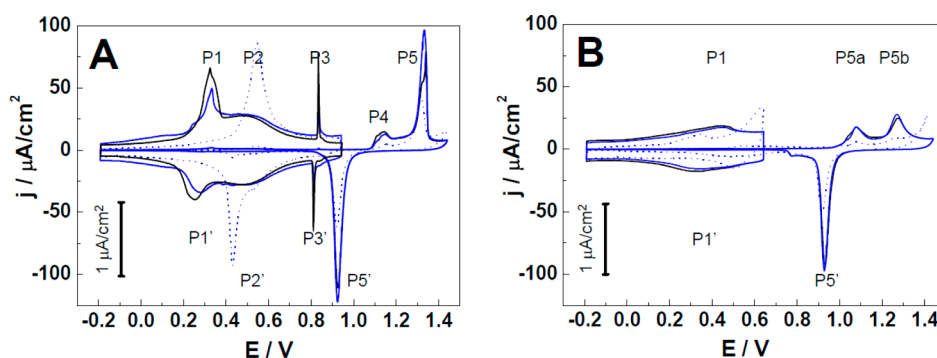
**Figure 2.** CVs of Au(111)-(1 × 1) single-crystal bead electrodes unmodified (black lines) and modified (solid blue lines) with Au@SiO$_2$ SHINERS NPs. The dotted blue traces were recorded with "as-prepared" NPs, while the solid blue lines represent data obtained with HER-SHINERS NPs. The voltammograms in the double layer region are displayed with a magnification factor of 30. Solution: 0.1 M (A) H$_2$SO$_4$ and (B) HClO$_4$. Scan rate: 10 mV/s.

the SHINERS NPs on the electrochemical response. As an example, Figure 2 displays the corresponding data for Au(111) in 0.1 M H$_2$SO$_4$ and 0.1 M HClO$_4$. The solid black lines represent the response of the unmodified, atomically flat Au(111) electrode, while the dotted blue curves are obtained in the presence of "as-prepared" SHINERS NPs following the procedure outlined in the literature[18,33] and summarized briefly in the Methods section. The double layer currents and the oxidation/reduction pattern are strongly distorted. The characteristic features in the charging current representing the lifting and reformation of the surface reconstruction Au(111)-(p × √3) → Au(111)-(1 × 1) (P1/P1'), the adsorption of sulfate ions (P2/P2') and the transition into the ordered (√3 × √7) sulfate phase (P3/P3')[27,34−39] are quenched for Au(111)/ 0.1 M H$_2$SO$_4$ in the presence of "as-deposited" NPs during both the anodic and the cathodic scans (Figure 2A). Extending the potential range up to 1.45 V demonstrates that the NPs diminish the Faraday charges representing the surface oxidation at step (P4) sites. The position of the reduction peak P5' appears to be not influenced by the presence of the "as-prepared" SHINERS NPs (Figure 2A). However, the current magnitude is reduced. Inspection of the surface by AFM reveals that multiple cycling the potential in the double layer regions and upon oxidation/reduction does not modify the coverage of the SHINERS NPs.

Similar trends as for Au(111)/0.1 M H$_2$SO$_4$ were also observed in 0.1 M HClO$_4$ (Figure 2B). The weaker specific adsorption of ClO$_4^-$ anions, as compared to SO$_4^{2-}$, leads to rather broad features for the lifting (P1) and reformation (P1') of the surface reconstruction within the time scale of the voltammetric experiments. Oxide formation on terrace sites and the AuO place exchange take place on energetically different steps as represented by the occurrence of two current peaks labeled P5a and P5b.[38,39] Their exact nature is still not clear.

In conclusion, we may state that the as-prepared SHINERS NPs influence the double layer and the oxidation/reduction response of Au(111) in H$_2$SO$_4$ and in

HClO$_4$ electrolytes severely. Possible reasons are blocking of surface sites or organic contaminants released from the NPs upon deposition and polarization.

In an attempt to overcome the undesired electrochemical response, we developed a protocol based on polarization in the hydrogen evolution range (HER) followed by sequences of electrolyte-exchange cycles. The Raman spectra were monitored simultaneously: An electrode (Au(hkl) or Pt(hkl)) modified with a submonolayer of SHINERS NPs was mounted in a three-electrode thin-layer cell (Au or Pt wires as counter electrodes, and Ag/AgCl as reference electrode) filled with deoxygenated neutral electrolyte, such as 0.1 M NaClO$_4$. We typically used a spectro-electrochemical cell in a vertical configuration (Figure 3A). A thin electrolyte film was established by positioning the working electrode close to the optical quartz window (less than 50 $\mu$m). Next, the electrode was polarized at −2.00 V vs Ag/AgCl for 50−100 s. The HER proceeds vigorously. However, the thin layer geometry prevents the formation of big hydrogen bubbles, which keeps the submonolayer of NPs rather stable. This polarization procedure was repeated 3 to 4 times, accompanied by cycles of solution exchange to remove the desorbed impurities.

The efficiency of the procedure is illustrated in the sequence of Raman spectra displayed in Figure 3B. *Trace a* was recorded at 0.00 V in 0.1 M NaClO$_4$ for Au(111) covered with 0.2 mL of Au(55 nm)@SiO$_2$ NPs. We observed broad peaks at ~1308, ~1565 and ~2883 cm$^{-1}$, which are assigned to C−C, C═C and C−H vibration modes of adsorbed organics. Polarization at −2.00 V leads to the desorption of these species as indicated by the absence of the three bands in the SHINERS *trace b* of Figure 3B. The feature at 1618 cm$^{-1}$ corresponds to the bending mode of interfacial water. Electrolyte exchange and several repetitions of the polarization at −2.00 V resulted in Raman spectra without any impurity contribution as illustrated by *trace c* in Figure 3B. The spectrum was recorded at 0.00 V. Comparison with *trace a* demonstrates the
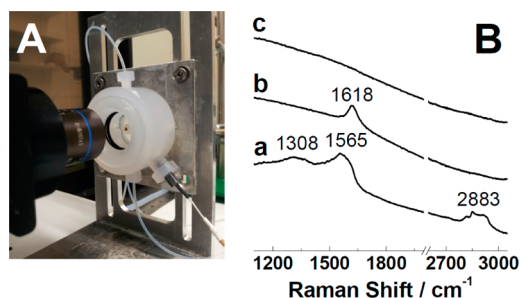
Figure 3. (A) Picture of the thin-layer electrochemical Raman cell employed for the HER-cleaning and the spectroscopic characterization. (B) SHINERS spectra of a Au(111) single-crystal electrode (a) before ($E = 0.00$ V), (b) during ($E = -2.00$ V), and (c) after ($E = 0.0$ V) the HER cleaning procedure in 0.1 M NaClO$_4$ solution.

efficiency of the HER-polarization and electrolyte exchange procedure. The SHINERS spectra plotted in Figure 3B are typical representations of properties of the entire NP-modified Au(111) surface. AFM inspection of the polarized Au(111) surface reveals a ∼5% decrease of the NP coverage and a slight increase of the island size (Figure 1F). Finally, we also like to emphasize that the HER in *acidic electrolyte* does not lead to the complete removal of organic adsorbates, as monitored by *in situ* Raman experiments.

Employing the HER-treated Au(111) electrode in voltammetric experiments in 0.1 M H$_2$SO$_4$ or 0.1 M HClO$_4$ leads to curves (solid blue lines in Figure 2) that are almost identical to the response of the NP-free surface (black lines in Figure 2). The most pronounced difference is a 10% increase of the double layer charging current at $E < E$(P1), *i.e.*, at a negatively charged surface, and a *ca.* 10% reduction of the charge consumed during lifting/reformation of the surface reconstruction (P1/P1′), as well as of the disorder/order phase transition within the sulfate adlayer (P3/P3′ in Figure 2A). Position and charge of the characteristic current peaks of surface oxidation (P4, P5) and reduction (P5′) appear to be unaltered in both electrolytes.

We also performed control experiments with NP-free Au(111) electrodes. The HER-treatment following a similar protocol as described above does not change the shape of the current−voltage response. The double layer responses and the characteristics in the gold surface oxidation/reduction regions are identical to the black traces in Figure 2.

**Cyclic Voltammograms of Au(100)-(1 × 1) in the Presence of SHINERS NPs.** In an attempt to generalize the HER-treatment for preparing high-quality SHINERS-NP modified electrodes, we investigated next the electrochemical response of Au(100)-(1 × 1) electrodes in 0.1 M H$_2$SO$_4$ and 0.1 M HClO$_4$ (Figure 4). The Au(100)-(hex) reconstruction was lifted prior to the electrochemical experiments following a previously described protocol,[40] which gives rise to large, island-free terraces of several hundreds of nm$^2$ with a nominal quadratic arrangement

of the gold surface atoms.[40] The coverage of the SHINERS NPs was estimated to approximately 20%. To eliminate possible interference with the potential-induced reformation of the Au(100)-(hex) surface reconstruction,[40,41] all experiments started at 0.60 V. The black and blue solid traces, which represent the current *vs* potential response of the bare and of the cleaned NP-modified Au(100)-(1 × 1) electrodes, are basically identical in the double layer region as well as upon extension toward surface oxidation/reduction in both electrolytes. The voltammograms reveal signatures of nearly perfect, defect-free Au(100)-(1 × 1) electrodes in both electrolytes.[38−40,42,43] P1, which is located at 0.34 V in H$_2$SO$_4$, and more positive at 0.57 V in HClO$_4$, represents the charge contributions due to the lifting of a small fraction of potential-induced Au(100)-(hex) reconstructed patches (<5%).

The current response in the surface oxidation/reduction regions reveals the characteristic current peaks P4 and P5 representing surface oxidation at step and terrace sites as well as a single cathodic reduction peak P5′. The corresponding charges of 640 $\mu$C cm$^{-2}$ (H$_2$SO$_4$) and 620 $\mu$C cm$^{-2}$ (HClO$_4$) decrease by less than 10% in the presence of the "cleaned" SHINERS NPs. AFM experiments demonstrated that the NP coverage is not changing during multiple oxidation/reduction cycles.

Finally, we notice in Figure 4 the distinct difference in the current response of Au(100)-(1 × 1) modified with HER-SHINERS (solid blue line) and "as-deposited" SHINERS NPs (dotted blue lines). This comparison illustrates the importance for establishing carefully designed and evaluated experimental protocols for SHINERS NPs on electrode surfaces to obtain meaningful electrochemical and Raman signatures on atomically smooth single-crystal electrode surfaces.

**SHINERS NPs on Pt(111)-(1 × 1) and Pt(100)-(1 × 1).** Next we adopted the HER-based SHINERS-NP post-treatment to Pt(111) and Pt(100) electrodes. The Pt(hkl) bead electrodes, as prepared by flame-annealing and subsequent cooling in Ar/H$_2$, revealed high quality voltammograms of low-defect surfaces (black lines in Figure 5), which agree with literature data.[34−37,44] The data for Pt(111)/0.1 M H$_2$SO$_4$ show at $E < 0.10$ V, a clear signature P1/P1′ of hydrogen adsorption on terrace sites. The charge in $-0.20$ V $\leq E \leq 0.10$ V is estimated to 160 $\mu$C cm$^{-2}$. The additional small peaks at $-0.13$ and 0.02 V represent hydrogen adsorption on (110) and (100) step sites.[35−37] P2/P2′ at $E > 0.10$ V represents a disordered adlayer of sulfate anions, which undergoes a disorder/order phase transition at P3/P3′. The height and the shape of this pair of current peaks is a measure of the long-range order and cleanliness of the Pt(111) terrace sites.[45] P4/P4′ at more positive potentials is assigned to a structure transition within the ordered sulfate layer.[46] The voltammogram of a cleaned Pt(111) electrode modified with a submonolayer of SHINERS NPs reproduces nearly all features of the bare Pt(111)
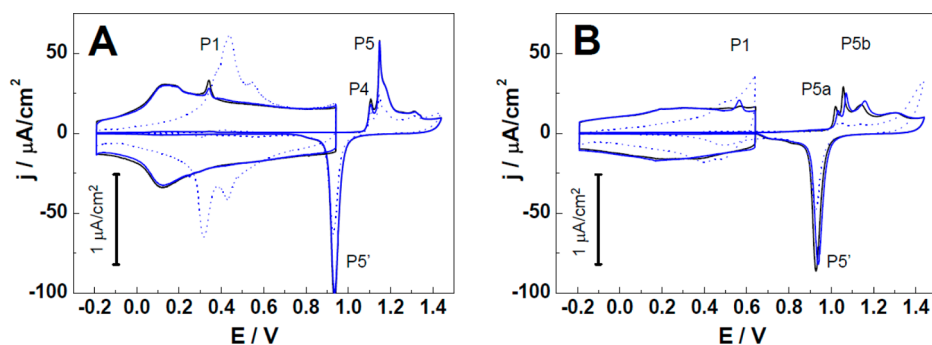
**Figure 4.** CVs of Au(100)-(1 × 1) single-crystal bead electrodes unmodified (black lines) and modified (solid blue lines) with Au@SiO$_2$ SHINERS NPs. The dotted blue traces were recorded with "as-prepared" NPs, while the solid blue lines represent data obtained with HER-SHINERS NPs. The voltammograms in the double layer region are displayed with a magnification factor of 30. Solution: 0.1 M (A) H$_2$SO$_4$ and (B) HClO$_4$. Scan rate: 10 mV/s.
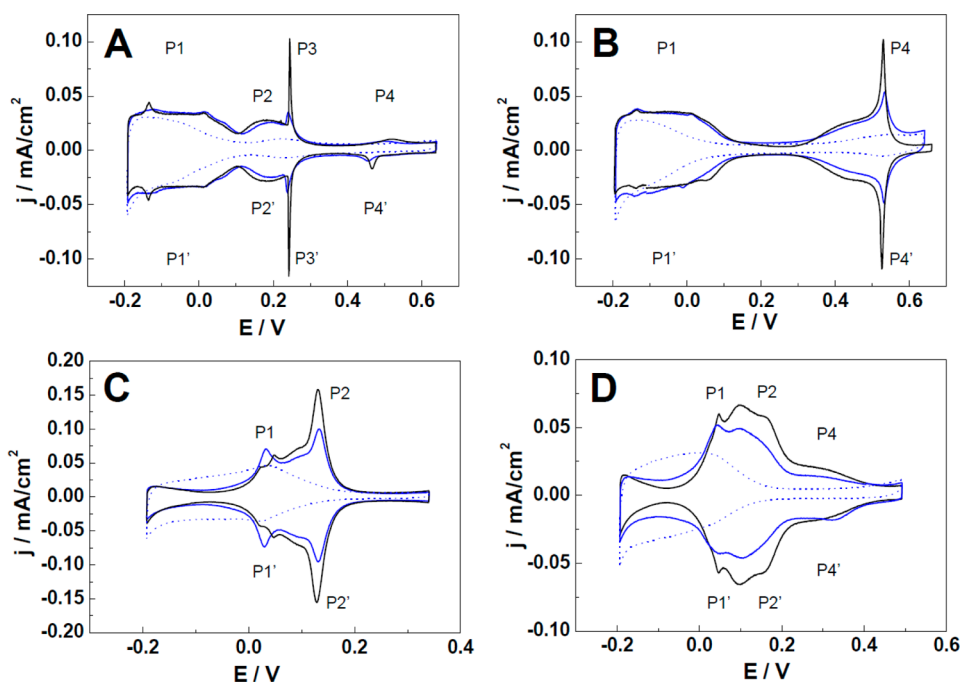


**Figure 5.** CVs of (A,B) Pt(111)-(1 × 1) and (C,D) Pt(100)-(1 × 1) single-crystal bead electrodes unmodified (black lines) and modified (solid blue lines) with Au@SiO$_2$ SHINERS NPs. The dotted blue traces were recorded with "as-prepared" NPs, while the solid blue lines represent data obtained with HER-SHINERS NPs. Solution: 0.1 M (A,C) H$_2$SO$_4$ and (B,D) HClO$_4$. Scan rate: 50 mV/s.

electrode in 0.1 M H$_2$SO$_4$. A comparison of the solid blue and black traces in Figure 5 reveals only a decrease of the charge consumed in P3/P3′ (<30%). On the other hand, experiments with "as prepared" SHINERS NPs lead to a significant depression of hydrogen adsorption until the onset of hydrogen evolution at $E < -0.20$ V, as well as to the blocking of sulfate and hydroxide adsorption at more positive potentials, which is indicated by the dotted blue line in Figure 5A.

Similar trends were observed for Pt(111) in 0.1 M HClO$_4$ (Figure 5B). The HER-SHINERS NPs do not alter the voltammogram for hydrogen adsorption (P1/P1′) and in the double layer charging region until $E \leq 0.30$ V. The charge consumed in $-0.20$ V $\leq E \leq 0.10$ V is estimated to 160 $\mu$C cm$^{-2}$. However, the so-called

Butterfly peak P4/P4′ at $E > 0.30$ V, which is assigned to the reversible OH-adsorption,[47] decreases moderately in the presence of SHINERS NPs. The current response of the NP-modified Pt(111) electrodes without treatment by HER reveals the complete blocking of this region and a significant reduction of available (111) terrace sites in the potential region of hydrogen adsorption (dotted blue line in Figure 5B).

The situation is more complex for Pt(100)-(1 × 1) in 0.1 M H$_2$SO$_4$ and in 0.1 M HClO$_4$. The voltammogram of Pt(100)-(1 × 1) in 0.1 M H$_2$SO$_4$ (black line in Figure 5C) shows two characteristic current peaks labeled P1/P1′ at $E = 0.05$ V and P2/P2′ at $E = 0.13$ V. The latter is assigned to the adsorption/desorption of hydrogen and sulfate ions on (100) terrace sites, and the former to

that on (111) step and/or step-edge sites.[44,48−54] The total charge consumed in $-0.10 \text{ V} \leq E \leq 0.50 \text{ V}$ amounts to $(220 \pm 10) \mu\text{C cm}^{-2}$. STM measurements demonstrated that Pt(100) electrodes, cooled down after flame-annealing in an Ar/H$_2$ atmosphere, are unreconstructed and composed of long and wide terraces, which alternate with step-bunched regions. On terraces wider than 500 nm, we also observed square-shaped Pt ad-islands of 0.21 nm height and 10 to 40 nm in $x−y$ dimensions.[44] This higher defect density, as compared to Pt(111)-(1 × 1), might explain why the HER-treatment of SHINERS-NP-modified Pt-(100) electrodes is less effective. The solid blue line in Figure 5C reveals an increase of the number of (111) defect sites of type P1/P1′ and a significant reduction of accessible (100) terrace sites for hydrogen/sulfate adsorption respective desorption in the presence of SHINERS NPs. The total charge consumed in the double layer region is reduced by ∼15% with respect to the NP-free surface. However, the effect is still rather small as compared to the current response of an electrode, which was not exposed to HER conditioning. The dotted blue line in Figure 5C shows that all characteristic features of an ideal Pt(100)-(1 × 1) electrode in H$_2$SO$_4$ are blocked completely.

The voltammogram of a bare Pt(100)-(1 × 1) electrode in 0.1 M HClO$_4$ displays a broad current feature between −0.10 to 0.25 V, which is composed of at least two current peaks labeled P1/P1′ and P2/P2′. This potential region is assigned to hydrogen ad/desorption.[55] The broad peak P4/P4′ in 0.25 V $\leq E \leq$ 0.45 V is related to OH-adsorption. The charge consumed in $-0.10 \text{ V} \leq E \leq 0.50 \text{ V}$ is estimated as $q = 250 \mu\text{C cm}^{-2}$. We observed a reduction of the charging current in the hydrogen- and OH-adsorption regions for a Pt(100) electrode modified with SHINERS NPs, even after extended conditioning in the potential region of HER (blue line in Figure 5D). The total charge in both potential regions decreases by ca. 30%. The current response of Pt(100)-(1 × 1) in 0.1 M HClO$_4$ with "as-deposited" SHINERS NPs is similar to observations in 0.1 M H$_2$SO$_4$ (dotted blue lines in Figure 5C,D). No anion-specific signature could be extracted.

**In Situ SHINERS Case Study: Pyridine Adsorption on Au(hkl) and Pt(hkl).** We present in this paragraph an application study of the spectro-electrochemical response of 1 mM pyridine dissolved in 0.1 M NaClO$_4$ in contact with Me(111)-(1 × 1) and Me(100)-(1 × 1), Me = Au and Pt, which demonstrates convincingly the great potential of HER-SHINERS in electrochemical surface-science based studies of nanoscale interfacial phenomena. Pyridine qualifies as an ideal compound for model studies on adsorption, orientation and surface coordination of molecules at electrified solid/liquid interfaces.[56,57] Pyridine was the first molecule used in demonstrating the SERS effect and has been an important probe molecule thereafter to test SERS activity and surface properties of SERS substrates.[1−3,58] However, most of these studies were carried out on roughened or colloidal surfaces and interfaces.[6,10,59] Only very few papers report data on atomically flat, truly single-crystalline surfaces.[60] The approaches chosen use either an attenuated total reflection configuration (ATR)[15,61] or SHINERS NPs as plasmonic antennas, as illustrated in our recent preliminary communication.[20]

Figure 6A shows typical voltammograms of a bare (black line) and a HER-SHINERS-NP-modified Au(111) electrode in 1 mM pyridine/0.1 M NaClO$_4$. The current response of the NP-free gold electrode reveals three characteristic pairs of peaks P1/P1′, P2/P2′ and P3/P3′. P1/P1′ is assigned to the ad/desorption of pyridine with the π-system oriented flat on a negatively charged electrode surface.[57,58,62] The coverage increases at more positive potentials, and a certain fraction appears to assume a tilted N-coordinated orientation at defect sites.[63] This process is proposed to start around P2/P2′. Chronocoulometric measurements by Lipkowski et al. suggest that a maximum coverage of $1.4 \times 10^{-10} \text{ mol cm}^{-2}$ is reached.[62] Next, and close to the potential of zero charge of the pyridine-covered Au(111) surface ($E_{\text{pzc}} \approx 0.13 \text{ V}$) an adlayer structure transition from planar to N-coordinated vertically standing molecules takes place.[62−64] This process is marked by the current peak P3/P3′ and leads to a π-stacked assembly of pyridine molecules on a positively charged electrode at $E >$ P3/P3′ with $\Gamma = 6.7 \times 10^{-10} \text{ mol cm}^{-2}$.[62] We note that within the transition region marked by P3/P3′ a certain tilted orientation with a rather small tilt angle referring to the surface normal forms a stable intermediate adlayer,[64] as indicated by the sharp current spikes in 0.10 V $\leq E \leq$ 0.20 V in Figure 6A.

The voltammogram of the NP-modified Au(111) electrode (solid blue line in Figure 6A) reproduces the current profile of pyridine adsorption in the double layer region in −0.70 V $\leq E \leq$ 0.05 V and in 0.20 V $\leq E \leq$ 0.40 V. The charge involved in the structure transition region around P3/P3′ is reduced by ca. 30%, and the sharp current spikes are not resolved. Most probably, the SHINERS NPs act as local defects on the electrode surface preventing the formation of a long-range, two-dimensionally ordered adlayer and the phase transition accompanied with it.

The simultaneously recorded SHINERS spectra of pyridine adsorbed on Au(111) are plotted in Figure 6C. Data acquisition started at 0.40 V. We observed four pyridine-related bands, which are assigned to the following A$_1$ modes: 1009−1012 cm$^{-1}$ ($\nu_1$, ring breathing), 1033−1035 cm$^{-1}$ ($\nu_{12}$, symmetric trigonal ring breathing), 1207−1209 cm$^{-1}$ ($\nu_{9a}$, C−H deformation) and 1593−1597 cm$^{-1}$ ($\nu_{8a}$, ring stretching).[6,10,65−68] The band at 933 cm$^{-1}$, marked by "*" in Figure 6C, is attributed to coadsorbed perchlorate ions.[24] The pyridine modes are blue-shifted with respect to those in neat pyridine solution. The frequency of the ring breathing mode $\nu_1$ is
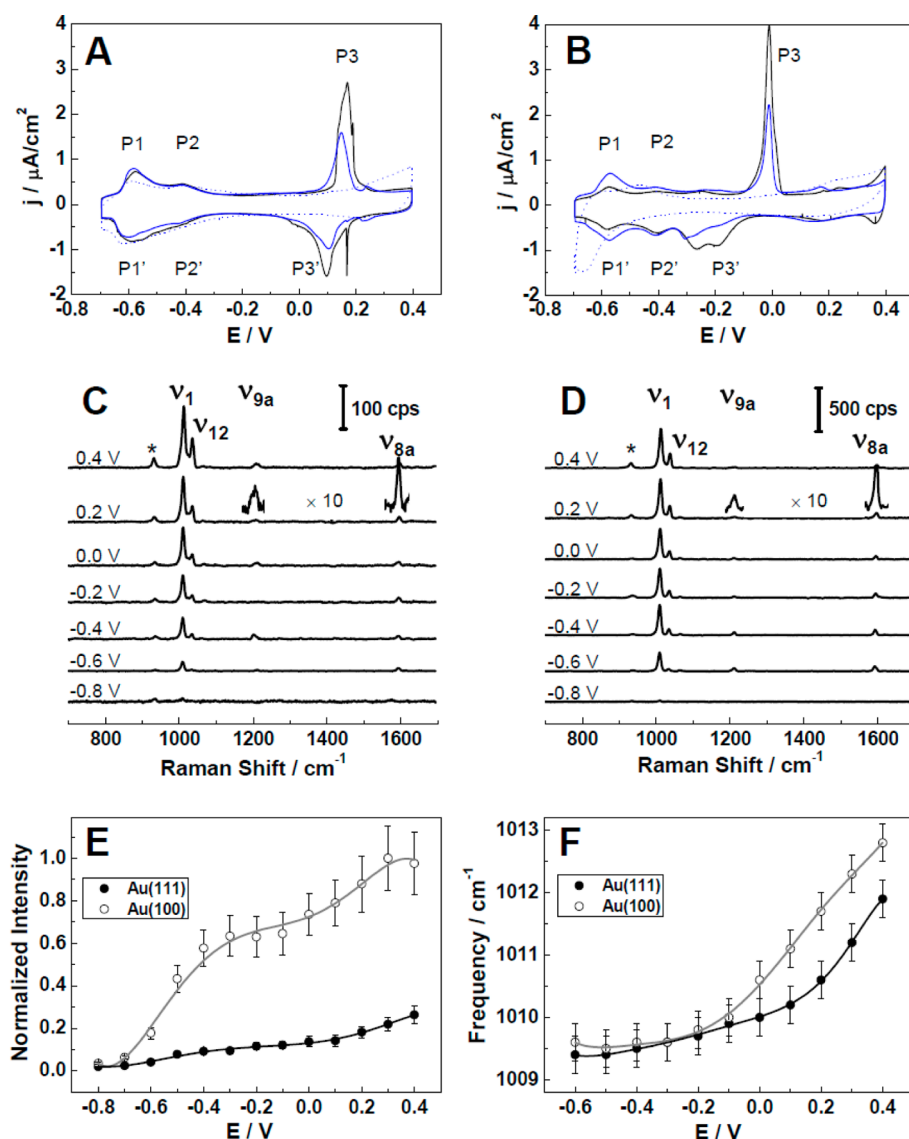
**Figure 6.** CVs of (A) Au(111)-(1 × 1) and (B) Au(100)-(1 × 1) single-crystal bead electrodes unmodified (black lines) and modified with Au@SiO$_2$ SHINERS NPs. The dotted blue traces were recorded with "as-prepared" NPs, while the solid blue lines represent data obtained with HER-SHINERS NPs. Solution: 1 mM Py + 0.1 M NaClO$_4$. Scan rate: 10 mV/s. *In situ* SHINER spectra of pyridine adsorbed on (C) Au(111) and (D) Au(100) single-crystal electrode surfaces. Laser power: 1 mW; Collecting time: 10 s. (E) Normalized Raman intensities and (F) Raman frequencies of the ring breathing mode $\nu_1$ in dependence on the applied potentials.

particularly sensitive to potential-dependent structure changes of the pyridine adlayer including electrostatic effects, $\sigma$-donation and $\pi$-back-donation *etc.*[66−68] Figure 6E,F displays the potential dependence of integrated intensity and peak position of the $\nu_1$ mode. We note that the Raman spectra plotted in Figure 6 are typical data of the HER-SHINERS NPs modified surfaces. Our preparation procedure guarantees a rather uniform size distribution of islands containing 15−20 NPs (see Supporting Information for a characteristic histogram), which can be identified and localized with the help of the CCD-camera of the spectrometer. Typically, we recorded the SHINERS intensity of up to 20 distinct island sites. Employing our preparation procedure of submonolayer HER-SHINERS NPs, we observed a variation in intensity of less than 15%.

We also notice that the SHINERS signal is dominated by contributions from the NP/substrate interface (see FDTD simulations in ref 19), where the pyridine adlayer is well established on unperturbed terrace sites. In consequence, one should expect a strong correlation between the spectroscopic data and other surface electrochemical studies, such as chronocoulometry[62] and cyclic voltammetry. And indeed, the following characteristics were obtained (Figure 6): The $\nu_1$ mode appears with the onset of pyridine adsorption at $E \geq$ −0.60 V and grows until −0.40 V, where a first plateau is reached. The corresponding region in the voltammogram is marked by the peaks P1/P1' and P2/P2'. The peak position varies in this potential region less than 1 cm$^{-1}$, which points to a slight deviation from a fully planar orientation of the $\pi$-system. This interpretation

agrees with conclusions from IR-spectroscopy.[63] An additional increase in intensity is observed at $E \geq 0.10$ V, simultaneously with the appearance of the current peak P3/P3′ in the voltammogram. The signal seems to level off at $E \geq 0.40$ V. $\delta\nu_1/\delta E$ is estimated to 6 cm$^{-1}$/V. This value of the Stark shift is rather typical for molecular adsorption at electrochemical interfaces with a dipole contribution aligned perpendicularly to the electrode surface.[69] All four pyridine-related A$_1$ modes scale similarly in their potential dependence of peak intensities and wave numbers.

The above SHINERS data demonstrate unambiguously that pyridine is adsorbed already at a negatively charged Au(111) surface in a none-parallel, most probably slightly tilted orientation with respect to the plane surface, and reorients into a fully upright orientation upon pathing the potential of zero charge at $E > 0.10$ V. Possible complications of this behavior due to reformation of the reconstructed Au(111)-(p $\times$ √3) surface or gold island formation upon the subsequent lifting of the reconstruction (see Methods section for details) should be of rather little influence since (1) all experiments started with a fully unreconstructed surface at positive potentials and (2) pyridine blocks drastically the potential-induced surface reconstruction, even at rather negative potentials.[70]

Similar spectro-electrochemical properties were also observed with pyridine on Au(100)-(1 $\times$ 1) modified with HER-SHINERS NPs (Figure 6B,D–F). The voltammogramms in the absence (solid black line) and in the presence (solid blue line) of NPs coincide in the double layer region in $-0.70$ V $\leq E \leq -0.30$ V and in 0.10 V $\leq E \leq 0.40$ V. Chronocoulometric experiments revealed that the pyridine coverage increases from 0 to ca. $3.0 \times 10^{-10}$ mol cm$^{-2}$ gradually in $-0.60$ V $\leq E \leq E$(P3), and reaches its saturation value $6.0 \times 10^{-10}$ mol cm$^{-2}$ at $E > E$(P3) in a step-like manner. This coverage is attributed to pyridine molecules adsorbed in a vertical orientation with the nitrogen atom facing the positively charged Au(100)-(1 $\times$ 1) surface.[71] Pyridine adsorption seems to facilitate structure changes of the Au(100) surface, such as the reformation of the Au(100)-(hex) reconstruction at sufficiently negative potentials and its lifting toward the Au(100)-(1 $\times$ 1) geometry around 0.0 V upon crossing the potential of zero charge ($E_{pzc} = -0.05$ V), which coincides with the position of P3.[41,70–73] The current peak P3 contains charge contribution from both, the reorientation of adsorbed pyridine as well as of the restructuring of the electrode surface.[57,73]

This complex behavior is also reflected in the voltammogram with HER-SHINERS NPs (Figure 6B). The current peak P3 is reduced by 52% (blue line) as compared to the bare (black line) Au(100) surface. The cathodic counter feature P3′ around $-0.20$ V is quenched. The corresponding SHINERS spectra, as recorded from 0.40 V toward more negative potentials, are displayed in

Figure 6D. Qualitatively, we observed the same pyridine-related bands as for Au(111). Figure 6E,F displays, as a representative example, the potential-dependencies of integrated band intensity and position of the symmetric $\nu_1$ breathing mode. Similar to trends for pyridine on Au(111), the Raman intensity increases from the onset of pyridine adsorption at $E \geq -0.60$ V up to a plateau in $-0.40$ V $\leq E \leq -0.10$ V, and subsequently raises further in the transition region P3/P3′ until saturation at $E \geq 0.30$ V. The position of the $\nu_1$-mode changes gradually with potential in $-0.60$ V $\leq E \leq -0.10$ V with $\delta\nu/\delta E \approx 1$ cm$^{-1}$/V and at $E > -0.10$ V with $\delta\nu/\delta E \approx 6$ cm$^{-1}$/V. The latter Stark shift is the same as for pyridine/Au(111) at a positively charged electrode. The detection of the $\nu_1$ mode as well as the other pyridine-related modes at $E < E_{pzc}$ and their evolution in dependence on the applied potential demonstrate that pyridine is adsorbed on the negatively charged Au(100) surface in a tilted orientation with the nitrogen atom directed toward the surface and undergoes a structure transition in a N-coordinated vertical adsorption geometry at $E > E$(P3), where the electrode surface bears a positive charge. The data in Figure 6E,F also demonstrate that this transition occurs at more negative potentials on Au(100)-(1 $\times$ 1) as compared to Au(111)-(1 $\times$ 1). This trend correlates with the more negative value of $E_{pzc}$ of the former.

Finally, we comment on the higher integrated intensity of the pyridine-related Raman bands on Au-(100). We have shown in a previous communication,[20] on the basis of periodic DFT calculations and a theoretical analysis of the dielectric functions, that the facet-dependence is predominantly governed by the dielectric properties of the surface. The much smaller imaginary part of the dielectric function for the (110) plane as compared to the other low-index planes leads to a higher electroreflectance and a much stronger electromagnetic field.

Pyridine adsorption on Pt(111)-(1 $\times$ 1) and Pt(100)-(1 $\times$ 1) in 0.1 M NaClO$_4$ appears to be less complex as compared to the two gold single-crystal surfaces described above. The voltammograms are displayed in Figure 7A,B. They illustrate that pyridine adsorption starts at potentials $E \geq -0.70$ V, slightly more negative than the onset of hydrogen adsorption and the position of P$_1$. P$_1$ is thought to represent the adsorption of neutral pyridine, while features at more negative potentials are attributed tentatively to the protonated form. The pyridine adlayer blocks the adsorption of hydrogen and perchlorate ions, which corroborates with a low double layer charging current (or capacitance) in $-0.20$ V $\leq E \leq 0.30$ V. The latter assumes smaller values on Pt(111), which reflects the atomically somewhat larger roughness of the unreconstructed Pt(100)-(1 $\times$ 1) surface, as obtained after flame annealing and cooling in an Ar/H$_2$ atmosphere.[34,44] The voltammograms of pyridine on Pt(111) and Pt(100) in the absence and in the presence of HER-SHINERS NPs superimpose.
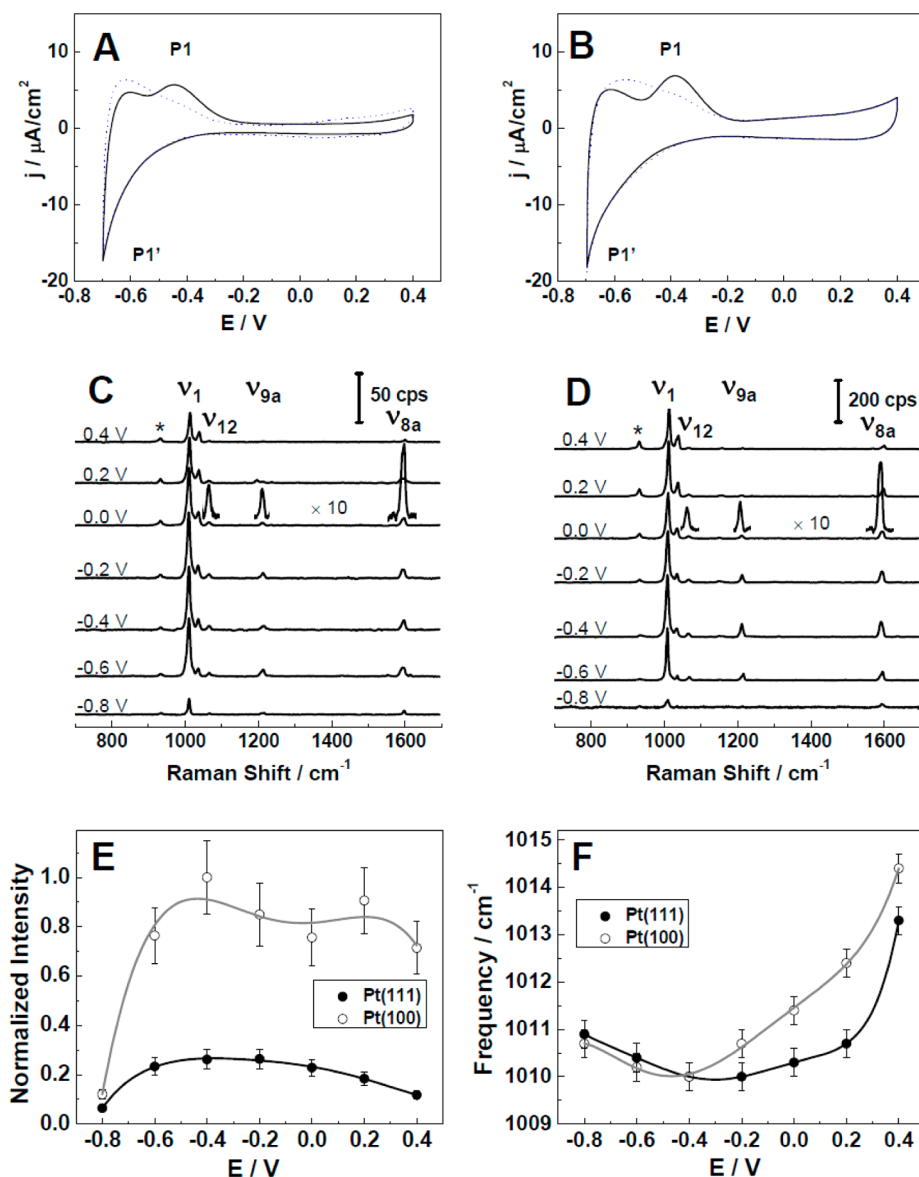
**Figure 7.** CVs of unmodified (A) Pt(111)-(1 × 1) and (B) Pt(100)-(1 × 1) single-crystal bead electrodes (black lines). The dotted blue traces were recorded with "as-prepared" Au@SiO$_2$ SHINERS NPs. Solution: 1 mM Py + 0.1 M NaClO$_4$. Scan rate: 50 mV/s. *In situ* SHINER spectra of pyridine adsorbed on (C) Pt(111) and (D) Pt(100) single-crystal electrode surfaces. Laser power: 1 mW. Collecting time: 30 s. (E) Normalized Raman intensities and (F) Raman frequencies of the ring breathing mode $\nu_1$ in dependence on the applied potentials.

The corresponding HER-SHINERS spectra are shown in Figure 7C,D. In addition to the four A$_1$-modes of pyridine, a fifth band occurs at 1064−1066 cm$^{-1}$, which is attributed to the C−H deformation A$_1$-mode $\nu_{18a}$.[66−68] All A$_1$ modes reveal a similar behavior with increasing electrode potential. Figure 7E,F demonstrates the trend for $\nu_1$. The integrated intensities increase steeply at $E = -0.60$ V and reach a plateau at $E \geq -0.40$ V. The latter decreases slightly at $E \geq$ 0.20 V, which is attributed to the onset of competitive adsorption of OH-species.[74] Simultaneously, $\delta\nu_1/\delta E$ increases from 1 cm$^{-1}$/V at $-0.40$ V up to 7 cm$^{-1}$/V at $E > 0.00$ V for both electrodes. These characteristic vibration signatures are interpreted as gradual transfer from an N-coordinated tilted adsorption geometry of

pyridine at $E < -0.40$ V to a vertical orientation at $E \geq -0.40$ V. This interpretation is in agreement with conclusions from UHV-transfer experiments at controlled potential and a subsequent analysis of the pyridine adlayer on Pt(111) by Auger electron spectroscopy (AES) and electron energy loss spectroscopy (EELS).[75]

Similar as for pyridine on the two gold facets investigated, the SHINERS signal on Pt(100) is larger as compared to that on Pt(111). This trend is also supported by the different dielectric properties of the two crystallographic orientations.[20]

## CONCLUSIONS

We have studied Au(55 nm)@SiO$_2$ shelled insulated nanoparticles on four low-index phases of gold and

platinum Clavilier-type single-crystal bead electrodes by both electrochemical methods and *in situ* Raman spectroscopy. We demonstrated that Au(hkl) and Pt(hkl) surfaces modified with a submonolayer (and more!) of "as-prepared" SHINERS nanoparticles show distorted voltammetric and spectroscopic responses (see Supporting Information). The electrode surfaces are blocked with surfactants originating from the synthesis of the Au(55 nm)@SiO$_2$ nanoparticles, which give rise to additional current and spectroscopic features, and therefore cause artifacts in data interpretation and assignment.

We developed an efficient strategy to overcome this problem. Our approach is based on the treatment of surfaces modified with SHINERS NPs in the potential region of hydrogen evolution in 0.1 M aqueous NaClO$_4$. Case studies with Me(111)-(1 × 1) and Me(100)-(1 × 1), Me = Au, Pt, demonstrate the efficiency of our method. Voltammetric experiments in 0.1 M H$_2$SO$_4$ and 0.1 M HClO$_4$ reveal that all characteristic double layer features of Au(111) and Au(100) electrodes in contact with these electrolytes coincide in the absence as well as in the presence of the HER-SHINERS NPs. Rather good agreement was also obtained with Pt(111)-(1 × 1) electrodes in both electrolytes. In case of Pt(100)-(1 × 1), qualitative agreement is reached; however, the hydrogen and anion adsorption regions are slightly blocked by the presence of the HER-SHINERS NPs, even after extended cycles of HER treatment. Application studies with these electrodes require some caution and careful control experiments.

Pyridine adsorption and phase formation on Me-(111)-(1 × 1) and Me(100)-(1 × 1), Me = Au, Pt, were chosen as a case study to demonstrate the potential of HER-SHINERS for *in situ* investigations of nanoscale phenomena and processes at electrified solid/liquid interfaces. We obtained high-quality Raman spectra on these well-defined and structurally carefully characterized Au(hkl) and Pt(hkl) single-crystal surfaces. The analysis of the characteristic A$_1$ vibrational modes revealed perfect agreement with the interpretation of single-crystal voltammetric and chronoamperometric experiments. Our study demonstrates convincingly that the SHINERS protocol as developed in this study qualifies this unique Raman method as a highly promising approach for *in situ* structure and reactivity studies at well-defined electrochemical solid/liquid interfaces. The study also reveals the need of combining the spectro-electrochemical investigations with morphology studies of the respective substrate surface and control experiments on the inertness of the plasmonic nanoparticles with respect to the process under investigation.

## METHODS

**Chemicals.** Chloroauric acid, (3-aminopropyl)trimethoxysilane (97 *M*%; *M*% = mass %), sodium citrate (99 *M*%) and sodium perchlorate (98−100 *M*%) were purchased from Alfa Aesar; sodium silicate solution (27 *M*% SiO$_2$) and pyridine (≥99.8 *M*%), were obtained from Sigma Aldrich; hydrochloric acid (30%) and suprapure sulfuric acid (96 *M*%) were purchased from Merck. All chemicals were used as received. Water was purified with a Milli-Q system (18.2 MΩ cm, 2−3 ppb total organic content) before use.

**Preparation of Au NPs.** 55 nm Au NPs were prepared according to the standard sodium citrate reduction method.[76] Briefly, 200 mL of 0.294 mM chloroauric acid were placed in a round-bottom flask and brought to boiling. Next, 1.4 mL of 38.8 mM sodium citrate was added quickly to the boiling solution. The mixture was refluxed for 40 min and then allowed to cool to room temperature.

**Preparation of Au@SiO$_2$ (SHINERS) NPs.** Au@SiO$_2$ SHINERS NPs were prepared by placing 30 mL of the gold NPs solution into a round-bottom flask, adding 0.4 mL of 1 mM (3-aminopropyl-)trimethoxysilane, and stirring for 15 min at room temperature. Next, a 27 *M*% sodium silicate solution was diluted to 0.54 *M*% (~90.0 mM) and adjusted to pH ~10.3 with hydrochloric acid. 3.2 mL of the diluted and acidified sodium silicate solution were then added to the reaction mixture, which was stirred afterward at room temperature for 3 more min. The solution was then transferred to a 90 °C bath and stirred for a certain period of time. The shell thickness could be tuned from a few nanometers to tens of nanometers by controlling the reaction time. For example, 30 min or 1 h of heating time resulted in coating the gold core with a layer of about 3 or 5 nm thickness, respectively.[18,33] In this paper, we controlled the reaction time to 30 min, which leads to a silica shell thickness of ~3 nm (see Figure 1A). The shell is pinhole-free and provides a sufficiently strong enhancement of the pyridine-related Raman signals. Electrochemical and Raman experiments were carried out to ensure that the as-prepared SHINERS NPs are free of pinholes. The test protocols were described in our previous papers.[18,19,24]

The hot NP mixture was then transferred into test tubes of 1.5 mL volume and cooled down in an ice bath, which quenches the reaction. Upon cooling down to room temperature, the samples were centrifuged at 5500 rpm for 15 min. The supernatant was removed afterward. The concentrated SHINERS NPs at the bottom of the test tube were diluted and centrifuged again. This procedure was repeated several times. The cleaned Au@SiO$_2$ NPs were dissolved in 200 µL of Milli-Q water, which leads to a solution containing ~1.97 mM total gold. Two microliters of this solution were then casted onto a freshly prepared Au(hkl) or Pt(hkl) single-crystal bead electrode (Figure 1B) and subsequently dried in a gentle stream of argon. The SHINERS NPs form a submonolayer of small, statistically distributed two-dimensional islands, which contain typically 15−20 NPs. The NP-coverage as obtained from SEM and AFM measurements (Figure 1) is estimated to range between 20 to 30%. We note that the silicon shell prevents the formation of three-dimensional aggregates.

**Preparation of Au(hkl) and Pt(hkl) Single-Crystal Electrodes.** The electrodes used were Clavilier-type half-bead single-crystal Au-(hkl) and Pt(hkl) electrodes (~ 2 mm diameter, Figure 1B). Island-free and unreconstructed Au(hkl)-(1 × 1) electrodes were prepared according to a previously described procedure.[40] Briefly, the electrode was annealed in a butane flame for about 2 min and cooled down to room temperature in an argon atmosphere. The flame-annealed Au(hkl) electrode was then immersed into 10 mM HCl at open circuit for 10 min to lift the reconstruction, which leads to island-free Au(hkl)-(1 × 1) surfaces with rather large terraces. The chloride ions were removed by extended rinsing with Milli-Q water. The electrode was finally dried in a stream of argon.

The Pt(hkl) electrodes were annealed in a hydrogen flame for 1 min. The hot electrodes were quickly transferred into a closed flask filled with a mixture of Ar/H$_2$ (4:1) and allowed to

cool down to room temperature. The procedure leads to the lifting of the surface reconstruction.[34,44] Flow and composition of the gases in the flask were adjusted to ensure a slow cooling rate. The cooled electrode was subsequently immersed into deaerated Milli-Q water, which was saturated with hydrogen, and then transferred with a protecting droplet of water adhering to the polished surface into the electrochemical cell for further characterization and/or modification.

**Cyclic Voltammetry.** The electrochemical measurements were conducted in a three compartment all-glass cell with a platinum or gold coil as auxiliary electrode and a leakless Ag/AgCl reference electrode in 0.1 M NaClO$_4$ or a trapped, reversible hydrogen reference electrode (RHE) in 0.1 M H$_2$SO$_4$ and HClO$_4$, respectively. High-purity Ar (Alphagaz 99.999%) was employed to deaerate the solutions. Ar was also passed above the solutions during the experiments. The freshly prepared electrodes were brought in contact with the electrolyte under potential control in a hanging meniscus configuration. The electrochemical measurements were carried out with an Autolab PGSTAT30.

**Raman Spectroscopy.** Raman spectra were recorded with a LabRam HR800 confocal microprobe Raman system (HORIBA Jobin Yvon). The excitation wavelength was 632.8 nm from a He−Ne laser. The power on the sample was typically about 1 mW. A 50× magnification long-working-distance objective (8 mm) was used to focus the laser onto the sample and to collect the scattered light in a backscattering geometry. A lab-made spectro-electrochemical cell with a Pt or a Au wire and an Ag/AgCl electrode serving as the counter and the reference electrodes was used for the electrochemical SERS measurements (Figure 3A). All in situ Raman experiments were carried out in the strict absence of oxygen. The simultaneous electrochemical control was achieved by employing a lab-built potentiostat and software developed in our group.

*Conflict of Interest:* The authors declare no competing financial interest.

*Supporting Information Available:* Size-distribution of HER-SHINERS NP islands, SHINERS spectra of Py on Au(111) and Pt(111) with and without HER cleaning procedure, and surface enhancement factor (SEF) calculation. This material is available free of charge via the Internet at http://pubs.acs.org.

## REFERENCES AND NOTES

1. Fleischmann, M.; Hendra, P. J.; McQuillan, A. J. Raman Spectra of Pyridine Adsorbed at a Silver Electrode. *Chem. Phys. Lett.* **1974**, *26*, 163–166.
2. Jeanmaire, D. L.; Vanduyne, R. P. Surface Raman Spectroelectrochemistry. 1. Heterocyclic, Aromatic, and Aliphatic Amines Adsorbed on Anodized Silver Electrode. *J. Electroanal. Chem.* **1977**, *84*, 1–20.
3. Albrecht, M. G.; Creighton, J. A. Anomalously Intense Raman-Spectra of Pyridine at a Silver Electrode. *J. Am. Chem. Soc.* **1977**, *99*, 5215–5217.
4. Ren, B.; Liu, G. K.; Lian, X. B.; Yang, Z. L.; Tian, Z. Q. Raman Spectroscopy on Transition Metals. *Anal. Bioanal. Chem.* **2007**, *388*, 29–45.
5. Tian, Z. Q.; Ren, B.; Li, J. F.; Yang, Z. L. Expanding Generality of Surface-Enhanced Raman Spectroscopy with Borrowing SERS Activity Strategy. *Chem. Commun.* **2007**, 3514–3534.
6. Wu, D. Y.; Li, J. F.; Ren, B.; Tian, Z. Q. Electrochemical Surface-Enhanced Raman Spectroscopy of Nanostructures. *Chem. Soc. Rev.* **2008**, *37*, 1025–1041.
7. Kneipp, K.; Moskovits, M.; Kneipp, H. *Surface-Enhanced Raman Scattering Physics and Applications*; Springer: Berlin/Heidelberg, 2006; Vol. 103.
8. Schatz, G. C.; Young, M. A.; Van Duyne, R. P. Electromagnetic Mechanism of SERS. *Top. Appl. Phys.* **2006**, *103*, 19–45.
9. Moskovits, M. Surface-Enhanced Raman Spectroscopy: A Brief Perspective. *Top. Appl. Phys.* **2006**, *103*, 1–17.
10. Creighton, J. A.; Blatchford, C. G.; Albrecht, M. G. Plasma Resonance Enhancement of Raman Scattering by Pyridine Adsorbed on Silver or Gold Sol Particles of Size Comparable to the Excitation Wavelength. *J. Chem. Soc., Faraday Trans. 2* **1979**, *75*, 790–798.
11. Wetzel, H.; Gerischer, H.; Pettinger, B. Comparison of the Potential Dependence of the Surface-Enhanced Raman Effect at Colloid Silver Particles and Bulk Silver Electrodes. *Chem. Phys. Lett.* **1982**, *85*, 187–189.
12. Nikoobakht, B.; Wang, J. P.; El-Sayed, M. A. Surface-Enhanced Raman Scattering of Molecules Adsorbed on Gold Nanorods: Off-Surface Plasmon Resonance Condition. *Chem. Phys. Lett.* **2002**, *366*, 17–23.
13. Willets, K. A.; Van Duyne, R. P. Localized Surface Plasmon Resonance Spectroscopy and Sensing. *Annu. Rev. Phys. Chem.* **2007**, *58*, 267–297.
14. Mahajan, S.; Abdelsalam, M.; Suguwara, Y.; Cintra, S.; Russell, A.; Baumberg, J.; Bartlett, P. Tuning Plasmons on Nano-Structured Substrates for NIR-SERS. *Phys. Chem. Chem. Phys.* **2007**, *9*, 104–109.
15. Bruckbauer, A.; Otto, A. Raman Spectroscopy of Pyridine Adsorbed on Single Crystal Copper Electrodes. *J. Raman Spectrosc.* **1998**, *29*, 665–672.
16. Ikeda, K.; Suzuki, S.; Uosaki, K. Crystal Face Dependent Chemical Effects in Surface-Enhanced Raman Scattering at Atomically Defined Gold Facets. *Nano Lett.* **2011**, *11*, 1716–1722.
17. Cui, L.; Liu, B.; Vonlanthen, D.; Mayor, M.; Fu, Y. C.; Li, J. F.; Wandlowski, T. In-Situ Gap-Mode Raman Spectroscopy on Single-Crystal Au(100) Electrodes: Tuning the Torsion Angle of 4,4′-Biphenyldithiols by an Electrochemical Gate Field. *J. Am. Chem. Soc.* **2011**, *133*, 7332–7335.
18. Li, J. F.; Huang, Y. F.; Ding, Y.; Yang, Z. L.; Li, S. B.; Zhou, X. S.; Fan, F. R.; Zhang, W.; Zhou, Z. Y.; Wu, D. Y.; et al. Shell-Isolated Nanoparticle-Enhanced Raman Spectroscopy. *Nature* **2010**, *464*, 392–395.
19. Anema, J. R.; Li, J. F.; Yang, Z. L.; Ren, B.; Tian, Z. Q. Shell-Isolated Nanoparticle-Enhanced Raman Spectroscopy: Expanding the Versatility of Surface-Enhanced Raman Scattering. *Annu. Rev. Anal. Chem.* **2011**, *4*, 129–150.
20. Li, J. F.; Ding, S. Y.; Yang, Z. L.; Bai, M. L.; Anema, J. R.; Wang, X.; Wang, A.; Wu, D. Y.; Ren, B.; Hou, S. M.; et al. Extraordinary Enhancement of Raman Scattering from Pyridine on Single Crystal Au and Pt Electrodes by Shell-Isolated Au Nanoparticles. *J. Am. Chem. Soc.* **2011**, *133*, 15922–15925.
21. Uzayisenga, V.; Lin, X. D.; Li, L. M.; Anema, J. R.; Yang, Z. L.; Huang, Y. F.; Lin, H. X.; Li, S. B.; Li, J. F.; Tian, Z. Q. Synthesis, Characterization, and 3D-FTDT Simulation of Ag@SiO$_2$ Nanoparticles for Shell-Isolated Nanoparticle-Enhanced Raman Spectroscopy. *Langmuir* **2012**, *28*, 9140–9146.
22. Pettinger, B.; Schambach, P.; Villagomez, C. J.; Scott, N. Tip-Enhanced Raman Spectroscopy: Near-Fields Acting on a Few Molecules. *Annu. Rev. Phys. Chem.* **2012**, *63*, 379–399.
23. Schmid, T.; Yeo, B. S.; Leong, G.; Stadler, J.; Zenobi, R. Performing Tip-Enhanced Raman Spectroscopy in Liquids. *J. Raman Spectrosc.* **2009**, *40*, 1392–1399.
24. Liu, B.; Blaszczyk, A.; Mayor, M.; Wandlowski, T. Redox-Switching in a Viologen-Type Adlayer: An Electrochemical Shell-Isolated Nanoparticle Enhanced Raman Spectroscopy Study on Au(111)-(1 × 1) Single Crystal Electrodes. *ACS Nano* **2011**, *5*, 5662–5672.
25. Butcher, D. P.; Boulos, S. P.; Murphy, C. J.; Ambrosio, R. C.; Gewirth, A. A. Face-Dependent Shell-Isolated Nanoparticle Enhanced Raman Spectroscopy of 2,2′-Bipyridine on Au(100) and Au(111). *J. Phys. Chem. C* **2012**, *116*, 5128–5140.
26. Honesty, N. R.; Gewirth, A. A. Shell-Isolated Nanoparticle Enhanced Raman Spectroscopy (Shiners) Investigation of Benzotriazole Film Formation on Cu(100), Cu(111), and Cu(Poly). *J. Raman Spectrosc.* **2012**, *43*, 46–50.
27. Zhumaev, U.; Rudnev, A. V.; Li, J. F.; Kuzume, A.; Vu, T. H.; Wandlowski, T. Electro-Oxidation of Au(111) in Contact with Aqueous Electrolytes: New Insight from in-Situ Vibration Spectroscopy. *Electrochim. Acta* **2013**, 10.1016/j.electacta.2013.02.105.

28. Attard, G.; Bennett, J. A.; Mikheenko, I.; Jenkins, P.; Guan, S.; Macaskie, L. E.; Wood, J.; Wain, A. J. Semi-Hydrogenation of Alkynes at Single Crystal, Nanoparticle and Biogenic Nanoparticle Surfaces: The role of Defects in Lindlar-Type Catalysts and the Origin of their Selectivity. *Faraday Discuss.* **2013**, *62*, 57–75.

29. Li, M. D.; Cui, Y.; Gao, M. X.; Luo, J.; Ren, B.; Tian, Z. Q. Clean Substrates Prepared by Chemical Adsorption of Iodide Followed by Electrochemical Oxidation for Surface-Enhanced Raman Spectroscopic Study of Cell Membrane. *Anal. Chem.* **2008**, *80*, 5118–5125.

30. Bewick, A.; Thomas, B. Optical and Electrochemical Studies of Underpotential Deposition of Metals 1: Thallium Deposition on Single-Crystal Silver Electrodes. *J. Electroanal. Chem.* **1975**, *65*, 911–931.

31. Taylor, C. E.; Garvey, S. D.; Pemberton, J. E. Carbon Contamination at Silver Surfaces: Surface Preparation Procedures Evaluated by Raman Spectroscopy and X-Ray Photoelectron Spectroscopy. *Anal. Chem.* **1996**, *68*, 2401–2408.

32. Vidal-Iglesias, F. J.; Solla-Gullon, J.; Herrero, E.; Montiel, V.; Aldaz, A.; Feliu, J. M. Evaluating the Ozone Cleaning Treatment in Shape-Controlled Pt Nanoparticles: Evidences of Atomic Surface Disordering. *Electrochem. Commun.* **2011**, *13*, 502–505.

33. Li, J. F.; Li, S. B.; Anema, J. R.; Yang, Z. L.; Huang, Y. F.; Ding, Y.; Wu, Y. F.; Zhou, X. S.; Wu, D. Y.; Ren, B.; *et al.* Synthesis and Characterization of Gold Nanoparticles Coated with Ultrathin and Chemically Inert Dielectric Shells for SHINERS Applications. *Appl. Spectrosc.* **2011**, *65*, 620–626.

34. Kibler, L. A. *Preparation and Characterization of Noble Metal Single Crystal Electrode Surfaces*; ISE: Barcelona, 2003.

35. Clavilier, J. Flame-Annealing and Cleaning Technique. In *Interfacial Electrochemistry: Theory, Experimental, and Applications*; Wieckowski, A., Ed.; Marcel Dekker: New York, 1999; pp 231–248.

36. Clavilier, J.; Faure, R.; Guinet, G.; Durand, R. Preparation of Mono-Crystalline Pt Microelectrodes and Electrochemical Study of the Plane Surfaces Cut in the Direction of the (111) and (110) Planes. *J. Electroanal. Chem.* **1980**, *107*, 205–209.

37. Clavilier, J. Role of Anion on the Electrochemical-Behavior of a (111) Platinum Surface—Unusual Splitting of the Voltammogram in the Hydrogen Region. *J. Electroanal. Chem.* **1980**, *107*, 211–216.

38. Angerstein-Kozlowska, H.; Conway, B. E.; Hamelin, A.; Stoicoviciu, L. Elementary Steps of Electrochemical Oxidation of Single-Crystal Planes of Au 1: Chemical Basis of Processes Involving Geometry of Anions and the Electrode Surfaces. *Electrochim. Acta* **1986**, *31*, 1051–1061.

39. Angerstein-Kozlowska, H.; Conway, B. E.; Hamelin, A.; Stoicoviciu, L. Elementary Steps of Electrochemical Oxidation of Single-Crystal Planes of Au 2: A Chemical and Structural Basis of Oxidation of the (111) Plane. *J. Electroanal. Chem.* **1987**, *228*, 429–453.

40. Holzle, M. H.; Wandlowski, T.; Kolb, D. M. Phase-Transition in Uracil Adlayers on Electrochemically Prepared Island-Free Au(100)-(1 × 1). *J. Electroanal. Chem.* **1995**, *394*, 271–275.

41. Kolb, D. M. Reconstruction Phenomena at Metal-Electrolyte Interfaces. *Prog. Surf. Sci.* **1996**, *51*, 109–173.

42. Dakkouri, A. S.; Kolb, D. M. Reconstruction of Gold Surfaces. In *Interfacial Electrochemistry*; Wieckowski, A., Ed.; Marcel-Dekker: New York, 1999; pp 151–173.

43. Dretschkow, T.; Wandlowski, T. In *Topics in Applied Physics*; Wandelt, K., Thurgate, S., Eds.; Springer: Berlin, 2003; Vol. 85, pp 259–321.

44. Rudnev, A. V.; Wandlowski, T. An Influence of Pretreatment Conditions on Surface Structure and Reactivity of Pt(100) Towards Co Oxidation Reaction. *Russ. J. Electrochem.* **2012**, *48*, 259–270.

45. Scherson, D. A.; Kolb, D. M. Voltammetric Curves for Au(111) in Acid-Media—A Comparison with Pt(111) Surfaces. *J. Electroanal. Chem.* **1984**, *176*, 353–357.

46. Garcia-Araez, N.; Climent, V.; Rodriguez, P.; Feliu, J. M. Thermodynamic Analysis of (Bi)Sulphate Adsorption on a Pt(111) Electrode as a Function of pH. *Electrochim. Acta* **2008**, *53*, 6793–6806.

47. Wagner, F. T.; Ross, P. N. Leed Analysis of Electrode Surfaces—Structural Effects of Potentiodynamic Cycling on Pt Single-Crystals. *J. Electroanal. Chem.* **1983**, *150*, 141–164.

48. Clavilier, J.; Armand, D.; Sun, S. G.; Petit, M. Electrochemical Adsorption Behavior of Platinum Stepped Surfaces in Sulfuric-Acid-Solutions. *J. Electroanal. Chem.* **1986**, *205*, 267–277.

49. Clavilier, J.; Feliu, J. M.; Fernandez-Vega, A.; Aldaz, A. Electrochemical-Behavior of Irreversibly Adsorbed Bismuth on Pt(100) with Different Degrees of Crystalline Surface Order. *J. Electroanal. Chem.* **1989**, *269*, 175–189.

50. Feliu, J. M.; Orts, J. M.; Gomez, R.; Aldaz, A.; Clavilier, J. New Information on the Unusual Adsorption States of Pt(111) in Sulfuric-Acid-Solutions from Potentiostatic Adsorbate Replacement by CO. *J. Electroanal. Chem.* **1994**, *372*, 265–268.

51. Armand, D.; Clavilier, J. Quantitative-Analysis of the Distribution of the Hydrogen Adsorption States at Platinum Surfaces. 1. Application to Pt(100) in Sulfuric-Acid Medium. *J. Electroanal. Chem.* **1987**, *225*, 205–214.

52. Armand, D.; Clavilier, J. Quantitative-Analysis of the Distribution of the Hydrogen Adsorption States at Platinum Surfaces 2: Application to Pt(110), Stepped and Polyoriented Platinum Surfaces in Sulfuric-Acid Medium. *J. Electroanal. Chem.* **1987**, *233*, 251–265.

53. Rodes, A.; Zamakhchari, M. A.; Elachi, K.; Clavilier, J. Electrochemical-Behavior of Pt(100) in Various Acidic Media 1: On a New Voltammetric Profile of Pt(100) in Perchloric-Acid and Effects of Surface-Defects. *J. Electroanal. Chem.* **1991**, *305*, 115–129.

54. Francke, R.; Climent, V.; Baltruschat, H.; Feliu, J. M. Electrochemical Deposition of Copper on Stepped Platinum Surfaces in the 011 Zone Vicinal to the (100) Plane. *J. Electroanal. Chem.* **2008**, *624*, 228–240.

55. Garcia-Araez, N.; Climent, V.; Feliu, J. M. Analysis of Temperature Effects on Hydrogen and OH Adsorption on Pt(111), Pt(100) and Pt(110) by Means of Gibbs Thermodynamics. *J. Electroanal. Chem.* **2010**, *649*, 69–82.

56. Lipkowski, J.; Stolberg, L. Molecular Adsorption at Gold and Silver Electrodes. In *Adsorption of Molecules at Metal Electrodes*; Lipkowski, J., Ross, P. N., Eds.; VCH: New York, 1992; pp 171–238.

57. Lipkowski, J.; Stolberg, L.; Yang, D. F.; Pettinger, B.; Mirwald, S.; Henglein, F.; Kolb, D. M. Molecular Adsorption at Metal Electrodes. *Electrochim. Acta* **1994**, *39*, 1045–1056.

58. Stolberg, L.; Lipkowski, J.; Irish, D. E. An Examination of the Relationship Between Surface Enhanced Raman Scattering (SERS) Intensities and Surface Concentration for Pyridine Adsorbed at the Polycrystalline Gold/Aqueous Solution Interface. *J. Electroanal. Chem.* **1991**, *300*, 563–584.

59. Wetzel, H.; Gerischer, H.; Pettinger, B. Surface Enhanced Raman-Scattering from Silver-Halide and Silver-Pyridine Vibrations and the Role of Silver Ad-Atoms. *Chem. Phys. Lett.* **1981**, *78*, 392–397.

60. Campion, A.; Mullins, D. R. Normal Raman Scattering from Pyridine Adsorbed on the Low-Index Faces of Silver. *Chem. Phys. Lett.* **1983**, *94*, 576–579.

61. Futamata, M. Highly-Sensitive Raman Spectroscopy to Characterize Adsorbates on the Electrode. *Surf. Sci.* **1997**, *386*, 89–92.

62. Stolberg, L.; Morin, S.; Lipkowski, J.; Irish, D. E. Adsorption of Pyridine at the Gold(111)-Solution Interface. *J. Electroanal. Chem.* **1991**, *307*, 241–242.

63. Hoon-Khosla, M.; Fawcett, W. R.; Chen, A. C.; Lipkowski, J.; Pettinger, B. A SNIFTIRS Study of the Adsorption of Pyridine at the Au(111) Electrode-Solution Interface. *Electrochim. Acta* **1999**, *45*, 611–621.

64. Cai, W. B.; Wan, L. J.; Noda, H.; Hibino, Y.; Ataka, K.; Osawa, M. Orientational Phase Transition in a Pyridine Adlayer on Gold(111) in Aqueous Solution Studied by *in-Situ* Infrared Spectroscopy and Scanning Tunneling Microscopy. *Langmuir* **1998**, *14*, 6992–6998.

65. Wu, D. Y.; Ren, B.; Jiang, Y. X.; Xu, X.; Tian, Z. Q. Density Functional Study and Normal-Mode Analysis of the Bindings and Vibrational Frequency Shifts of the Pyridine-M (M = Cu, Ag, Au, $Cu^+$, $Ag^+$, $Au^+$, and Pt) Complexes. *J. Phys. Chem. A* **2002**, *106*, 9042–9052.

66. Wu, D. Y.; Liu, X. M.; Duan, S.; Xu, X.; Ren, B.; Lin, S. H.; Tian, Z. Q. Chemical Enhancement Effects in Sers Spectra: A Quantum Chemical Study of Pyridine Interacting with Copper, Silver, Gold and Platinum Metals. *J. Phys. Chem. C* **2008**, *112*, 4195–4204.

67. Wu, D. Y.; Hayashi, M.; Lin, S. H.; Tian, Z. Q. Theoretical Differential Raman Scattering Cross-Sections of Totally-Symmetric Vibrational Modes of Free Pyridine and Pyridine-Metal Cluster Complexes. *Spectrochim. Acta A* **2004**, *60*, 137–146.

68. Zhao, L. L.; Jensen, L.; Schatz, G. C. Pyridine-Ag-20 Cluster: A Model System for Studying Surface-Enhanced Raman Scattering. *J. Am. Chem. Soc.* **2006**, *128*, 2911–2919.

69. Wasileski, S. A.; Koper, M. T. M.; Weaver, M. J. Field-Dependent Electrode-Chemisorbate Bonding: Sensitivity of Vibrational Stark Effect and Binding Energetics to Nature of Surface Coordination. *J. Am. Chem. Soc.* **2002**, *124*, 2796–2805.

70. Hamm, U. W.; Kolb, D. M. On the Stability of Reconstructed Au(100) Surfaces in the Presence of Organic-Molecules. *J. Electroanal. Chem.* **1992**, *332*, 339–347.

71. Stolberg, L.; Lipkowski, J.; Irish, D. E. Adsorption of Pyridine at the Gold(100)-Solution Interface. *J. Electroanal. Chem.* **1987**, *238*, 333–353.

72. Wu, S.; Lipkowski, J.; Magnussen, O. M.; Ocko, B. M.; Wandlowski, T. The Driving Force for (p $\times$ $\sqrt{3}$)<—>(1 $\times$ 1) Phase Transition of Au(111) in the Presence of Organic Adsorption: A Combined Chronocoulometric and Surface X-Ray Scattering Study. *J. Electroanal. Chem.* **1998**, *446*, 67–77.

73. Skoluda, P.; Holzle, M.; Lipkowski, J.; Kolb, D. M. Pyridine Adsorption on Reconstructed and Unreconstructed Au-(100). *J. Electroanal. Chem.* **1993**, *358*, 343–349.

74. Conway, B. E. Electrochemical Oxide Film Formation at Noble-Metals as a Surface-Chemical Process. *Prog. Surf. Sci.* **1995**, *49*, 331–452.

75. Stern, D. A.; Lagurendavidson, L.; Frank, D. G.; Gui, J. Y.; Lin, C. H.; Lu, F.; Salaita, G. N.; Walton, N.; Zapien, D. C.; Hubbard, A. T. Potential-Dependent Surface-Chemistry of 3-Pyridinecarboxylic Acid (Niacin) and Related-Compounds at Pt(111) Electrodes. *J. Am. Chem. Soc.* **1989**, *111*, 877–891.

76. Frens, G. Controlled Nucleation for Regulation of Particle-Size in Monodisperse Gold Suspensions. *Nature (London), Phys. Sci.* **1973**, *241*, 20–22.

# SUPPORTING INFORMATION

# *In-situ* SHINERS at Electrochemical Single Crystal Electrode/Electrolyte Interfaces: Tuning Preparation Strategies and Selected Applications

*Jian-Feng Li[a]‡, Alexander Rudnev[a,b]‡, Yongchun Fu[a], Nataraju Bodappa[a] and Thomas Wandlowski[a]\**

[a] Department of Chemistry and Biochemistry, University of Bern, Freiestrasse 3, Bern CH-3012, Switzerland. [b] Frumkin Institute of Physical Chemistry and Electrochemistry, Russian Academy of Sciences, Leninskii pr. 31, Moscow 119991, Russia

**Cluster size distribution**

Drop-casting from a dilute NP solution and subsequent drying in a gentle stream of argon under reduced pressure led to a submonolayer of nanoparticle islands. Spin-coating has also been applied, and led to a further increase of the uniformity. The coverage of the as-deposited NPs ranges typically between 20 to 30 %. The NPs are assembled in small islands containing 4 up to NPs. The islands are rather uniformly distributed on the substrate surface. HER-treatment
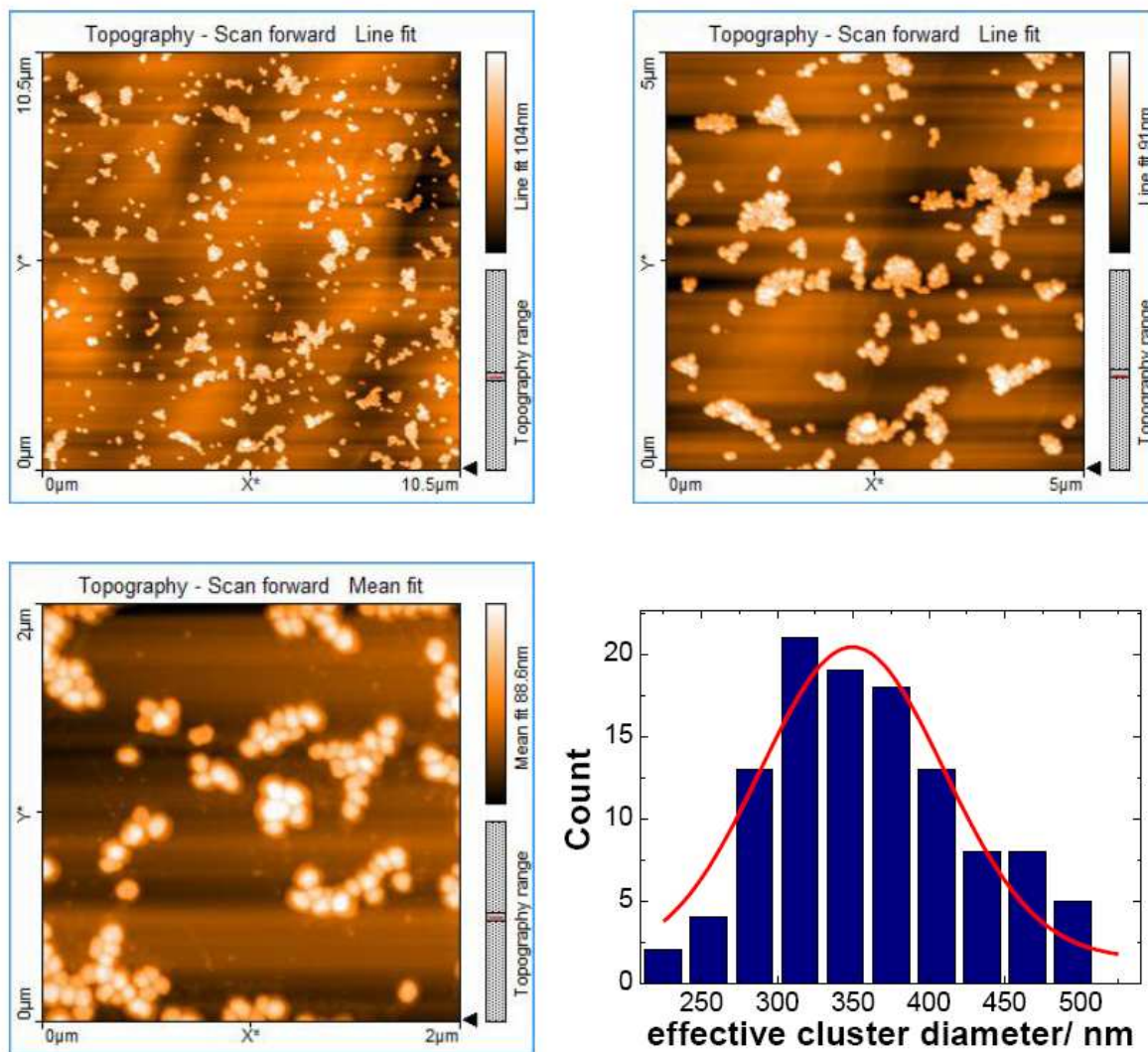
**Figure SI1.** Typical submonolayer of SHINERS NP islands (shown in different resolution) as deposited on Au(111) after HER-treatment. The histogram is based on the statistical analysis of 120 NP-islands of the upper left panel. The effective cluster diameter was derived from the experimentally estimated area of the islands transformed into area-equivalent circular patches.

reduced the coverage by approximately 5 %. No isolated NPs nor 3D islands remain. The statistical analysis of the HER-treated NP-modified surfaces demonstrates that the islands contain typically 15 to 20 NPs. Fig. SI1 shows representative data. The latter estimation was

derived from the effective diameter of the islands as obtained from the experimentally estimated area of the islands transformed into area-equivalent circular patches.

Our preparation procedure guarantees a rather uniform size distribution of islands containing 15 to 20 NPs. Employing our preparation procedure of sub-monolayer HER-SHINERS NPs, we observed a variation in intensity of less than 15 %. Isolated NPs or three-dimensional clusters are rarely being observed on the HER-treated SHINERS-NP modified surfaces. We also note that FDTD simulations revealed that the SHINERS intensity of islands containing more than 4 NPs in one island seems to level off [S1], guaranteeing that the signals observed in our current study, which originate from islands containing 15 to 20 NP, are highly reproducible.

**SHINERS spectra of Py on Au(111) and Pt(111) with and without HER cleaning procedure**

We have compared the SHINERS spectra of Au(111) (Fig. S1A) and Pt(111) (Fig. S1B) electrodes modified with HER-SHINERS NPs (traces a) and "as-prepared" SHINERS-NPs (traces b). In the latter case the spectrum displays additional peaks at around 1160 $cm^{-1}$, 1440 $cm^{-1}$ and 1560 $cm^{-1}$. The additional featuers are atributed to organic contaminants resulting from the SHINERS NP preparation process. Neglecting the influence of these additional species may lead to artifacts and mis-interpetation of surface Raman-spectra..
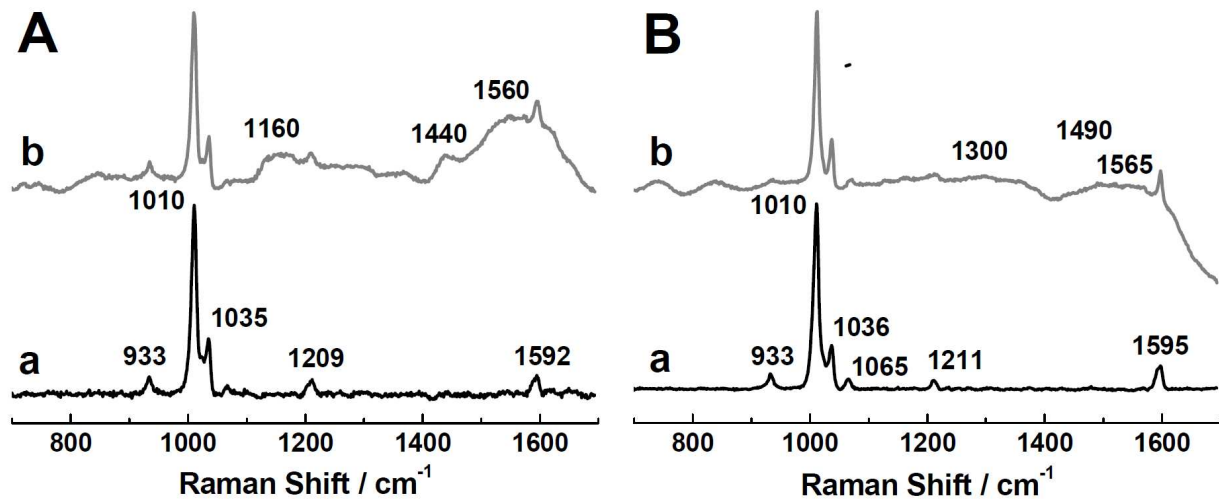
**Figure S1.** SHINER spectra of Py adsorbed on (A) Au(111) and (B) Pt(111) single crystal electrodes at 0.0 V (vs. Ag/AgCl). (a) SHINERS NP prepared by HER und (b) "as-deposited" SHINERS NPs.

**Calcaulation of the surface enhancement factor (SEF)**

The estimation of the SEF is based on the following equation

$$G = \left( \frac{I_{surface}}{N_{surface}} \right) / \left( \frac{I_{soln}}{N_{soln}} \right) \tag{S1}$$

where $I_{surface}$ and $I_{soln}$ are the integrated intensities of the pyridine $\upsilon_1$ ring breathing mode for surface and solution species, respectively. $N_{surface}$ and $N_{soln}$ represent the amount of the surface and solution molecules in the laser beam.

The average experimental SEFs can be obtained using the following equation [S2]:

$$G = \frac{I_{surface} c N_A \sigma h}{I_{soln} R} \tag{S2}$$

4

where $c$ is the concentration of pyridine in solution, $N_A$ is Avogadro's number, $\sigma$ is the cross section area of one adsorbed molecule in a full monolayer, $h$ is the focal depth of the laser and $R$ is the surface roughness.

In our experiments the concentration of pyridine in solution was 1 mM, the area of one absorbed pyridine molecule is estimated as 0.21 nm [S3], and the focal depth of our laser is about 60 μm. The roughness of the single crystals employed in this study is set to R = 1. The integrated intensity of the ring breathing mode of pyridine at ~1010 cm$^{-1}$, $\upsilon_I$, is about 2 counts (1 s) for a 1 mM solution. The integrated surface Raman intensity was 13600 counts (1 s) for Au@SiO$_2$ on Au(111) at 0.4 V. Inserting these data in eqn. (S1) results in an SEF of $6.9 \times 10^4$. Using the same method, we obtained SEFs of $2.6 \times 10^5$, $2.1 \times 10^4$ and $7.0 \times 10^4$ for SHINERS of pyridine on Au(100), Pt(111) and Pt(100), respectively.

**REFERENCES**

S1.    Anema, J. R.; Li, J. F.; Yang, Z. L.; Ren, B.; Tian, Z. Q. Shell-Isolated Nanoparticle-Enhanced Raman Spectroscopy: Expanding the Versatility of Surface-Enhanced Raman Scattering. *Annu. Rev. Anal. Chem.* **2011**, 4, 129-150.

S2.    Lin, X. M.; Cui, Y.; Xu, Y. H.; Ren, B.; Tian, Z. Q. Surface-Enhanced Raman Spectroscopy: Substrate-Related Issues. *Anal. Bioanal. Chem.* **2009**, 394, 1729-1745.

S3.    Lipkowski, J.; Stolberg, L. *Adsorption of Molecules at Metal Electrodes. In Frontiers of Electrochemistry*. Lipkowski, L.; Ross, P. N. eds. VCH: New York, Weinheim, 1992, Vol. 1, pp 171-238.

## 4.1   Publication 2:

## Controlled assembly and single electron charging of monolayer protected Au$_{144}$ clusters: electrochemistry and scanning tunneling spectroscopy study

Authors: **Nataraju Bodappa**, Ulrike Fluch, Yongchun Fu, Marcel Mayor, Pavel Moreno-García, Hans Siegenthaler, Thomas Wandlowski

N. Bodappa's contribution in this publication:

• Developing the self-assembly process of the Au$_{144}$ mixed monolayer protected clusters (MPCs) and *ex-situ*-STM imaging of the electrode surfaces modified with MPCs.

• Voltammetric investigations of the MPCs in bulk electrolyte and assembled on electrode surfaces.

• Quantized charging studies of an array and an isolated particle by electrochemical scanning tunnelling spectroscopy.

• Preparation of the publication manuscript.

## ARTICLE TYPE

# Controlled assembly and single electron charging of monolayer protected Au$_{144}$ clusters: electrochemistry and scanning tunneling spectroscopy study

Nataraju Bodappa[a], Ulrike Fluch[b], Yongchun Fu*[a], Marcel Mayor*[b,c], Pavel Moreno-García[a], Hans
5 Siegenthaler[a] and Thomas Wandlowski[a]

Single gold particles may serve as room temperature single electron memory units due to their size
dependent electronic level spacing. Here we present a proof of concept study by electrochemically
10 controlled scanning probe experiments performed on tailor-made Au particles of narrow dispersity. In
particular the charge transport characteristics through chemically synthesized hexane-1-thiol and 4-
pyridylbenzene-1-thiol mixed monolayer protected Au$_{144}$ clusters (MPCs) by differential pulse
voltammetry (DPV) and electrochemical scanning tunneling spectroscopy (EC-STS) are reported. The
pyridyl groups exposed by the Au-MPCs enable their immobilization on Pt(111) substrates. By varying
15 the humidity during their deposition, samples coated by stacks of compact monolayers of Au-MPCs or
decorated with individual, laterally separated Au-MPCs are obtained. DPV experiments with stacked
monolayers of Au$_{144}$-MPCs and EC-STS experiments with laterally separated individual Au$_{144}$-MPCs are
performed both in aqueous and ionic liquid electrolytes. Lower capacitance values were observed for
individual clusters compared to ensemble clusters. This trend remains the same irrespective of the
20 composition of the electrolyte surrounding to the Au$_{144}$-MPC. The resolution of the energy level spacing
of single clusters however, is strongly affected by the proximity of neighboring particles.

**ARTICLE TYPE**

## 1. Introduction

The miniaturization trend of electronic circuits is focusing on new materials and methods to fabricate devices with feature sizes in the scale below the state-of-art of the current CMOS
5 technique.[1] Most of these devices described in the literature are based on metal or semiconductor nanoparticles (NPs) and are mainly conceptual demonstrators working at low temperatures[2-5] and in vacuum.[6, 7] Nanoelectronic devices operating at a single electron level in ambient environment and at room temperature
10 require rigorous control over the atomic scale dimensions and interactions of their building blocks,[8] involving very small components with precise dimensional control. Objects in a suitable size range are large aromatic molecules or NPs with diameters below 5 nm. Aromatic molecular systems have recently
15 received great attention due to their well defined structure for the exploration of a series of single molecule based transistors and switches.[9]

A very interesting pathway is based on monolayer-protected gold clusters (Au MPCs) coated with thiols, phosphenes or
20 acetylenes as protecting ligands. The syntheses of these Au MPCs have been extensively studied and improved to almost atomic scale precision in the last decade.[10] As these particles have a size of less than 2 nm, they fulfill all the required conditions to observe single electron charging phenomena at room
25 temperature.[11, 12] They have also been suggested to be suitable systems for the fabrication of single electron transistors,[7, 13-15] switches,[16, 17] sensors,[18, 19] symmetric metal-insulator-NP-insulator-metal capacitors[20] and charge trap memory devices.[21, 22] However, only a few studies have been reported on their practical
30 applications at ambient temperature.[15, 23-28] Due to the property of quantized charging at room temperature, Au MPCs can be used to manipulate the electronic function in integrated electronic circuits at the single electron level.[12] This feature of Au MPCs is particularly appealing as it provides the required digital
35 information triggered on a single electron level. Electrochemical techniques play a crucial role in understanding many aspects of Au MPCs,[12, 29-31] such as their charging behavior, size dispersion, HOMO-LUMO gap and electron transfer kinetics. However, conventional electrochemical techniques are limited to the study
40 of Au MPC ensembles, and therefore probe only their average response. To understand the electron transport through the individual Au MPCs in electrical circuits, electrochemical scanning tunneling microscopy (STM) combined with spectroscopic (STS) techniques appears to be a useful method.
45 These techniques provide insight into the tunneling current characteristics of a single NP enclosed between the STM tip and the substrate. Recently, redox mediated single molecule-based transistors [32-38] and switches [39-42] were explored with these techniques by several research groups. On the other hand, to
50 manipulate the charging of an Au$_{144}$ cluster device, the concept of electrochemical gating was introduced.[26]

The practical application of aqueous electrolytes in previous studies[26] is limited to ambient or lower temperatures due to their relatively high volatility. In experiments requiring elevated
55 temperature a highly stable and non-volatile environment is desired. These boundary conditions are perfectly matched by room temperature ionic liquids (RTILs). Their high thermal stability, non-volatility, as well as a considerably broader potential window (often exceeding 4–5 V) of RTILs compared to
60 the aqueous environment enables to access more charging states in a wide temperature range. However, their real accessible potential/temperature window is still restricted by the residue water, which is difficult to be removed completely. These favorable features considerably improve the application potential
65 with respect to future nanoelectronic devices based on single-electron redox switching. Inspired by this, we have addressed quantized double-layer charging dynamics of hexanethiolate protected Au$_{144}$ clusters in various hydrophobic RTILs.[43, 44]

In the nanometer scale, most of the electronic properties of
70 NPs are very sensitive to inter-particle interactions. In the case of semiconductor NPs, it has been shown that interparticle inter-actions are quite significant for their local electronic properties.[45, 46] However, to the best of our knowledge, the observation of neighboring particle effects upon local electronic properties is
75 quite limited in the case of metal NPs. Over the past years, NP assemblies moved into the focus of interest[47] due to the diversity of their possible applications in electronics, magnetism, optics, and catalysis. Improved handling and control of NP assemblies is also of benefit for the integration of NPs into electrical circuits.
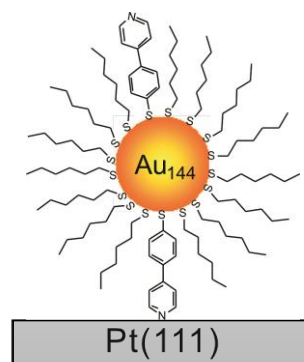80



**Fig. 1** Schematic of the hehane-1-thiol and 4-pyridylbenzene-1-thiol monolayer protected Au$_{144}$ clusters (Au$_{144}$ MPCs) assembled
85 on Pt(111) surface.

In this work, we present the controlled assembly of tailor-made monolayer protected Au$_{144}$ clusters (Au$_{144}$ MPCs) which are mainly protected by hexylthiolates, but comprise also a few 4-
90 (pyridin-4'-yl)benzenethiolates to immobilize the Au$_{144}$ cluster on a Pt(111) substrate (**Fig. 1**). Depending on the assembly conditions, the Au$_{144}$ MPC coverage ranges from stacks of several densely packed monolayers to individual clusters in sub-monolayers. We have subsequently investigated the electronic
95 properties of Au$_{144}$ MPCs by differential pulse voltammetry (DPV) and scanning tunneling spectroscopy (STS) in three different types of electrolytes: An organic solvent (0.01 M BTPPA-TPFB, bis(triphenylphosphoranylidene) ammonium tetrakis(penta-fluorophenyl)borate/CH$_3$CN), an aqueous electro-
100 lyte (0.1 M NaClO$_4$), and a RTIL, [C$_6$C$_1$Im][FEP]. Thereby we are not only able to demonstrate single electron switching at room temperature, but also to establish the influence of the immediate proximity of the Au$_{144}$ MPC on its electronic features. In addition, we have compared the tunneling current characteristics

of an array (collective) of clusters and of an isolated single cluster.

## 2. Experimental section

### 2.1 Materials and chemicals

1-hexyl-3-methylimidazolium tris(pentafluoroethyl)trifluorophosphate ($[C_6C_1Im][FEP]$) RTIL (high purity), and tetrabutylammonium hexafluorophosphate (≥99.0%, electrochemical analysis) were purchased from Merck and Fluka respectively. The $[C_6C_1Im][FEP]$ mixed with molecular sieve was heated up at 85 °C under vacuum ($10^{-6}$ mBar) overnight before use in order to remove the residue water. Sodium perchlorate (>99%, anhydrous) and acetonitrile (≥99.8%, anhydrous) were purchased from Alfa Aesar and Aldrich, respectively. BTPPA-TPFB was synthesized by metathesis of BTPPA-Cl and LiTPFB in 2 : 1 mixtures of methanol and water[48]. Water with the resistivity of 18.2 MΩ.cm was prepared by a Millipore purification system.

*Ligand synthesis:* 4-(pyridin-4'-yl)benzenethiol was synthesized according to literature[49, 50] with minor modifications. A detailed protocol is available in the electronic supporting information (ESI). In short, 4-Bromopyridine hydrochloride and 4-(methylthio)phenylboronic acid were coupled in a Suzuki reaction providing the methyl protected ligand. Subsequent treatment with an alkyl-thiolate resulted in the deprotected 4-(pyridin-4'-yl)benzenethiol, which oxidized in the presence of oxygen to 1,2-bis(4'-(pyridin-4''-yl)-phenyl)disulfane.

### 2.2 Synthesis of mixed monolayer protected $Au_{144}$ clusters

The synthesis of Au MPC was carried out under air atmosphere. $HAuCl_4$ (0.36 mmol, 1 eq) and TOABr (0.38 mmol, 1.1 eq.) were added to a round bottom flask and dissolved in methanol (10 mL). After stirring for 5 min., the solution color had changed from yellow to red. Then 1,2-bis(4'-(pyridin-4'-yl)phenyl)disulfane (0.19 mmol, 0.53 eq.) dissolved in MeOH (5 mL) was added to the stirred solution and cooled to 0 °C. This mixture was stirred for 10 min. before 1-hexanethiol (1.53 mmol, 4.24 eq.) was added, followed by the immediately addition of a freshly prepared $NaBH_4$ solution (3.6 mmol, 10 eq. in 2 mL NanoPure water). The solution turned immediately black, indicating the formation of gold particles. After stirring for 1 h, the mixture was allowed to warm up to room temperature and stirred for another 3 hours at that temperature. The black NP were collected and centrifuged at 4000 rpm for 10 min. The supernatant was discarded and the pellet was washed 3 more times with fresh methanol to wash off the excess of organic molecules.

The formed particles were separated by their different solubility. The Au NP-mixture was suspended in acetone and centrifuged for 10 min. at 4000 rpm. Small Au clusters remained in solution whereas $Au_{144}$ MPCs precipitated and could be separated from bigger particles and gold-thiol-polymer with dichloromethane as solvent. The yield of $Au_{144}$ MPC was 5-10% with respect to the gold salt starting material. The clusters were analyzed by transmission electron microscopy (TEM), MALDI-ToF mass spectrometry, elemental analysis (EA) and thermogravimetric analysis (TGA). TEM pictures displayed Au particles with diameters of 1.7±0.6 nm and MALDI-ToF MS displayed a broad peak between 30 000 and 34 000 amu which are both in agreement with reported values for hexylthiol stabilized $Au_{144}$ particles. As only the pyridyl-functionalized ligand comprises a N atom, the ratio between both ligands was calculated to be 10/1 from the weight percent of N (0.32) and C (17.82) obtained by EA. The TGA experiment displays the loss of 22.38 weight % attributed to the mass of the organic coating. These numbers are in agreement with the composition of a hypothetical average particle as $Au_{144}(SC_6H_{13})_{60}(SC_6H_4C_5NH_4)_6$.

### 2.3 Self-assembly

The $Au_{144}(C_6S)_{60}(C_{11}H_8NS)_6$ MPCs (m = 2.1 mg, M = 36 520 g/mol, n = 57 nmol) were dissolved in $CH_2Cl_2$ (3 mL), forming a solution with the concentration of 19 μM. The hanging-meniscus type Pt(111) electrode was flame-annealed with butane flame (red heat, one minute) and subsequently cooled down in two different ways: (1) under dry Ar stream for about 10 min and (2) cooling in a closed flask containing water-saturated mixture of $Ar/H_2$ (4:1 v/v). After that, the electrode was immersed into the above cluster solution for 1 hour and rinsed by 10 ml of $CH_2Cl_2$ to remove all physisorbed MPC layers. The electrode was then immediately transferred into the deareated electrochemical cell.

### 2.4 Electrochemistry

All electrochemical measurements (DPV) were carried out with an Autolab PGSTAT system. High-purity Ar gas (99.999%) was used to dearate the electrochemical cell both before and during the measurement. An aqueous solution of 0.1 M $NaClO_4$, acetontrile containing 0.01 M BTAPPA-TPFB and $[C_6C_1Im][FEP]$ IL served as the electrolyte. Blank experiments (without $Au_{144}$ MPCs in the system) were carried out to confirm the absence of charging peaks. A Pt wire served as both counter (CE) and reference (RE) electrodes in all DPV measurements. All potential scales were calibrated with respect to $Fc/Fc^+$ redox couple. Pulse width: 60 ms, pulse height: 50 mV, period: 200 ms. The scan-rate in all experiments was 20 mVs$^{-1}$.

### 2.5 STM and STS measurements

Ex-situ STM images of the $Au_{144}$ MPCs were obtained by a Nanoscope E (Digital Instrument, DI). STS experiments were performed using a PicoSPM (Molecular Imaging, MI) under electrochemical conditions. A gold oxide-covered gold and a platinum electrode served as the reference electrode in aqueous solution and RTIL, respectively, and a platinum wire was used as counter electrode for both electrolytes. STM tips were prepared from mechanically cut Pt-Ir wires (diameter 0.25 mm, 80:20%) coated by polyethylene. Since the quality of STM tip coating is crucial for successful STS measurements, a cyclic voltammetric investigation of the STM tip was performed in situ before carrying out a STS measurement. The recorded double layer current should be less than 1 pA. The setpoint of tunneling current ranges from 60 to 150 pA and the bias voltage varies from 50 to 100 mV for a typical STS measurements.

## 3. Results and discussion

### 3.1 Controlled assembly of $Au_{144}$ MPCs on Pt(111)

Self-assembly of Au MPCs on surfaces has mostly been based on the covalent Au–S interaction (α,ω-dithiols linking the Au MPC to the gold surface).[51] However, disintegration of Au MPCs usually takes place on an Au substrate. This is most likely related to the large thermodynamic imbalance between the bulk gold and the nanometer size gold cluster, where the ligand on the gold surface loses the contact with the cluster and forms a new bond with the Au substrate. We therefore developed a more stable Au MPC/substrate system. Initial attempts profiting from Au clusters coated by macromolecules exposing an integer number of functional groups as coupling units failed.[52-55] A more robust Pt(111) surface has been chosen as the substrate which is known to coordinate to the lone pair of the pyridine nitrogen. As Au MPCs interacting with the Pt(111) substrate, gold clusters of narrow dispersity which were stabilized by a mixture of two

ligands were synthesized and isolated (see "Experimental section"). In brief, the synthesized Au clusters comprise in average 144 Au atoms functionalized with about 6 ligands exposing a pyridyl anchor unit (4-(4'-pyridyl)-thiophenolates) in a compact stabilizing coating consisting of about 60 hexylthiolate groups. It is noteworthy that the ratios between Au atoms of the cluster core and both ligands are numbers obtained by analytical methods involving large amounts of Au MPCs. Therefore, the obtained ratios are averaged numbers representing the most prominent composition of Au MPCs (which is $Au_{144}$ ($SC_6H_{13}$)$_{60}$ ($SC_4H_4C_5NH_4$)$_6$). Minor variations in the number of gold atoms forming the cluster core and the numbers of different ligands exposed are very likely. The coordinating interaction of the peripheral pyridine subunits of the Au MPC with the Pt(111) substrate are expected to immobilize the particle at the surface as sketched in **Fig. 1**, while the poor attraction of the Pt(111) with the Au cluster capturing thiolates guarantees the integrity of the Au MPC on the substrate. **Fig. 1** depicts the concept of an $Au_{144}$ MPC adsorbed on a Pt(111) surface through Pt-N coordinative bonding. Here, we report for the first time a new approach to control the Au MPCs on well defined surfaces.
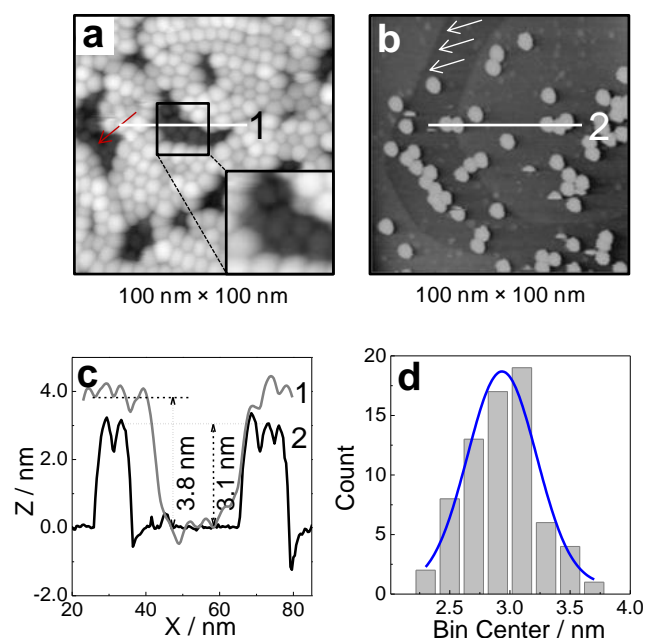


**Fig. 2** (**a, b**) STM images of $Au_{144}$ MPCs assembled on a Pt(111) surface after cooling down in pure Ar (**a**) and in a water-saturated $H_2$/Ar mixture (**b**). The inset picture, 19 × 19 nm$^2$, in (a) shows an enlarged part of a "hole" in the top monolayer (marked with red arrows) displaying the nanoparticle assembly of the layer underneath. (**c**) Cross-section profiles from position 1 in (**a**) (grey profile) and 2 in (**b**) (black profile) as indicated by white lines. (**d**) Histogram of height distribution of individual clusters in (**c**).

Scanning tunneling microscopy (STM) was used to explore the surface morphology of $Au_{144}$ MPCs on Pt(111). It was found that the morphology of $Au_{144}$ MPCs on Pt(111) strongly depends on the pretreatment method of the Pt(111) substrate as well as on the concentration of $Au_{144}$ MPCs in the solution for assembling. The clusters tend to form stacks of several densely packed monolayers with a hexagonally close-packed structure of each layer, if the Pt(111) surface has been cooled down in Ar atmosphere, as shown in **Fig. 2a**. The red arrows in **Fig. 2a** and the enlarged inset picture show the close-packed monolayer underneath the top layer. As it was not possible to determine the number of stacked monolayers in such a multilayer system, we just name this stacked multilayer system throughout this paper with the term "stacked monolayers". However, cooling the Pt(111) surface in a

water saturated hydrogen/argon mixture (1:4) atmosphere led to the formation of a single sub-monolayer with individual clusters sparingly distributed on the surface (**Fig. 2b**). The atomic steps of the Pt(111) substrate are indicated by white arrows. **Fig. 2c** shows cross-section profiles of the white lines in **Fig. 2a** and **b**, revealing a typical monolayer height of 3.8 nm for the stacked monolayers, and 3.1 nm for the sub-monolayer, respectively. **Fig. 2d** shows the histogram of the height of $Au_{144}$ MPCs constructed from more than one hundred individual clusters as shown in **Fig. 2b**, revealing a narrow distribution of height with the most probable value of 2.9 nm, which is very close to the theoretically predicted size of $Au_{144}$ MPCs (3.2 nm, $Au_{144}$ core + ligands). However, the measured diameter of each MPC (7.7 nm) is considerably larger than the theoretically predicted value. This discrepancy can be attributed to the convolution effect of the STM tip in X-Y direction. In addition, high resolution transmission electron microscopy (HR-TEM) was employed to determine the real average diameter of $Au_{144}$ MPCs to be 1.7 nm, corresponding to the characteristic core size of $Au_{144}$ MPCs. We already emphasize here that the narrow size distribution of $Au_{144}$ MPCs plays an important role for obtaining reproducible data by single electron tunneling experiments on different clusters (see section 3.3).
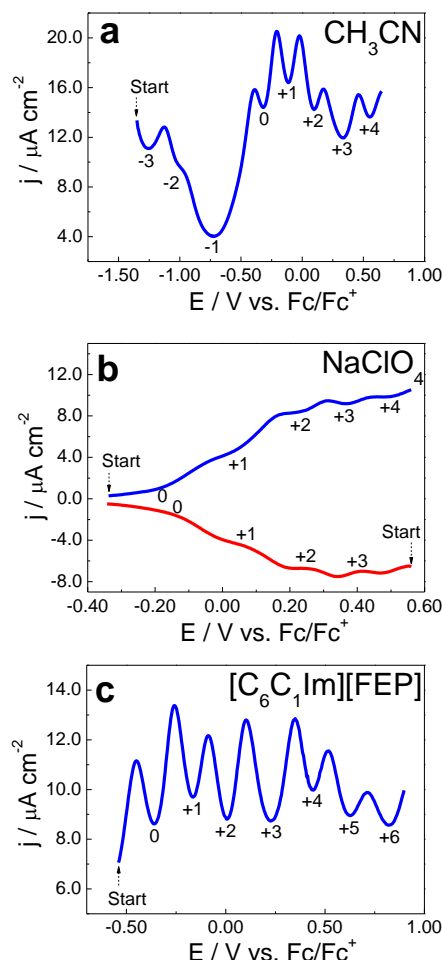


**Fig. 3** Differential Pulse Voltammograms (DPV) of $Au_{144}$ MPCs of a substrate with stacked monolayers on a Pt(111) electrode (as shown in Fig. 2a.) (**a**): In 0.01 M BTPPA-TPFB/$CH_3CN$, (**b**): In 0.1 M aqueous $NaClO_4$, (**c**): in RTIL [$C_6C_1Im$][FEP]. Pulse width: 60 ms, pulse height: 50 mV, period: 200 ms, scan rate 20 mVs$^{-1}$.

The pronounced dependence of the surface morphology of $Au_{144}$ MPCs on Pt(111) on the cooling conditions of the Pt(111) substrate could be due to the presence or absence of a water film on the Pt(111) surface under different atmospheric cooling

conditions. The water film is believed to exist on the Pt(111) surface if it is cooled down in a water-saturated Ar/H$_2$ mixture, which serves as an interface between the Pt(111) surface and the organic phase containing the dissolved Au$_{144}$ MPCs during assembling. Therefore, the Au$_{144}$ clusters diffusing towards the Pt(111) surface from the bulk of the solution must penetrate initially through this water film, which is energetically unfavorable considering the hydrophobic nature of the Au$_{144}$ MPCs ligand shell, and therefore prevents the formation of stacked monolayers. This condition was then further chosen as the typical method of sample preparation with the formation of a sub-monolayer, which plays an important role for the subsequent charge transport studies.

### 3.2 Electrochemical characterization of Au$_{144}$ MPC assemblies

Prior to investigating the electrical properties of Au MPCs immobilized on electrode surface, the electrochemical properties of Au$_{144}$ MPCs were first examined in the bulk phase of organic solution (0.1 M TBAPF$_6$/CH$_3$CN + Toluene) using the standard procedure of differential pulse voltammetry (DPV, **Fig. S1** in the ESI). The DPV curve reveals a typical multiple quantized charging up to thirteen states with an average peak-to-peak spacing ($\Delta E$, only considered as marked with asterisks) of 0.264 $\pm$ 0.02 V (**Fig. S1**), which confirms electrochemically the existence of Au MPCs of the expected size. The average cluster capacitance (C$_{MPC}$) corresponds to a value of 0.608 $\pm$ 0.05 aF derived from peak-to-peak potential spacing with the formula C = e/$\Delta E$. This multiple charging feature, as well as the assignment of charge states, fully agree with the data reported in the literature,[56, 57] where Au$_{144}$ (C$_6$H$_{13}$S)$_{60}$ MPCs were employed.

Fig. 3a shows the anodic DPV scan obtained for a substrate with stacked monolayers of Au$_{144}$ MPCs on a Pt(111) electrode surface in deoxygenated acetonitrile containing 0.01 M BTPPA-TPFB as the supporting electrolyte. Six well-defined maxima are observed within the potential range between -1.50 and +1.0 V vs. Fc/Fc$^+$. These maxima are attributed to the discrete charging of Au MPCs within the monolayer i.e. the electrochemical double layer charging.[12, 31] The large wide gap at charge state -1 in **Fig. 3a** is due to the very large bulky size of both the cation and the anion of the supporting electrolyte, as described in the recent literature.[58] The average peak-to-peak spacing ($\Delta E$, only considered from the 0 to +4 states) amounts to 0.188 $\pm$ 0.01 V, which translates itself into an average capacitance per cluster of 0.852 $\pm$ 0.04 aF.

The DPV of the substrate with Au$_{144}$ stacked monolayers in 0.1 M NaClO$_4$ (**Fig. 3b**) shows that only the positive charge states of the cluster were accessible. This observation is ascribed to ion-induced rectification[59] and ion-coupled electron transfer[60]. I.e, the incorporation of ions into the cluster ligand shell controls the electron transfer between the MPC and the electrode, which in turn limits the accessibility of charge states in the DPV.[61] In the present case, the Na$^+$ cation cannot enter, whereas the ClO$_4^-$ anion, due to its hydrophobic nature, can penetrate into the hydrophobic ligand shell leading to the absence of negative and the appearance of positive charge states in the DPV (**Fig. 3b**). This results in an average peak-to-peak spacing of 0.134 V corresponding to a capacitance value of 1.20 aF, which is close to the result reported in the literature.[59, 62]

The same Au$_{144}$ MPCs stacked monolayer was further investigated in RTIL. The use of an ionic liquid as the electrolyte may enable to access more charging states due to the wide potential window. In addition it allows long-term stability by its unique property of non-volatility, which is highly required for the subsequent STS measurements. **Fig. 3c** shows the DPV of stacked Au$_{144}$ MPCs monolayers on a Pt(111) surface in [C$_6$C$_1$Im][FEP] RTIL. Compared to the case of organic (**Fig. 3a**) and aqueous solvent (**Fig. 3b**), not only uniform charging states but also much more intensive DPV peak current signals were observed in the ionic liquid. These intense DPV current signals observed in IL may be attributed to the higher total ionic concentration and better incorporation of ions compared to the other two electrolytes.[63] An average peak-to-peak spacing of 0.194 $\pm$ 0.03 V was observed with a corresponding capacitance value of 0.84 $\pm$ 0.11 aF, which ranges between the value obtained for organic (CH$_3$CN) and aqueous solution. The different capacitance values for the same cluster in the different three electrolytes (**Table 1 and Table S2**) mainly arise from different ion permeability into the ligand shell and the different dielectric permeability of the solvents.[61, 63, 64]

The assignment of the charge state of an immobilized stacked monolayer was done by the so-called immersion technique.[58, 65] A selected example is demonstrated in the ionic liquid case in **Fig. S2** of the ESI. A series of current transients against time due to double layer charging was recorded by changing the immersion potential. The charging current is either negative or positive (inset, **Fig. S2**), and varies systematically with the chosen immersion potential. A series of systematically recorded current transients is integrated at a fixed time scale (5 s after immersion) yielding a charge density which represents the consumed charge for building up the electrochemical double layer, and is plotted *versus* the immersion potential. The potential of zero-crossing represents an estimation of PZTC. The PZTC of Au$_{144}$ stacked monolayers in [C$_6$C$_1$Im][FEP] is -0.34 V vs. Fc/Fc$^+$, which is close to the minimum of the DPV curve, as indicated in **Fig. S2**. As a consequence, the charge state of this minimum at -0.34 V is assigned to the zero charge state. These electrochemical studies show the multiple discrete states accessible in one single element at room temperature, which may enable an increased data storage density of such a prototype switch. Additionally, the strong dependence of the electrochemical characteristics of the MPCs on the chosen electrolyte shows that this system can be finely tuned to control each single electron transport event. These features make our MPCs versatile and appealing materials for molecular electronics applications. However, the electrochemical studies only give the overall current signal from assemblies. Indeed, for realizing the future nano/molecular electronics, it is necessary to understand the charge transport behavior of individual clusters by incorporating them in between two electrodes. Therefore, we use EC-STS for characterizing the electrical properties of individual clusters.

### 3.3 Scanning tunneling spectroscopy (STS) of single Au$_{144}$ MPCs

All STS experiments were done on the sample shown in **Fig. 2b**, since the surface contains both "stand-alone" and "grouped" Au$_{144}$ MPCs. For STS measurements, both types are available on one sample. Due to the fast evaporation of the organic solvent as well as the problem of the instability of STM tip coating, the STS measurements are limited to aqueous solution and ionic liquid.

In order to obtain reliable STS traces, the whole system requires an extremely high mechanical stability. In order to achieve this, the setup was at least stabilized for more than twelve hours prior to the experiment and the STS experiments were typically performed around midnight in order to minimize the disturbance from environments. To verify the stability of the setup practically, a small surface area of 20 $\times$ 20 nm$^2$ was repeatedly imaged and the stability was evaluated from the drift of the STM image. The STM tip was finally positioned on the

central top of one $Au_{144}$ MPC by gradually decreasing the scanning area if no obvious drift was observed (< 2 nm/image, **Fig. S3** of the ESI). The tunneling current response was recorded at a constant position of the tip while simultaneously sweeping both, the substrate potential $E_s$ and the tip potential $E_t$ at a constant bias mode with the feedback loop disabled. In this case, each equilibrium redox charge state of the $Au_{144}$ MPCs comes into resonance while sweeping both, the Fermi levels of the substrate and the tip. The single electron transfer takes place from the Pt substrate to the STM tip, if a positive bias was applied, through the $Au_{144}$ MPCs via a two-step electron transfer mechanism, **Fig. 4a**.



1-undecanethiol on an Au(111) surface in 0.1 M $HClO_4$ (**Fig. S6** of the ESI). Evidently no enhancement of the tunneling current was observed during the potential sweep, but only a stable background tunneling current of 0.1 nA. This result supports unambiguously that the enhancement of the tunneling current in **Fig. 4b** indeed originates from the existence of $Au_{144}$ MPCs trapped between the STM tip and the substrate.

**Table 1.** Comparison of the average peak potential spacing and single cluster capacitance values measured in various electrolytes by DPV and STS.

| Electrolyte | Method | $\Delta E$ / V | C / aF |
|---|---|---|---|
| $CH_3CN$ | DPV | 0.188 | 0.852 |
| $NaClO_4$ | DPV | 0.134 | 1.198 |
| | STS | 0.219 | 0.730 |
| $[C_6C_1Im][FEP]$ | DPV | 0.194 | 0.840 |
| | STS | 0.297 | 0.540 |

The blue curve in **Fig. 4b** shows a typical STS profile recorded in 0.1 M $NaClO_4/H_2O$ with the tip on the top of an isolated $Au_{144}$ MPC. The peak position and the magnitude of the enhancement of tunneling current are found to be reproducible within several subsequent measurements on one cluster (**Fig. S4** in the ESI). As displayed in **Fig. S5** in the ESI, the peak positions of the charging current in the DPV studies are independent of the amount of clusters on the electrode surface. The assignment of the charge states in the tunneling current spectra was based on the potential scale of the DPV experiment, as indicated by the numerical labels in **Fig. 4b**. The average peak-to-peak spacing in the tunneling current traces amounts to 0.219 ± 0.01 V, corresponding to an average capacitance value of 0.730 aF, which is by ~ 40% smaller than the value determined by DPV (**Table 1**). This significant discrepancy of the capacitance value was also reported by Albrecht et. al,[26] where a very similar cluster of $Au_{145}$ (hexylmercaptane)$_{38}$(4-mercaptopyridine)$_{12}$ MPCs (abbreviated as $Au_{145}(C_6S)_{38}(4MP)_{12}$) was studied under electrochemical control (0.1 M $KClO_4$). The authors suggested that this discrepancy could be due to a smaller contribution of capacitance from the diffuse layer in the STS configuration compared to DPV, and a substrate-solution potential drop parameter ($\xi$).[63, 66] In more details, the conductance of the tunneling current mainly happens through the minority ligand of 4-pyridylbenzene-1-thiol due to the coordinating bond between platinum and pyridyl. However, the capacitance measured by DPV is contributed collectively by the entire mixed monolayer, mainly from the majority ligand of hexane-1-thiol (90%). This explanation is further supported by the fact that a very close capacitance value (1.20 aF (ours) vs. 1.08 aF (ref. 26)) as determined by DPV was observed for both systems, since they bear the common dominant ligand, namely hexane-1-thiol. However, the capacitance value determined by STS in our case (0.73 aF) is by ~15% lower than that reported in the literature (0.86 aF),[26] indicating that STS is more sensitive to the local environment, i.e. the local dielectric constant ($C = \varepsilon_0\varepsilon_r A/d$), which highly depends on the nature of ligands.

STS was further applied to investigate the local electrical properties of individual $Au_{144}$ MPCs in $[C_6C_1Im][FEP]$ RTIL. The potential of the STM tip was swept between -0.64 and 0.9 V by keeping a constant bias of 0.10 V. **Fig. S7** in the ESI shows the highly reproducible STS traces obtained on one cluster, indicating the high stability of the tip-cluster-substrate junction. Moreover, we also conducted the STS measurements on different clusters, and a selection of representative traces from five different clusters are plotted together and shown in **Fig. S8** of the

**Fig. 4** (**a**) Schematic of scanning tunneling spectroscopy (STS). (**b**) Tunneling current response with respect to substrate potential on an individual well-separated $Au_{144}$ MPCs on Pt(111) surface. Black curve: in $[C_6C_1Im][FEP]$ RTIL $I_{set}$: 50 pA, $V_{bias}$ ($E_{tip} - E_{substrate}$): +0.1 V, sweep rate: 0.8 V s$^{-1}$. Blue curve: in 0.1 M $NaClO_4$ aqueous solution. $I_{set}$: 60 pA, $V_{bias}$: +0.05 V, sweep rate: 0.8 V s$^{-1}$. The numerical labels describe the charge state of $Au_{144}$ MPCs under different potentials. (**c**) A comparison of tunneling current peak intensities of an individual $Au_{144}$ MPCs in RTIL $[C_6C_1Im][FEP]$ (black curve) with 0.1 M $NaClO_4$ aqueous solution (blue curve). The numerical labels describe the transition of the charge states that are associated with the peaks in **Fig. 4b**.

In order to avoid artifacts from the STS curves, a control experiment was firstly carried out with a redox inactive SAM of

ESI. Evidently, the traces coincide well with little deviation, which demonstrates the reproducibility and reliability of our measurements. One typical STS curve was shown in the black curve in **Fig. 4b**. Compared to the case in aqueous solution (blue curve), the enhancement of tunneling current was observed in a wider potential window, however. The average peak-to-peak spacing amounts to $0.297 \pm 0.02$ V, corresponding to an average capacitance of 0.54 aF, which is by $\sim 40\%$ smaller than the value obtained from an ensemble of $Au_{144}$ MPCs by DPV (0.84 aF, **Table 1** ). This trend in the ionic liquid is in accordance with that observed in aqueous electrolyte and can also be explained by the same mechanism of diffuse layer contribution.

The average tunnelling conductance values at each charge state are 1.7, 4.0, 7.9 and 2.4, 2.3, 3.2, 4.8, 5.9 nS in 0.1 M $NaCO_4$ and RTIL, respectively, and are plotted in **Fig. 4c**. The increase of tunneling current at more positively charged states was observed in both electrolytes, which strongly supports the qualitative explanation by Albrecht et al.,[26] who ascribed it to an increase of dielectric saturation i.e., the organisation of solvent molecules with increased charge state. As a result, a decrease of re-organisation energy of solvent molecules increases the tunneling rate values. Therefore, the dielectric saturation phenomenon is more predominant than the electronic coupling between clusters. However, we note that this monotonous increase of the tunneling current with increasing charge state was not always observed (see **Fig. 5**). This could be explained by either i) the high sensitivity of the tunneling current to the exact tip position relative to the $Au_{144}$ MPC surface; ii) fluctuations of the gap between STM tip and $Au_{144}$ MPC .

### 3.4 Comparison between single clusters and arrays of clusters: inter-particle interactions

The EC-STS data showed that the tunneling response depends strongly on the average distance between the particles. This was realized by comparing the STS results for individual but well-separated NPs with those of individual NPs in a close-packed monolayer domain of the same substrate. **Fig. 5** shows such a comparison recorded in $[C_6C_1Im][FEP]$ RTIL. $Au_{144}$ MPCs in a close-packed environment (**Fig. 5a**) show no doublet peaks in their EC-STS traces, whereas the STS response of individual well-separated NPs (**Fig. 5b**) shows doublet peaks as indicated by dp1 and dp2.

The peak to peak spacing and the cluster capacitance for both close-packed and individual particles are shown in **Table S1** of

the ESI. For close packed particles (**Fig. 5a**), the peak to peak spacing is 0.25, 0.28, 0.39, 0.26 V, and for individual particles (**Fig. 5b**) 0.36, 0.22, 0.29, 0.21 and 0.32 V. The large gap in **Fig. 5a** corresponds to the gap observed at the charge state +3 in the DPV, which was induced by the ionic liquid electrolyte (**Fig. 3**). Each peak in dp1 and dp2 are separated by $\sim 0.22$ V, which is the Coulomb repulsion energy between the electrons (charging energy). The wide gap in-between the -1/0 and 0/+1 transition corresponds to the HOMO-LUMO gap of 0.14 V, indicating that the single $Au_{144}$ MPC has a molecular nature as opposed to the observation in array of clusters and ensembles measured by STS and DPV experiments (**Fig. 5a** and **Fig. 3c**). Recently, the discrete nature of electronic spectra was observed for $Au_{144}$ $(C_6H_{14})_{60}$ ensemble clusters by lowering the temperature to 77 K.[67, 68] Thus the disappearance of the HOMO-LUMO gap in the ensemble clusters at room temperature could arise from the Coulomb coupling between neighboring NPs. This clearly confirms that inter-particle interactions strongly influence the electrical properties and corresponding energy level spectra of Au MPCs and will have to be considered when using them as electronic elements in potential multistate electronic switches. These detailed studies reveal the potential of MPC based materials for future nano electronic devices. Engineering of the individual cluster materials into electronic circuits remains challenging however.

## 4. Conclusions

In conclusion, we demonstrate an increased control over both, the assembly and the electronic coupling of Au MPCs on an atomically flat electrode. By choosing Pt(111) as substrate and by synthesizing Au MPCs exposing a few pyridyl-groups coordinating to the substrate, the stability of the immobilized clusters is considerably improved. By varying the deposition conditions, samples coated with stacked layers consisting of closely packed Au MPCs or samples decorated with laterally separated individual Au MPCs are obtained. Electrochemical experiments were performed with samples ranging from dissolved Au MPCs in bulk solution, over stacked layers of Au MPCs down to single laterally separated Au MPCs. In all electrochemical experiments discrete charging events are resolved corroborating the narrow dispersity of the Au MPCs and demonstrating their potential as single electron switches. The spacing of the electrochemically addressed energy levels and thus also the capacity of the Au MPCs however, depends on the surrounding electrolyte. This was demonstrated for stacked layers of Au MPCs by DPV, and for individual immobilized Au MPCs by STS experiments. The latter studies also demonstrate that the energy level mapping of single Au MPC depends on the proximity of the neighboring clusters. The tunneling conductance increases and the HOMO-LUMO gap appears in the case of the isolated $Au_{144}$ clusters compared to the stacked array of clusters.

All together the lateral control of the Au MPC assembly provides samples fulfilling all requirements for room temperature single electron switches. In particular their multistate character observed in ionic liquids is appealing with respect to future applications. The single Au MPC tunneling characteristics (electron transport) depends on both, the composition of the surrounding electrolyte and the cluster arrangement. These aspects enhance the versatility of the system for molecular electronics applications and are the subject of current investigations. A possible combination of electrochemisty, STM/STS with other accessible single electron tunneling techniques, e.g. dynamic tunneling force microscopy (DTFM) should provide the power

for gaining new insight into the electronic and electron transport properties of many interesting nanoscale systems beyond our current understanding.[69]

## Acknowledgements

## Notes and references

*a Freiestrasse 3, 3012 Bern, Switzerland. Fax: +41-(0)31-631-3993; Tel: +41-(0)31-631-4254; E-mail:fu@dcb.unibe.ch*

*b St. Johannsring 19, 4056 Basel, Switzerland. Fax: +41-(0)61-267-1016; Tel: +41-(0)61-267-1006; E-mail: Marcel.Mayor@unibas.ch*

*c P. O. Box 3640, 76021 Karlsruhe, Germany.*

† Electronic Supplementary Information (ESI) available: See DOI: 10.1039/b000000x/

1. W. Lu and C. M. Lieber, *Nat. Mater.*, 2007, 6, 841-850.
2. S. Kubatkin, A. Danilov, M. Hjort, J. Cornil, J. L. Bredas, N. Stuhr-Hansen, P. Hedegard and T. Bjornholm, *Nature*, 2003, 425, 698-701.
3. E. Lortscher, J. W. Ciszek, J. Tour and H. Riel, *Small*, 2006, 2, 973-977.
4. H. Song, M. A. Reed and T. Lee, *Advanced Materials*, 2011, 23, 1583-1608.
5. J.-F. Dayen, E. Devid, M. V. Kamalakar, D. Golubev, C. Guédon, V. Faramarzi, B. Doudin and S. J. van der Molen, *Adv. Mater.*, 2013, 25, 400-404.
6. A. M. Ionescu and H. Riel, *Nature*, 2011, 479, 329-337.
7. S. W. Boettcher, N. C. Strandwitz, M. Schierhorn, N. Lock, M. C. Lonergan and G. D. Stucky, *Nat. Mater.*, 2007, 6, 592-596.
8. W. Haiss, C. S. Wang, I. Grace, A. S. Batsanov, D. J. Schiffrin, S. J. Higgins, M. R. Bryce, C. J. Lambert and R. J. Nichols, *Nat. Mater.*, 2006, 5, 995-1002.
9. J. C. Cuevas and E. Scheer, *Molecular Electronics: An Introduction to Theory and Experiment*, World Scientific, Singapore, 2010.
10. H. Qian, M. Zhu, Z. Wu and R. Jin, *Acc. Chem. Res.*, 2012, 45, 1470-1479.
11. S. Chen, R. S. Ingram, M. J. Hostetler, J. J. Pietron, R. W. Murray, T. G. Schaaff, J. T. Khoury, M. M. Alvarez and R. L. Whetten, *Science*, 1998, 280, 2098-2101.
12. T. Laaksonen, V. Ruiz, P. Liljeroth and B. M. Quinn, *Chem. Soc. Rev.*, 2008, 37, 1836-1846.
13. D. L. Klein, R. Roth, A. K. L. Lim, A. P. Alivisatos and P. L. McEuen, *Nature*, 1997, 389, 699-701.
14. D. N. Weiss, X. Brokmann, L. E. Calvet, M. A. Kastner and M. G. Bawendi, *Appl. Phys. Lett.*, 2006, 88, 143507-143503.
15. G. Schmid and U. Simon, *Chem. Commun.*, 2005, DOI: 10.1039/b411696h, 697-710.
16. D. I. Gittins, D. Bethell, D. J. Schiffrin and R. J. Nichols, *Nature*, 2000, 408, 67-69.
17. L. C. Brousseau, Q. Zhao, D. A. Shultz and D. L. Feldheim, *J. Am. Chem. Soc.*, 1998, 120, 7645-7646.
18. E. Katz and I. Willner, *Angew. Chem. Int. Ed.*, 2004, 43, 6042-6108.
19. M. Hesari, Z. Ding and M. S. Workentin, *Organometallics*, 2014, DOI: 10.1021/om500112j.
20. D. L. Feldheim, K. C. Grabar, M. J. Natan and T. E. Mallouk, *J. Am. Chem. Soc.*, 1996, 118, 7640-7641.
21. R. J. Tseng, C. Tsai, L. Ma, J. Ouyang, C. S. Ozkan and Y. Yang, *Nat Nano*, 2006, 1, 72-77.
22. R. J. Tseng, J. Ouyang, C.-W. Chu, J. Huang and Y. Yang, *Appl. Phys. Lett.*, 2006, 88, 123506-123503.
23. G. Schmid and B. Corain, *Eur. J. Inorg. Chem.*, 2003, 2003, 3081-3098.
24. B. A. Korgel, *Nat. Mater.*, 2007, 6, 551-552.
25. M. Homberger and U. Simon, *Philosophical Transactions of the Royal Society A: Mathematical, Physical and Engineering Sciences*, 2010, 368, 1405-1453.
26. T. Albrecht, S. F. L. Mertens and J. Ulstrup, *J. Am. Chem. Soc.*, 2007, 129, 9162-9167.
27. P. Yang, I. Arfaoui, T. Cren, N. Goubet and M.-P. Pileni, *Nano Lett.*, 2012, 12, 2051-2055.
28. V. Torma, T. Reuter, O. Vidoni, M. Schumann, C. Radehaus and G. Schmid, *ChemPhysChem*, 2001, 2, 546-548.
29. J.-P. Choi and R. W. Murray, *J. Am. Chem. Soc.*, 2006, 128, 10496-10502.
30. D. Lee, R. L. Donkers, J. M. DeSimone and R. W. Murray, *J. Am. Chem. Soc.*, 2003, 125, 1182-1183.
31. R. W. Murray, *Chemical Reviews (Washington, DC, United States)*, 2008, 108, 2688-2720.
32. A. M. Ricci, E. J. Calvo, S. Martin and R. J. Nichols, *J. Am. Chem. Soc.*, 2009, 132, 2494-2495.
33. P. Salvatore, A. Glargaard Hansen, K. Moth-Poulsen, T. Bjornholm, R. John Nichols and J. Ulstrup, *PCCP*, 2011, 13, 14394-14403.
34. T. Albrecht, A. Guckian, J. Ulstrup and J. G. Vos, *Nanotechnology, IEEE Transactions on*, 2005, 4, 430-434.
35. T. Albrecht, K. Moth-Poulsen, J. B. Christensen, J. Hjelm, T. Bjornholm and J. Ulstrup, *J. Am. Chem. Soc.*, 2006, 128, 6574-6575.
36. T. Albrecht, K. Moth-Poulsen, J. B. Christensen, A. Guckian, T. Bjornholm, J. G. Vos and J. Ulstrup, *Faraday Discuss.*, 2006, 131, 265-279.
37. N. J. Kay, S. J. Higgins, J. O. Jeppesen, E. Leary, J. Lycoops, J. Ulstrup and R. J. Nichols, *J. Am. Chem. Soc.*, 2012, 134, 16817-16826.
38. P. Petrangolini, A. Alessandrini, M. L. Navacchia, M. L. Capobianco and P. Facci, *The Journal of Physical Chemistry C*, 2011, 115, 19971-19978.
39. Z. Li, Y. Liu, S. F. L. Mertens, I. V. Pobelov and T. Wandlowski, *J. Am. Chem. Soc.*, 2010, 132, 8187-8193.
40. A. Mishchenko, M. Abdualla, A. Rudnev, Y. Fu, A. R. Pike and T. Wandlowski, *Chem. Commun.*, 2011, 47, 9807-9809.
41. I. V. Pobelov, Z. Li and T. Wandlowski, *J. Am. Chem. Soc.*, 2008, 130, 16045-16054.
42. Pavel Moreno-García, Hennie Valkenier, Yongchun Fu, Ilya Pobelov, Wenjing Hong, Jan C. Hummelen and T. Wandlowski, 2014, In preparation.
43. S. F. L. Mertens, K. Blech, A. S. Sologubenko, J. Mayer, U. Simon and T. Wandlowski, *Electrochim. Acta*, 2009, 54, 5006-5010.
44. S. F. L. Mertens, G. Meszaros and T. Wandlowski, *Phys. Chem. Chem. Phys.*, 2010, 12, 5417-5424.
45. D. Steiner, A. Aharoni, U. Banin and O. Millo, *Nano Lett.*, 2006, 6, 2201-2205.
46. P. Liljeroth, K. Overgaag, A. Urbieta, B. Grandidier, S. G. Hickey and D. Vanmaekelbergh, *Phys. Rev. Lett.*, 2006, 97, 096803.
47. M. A. Mezour, I. I. Perepichka, J. Zhu, R. B. Lennox and D. F. Perepichka, *ACS Nano*, 2014, 8, 2214-2222.
48. D. J. Fermín, H. Dung Duong, Z. Ding, o. Brevet and H. H. Girault, *PCCP*, 1999, 1, 1461-1467.
49. A. Gallardo-Godoy, M. I. Torres-Altoro, K. J. White, E. L. Barker and D. E. Nichols, *Bioorg. Med. Chem.*, 2007, 15, 305-311.
50. H. Qian and R. Jin, *Chem. Mater.*, 2011, 23, 2209-2217.
51. S. Chen, *The Journal of Physical Chemistry B*, 2000, 104, 663-667.
52. T. Peterle, A. Leifert, J. Timper, A. Sologubenko, U. Simon and M. Mayor, *Chemical Communications*, 2008, DOI: 10.1039/B802460J, 3438-3440.
53. T. Peterle, P. Ringler and M. Mayor, *Adv. Funct. Mater.*, 2009, 19, 3497-3506.
54. J. P. Hermes, F. Sander, T. Peterle, R. Urbani, T. Pfohl, D. Thompson and M. Mayor, *Chemistry – A European Journal*, 2011, 17, 13473-13481.
55. J. P. Hermes, F. Sander, U. Fluch, T. Peterle, D. Thompson, R. Urbani, T. Pfohl and M. Mayor, *J. Am. Chem. Soc.*, 2012, 134, 14674-14677.
56. B. M. Quinn, P. Liljeroth, V. Ruiz, T. Laaksonen and K. Kontturi, *J. Am. Chem. Soc.*, 2003, 125, 6644-6645.
57. J. F. Hicks, D. T. Miles and R. W. Murray, *J. Am. Chem. Soc.*, 2002, 124, 13322-13328.
58. K. Cui, S. De Feyter and S. F. L. Mertens, *Electrochem. Commun.*, 2012, 25, 128-131.
59. S. Chen and R. Pei, *J. Am. Chem. Soc.*, 2001, 123, 10607-10615.
60. W. Li, D. Wang, Q. Sun and B. Su, *Electrochem. Commun.*, 2011, 13, 875-878.

61. T. Laaksonen, O. Pelliniemi and B. M. Quinn, *J. Am. Chem. Soc.*, 2006, 128, 14341-14346.
62. S. Chen, *J. Am. Chem. Soc.*, 2000, 122, 7420-7421.
63. R. Guo, D. Georganopoulou, S. W. Feldberg, R. Donkers and R. W. Murray, *Anal. Chem.*, 2005, 77, 2662-2669.
64. B. Su, M. Zhang, Y. Shao and H. H. Girault, *The Journal of Physical Chemistry B*, 2006, 110, 21460-21466.
65. U. W. Hamm, D. Kramer, R. S. Zhai and D. M. Kolb, *J. Electroanal. Chem.*, 1996, 414, 85-89.
66. A. M. Kuznetsov and J. Ulstrup, *The Journal of Physical Chemistry A*, 2000, 104, 11531-11540.
67. H. C. Weissker, H. B. Escobar, V. D. Thanthirige, K. Kwak, D. Lee, G. Ramakrishna, R. L. Whetten and X. Lopez-Lozano, *Nat Commun*, 2014, 5, 3785.
68. J. Koivisto, S. Malola, C. Kumara, A. Dass, H. Häkkinen and M. Pettersson, *The Journal of Physical Chemistry Letters*, 2012, 3, 3076-3080.
69. N. Zheng, J. P. Johnson, C. C. Williams and G. Wang, *Nanotechnology*, 2010, 21, 295708.

# Supporting information of the manuscript:

# Controlled assembly and single electron charging of monolayer protected Au$_{144}$ clusters: electrochemistry and scanning tunneling spectroscopy study

Nataraju Bodappa,[a] Ulrike Fluch,[b] Yongchun Fu,*[a] Marcel Mayor,*[b,c] Pavel Moreno-garcía,[a] Hans Siegenthaler[a] and Thomas Wandlowski[a]

[a] Department of Chemistry and Biochemistry, University of Bern, Freiestrasse 3, 3012 Bern, Switzerland
[b] Department of Chemistry, University of Basel, St. Johannsring 19, 4056 Basel, Switzerland
[c] Institute for Nanotechnology (INT), Karlsruhe Institute of Technology (KIT), P. O. Box 3640, 76021 Karlsruhe, Germany

## Table of content

**Synthesis and characterization of the ligand molecules:**

The ligand 1,2-bis(4'-(pyridin-4''-yl)-phenyl)disulfane **1** was synthesized follwing slightly modified literature procedures.[1,2] The 4-bromopyridine hydrochloride (**2**) and 4-(methylthio)-phenylboronoic acid (**3**) were coupled in a Suzuki reaction providing 4-(4-(methylthio)phenyl)-pyridine (**4**) in good yields. Treatment of **4** with an alkylthiolate in dimethylformamide (DMF) gave the deprotected 4-(pyridin-4'-yl)benzenethiol **5** as free thiophenol derivative. In the presence of oxygen, **5** oxidized quickly to the stable disulfide **1**. It is noteworthy that under the applied reductive conditions used for the synthesis of the Au MPCs, **1** is rduced back to the free thiophenol **5**.
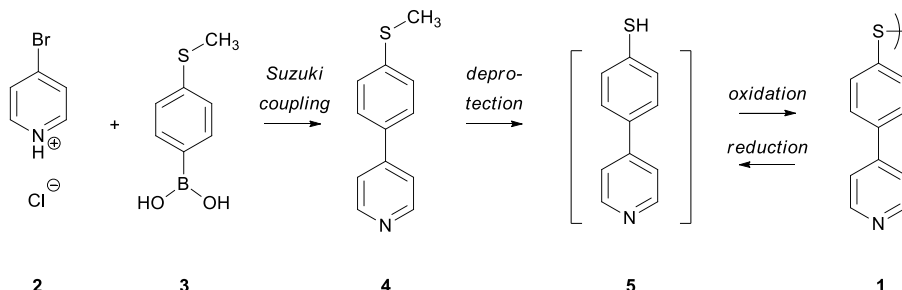


**General remarks:** All chemicals were commercially available and were used as received. 4-Bromopyridine hydrochloride was obtained from Fluorochem. 4-(Methylthio)phenylboronic acid, sodium 2-methyl-2-propanethiolate, tetraoctylammonium bromide (TOABr, >98%) sodium borohydride ($NaBH_4$, 96%) and dimethylformamide (DMF) were obtained from Aldrich. Tetrakis(triphenylphosphine)palladium (0), 99%, tetrabutylammonium bromide (TBABr, 99%), 1-hexanethiol (96%) and tetrachloroauric(III) acid ($HAuCl_4$ $H_2O$, >49% Au) were purchased from Acros. 1,2-Dimethoxyethane (DME, 99%) was obtained from Alfa Aesar, HPLC solvents (acetone, methanol and dichloromethane) were purchased from Baker.

**Suzuki coupling:** 4-Bromopyridine hydrochloride (2.44 mmol, 1 eq.), 4-(methylthio)phenyl-boronic acid (2.44 mmol, 1 eq.) together with KOH (12.2 mmol, 5 eq.) as base, TBABr (12 mol%) as phase transfer catalyst, tetrakis(triphenylphosphine)palladium (6 mol%) as catalyst and DME (15 ml) and water (5 ml) as solvents were put in the reaction vessel. The reaction mixture was degassed by bubbling argon through the solution for 10 minutes before heating it up by microwave to 160 °C for 1.5 h. After aqueous work up and extraction with diethylether, the combined organic phases were washed with water and brine before drying over $Na_2SO_4$. Evaporation of the solvent provided the crude product which was purified by sublimation to provide 4-(pyridin-4'-yl)thioanisole in 97 % yield as white solid. $^1$H NMR (400 MHz, $CDCl_3$) δ 8.63 (d, J = 6.2 Hz, 2H), 7.56 (d, J = 8.5 Hz, 2H), 7.46 (d, J = 6.3 Hz, 2H), 7.34 (d, J = 8.5 Hz, 2H), 2.51 (s, 3H); $^{13}$C NMR (101 MHz, $CDCl_3$) δ 150.42, 147.71, 140.45, 134.64, 127.36, 126.79, 121.28, 15.60; GC-MS (EI) m/z: 201.0 [M]$^+$, 186.0 [M-Me]$^+$; MS (DART-EI) m/z: 201.8 [M+H]$^+$, 403.0 [2M+H]$^+$.

**Deprotection:** 4-(Pyridin-4'-yl)thioanisole (1.31 mmol, 1 eq.) and sodium 2-methyl-2-propanethiolate (3.6 mmol, 2.8 eq.) were dissolved in dry DMF (10 ml), degassed by bubbling argon through the solution for 10 minutes before heating the mixture to 160 °C for 4 h. After

[1] A. Gallardo-Godoy, M. I. Torres-Altoro, K. J. White, E. L. Barker and D. E. Nichols, *Bioorg. Med. Chem.*, **2007**, *15*, 305-311.
**2** H. Qian and R. Jin, *Chem. Mater.*, **2011**, *23*, 2209-2217.

cooling to room temperature, the solution was poured on ice and the pH was adjusted to 6 with aq. HCl (1M). Extraction with $CH_2Cl_2$ followed by drying the combined organic phases over $Na_2SO_4$ and evaporation of the solvent under reduced pressure provided the crude product, which was further purified by column chromatography ($SiO_2$, $EtOAc/CH_2Cl_2$: 4/1) to yield in 4-(pyridin-4'-yl)benzenethiol (51%) as yellow solid. The ligand is prone to form disulfides in the presence of oxygen. As the disulfide is cleaved in the reducing conditions during Au particle formation, we used the disulfide 1,2-bis(4'-(pyridin-4''-yl)phenyl)disulfane for the synthesis of the Au MPCs. $^1$H NMR (400 MHz, $CDCl_3$) δ = 8.66 (d, J = 6.1 Hz, 4H), 7.62 (d, J = 6.9 Hz, 8H), 7.50 – 7.43 (m, 4H); $^{13}$C NMR (101 MHz, CDCl3) δ = 133.03, 132.29, 132.19, 131.99, 128.70, 128.58.
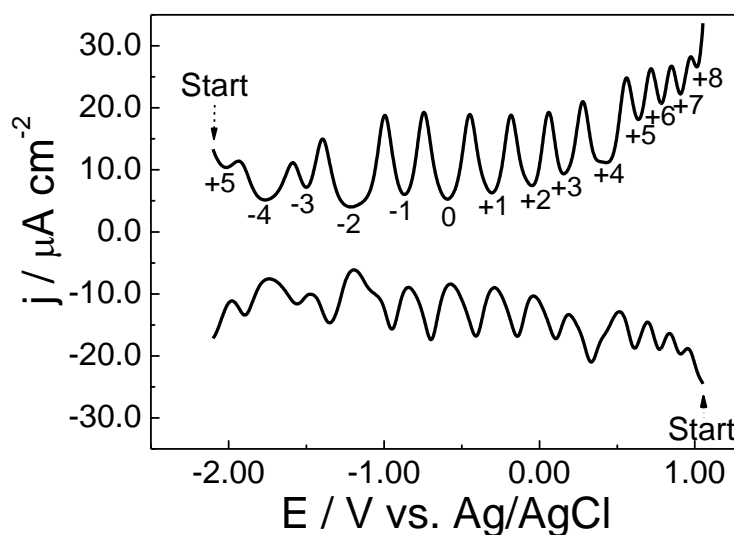


**Fig. S1** DPV of a Pt electrode in a 0.1 mM solution of $Au_{144}$ MPCs dissolved in a mixture of toluene and acetonitrile (2:1) containing 0.1 M of $TBAPF_6$ as supporting electrolyte. Pulse width: 60 ms, pulse height: 50 mV, period: 200 ms, scan rate: 20 mVs$^{-1}$.
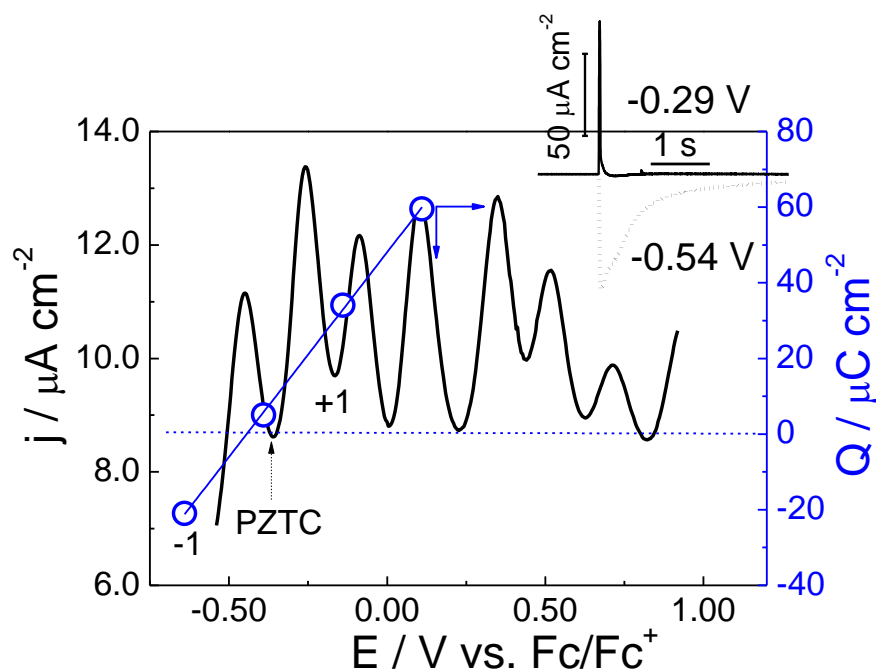
**Fig. S2** DPV of a self-assembled layer of $Au_{144}$ MPCs on a Pt(111) electrode in $[C_6C_1Im][FEP]$ ionic liquid. The inset shows the current transient curves at -0.29 V and -0.54 V vs. $Fc/Fc^+$. Pulse width: 60 ms, pulse height: 50 mV, period: 200 ms, scan rate: 20 mVs$^{-1}$.
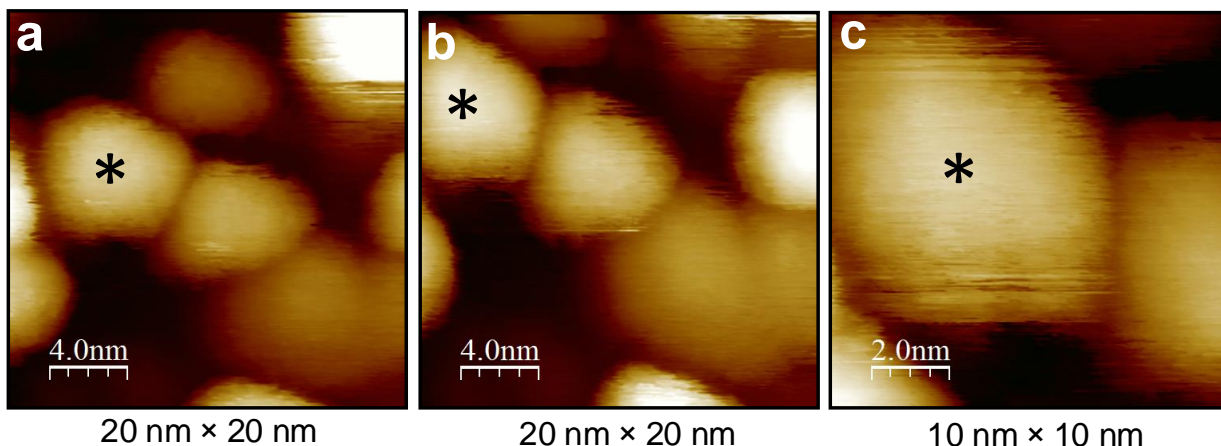


**Fig. S3** In-situ STM images of $Au_{144}(C_6S)_{60}(C_{11}H_8NS)_6$ MPCs on a Pt(111) surface in 0.1 M $NaClO_4$. Scanning aize (**a**) $20 \times 20$ nm$^2$, (**b**) $20 \times 20$ nm$^2$, (**c**) $10 \times 10$ nm$^2$. Set point current $I_{set}$: 60 pA, bias voltage $V_{bias}$: +0.3 V, $E_S$: -0.6 V, $E_t$: +0.3 V.
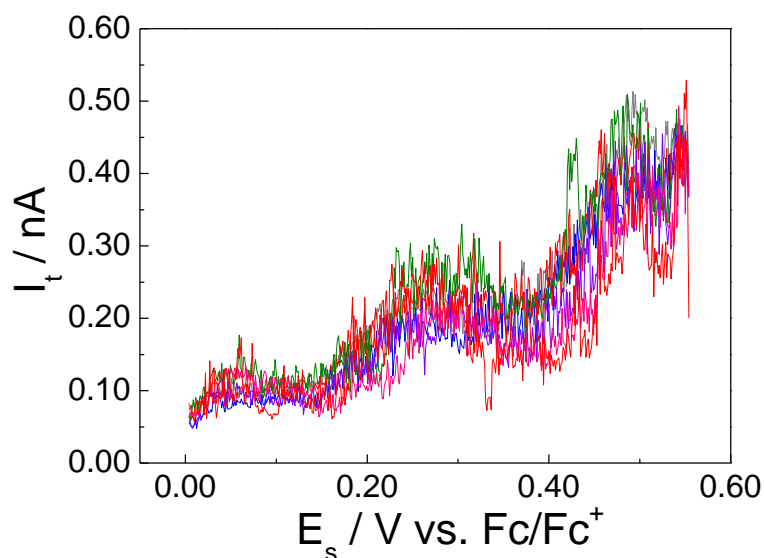
**Fig. S4** Overlay of the STS traces: constant bias tunneling current-voltage response of a single Au$_{144}$ cluster obtained in 0.1 M NaClO$_4$ on a Pt(111) surface; I$_{set}$: 60 pA, V$_{bias}$: +0.05 V, sweep rate 0.8 Vs$^{-1}$.
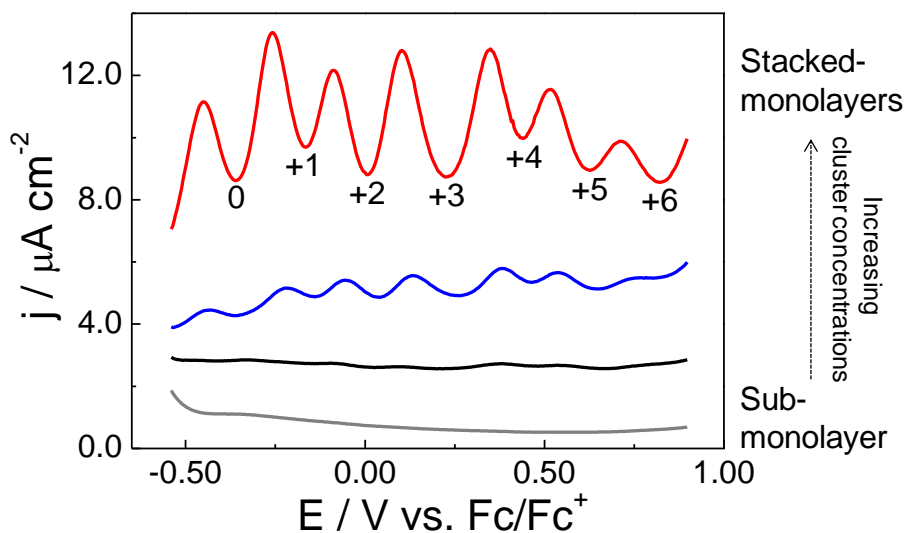


**Fig. S5** DPV of a multilayer Au$_{144}$ MPCs on a Pt(111) electrode in [C$_6$C$_1$Im][FEP] ionic liquid. Pulse width: 60 ms, pulse height: 50 mV, period: 200 ms, scan rate 20 mVs$^{-1}$. The cluster concentration on the electrode surface was increased as shown in the figure.
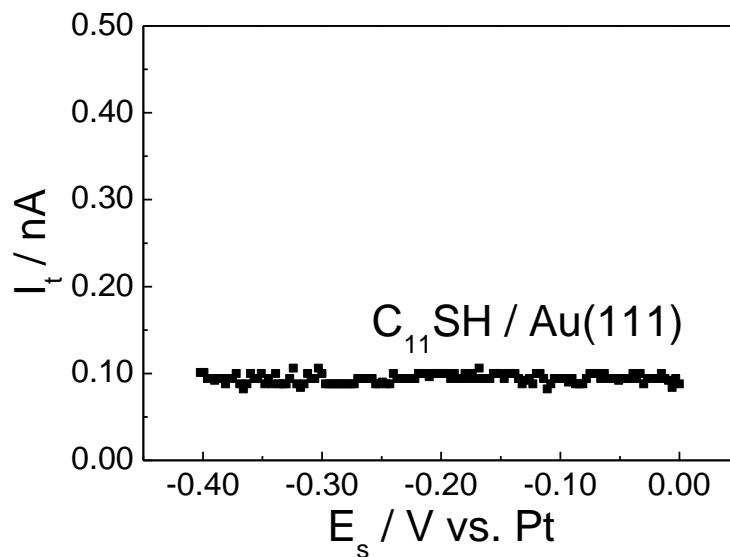
**Fig. S6** Constant bias tunneling current-voltage response of a self-assembled monolayer of 1-undecanethiol SAM on a Au (111) surface recorded in the aqueous solution of 0.1 M $HClO_4$. $I_{set}$: 0.1 nA, $V_{bias}$: +0.1 V, $E_s$: -0.5 V, $E_t$: -0.4 V, sweep rate: 0.6 $Vs^{-1}$. The represented data is averaged from 25 individual runs.
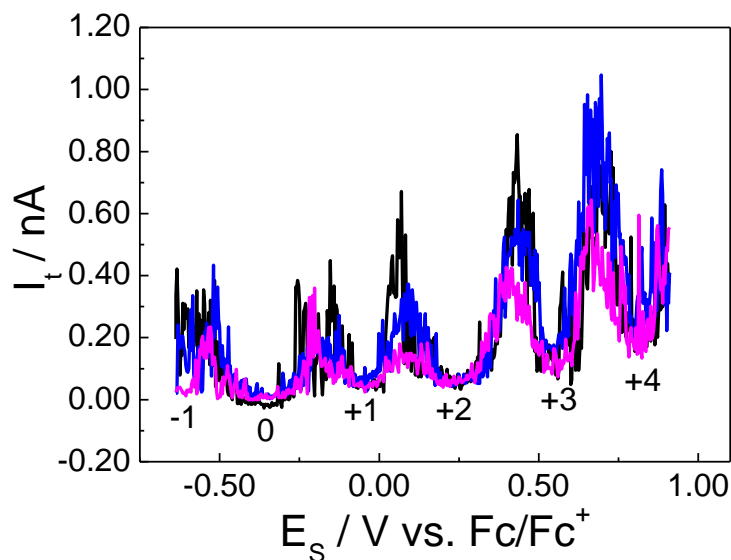


**Fig. S7** Overlay of the STS traces: constant bias tunneling current-voltage response of a single cluster on a Pt(111) surface in $[C_6C_1Im][FEP]$ IL. $I_{set}$: 50 pA, $V_{bias}$: +0.10 V, sweep rate 0.8 $Vs^{-1}$.
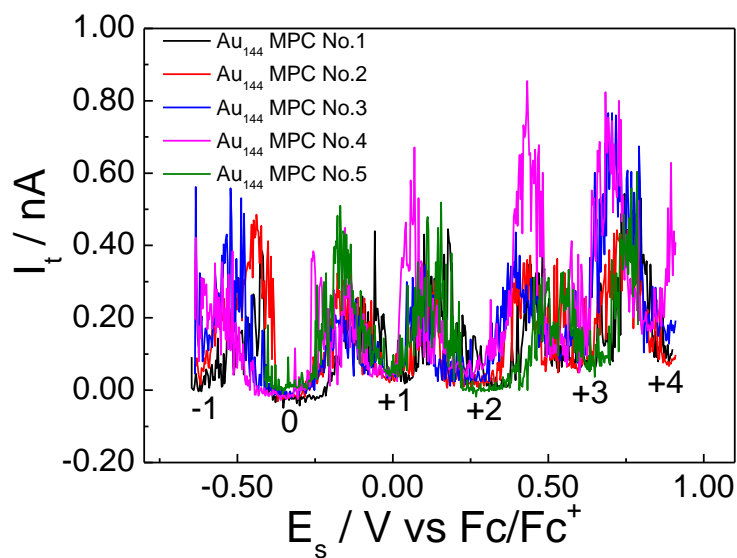
**Fig. S8** Overlay of the STS traces obtained from different $Au_{144}$ MPCs in $[C_6C_1Im][FEP$. $I_{set}$: 50 pA, $V_{bias}$: +0.10 V, sweep rate 0.8 V s$^{-1}$.

**Table S1.** STS peak potential spacing ($\Delta E$) and cluster capacitance (c) values measured in $[C_6C_1Im][FEP]$ ionic liquid. The averaged values for $\Delta E$ and C are shown in Table 1 of the main paper.

| Charge state | $\Delta E$ / V (cp)[a] | C / aF (cp) | $\Delta E$ / V (i)[b] | C / aF (i) |
|---|---|---|---|---|
| $\Delta E_{0/+1}$ | 0.253 | 0.634 | 0.356 | 0.451 |
| $\Delta E_{+1/+2}$ | 0.275 | 0.583 | 0.220 | 0.722 |
| $\Delta E_{+2/+3}$ | 0.390 | 0.411 | 0.288 | 0.558 |
| $\Delta E_{+3/+4}$ | 0.257 | 0.625 | 0.208 | 0.742 |
| $\Delta E_{+4/+5}$ | --- | --- | 0.322 | 0.498 |

[a] CP = closely packed; [b] i = isolated

**Table S2.** STS and DPV peak potential spacing ($\Delta E$) and cluster capacitance (c) values measured for the $Au_{144}$ MPCs in different electrolytes. The represented STS data is for *isolated particle* measurements. The averaged values for $\Delta E$ and C are shown in Table 1 of the main paper.

| Electrolyte | Charge state | DPV | | STS (i)[a] | |
|---|---|---|---|---|---|
| | | $\Delta E$ / V | C / aF | $\Delta E$ / V | C / aF |
| $CH_3CN$ (0.01 M BTPPA-TPFB) | $\Delta E_{0/+1}$ | 0.181 | 0.884 | | |
| | $\Delta E_{+1/+2}$ | 0.185 | 0.864 | Note[b] | |
| | $\Delta E_{+2/+3}$ | 0.198 | 0.810 | | |
| | Average | 0.188 | 0.852 | | |
| $H_2O$ (0.1 M $NaClO_4$) | $\Delta E_{+1/+2}$ | 0.132 | 1.214 | --- | --- |
| | $\Delta E_{+2/+3}$ | 0.135 | 1.183 | 0.211 | 0.759 |
| | $\Delta E_{+3/+4}$ | --- | --- | 0.227 | 0.704 |
| | Average | 0.134 | 1.198 | 0.219 | 0.730 |
| $[C_6C_1Im][FEP]$ | $\Delta E_{0/+1}$ | 0.192 | 0.835 | 0.361 | 0.444 |
| | $\Delta E_{+1/+2}$ | 0.171 | 0.939 | 0.245 | 0.653 |
| | $\Delta E_{+2/+3}$ | 0.189 | 0.843 | 0.333 | 0.481 |
| | $\Delta E_{+3/+4}$ | 0.247 | 0.649 | 0.247 | 0.650 |
| | $\Delta E_{+4/+5}$ | 0.167 | 0.959 | --- | --- |
| | $\Delta E_{+5/+6}$ | 0.197 | 0.813 | --- | --- |
| | Average | 0.194 | 0.840 | 0.297 | 0.540 |

[a] i = isolated; [b] Data not available. Due to the fast evaporation of the $CH_3CN$ solvent the STS measurements cannot be done in this solvent.

# 4.1   Publication 3:

## Temperature-Dependent Transport Properties of a Redox-Active Ionic Liquid with a Viologen Group

Authors: **Nataraju Bodappa**, Peter Broekmann, Yong-Chun Fu, Julien Furrer, Yutaro Furue, Takamasa Sagara, Hans Siegenthaler, Hironobu Tahara, Soma Vesztergom, Klaus Zick, Thomas Wandlowski

Status: Submitted

Journal: *Journal of Physical Chemistry C*

Year: 2014

N. Bodappa's contribution in this publication:

• Investigations of the thermal properties of the ionic liquid by temperature controlled polarization microscopy

• Temperature dependent electrochemical investigations, voltammetric and chronoamperometric measurements

• Temperature dependent conductivity and impedance spectroscopy measurements.

• Participation in the preparation of the publication manuscript.

# Temperature-Dependent Transport Properties of a Redox-Active Ionic Liquid with a Viologen Group

| | |
|---|---|
| Journal: | *The Journal of Physical Chemistry* |
| Manuscript ID: | Draft |
| Manuscript Type: | Article |
| Date Submitted by the Author: | n/a |
| Complete List of Authors: | Bodappa, Nataraju; University of Bern, Department of Chemistry and Biochemistry<br>Broekmann, Peter; University of Bern, Department of Chemistry and Biochemistry<br>Fu, Yong-Chun; University of Bern, Department of Chemistry and Biochemistry<br>Furrer, Julien; University of Bern, Department of Chemistry and Biochemistry<br>Furue, Yutaro; Nagasaki University, Graduate School of Engineering, Division of Chemistry and Materials Science<br>Sagara, Takamasa; Nagasaki University, Graduate School of Engineering, Division of Chemistry and Materials Science<br>Siegenthaler, Hans; University of Bern, Department of Chemistry and Biochemistry<br>Tahara, Hironobu; Nagasaki University, Graduate School of Engineering, Division of Chemistry and Materials Science<br>Vesztergom, Soma; University of Bern, Department of Chemistry and Biochemistry; Eötvös Loránd University, Department of Physical Chemistry<br>Zick, Klaus; Bruker BioSpin GmbH,<br>Wandlowski, Thomas; University of Bern, Department of Chemistry and Biochemistry |
| | |

SCHOLARONE™
Manuscripts

1
2
3
4
5
6
7
8
9
10
11
12
13
14
15
16
17
18
19
20
21
22
23
24
25
26
27
28
29
30
31
32
33
34
35
36
37
38
39
40
41
42
43
44
45
46
47
48
49
50
51
52
53
54
55
56
57
58
59
60
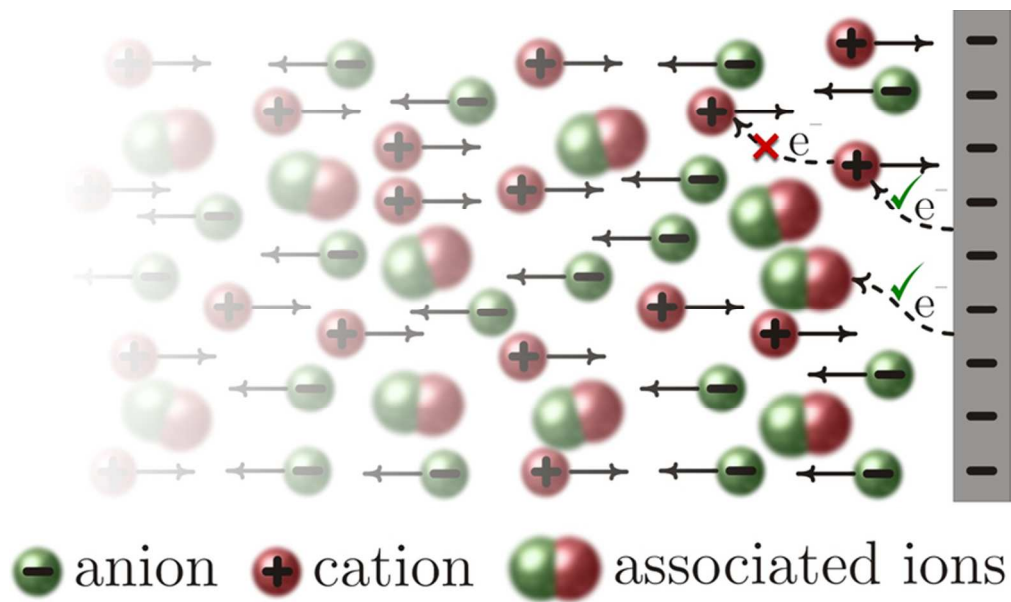


Graphics for the Abstract.
69x41mm (300 x 300 DPI)

# Temperature-Dependent Transport Properties of a Redox-Active Ionic Liquid with a Viologen Group

Nataraju Bodappa,[†] Peter Broekmann,[†] Yong-Chun Fu,[*,†] Julien Furrer,[†] Yutaro Furue,[‡] Takamasa Sagara,[*,‡] Hans Siegenthaler,[†] Hironobu Tahara,[‡] Soma Vesztergom,[*,†,¶] Klaus Zick,[§] and Thomas Wandlowski[†]

*University of Bern, Department of Chemistry and Biochemistry, Freiestraße 3, CH–3012 Bern, SWITZERLAND, University of Nagasaki, Graduate School of Engineering, Bunkyo 1-14, J–8528521 Nagasaki, JAPAN, Eötvös Loránd University, Department of Physical Chemistry, Pázmány Péter sétány 1/A, H–1117 Budapest, HUNGARY, and Bruker BioSpin GmbH, Silberstreifen 4, D–76287 Rheinstetten, GERMANY*

E-mail: fu@dcb-unibe.ch; sagara@nagasaki-u.ac.jp; vesztergom@chem.elte.hu

---
[*]To whom correspondence should be addressed
[†]University of Bern
[‡]University of Nagasaki
[¶]Eötvös Loránd University of Budapest
[§]Bruker BioSpin GmbH

## Abstract

A redox-active ionic liquid (IL), 1-butyl-1'-heptyl-4,4'-bipyridinium bis(trifluorome-thanesulfonyl)imide has been synthesized and its transport processes were investigated. The conductivity and viscosity of the IL, as well as the diffusion coefficients of its components were studied over a 50 °C wide temperature range: for the diffusivity studies, both the pulsed-gradient spin-echo (PGSE)–NMR technique and voltammetric measurements have been applied. The measured data are presented in the paper and are compared to each other. It was found that the diffusion coefficients determined by means of NMR and chronoamperometry measurements are, within the range of experimental error, equal — and they are (in accordance with other ionic liquid studies) higher than what the conductivity or viscosity measurements indicate. The results are interpreted in the light of the existing theories. The measured diffusion coefficients and bulk conductivities can be well interrelated based on the "ionicity" concept (that is, by treating the ionic liquid as a weak electrolyte). In agreement with the empirical Walden rule, a direct comparison between the measured conductivities and viscosities is also possible, for which a hole conduction model is utilized. Based on the fact that both the electrochemical and the NMR measurements yield practically the same diffusion coefficients in the system, there is no evidence that interpretations based in other redox-active IL systems on "homogeneous electron transfer" apply to the system studied here.

## Keywords

redox-active ionic liquids, transport mechanisms, ionicity, Nernst–Einstein relation

## Introduction

Ionic liquids (ILs) are defined as salts with melting points below 100 °C; many of them are fluid at room temperature. They have been attracting much interest recently in various areas of

chemistry, both in academia and in the chemical industry, because of their beneficial properties like non-volatility, high ionic conductivity and non-flammability.[1,2] These important features make them versatile alternatives to conventional solvent-based systems. Ionic liquids have found their application in the construction of batteries,[3] fuel cells[4] and solar cells,[5] but have also been used as lubricants and heat-transfer fluids[6] or as solvents for clean chemical synthesis and catalysis.[7]

From an electrochemical point of view, the most notable feature of *non-redox-active* ionic liquids is their high electrochemical stability. By bringing such an IL to contact with a noble metal, a nearly ideally polarisable electrode can be created, the voltammetric curves of which exhibit a 4–5 volts wide double-layer region.[8–10] Exceeding this potential range triggers strong currents that correspond to the decomposition (electrolysis) of the liquid.[11] The decomposition is usually irreversible, and as its products remain adherent to (and contaminate) the surface, it ultimately destroys the electrode functionality. In case of *redox-active* ionic liquids the redox processes occurring at the metal | liquid interface can be considered *reversible* over a relatively wide voltage range (that is, the reaction products – once formed – can later be transformed back to the original IL at a different electrode potential). While non-redox-active ILs can be ideally used as electrolytic media in the deposition processes of base metals and other reactive materials,[12] redox-active ILs usually find their application in dye-sensitized solar cells[13] or Li-ion batteries (where, acting as "redox shuttles", they protect the cell from the unwanted effects of overcharging).[14]

Due to their wide range of applicability, several redox-active and -inactive ionic liquids have been synthesized in the last decades. Numerous combinations of the cationic and anionic structures are possible, thus the physicochemical properties of ILs can be tuned by changing the structure of the constituting ions. For the design of ionic fluids, however, it is necessary to understand their basic physical and chemical properties. Yet interpreting the physicochemical behaviour of these concentrated electrolyte solutions is often found very challenging, and we still lack the complete understanding of the charge, momentum and mass

transport mechanisms in ionic liquid systems. Despite the large amount of research done to date,[15–31] there is no firm consensus as to the exact role that individual ionic diffusion, ionic association and ion/ion interactions play in these processes.

It is a well-established experimental observation that the individual (ionic) self-diffusion coefficients measurable in most ionic liquid systems are considerably higher than what could be expected based on the measured conductivities and the Nernst–Einstein relation; the interpretation of this effect is, however, rather unclear and several (often contradicting) explanations exist in the literature. Here we attempt to provide the reader with a brief overview of these.

  i.) *The "ionicity" based interpretation.* To the best of our knowledge it was the research group of Watanabe et al. who first applied the pulsed-gradient spin-echo (PGSE)–NMR technique[32] in ionic liquids in order to measure the individual diffusion coefficients of its constituting ions.[15–18] Using these values in the Nernst–Einstein equation, they calculated conductivities which they then compared to the results of direct conductometry — and found that the Nernst–Einstein equation gives a significant overestimation. In order to bridge the gap between the experimentally determined and the diffusion coefficient based conductivities, they introduced a certain deviation parameter $\alpha$ to the Nernst–Einstein equation:

$$\kappa = \frac{\alpha F^2 c}{RT} \sum_i D_i z_i^2 \nu_i, \tag{1}$$

  where $D_i$ denotes the self-diffusion coefficient, $z_i$ the charge number and $\nu_i$ the stoichiometric number of an ion $i$, and $c$ is the total concentration (inverse molar volume) of the ionic liquid.

  If $\alpha = 1$, Equation (1) is reduced to the classical Nernst–Einstein case, but in most ionic liquids a value of $\alpha < 1$ is needed to correlate the measured diffusion coefficients with the conductivities. Watanabe et al. explained this observation by assuming that to some extent, a certain association can occur between the ions, causing a significant

portion of them not to contribute to conduction.[15–18] This so-called "ionicity" concept (i.e., the approach of treating ionic liquids as weak electrolytes, and interpreting $\alpha$ as a degree of dissociation) got widely accepted by many researchers,[19] but it did not remain completely unchallenged.

*ii.) The "velocity cross-correlation" based interpretation.* Most notably, in a recent paper Harris has claimed that "[i]onicity as such is a somewhat ill-defined concept as any estimate of association or aggregation depends on the time-scale of the experiments used for its determination".[21] In agreement with early molecular dynamics simulations[33] Harris argued that the deviations from the Nernst–Einstein equation in an ionic liquid might not only be a result of ionic association, but it might also occur due to differences in the cross-correlation functions of the ionic velocities.[20–22] The like-ion and unlike-ion interactions in Harris's works are characterized by the velocity cross-correlation coefficients $f_{++}$, $f_{--}$ and $f_{+-}$, defined as

$$f_{++} \equiv \frac{N_A V}{3} \int_0^\infty \langle v_{+j}(0) v_{+k}(t) \rangle \, \mathrm{d}\, t, \qquad (2.\mathrm{a})$$

$$f_{--} \equiv \frac{N_A V}{3} \int_0^\infty \langle v_{-j}(0) v_{-k}(t) \rangle \, \mathrm{d}\, t \qquad (2.\mathrm{b})$$

and

$$f_{+-} \equiv \frac{N_A V}{3} \int_0^\infty \langle v_{+j}(0) v_{-k}(t) \rangle \, \mathrm{d}\, t. \qquad (2.\mathrm{c})$$

Here $V$ is the volume of the ensemble, $N_A$ is the Avogadro constant and the integrals represent cross-correlations of the velocities of different ions in the ensemble, as denoted by the indices $j$ and $k$.

Harris showed[21] that the Nernst–Einstein deviation parameter $\alpha$ (that is the reciprocal of the Haven-ratio $H_r$, often used to interpret conductivities in condensed matter

5

physics[34]) may be expressed by using the values of these integrals in Equation (3):

$$\alpha = 1 + \frac{c\,(f_{++} + f_{--} - 2f_{+-})}{\frac{D_+}{\nu_+} + \frac{D_-}{\nu_-}},\qquad(3)$$

where $D_+$ and $D_-$ denote the diffusion coefficients, while $\nu_+$ and $\nu_-$ the stoichiometric numbers of the cation and the anion, respectively.

*iii.) The "electron exchange" based interpretation.* Murray et al. have conducted electrochemical measurements in several redox-active IL systems (with[24–28] and without[23] metal ion complexes), and have found that the "apparent" diffusion coefficients ($D_{app}$) obtained by the analysis of voltammetric curves are significantly higher than the "physical" ones ($D_{phys}$) which could be deducted from the conductivity and viscosity measurements. They argued that the reason of this discrepancy is an electron self-exchange process taking place within the mixed valence-state diffuse layer. According to the Dahms–Ruff relation,[35–37]

$$D_{app} = D_{phys} + \frac{k_{ex}\delta^2 c}{6}\qquad(4)$$

(where $k_{ex}$ is the electron self-exchange rate constant, $c$ is the concentration of the redox group containing species, and $\delta$ is the site-to-site distance between the redox groups where electron self exchange occurs), this could lead to a noticeable enhancement of the electrochemically determined diffusion coefficients.

From the above cursory glance at the existing theories it is obvious that the interpretation of the diffusivity/conductivity discrepancies in IL systems is all but straightforward. An important point to note is that the results of the PGSE–NMR technique (when applied to a non-redox-active IL) and the analysis of voltammetric curves (taken in a redox-active IL) both indicate anomalously high diffusion coefficients. When used in the Nernst–Einstein equation, these yield conductivities that are higher than the experimentally determined values — yet we have no knowledge of any study whatsoever that would utilize *both* of these techniques

and make a comparison with the directly measured conductivities. With the present paper we attempt to fill this gap.

In this study a redox-active ionic liquid, 1-butyl-1'-heptyl-4,4'-bipyridinium bis(trifluoro-methanesulfonyl)imide ($[C_4VC_7][Tf_2N]_2$, Figure 1), has been synthesized and its transport processes were investigated. The conductivity and viscosity of the IL, as well as the diffusion coefficients of its components were studied over a 50 °C wide temperature range: for the diffusivity studies, both the PGSE–NMR technique and voltammetric measurements have been applied. The measured data were fitted with the Vogel–Fulcher–Tammann (VFT) equation;[38–40] the obtained transport parameter values are presented in the paper and are compared to each other.
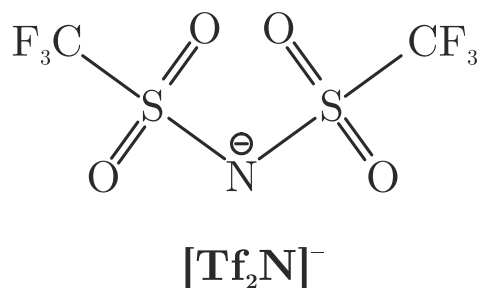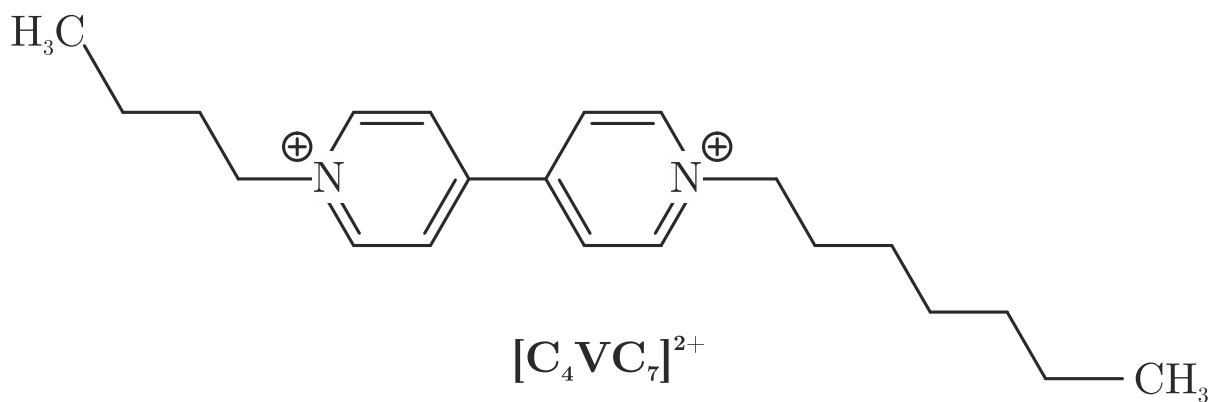
Figure 1: Chemical formulæ of the 1-butyl-1'-heptyl-4,4'-bipyridinium $\left([C_4VC_7]^{2+}\right)$ cation and the bis(trifluoromethanesulfonyl)imide $\left([Tf_2N]^-\right)$ anion, constituting the studied ionic liquid.

We have found that the diffusion coefficients determined by means of NMR and chronoamperometry measurements are, within the range of experimental error, equal — and they are (in accordance with previous ionic liquid studies) higher than what the conductivity or viscosity measurements indicate. Our aim in the present paper is three-fold: *i.)* to interpret these results in the light of the existing theories; *ii.)* to provide, thereby, a critical overview of the present state of transport studies; and *iii.)* to clarify the complementary nature of the various transport parameters.

# Experimental

## Synthesis

Milli-Q water was used for all experiments. 4,4'-bipyridyl (bpy, TCI) was purified by a single-step sublimation. 1-Bromobutane (Wako), 1-bromoheptane (TCI), potassium bis(trifluoromethanesulfonyl)imide (KTf$_2$N, Kanto), 1-hexyl-3-methylimidazolium bis(trifluoromethanesulfonyl)imide ([HMI] [Tf$_2$N], Merck) acetone (Nacalai Tesque), toluene (Nacalai Tesque), acetonitrile (Nacalai Tesque), dichloromethane (Nacalai Tesque) were of reagent grade and were used without further purification.

## Synthesis of [C$_4$bpy]Br

38.4 mmol of bpy was added to 50 cm$^3$ of acetone in a two-necked N$_2$-flushed flask and stirred at 40 °C. 114 mmol of 1-bromobutane was dissolved, and the solution was heated to reflux for 24 hours. The formed colourless precipitate ([C$_4$bpy]Br) was filtered and washed with acetone and toluene. A yield of 22.0 mmol (57.4 %) was obtained for [C$_4$bpy]Br.

## Synthesis of [C$_4$VC$_7$] [Tf$_2$N]$_2$

20 mmol of [C$_4$bpy]Br and 62 mmol of 1-bromoheptane was dissolved in 30 cm$^3$ of dry N,N'-dimethylformamide (DMF), and the solution was heated to 80 °C for 24 hours under N$_2$ atmosphere. The yellow precipitate (1-butyl-1'-heptyl-4,4'-bipyridinium dibromide, [C$_4$VC$_7$]Br$_2$) was filtered, washed with acetonitrile and dried in a desiccator. It was twice recrystallized from an ethanolic solution in order to obtain plate-like crystals of [C$_4$VC$_7$]Br$_2$ (yield: 71.0 %). Bromide was replaced with the [Tf$_2$N]$^-$ anions by adding a methanolic solution of excess amount of potassium bis(trifluoromethanesulfonyl)imide (K[Tf$_2$N]) to the methanolic solution of [C$_4$VC$_7$]Br$_2$. The mixture was stirred for 15 hours at room temperature. After evaporation of the solvent in vacuo, the colourless powder of [C$_4$VC$_7$] [Tf$_2$N]$_2$ was extracted from a yellowish residual mixture of viscous liquid. The final product, [C$_4$VC$_7$] [Tf$_2$N]$_2$,

Table 1: $^1$H-NMR chemical shifts ($\delta$) measured at 300 MHz in DMSO–*d6* vs. TMS reference; FAB–MS mass-to-charge ratios ($m/z$); and elemental analysis results ($w\%$, measured vs. calculated) of the synthesized compound $[C_4VC_7][Tf_2N]_2$.

| | Value | Assignment |
|---|---|---|
| $\delta$ | 0.87 | t, 3H |
| | 0.95 | t, 3H |
| | 1.32 | m, 10H |
| | 1.97 | q, 4H |
| | 4.69 | t, 4H |
| | 8.77 | d, 4H |
| | 9.38 | d, 4H |
| $m/z$ | 312.4 | $[C_4VC_7]^+$ |
| | 592.3 | $[C_4VC_7Tf_2N]^+$ |
| | 1464.4 | $[(C_4VC_7)_2(Tf_2N)_3]^+$ |
| | 280.0 | $[Tf_2N]^-$ |
| | 1152.0 | $[C_4VC_7(Tf_2N)_3]^-$ |
| $w\%$ | 34.57 vs. 34.40% | C |
| | 2.57 vs. 3.70% | H |
| | 6.34 vs. 6.42% | N |

was characterized by $^1$H NMR and FAB–MS measurements, and by elemental analysis (results are shown in Table 1). The bromide content in the final product was below the limit of detection ($\sim$ 1 ppm.

## Thermal Analysis

Differential scanning calorimetry (DSC) was carried out on a Shimadzu DSC–60 under nitrogen atmosphere. The samples were heated to 120 °C followed by cooling to −80 °C (the cycle was repeated several times with a rate of 2 °C min$^{-1}$). The melting and freezing points were determined from the DSC thermograms. The phase transitions were also studied by means of polarization microscopy (utilizing an Olympus BX51 instrument) at a heating rate of 2 °C min$^{-1}$.

1
2
3
4
5
6
7
8
9
10
11
12
13
14
15
16
17
18
19
20
21
22
23
24
25
26
27
28
29
30
31
32
33
34
35
36
37
38
39
40
41
42
43
44
45
46
47
48
49
50
51
52
53
54
55
56
57
58
59
60

## Density Measurements

As pure $[C_4VC_7][Tf_2N]_2$ was only available in a relatively small amount, density measurements have been carried out by using a Norell Standard Series 5 mm NMR tube as a "small-volume pycnometer". The tube was filled at 70 °C with $[C_4VC_7][Tf_2N]_2$, and the mass of the IL was determined. No changes of the liquid level could be observed as the tube was termostated to lower temperatures. The volume was calibrated by removing the IL from the tube, cleaning it thoroughly and by filling it up with a fluid of known density (water).

## Voltammetric Studies

Chronoamperometric measurements, as well as cyclic voltammetry and electrochemical impedance measurements in the temperature range of 25 to 60 °C have been carried out by the use of an Autolab PGSTAT302N potentiostat (EcoChemie, Netherlands) in a single compartment ($\sim 0.25$ cm$^3$) thermostated cell. A gold microdisk electrode (BASi) with a nominal radius of 5 µm was used as a working, a platinum sheet as a counter, and leakage-free Ag|AgCl|sat.KCl (BASi) as a reference electrode. The effective radius of the gold microelectrode, $r = 4.28$ µm was determined based on its chronoamperometric response measured in a 1 mmol dm$^{-3}$ $[Ru(NH_3)_6]Cl_3$ solution (containing 0.1 mol dm$^{-3}$ KCl as supporting electrolyte).

## Conductometry

The bulk ionic conductivity was studied in the temperature range of 25 to 60 °C, both by means of impedance spectroscopy (with the three-electrode configuration described above) and by the use of a 2-pole conductivity cell (CDC741T, Radiometer Analytical) with platinized platinum electrodes. The cell constant of the conductivity cell was determined as $K_{cond} = 1.629$ cm$^{-1}$ by means of calibration with KCl solutions of known concentration and conductivity. In case of the impedance measurements, a cell constant of $K_{EIS} = \frac{1}{4r} = 584.11$ cm$^{-1}$ has been

assumed.[41] Impedance spectra have been recorded over the frequency range from 100 mHz to 10 kHz; the bulk conductance was identified as the $\Re(Y)$ value corresponding to the phase angle minimum in the sound-frequency range (at $\sim 200$ Hz).

## Viscometry

Viscosity measurements in the temperature range of 20 to 75 °C have been carried out by using a Brookfield DV-I Prime rotational viscometer (spindle: SC4–15) equipped with a water-flow temperature control unit.

## PGSE–NMR measurements

The PGSE–NMR measurements[32] were performed by using a Bruker Avance III HD 500 WB spectrometer; i.e., an 11.7 T wide bore super conducting, ultra shielded magnet. The spectrometer was equipped with a Diff50 diffusion probe, capable to reach a maximum gradient strength of 30 T m$^{-1}$ at 60 A. The self-diffusion coefficients were measured using either a stimulated echo sequence[42] or a double stimulated echo sequence[43] in order to avoid convection effects at higher temperature. All sequences used sine shape gradient pulses with variable amplitudes. The signal attenuation can be described as

$$\ln \frac{S}{S_0} = -\gamma g^2 \delta^2 \left( \Delta - \frac{\delta}{3} D \right), \tag{5}$$

where $S$ is the stimulated echo signal amplitude, $S_0$ is the signal amplitude at gradient strength $g = 0$, $\delta$ is the effective gradient pulse duration (i.e., the length of a rectangular pulse with identical area as the used sine shape pulse), $\Delta$ is the diffusion time (i.e., the delay between the beginning of the first, diffusion encoding gradient pulse and the second, diffusion decoding pulse), $\gamma$ is the gyromagnetic ratio and $D$ the diffusion coefficient.[32] In case of the double stimulated echo, $\Delta$ is the sum of the diffusion times in both parts of the sequence. The experiments were performed in a temperature range of 30 to 70 °C in

steps of 10 °C. Diffusion experiments on $^1$H and $^{19}$F were conducted independently at each temperature step using a diffusion time $\Delta$ of 20 ms and of 100 ms, in order to prove the absence of convection. If convection seemed to be present, additional double stimulated echo experiments were performed. In order to avoid extensive relaxation delays, a so-called spoiler recovery sequence[44] was applied prior to the relaxation time.

# Results

## Thermal Properties (Differential Scanning Calorimetry)

It was found that pure $[C_4VC_7]\,[Tf_2N]_2$, which takes the form of a crystalline solid at ambient temperatures, melts at above 25 °C and forms a liquid phase. During cooling of the liquid, however, a phase transition usually occurs only at temperatures lower than 15 °C. The formation of liquid crystals accompanies both the solid-to-liquid and the liquid-to-solid transition, as it was studied by the means of polarization microscopy. It was found that the compound $[C_4VC_7]\,[Tf_2N]_2$, once it is in molten state, does not solidify at room temperature in the time range of a few days.

The described "thermal memory" of $[C_4VC_7]\,[Tf_2N]_2$ was taken into account when studying the temperature dependence of its transport properties. All the electrochemical, viscosity, conductivity and NMR measurements have thus been carried out at $T \gtrsim 25$ °C. Prior to each measurement, the IL was preheated to 70 °C while purged with argon at a slightly decreased pressure (in order to remove any traces of water). This pretreatment made it possible to study the transport properties in a purely liquid phase.

For the viscosity, NMR and electrochemical measurements, the temperature was measured with a precision of $\pm 2$ °C.

## Density and Molar Concentration

Since the synthesized $[C_4VC_7][Tf_2N]_2$ was only available in small amounts, its density was measured by the *ad hoc* method of using an NMR tube as a pycnometer. A density value of $\varrho = 1.467$ g cm$^{-3}$ has thus been obtained. The low sensitivity of this method, however, did not allow for the observation of any temperature dependence of the measured density, thus the above constant value was used in the calculations. Based on the measured density and a total molar mass of $M = 872.9$ g mol$^{-1}$, the concentration (inverse molar volume) $c$ of the ionic liquid has also been calculated:

$$c = \frac{\varrho}{M} = 1.772 \text{ mol dm}^{-3}. \tag{6}$$

Similarly to the density, this value was also considered temperature-independent.

## Ionic Radii

The ratio of hydrodynamic radii of the cations $(R_+)$ and the anions $(R_-)$ have been estimated by geometry optimization with the PM7 semi-empirical Hamiltonian implemented in the MOPAC2012 program suite.[45] For the anionic radius, a literature value[46] was taken, thus the values $R_+ = 0.503$ nm and $R_- = 0.362$ nm have been used in this study.

## Electrochemical Investigations

**Voltammetric behaviour**     In order to study the electrochemical behaviour of $[C_4VC_7][Tf_2N]_2$, the neat ionic liquid was first mixed with another (redox-inactive) IL, $[HMI][Tf_2N]$. In the thus obtained "diluted system", having a concentration of $\sim 9$ mmol dm$^{-3}$ with respect to $[C_4VC_7][Tf_2N]_2$, the cyclic voltammogram shown in Figure 2(a) has been measured at

$T = 60$ °C. This voltammogram is characteristic for the two-step reduction process

$$[C_4VC_7]^{2+} + e^- \rightarrow [C_4V^\bullet C_7]^+ \tag{7.a}$$

$$[C_4V^\bullet C_7]^+ + e^- \rightarrow C_4V^0C_7. \tag{7.b}$$

That is, at moderately cathodic electrode potentials ($-600$ mV $< E < -300$ mV), the dication is reduced to form a single-charged radical cation, while at potentials even more negative ($-1200$ mV $< E < -600$ mV) the radical cation is further reduced to the uncharged viologen $C_4V^0C_7$. While the first transition was shown to be reversible for most viologen systems, the second step is usually found to be less reversible.[47,48] For the sake of completeness it must be mentioned, however, that the above-mentioned two-step mechanism may be further nuanced by taking into consideration an additional conproportionation reaction between the uncharged (molecular) and the dicationic species,

$$C_4V^0C_7 + [C_4VC_7]^{2+} \rightarrow 2[C_4V^\bullet C_7]^+, \tag{8}$$

yielding as a product the single-charged $[C_4V^\bullet C_7]^+$ radical cation.[49,50]
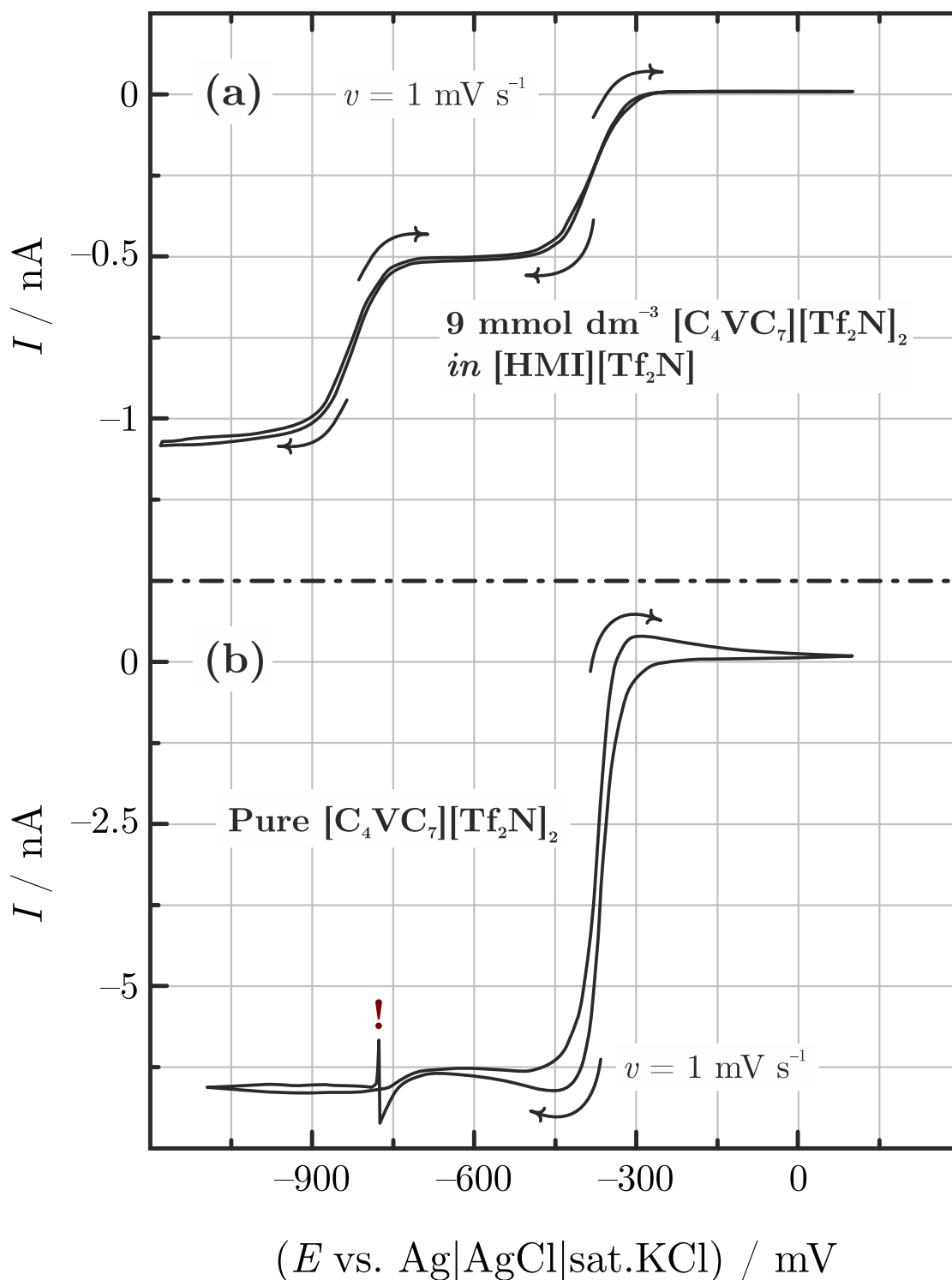
Figure 2: Cyclic voltammograms measured on a gold microdisk electrode **(a)** in $[C_4VC_7][Tf_2N]_2$ diluted with $[HMI][Tf_2N]$ and **(b)** in the neat ionic liquid. $T = 60\ °C$ in both cases. The feature shown by the exclamation mark in the latter case can be a result of a polymerization reaction or a 2D structural phase transitions within the viologen monolayer adsorbed to the electrode surface.

As shown in Figure 2(b), the voltammetric response of the *neat* ionic liquid differs substantially from that of the diluted system, and solely based on equations (7.a), (7.b) and (8), this response can no longer be interpreted. The CV (just like in case of the diluted system) clearly shows the first reduction step; however, shortly after the onset of the second step a sudden current spike appears (see the exclamation mark in Figure 2.b) and the current does not decrease any further.

A possible explanation of this feature would be the presence of a polymerization reaction,[49,51] yielding products which may remain adherent to the electrode surface[52,53] and thereby cause a decrease of the active surface area and/or a modified electrocatalytic activity. In addition to that, the electron transfer reactions following the first reduction step may as well lead to distinct 2D structural phase transitions within the viologen monolayer adsorbed to the electrode surface,[54] which can also explain the observed feature.

The complete understanding of the voltammetric behaviour of neat $[C_4VC_7][Tf_2N]_2$ will remain a challenge for future studies. In this paper we focus only on the first reduction step (the interpretation of which is clear) in order to determine the $D_+$ cationic diffusion coefficient.

**Electrochemical determination of the cationic diffusion coefficient $D_+$** The sigmoidal voltammograms measured at a microelectrode should provide straightforward means for determining the diffusion coefficient of a reacting species. Once a limiting current $I_\ell$ is reached, the diffusion coefficient $D_+$ can be readily determined:

$$I_\ell = 4rFD_+c_+, \tag{9}$$

where $r$ is the (effective) radius of the electrode and $c_+$ is the concentration of the cation. Our case is complicated by the fact that the cyclic voltammograms measured in the neat ionic liquid (Figure 2.b) are not ideally sigmoidal CVs, but despite the low sweep rate they still show a somewhat Cottrellian behaviour. That is, the cyclic voltammogram shown in

Figure 2.b is not entirely sigmoidal but also have "peak-shaped" features, thus Equation (9) cannot be directly used in order to determine the cationic diffusion coefficients. For this purpose, the more accurate method of chronoamperometry has to be applied.

By recording the current response of the system upon stepping the potential from a positive enough value to a sufficiently cathodic one (in our case, to $-600$ mV vs. Ag|AgCl|sat.KCl), decaying negative currents can be measured in the neat ionic liquid. The current traces (after a time when the double layer charging current has decayed) can well be fitted by using Equation (10),

$$I(\tau) = 4rFD_+c_+ \left(0.7854 + 0.8862\tau^{-1/2} + \right.$$
$$\left. +0.2146\exp\left[-0.7823\tau^{-1/2}\right]\right), \tag{10}$$

where $\tau = 4D_+t/r^2$.[55]

The current transients presented in Figure 3 were all measured for 250 seconds, but in case of the two lowermost temperatures the fitted interval was narrower due to instabilities of the recorded current response. The measured data, along with the fitted curves of Equation (10) are shown in the inset of Figure 3 in a logarithmic representation. Note that in the fitting procedure based on Equation (10), the only optimized parameter was $D_+$. The concentration used for the fitting was the constant determined from Equation (6), and the value of the effective electrode radius was determined by calibration (see Section ). The optimized $D_+$ values are shown in Figure 4, together with the diffusion coefficients yielded by NMR measurements.

1
2
3
4
5
6
7
8
9
10
11
12
13
14
15
16
17
18
19
20
21
22
23
24
25
26
27
28
29
30
31
32
33
34
35
36
37
38
39
40
41
42
43
44
45
46
47
48
49
50
51
52
53
54
55
56
57
58
59
60
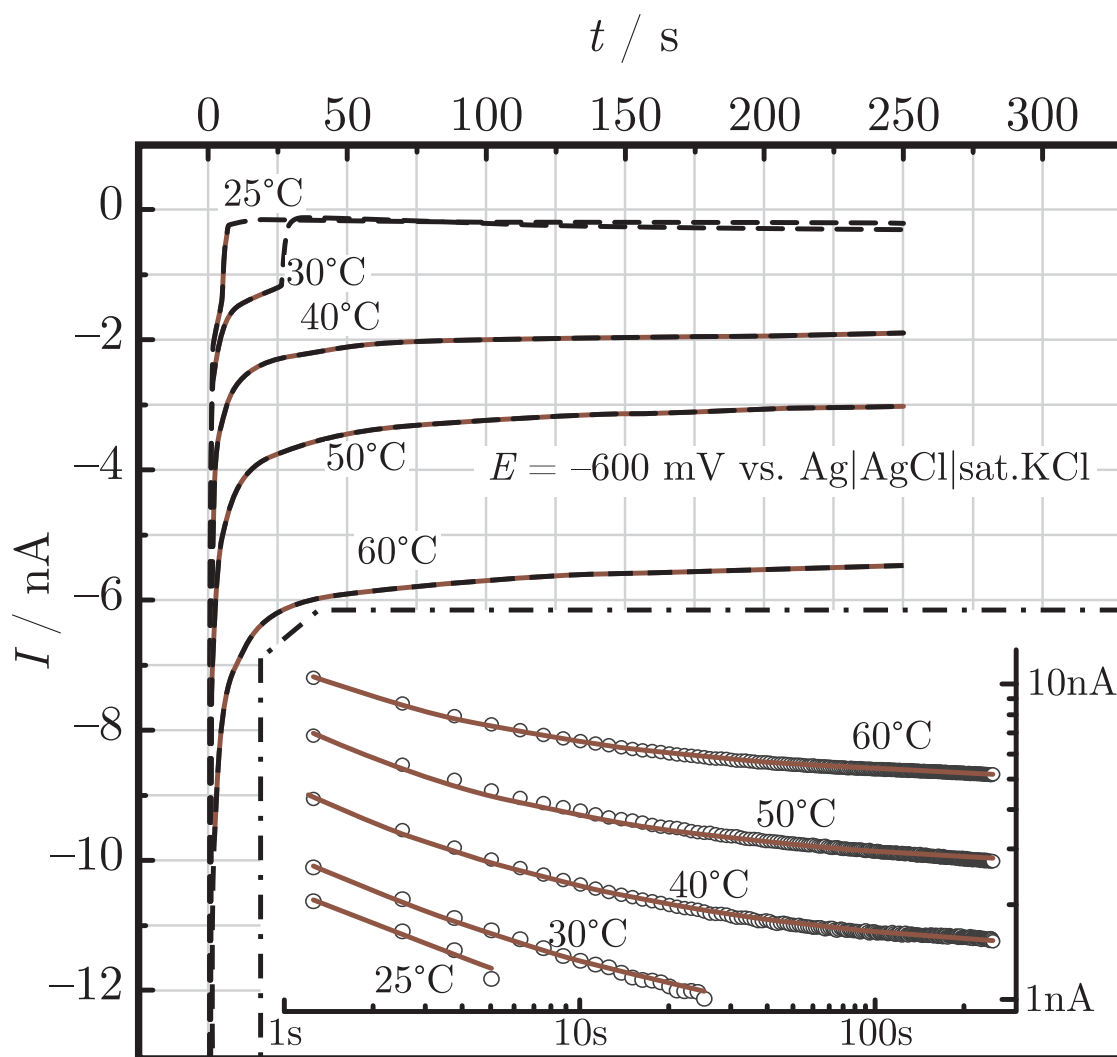


Figure 3: Chronoamperometric responses of the gold microelectrode in undiluted $[C_4VC_7][Tf_2N]_2$, measured at different temperatures. The highlighted segments of each amperograms have been fitted by the use of Equation (10), as shown in a logarithmic representation by the inset. The instabilities of the current traces measured at low temperature values can be attributed to possible phase transitions of the liquid.[54]

## NMR Measurements

The PGSE–NMR method allows for the determination of individual ionic diffusion coefficients: [1]H and ^{19}F in the cation and the anion, respectively, are NMR-sensitive nuclei. Figure 4 shows the temperature dependence of the cationic $(D_+)$ and anionic $(D_-)$ diffusion coefficients. As a comparison, in Figure 4 we have also plotted the $D_+$ values determined by the fitting of

the chronoamperometric curves in Figure 3. If we take into consideration that the value

of $c$ (used in Equation (10) for the fitting of the chronoamperometry curves) was obtained

by a less sensitive density measurement, it can be stated that the NMR-based and the

electrochemistry-based data are – within the range of experimental error – in a fair agreement

with each other.
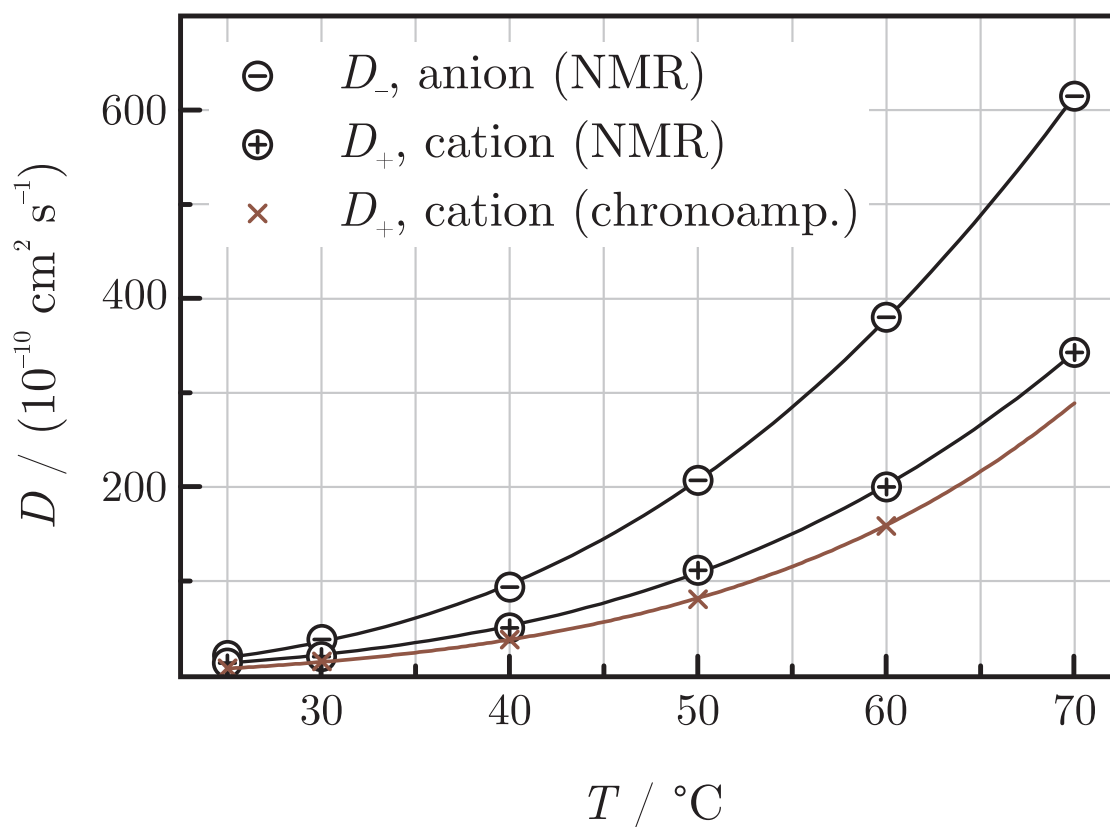


Figure 4: Individual diffusion coefficients of the $[C_4VC_7]^{2+}$ cations $(D_+)$ and the $[Tf_2N]^-$ anions $(D_-)$, as determined by the PGSE–NMR technique at different temperatures. For sake of comparison, the cationic diffusion coefficient $(D_+)$ values, as determined by chronoamperometry measurements, have also been plotted here. The solid curves show VFT fits to the measured data (for the values of the optimized VFT parameters, see Table 2).

An interpolation between the diffusion coefficient values measured at different temperatures

is possible by fitting the data with the VFT-equation. Fitted curves are also shown in Figure 4;

the optimized VFT parameters are listed in Table 2.

Table 2: 95% confidence intervals of the Vogel–Fulcher–Tammann parameters. The equation of the form $y(T) = y_0 \exp\left[-\frac{B}{T-T_0}\right]$ was fitted to the diffusivity, conductivity and viscosity data in Figures 4–6 by means of a weighted Levenberg–Marquardt non-linear least-squares optimization.[56,57] Weight factor: $y^{-2}$, calculated iteratively. Determination coefficient $(R^2)$ values are also reported in the table.

| Measurement | $y_0$ | $B$ | $T_0$ | $R^2$ |
|---|---|---|---|---|
| $D_{+,\text{ chronoamp.}}$ (Figure 4) | $(4.05 \pm 0.24) \cdot 10^{-4}$ cm$^2$ s$^{-1}$ | $(1.79 \pm 0.48) \cdot 10^3$ K | $(156 \pm 33)$ K | 0.99903 |
| $D_{+,\text{ NMR}}$ (Figure 4) | $(2.679 \pm 0.044) \cdot 10^{-5}$ cm$^2$ s$^{-1}$ | $(0.92 \pm 0.38) \cdot 10^3$ K | $(205.2 \pm 2.3)$ K | 0.99982 |
| $D_{-,\text{ NMR}}$ (Figure 4) | $(1.35 \pm 0.66) \cdot 10^{-5}$ cm$^2$ s$^{-1}$ | $(628 \pm 93)$ K | $(226.4 \pm 6.8)$ K | 0.99996 |
| $\kappa_{\text{meas}}$ (Figure 5) | $(21.08 \pm 8.27)$ S cm$^{-1}$ | $(2.20 \pm 0.76) \cdot 10^3$ K | $(132 \pm 22)$ K | 0.99909 |
| $\eta$ (Figure 6) | $(1.16 \pm 0.47) \cdot 10^{-4}$ Pa s | $-(1147 \pm 97)$ K | $(194.0 \pm 4.5)$ K | 0.99931 |

## Conductivity Measurements

The electrical conductivity (specific conductance, $\kappa_{\text{meas}}$) of $[\text{C}_4\text{VC}_7]\,[\text{Tf}_2\text{N}]_2$ has been determined both by means of direct conductometry (in a 2-poles cell with plane-parallel electrodes) and by the means of $ac$ impedance spectroscopy. By using the cell constant values given in Section , the measured conductivities are those presented in Figure 5. As it can be seen, practically the same conductivities can be determined, regardless to the applied cell geometry. In Figure 5, a VFT-like interpolation is applied to the $\kappa_{\text{meas}}$ values yielded by the conductometer.
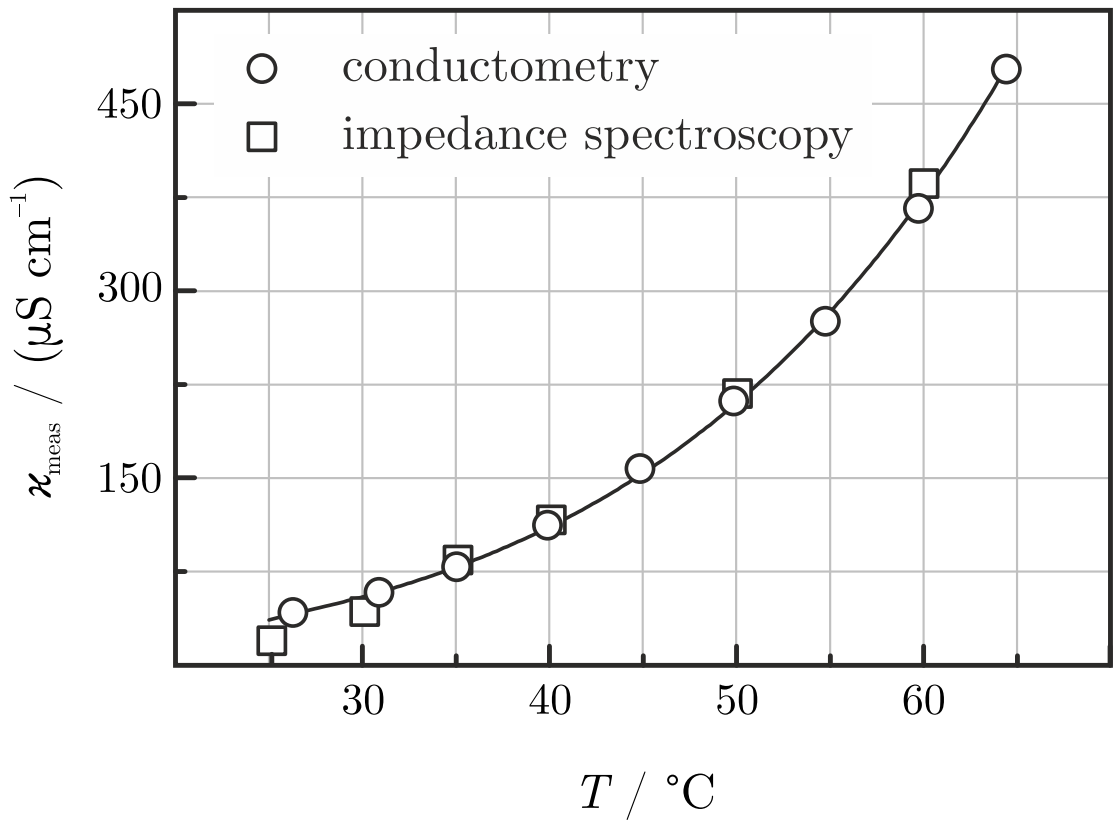
Figure 5: The specific conductivity of $[C_4VC_7][Tf_2N]_2$ changes as a function of temperature, as determined by means of *ac* impedance spectroscopy and by the use of a conductometer. The latter dataset was made subject to a curve fitting procedure based on the VFT-equation. The fitted curve is shown in the figure, for the values of the optimized VFT parameters, see Table 2.

## Viscosity Measurements

The viscosity of $[C_4VC_7][Tf_2N]_2$ has been measured at different temperatures. The measured dataset could again be well-fitted by using a VFT-like equation, as shown by Figure 6.
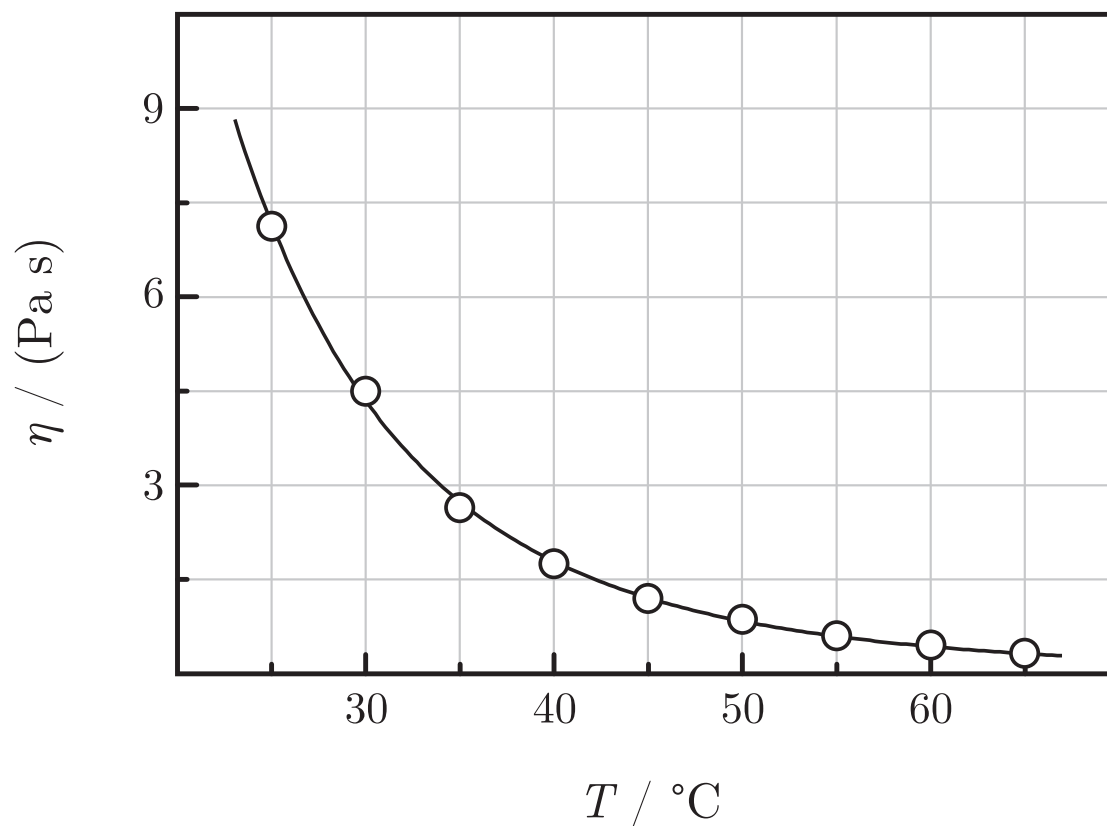
Figure 6: The viscosity of neat $[C_4VC_7][Tf_2N]_2$, measured at different temperatures. The solid curve represents a VFT-like fit (for the numerical values of the VFT parameters, see Table 2).

## Summarized Results

The viscosity, conductivity and ionic diffusion coefficients in the $[C_4VC_7][Tf_2N]_2$ ionic liquid have all been found heavily temperature dependent. For further discussion, the numerical values of the above transport parameters are summarized in Table 3.

# Discussion

Several methods – chronoamperometry, NMR measurements, conductometry and viscometry – have been applied in order to study the temperature dependent transport properties of the $[C_4VC_7][Tf_2N]_2$ IL. Amongst these techniques, NMR measurements have a distinguished role:

Table 3: Numerical values of the transport parameters ($D_+$, $D_-$, $\eta$ and $\kappa_{\text{meas}}$) in neat $[\text{C}_4\text{VC}_7]\,[\text{Tf}_2\text{N}]_2$, based on the interpolants of Figures 4–6. The bulk ionic conductivity values $\kappa_{\text{NMR}}$ and $\kappa_{\text{visc}}$, also listed in the table, are calculated based on the diffusion coefficient values (Equation (11)) and the viscosity values (Equation (15)), respectively.

| $\dfrac{T}{°\text{C}}$ | $\dfrac{D_{+,\text{ chronoamp.}}}{10^{-10}\text{ cm}^2\text{ s}^{-1}}$ | $\dfrac{D_{+,\text{ NMR}}}{10^{-10}\text{ cm}^2\text{ s}^{-1}}$ | $\dfrac{D_{-,\text{ NMR}}}{10^{-10}\text{ cm}^2\text{ s}^{-1}}$ | $\dfrac{\eta}{\text{Pa s}}$ | $\dfrac{\kappa_{\text{meas}}}{\mu\text{S cm}^{-1}}$ | $\dfrac{\kappa_{\text{NMR}}}{\mu\text{S cm}^{-1}}$ | $\dfrac{\kappa_{\text{visc}}}{\mu\text{S cm}^{-1}}$ |
|---|---|---|---|---|---|---|---|
| 25 | 13.76 | 13.47 | 21.34 | 7.036 | 37.44 | 61.46 | 27.21 |
| 30 | 21.11 | 22.33 | 37.74 | 4.248 | 55.13 | 105.1 | 45.35 |
| 35 | 31.49 | 35.23 | 62.24 | 2.681 | 79.40 | 168.7 | 72.17 |
| 40 | 45.78 | 53.30 | 96.92 | 1.759 | 112.1 | 256.8 | 110.3 |
| 45 | 65.04 | 77.72 | 143.8 | 1.194 | 155.3 | 373.6 | 162.8 |
| 50 | 90.49 | 109.8 | 204.8 | 0.8346 | 211.6 | 522.8 | 232.9 |
| 55 | 123.5 | 150.8 | 281.8 | 0.5994 | 283.7 | 707.9 | 324.3 |
| 60 | 165.6 | 202.0 | 376.2 | 0.4409 | 374.9 | 931.6 | 440.5 |

they allow for the determination of the individual diffusion coefficients of *both* the cations and the anions. While by means of chronoamperometry, *only one* of these parameters ($D_+$) is accessible, the information yielded by the other two methods (the $\kappa_{\text{meas}}$ specific conductance and the $\eta$ viscosity) describe the system as a whole, rather than its individual components.

This also suggests that the most straight-forward way of interrelating the transport parameters of Table 3 is to compare either the experimental viscosities or the experimental bulk conductivities with the corresponding values recalculated from the individual diffusion coefficients. In this paper, the latter approach is taken: the bulk conductivity of the ionic liquid is calculated first from the diffusion coefficients measured by NMR ($\kappa_{\text{NMR}}$), second from the determined viscosities ($\kappa_{\text{visc}}$); and these values are compared to the measured specific conductance ($\kappa_{\text{meas}}$). The method of discussion followed here has a significant advantage; i.e., it provides means for checking the validity of the Stokes–Einstein and the Nernst–Einstein relations in the studied IL.

## Relating the NMR and Chronoamperometry-Based Diffusion Coefficients to the Bulk Ionic Conductitivities

By means of NMR measurements, as noted above, it is possible to determine the individual diffusion coefficients of both the cation and the anion, respectively. As shown in Figure 4, the $D_+$ values provided by the two different methods agree fairly well — the diffusion coefficients measured by the NMR technique are equal to, or only slightly higher than those yielded by chronoamperometry.

By using the values obtained for $D_+$ and $D_-$ (determined from PGSE–NMR), it is possible to estimate the bulk ionic conductivity of $[C_4VC_7][Tf_2N]_2$ based on a modified version of the Nernst–Einstein relation: Equation (1) in the studied system can be written in the form

$$\kappa_{\text{NMR}} = \frac{2F^2\alpha c}{RT}\left(2D_+ + D_-\right).$$

(11)

If we assume that $\alpha = 1$ (i.e., that the Nernst-Einstein equation in its classical form applies to the system), the "NMR-based" conductivity ($\kappa_{\text{NMR}}$) values obtained from Equation (11) are those shown in Figure 7 (for the numerical data, see Table 3).
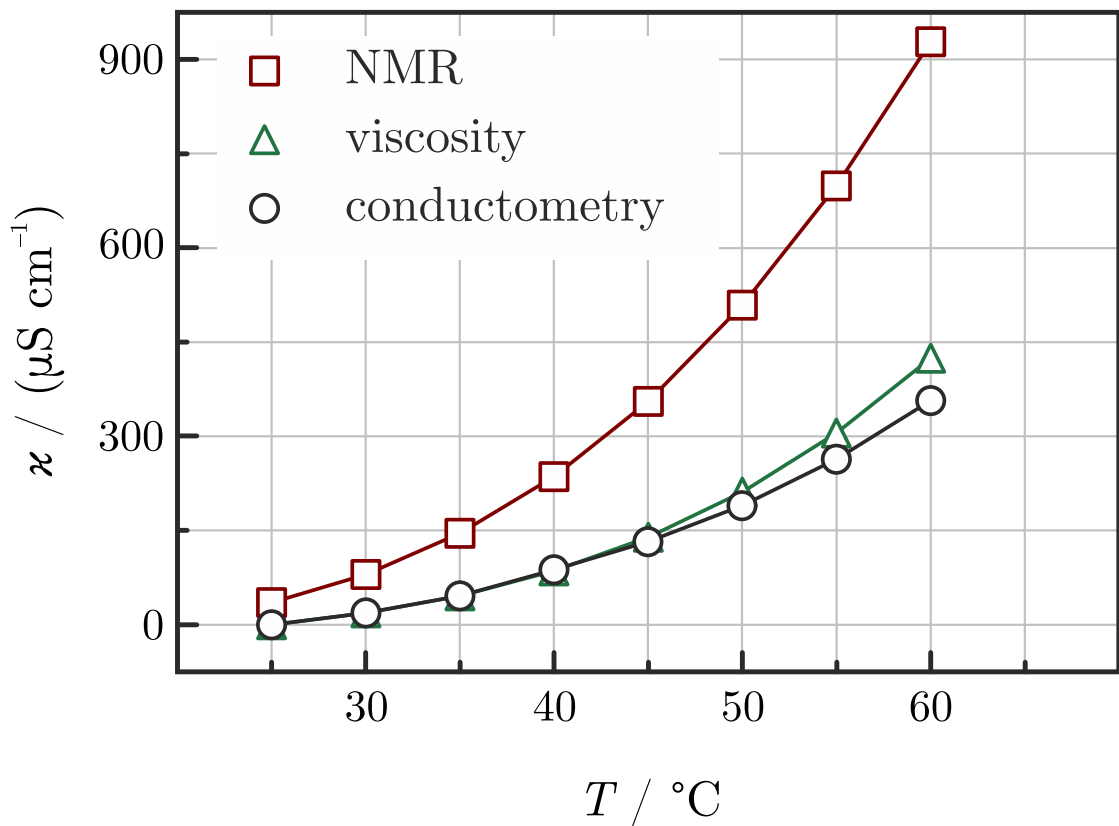
Figure 7: The $\kappa$ conductivity of the ionic liquid, determined in three different ways: by direct conductometry; by calculations based on the diffusion coefficients, using Equation (11); and by calculations based on the viscosity values, using Equation (15).

It can be seen that these values are considerably higher than the measured conductivities; thus the system shows deviations from the classical Nernst–Einstein equation and values of $\alpha < 1$ must be assumed.[15–22] Using Equation 11, we have calculated the values of $\alpha$ at different temperatures and have found them to be moderately temperature dependent (Figure 8).
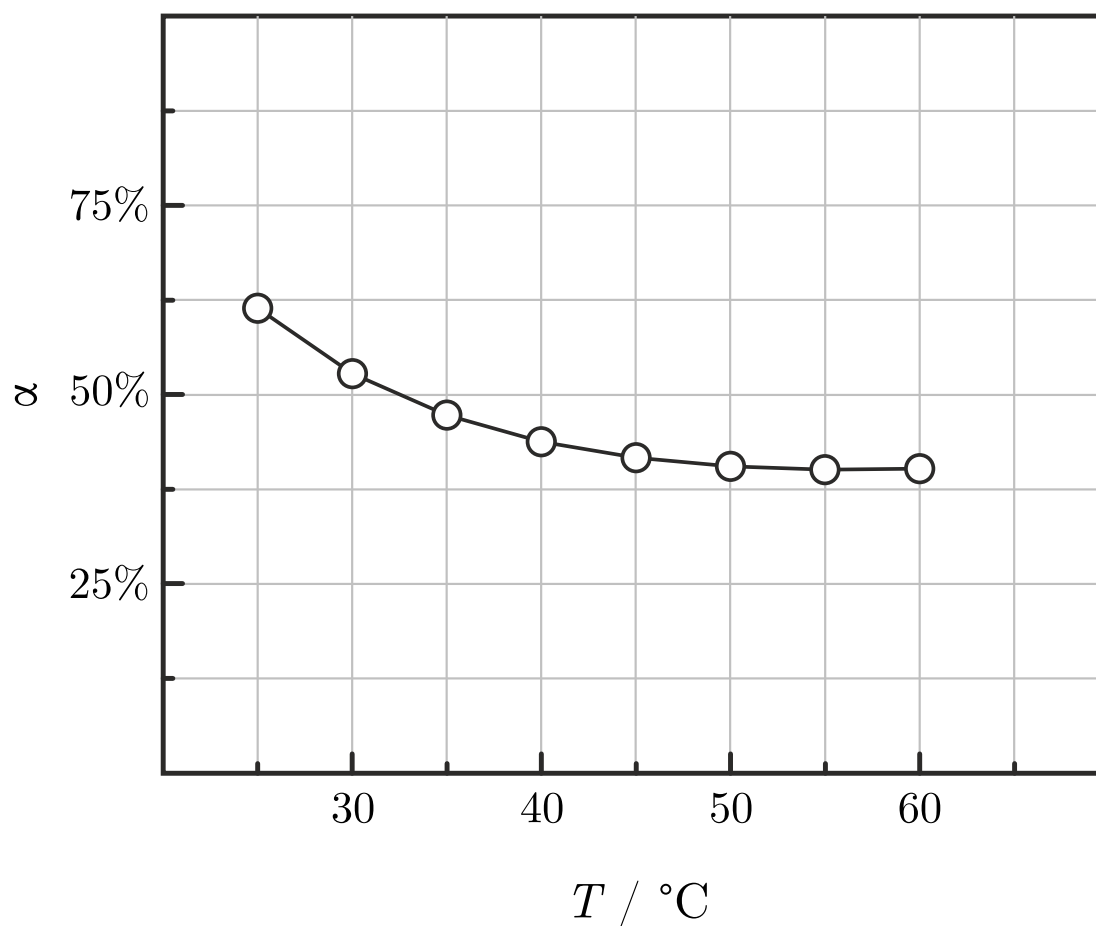
Figure 8: The $\alpha = \kappa_{\mathrm{meas}}/\kappa_{\mathrm{NMR}}$ ratio, appearing also in Equation (11), is less than 1, and is moderately temperature-dependent. $\alpha$ is a good measure of the "ionicity" in ionic liquids. [19]

With respect to what was said in the introduction concerning the interpretation of the $\alpha < 1$ values, there are two comments which are due here:

i.) *Comments on the "velocity cross-correlation" based interpretation.* In [21] Harris criticized the "ionicity" concept based on a claim that the extent of any ionic association should depend on the time-scale of the experiments used for its determination. As an alternative explanation he showed that reduced $\alpha$ values might also arise as a result of the differences in the cross-correlation functions of the ionic velocities. With respect to that we must point out that in our case not only the PGSE–NMR measurements, but also the analysis of the chronoamperometric curves have yielded similar (equally high) diffusion

coefficients[1]. This result, we believe, could be interpreted as an independent evidence that still supports the validity of the ionicity concept, since the time-scale of the electrochemical measurements is nearly 4 orders of magnitude higher than that of the NMR technique, and yet the two methods yield very similar results. This statement, however, is not strictly conclusive. Its validity should be further checked by molecular dynamics simulations: the velocity cross-correlation coefficients in form of the integrals (2.a)–(2.c) could then be evaluated. Here we provide the reader with an experimental forecast for these values based on Equations (12.a)–(12.c):[21]

$$f_{++} = RT\kappa_{\mathrm{meas}} \left( \frac{M_-}{z_- FcM} \right)^2 - \frac{D_+}{\nu_+ c} \tag{12.a}$$

$$f_{--} = RT\kappa_{\mathrm{meas}} \left( \frac{M_+}{z_+ FcM} \right)^2 - \frac{D_-}{\nu_- c} \tag{12.b}$$

$$f_{+-} = RT\kappa_{\mathrm{meas}} \frac{M_+ M_-}{z_+ z_- (FcM)^2}. \tag{12.c}$$

The values of these parameters are listed in Table 4, providing means for checking the validity of the "ionicity" concept in the studied IL. Namely, if such a molecular dynamics model could be developed, which based on Equations (2.a)–(2.c) would yield values similar to those listed in Table 4 for the velocity cross-correlation coefficients, the "ionicity" concept could be discarded.

---

[1]At least for the cations — the diffusion coefficient of the anions is not accessible for the electrochemical technique

**Table 4: Estimates for the values of the like-ion and unlike-ion velocity cross-correlation parameters $f_{++}$, $f_{--}$ and $f_{+-}$ based on the experimental data and Equations (12.a)–(12.c).**

| $\dfrac{T}{°C}$ | $\dfrac{10^6 f_{++}}{cm^5 mol^{-1} s^{-1}}$ | $\dfrac{10^6 f_{--}}{cm^5 mol^{-1} s^{-1}}$ | $\dfrac{10^6 f_{+-}}{cm^5 mol^{-1} s^{-1}}$ |
|---|---|---|---|
| 25 | 0.4286 | 0.4200 | 0.1839 |
| 30 | 0.7587 | 0.8602 | 0.2749 |
| 35 | 1.250 | 1.502 | 0.4019 |
| 40 | 1.948 | 2.416 | 0.5758 |
| 45 | 2.899 | 3.648 | 0.8098 |
| 50 | 4.149 | 5.230 | 1.119 |
| 55 | 5.751 | 7.187 | 1.523 |
| 60 | 7.738 | 9.530 | 2.042 |

*ii.) Comments on the "electron exchange" based interpretation.* It is not a new result that in a redox-active ionic liquid the diffusion coefficients determined from voltammetric analyses are higher than what the conductivity or viscosity measurements can yield. The same has been described by Murray et al. for another viologen group containing ionic liquid.[23] It was argued there that the enhancement of the electrochemically determined $D$ values over the "physical" diffusion coefficients could be a result of an electron self-exchange process taking place in the mixed valence state diffuse layer. We must point out, however, that in[23] no NMR measurements have been applied for studying the diffusivities and to support the validity of the electron exchange mechanism. In our IL system we have found that the electrochemically determined diffusion coefficients of the cationic redox species agree well with the values determined by NMR. This is a strong indication that electron self exchange processes between the two redox states (the $[C_4VC_7]^{2+}$ dication and the $[C_4V^\bullet C_7]^+$ radical cation in our case) are absent or occur only to a negligible extent that cannot be observed in the experimental results.

From the above comments it can be concluded that the most probable explanation of the Nernst–Einstein deviations could be based on the "ionicity" concept. What is still needed,

however, is to interrelate the results of the conductivity and viscosity measurements in a way that does not contradict this assumption.

## Relating the Measured Viscosity Data to the Bulk Ionic Conductivities

Recalculating the bulk ionic conductivities from the viscosity data is not straightforward.[29–31] For instance, Bonhôte et al. have claimed that the dependence of the bulk ionic conductivity on the viscosity can be written in a form

$$\kappa_{\text{visc}} = \frac{\alpha F^2 c}{6 N_\text{A} \pi \eta} \left( \xi_+ R_+^{-1} + \xi_- R_-^{-1} \right), \tag{13}$$

where the $\xi$ values are correction factors emerging due to the different shapes of the ions, and the equation contains the $\alpha$ degree of dissociation.[29] To this we must add that an equation of the same form (although not exactly of the same content) was used already in a 1902 paper by Sutherland,[58] dealing with the viscosity/conductivity relations of weak electrolytes.[2] Yet it was found that in case of the studied system, including the parameters $\alpha$, $\xi_+$ and $\xi_-$ to the Einstein relations (which results in Equation (13)) is not deemed necessary. Even in the case when all these parameters are equal to unity, the equation can well-correlate the measured viscosity and conductivity data.

This observation is in a good agreement with a model of Abbott,[30,31] describing the viscous flow as a process governed by the motion of holes present at an "infinite dilution" in the system. In[30] Abbott claims that the viscosity of ILs is limited by the low concentration of suitably sized voids, and in[31] he considers charge transfer in the very same manner. Namely, it is assumed in[31] that ion motion depends on the migration of holes in the opposite direction; and since the fraction of suitably sized holes in ambient-temperature ionic liquids is very low (about $10^{-6}$), the holes can be assumed to be at infinite dilution. As a consequence, the

---

[2]Note that the paper of Sutherland[58] was published three years before Einstein's publication of the equation that we now call Stokes–Einstein relation.[59]

migration of holes should be independent of each other, and they should be described by the Stokes–Einstein equation.

Thus the $\lambda_\pm$ molar ionic conductivities (of the cations and the anions, respectively) can be written in a form

$$\lambda_\pm = \frac{z_\pm^2 F^2}{6 N_A \pi \eta R_\pm},\tag{14}$$

and these values readily yield the conductivity:

$$\kappa_{\text{visc}} = c\left[\lambda_+ + 2\lambda_-\right] = \frac{cF^2}{6 N_A \pi \eta}\left(\frac{4}{R_+} + \frac{2}{R_-}\right).\tag{15}$$

Note that in Equation 15, the degree of dissociation $\alpha$ does not appear. Neglecting the ionic association in this model is, however, logical: with the concentration of holes being very low, single ions are always present in vast excess, almost irrespective of the value of $\alpha$.[31] This explains the good correlation (Figure 7) between the measured conductivity values and the specific conductances calculated from the viscosity data.

## Conclusion

A redox-active ionic liquid, 1-butyl-1'-heptyl-4,4'-bipyridinium bis(trifluoromethanesulfonyl)imide has been synthesized and its transport processes were investigated. The conductivity and viscosity of the IL, as well as the diffusion coefficients of its components were studied over a 50 °C wide temperature range. As a novel approach we have used both the PGSE–NMR technique and voltammetric measurements for the diffusivity studies.

It was found that the diffusion coefficients determined by means of NMR and chronoamperometry measurements are, within the range of experimental error, equal — and they are (in accordance with other ionic liquid studies) higher than what the conductivity or viscosity measurements would indicate. The results were interpreted in the light of the existing theories.[15–31]

The measured diffusion coefficients and bulk conductivities can be well interrelated based on the "ionicity" concept introduced by Watanabe et al. (that is, by treating the ionic liquid as a weak electrolyte,[15–18]). In agreement with the empirical Walden rule, a direct comparison between the measured conductivities and viscosities was also possible, for which the hole conduction model of Abbott[30,31] has been utilized.

Based on the fact that both the electrochemical and the NMR measurements yield practically the same diffusion coefficients, there is no experimental evidence that interpretations based in other systems on "homogeneous electron exchange"-based interpretations[23] apply to our viologen IL.

The equality of diffusion coefficients yielded by the NMR and the electrochemical studies could further be interpreted as an independent evidence supporting the validity of the "ionicity" concept over the "velocity cross-correlation" based explanations[20–22] of the Nernst–Einstein deviations. The time-scale of these measurements differ in nearly 4 orders of magnitude, and yet they yield essentially the same measure for the deviation. In order to provide some means for checking the validity of this conclusion, experimental estimates for the expected values of the like-ion and unlike-ion velocity cross-correlation parameters are given in the text.

As a continuation of this work, molecular dynamics simulations are planned in order to get a deeper insight into the nature of mass, charge and momentum transport mechanisms in redox-active ionic liquids. The electrochemical behaviour of $[C_4VC_7][Tf_2N]_2$ will also be further studied by the means of impedance spectroscopy and surface imaging techniques (*in-situ* STM and AFM).

# Acknowledgement

# References

## References

(1) Freemantle, M. *Introduction to ionic liquids*; RSC Publishing: Cambridge, 2009.

(2) Wasserscheid, P.; Welton, Th. *Ionic liquids in synthesis*, 2nd ed.; Wiley: New York, 2007.

(3) Seki, Sh.; Kobayashi, Y.; Miyashiro, H.; Ohno, Y.; Usami, A.; Mita, Y.; Watanabe, M.; Terada, N. Highly reversible lithium metal secondary battery using a room temperature ionic liquid/lithium salt mixture and a surface-coated cathode active material. *Chemical Communications* **2006**, *13*, 544–545.

(4) Xu, W.; Angell, C. A. Solvent-free electrolytes with aqueous solution-like conductivities. *Science* **2003**, *302*, 422–425.

(5) Wang, P.; Wenger, B.; Humphry-Baker, R.; Moser, J. E.; Teuscher, J.; Kantlehner, W.; Mezger, J.; Stoyanov, E. V.; Zakeeruddin, Sh. M.; Grätzel, M. Charge separation and efficient light energy conversion in sensitized mesoscopic solar cells based on binary ionic liquids. *Journal of the American Chemical Society* **2005**, *127*, 6850–6856.

(6) Ye, C.; Liu, W.; Chen, Y.; Yu, L. Room-temperature ionic liquids: a novel versatile lubricant. *Chemical Communications* **2001**, *8*, 2244–2245.

(7) Fegyverneki, D.; Orha, L.; Láng, G. G.; Horváth, I. T. Gamma-valerolactone-based solvents. *Tetrahedron* **2010**, *66*, 1078–1081.

(8) Müller, C.; Vesztergom, S.; Pajkossy, T.; Jacob, T. The interface between Au(100) and 1-butyl-3-methyl-imidazolium-bis(trifluoromethylsulfonyl)imide. *Journal of Electroanalytical Chemistry* **2014**, doi:10.1016/j.jelechem.2014.06.010.

(9) Fu, Y.-Ch.; Su, Y.-Zh.; Wu, D.-Y.; Yan, J.-W.; Xie, Zh.-X.; Mao, B.-W. Supramolecular aggregation of inorganic molecules at Au(111) electrodes under a strong ionic atmosphere. *Journal of the American Chemical Society* **2009**, *131*, 14728–14737.

(10) Su, Y.-Zh.; Fu, Y.-Ch.; Wei, Y.-M.; Yan, J.-W.; Mao, B.-W. The electrode/ionic liquid interface: electric double layer and metal electrodeposition. *ChemPhysChem* **2010**, *11*, 2764–2778.

(11) Borisenko, N.; Zein El Abedin, Sh.; Endres, F. *In-Situ* STM investigation of gold reconstruction and of silicon electrodeposition on Au(111) in the room temperature ionic liquid 1-butyl-1-methylpyrrolidinium bis(trifluoromethylsulfonyl)imide. *Journal of Physical Chemistry B* **2006**, *110*, 6250–6256.

(12) Endres, F., MacFarlane, D., Abbott, A. P., Eds. *Electrodeposition from ionic liquids*; Wiley: New York, 2008.

(13) Bidikoudi, M.; Zubeir, L. F.; Falaras, P. Low viscosity highly conductive ionic liquid blends for redox active electrolytes in efficient dye-sensitized solar cells. *Journal of Materials Chemistry* **2014**, *2*, 15326–15336.

(14) Rochefort, D.; Forgie, J.; MacNeil, D.; Gelinas, B.; El-Khakani, S. Redox-active ionic liq-

uids in energy storage: Application to Li-ion batteries for protection against overcharging. CA Patent PCT/CA2013/050247, March 27, 2013.

(15) Noda, A.; Hayamizu, K.; Watanabe, M. Pulsed-gradient spin-echo ^{1}H and ^{19}F NMR ionic diffusion coefficient, viscosity, and ionic conductivity of non-chloroaluminumate room-temperature ionic liquids. *Journal of Physical Chemistry B* **2001**, *105*, 4603–4610.

(16) Tokuda, H.; Hayamizu, K.; Ishii, K.; Susan, Md. A. bin H.; Watanabe, M. Physicochemical properties and structures of room temperature ionic liquids. Part 1. — Variation of anionic species. *Journal of Physical Chemistry B* **2004**, *108*, 16593–16600.

(17) Tokuda, H.; Hayamizu, K.; Ishii, K.; Susan, Md. A. bin H.; Watanabe, M. Physicochemical properties and structures of room temperature ionic liquids. Part 2. — Variation of alkyl chain length in imidazolium cation. *Journal of Physical Chemistry B* **2005**, *109*, 6103–6110.

(18) Tokuda, H.; Ishii, K.; Susan, Md. A. bin H.; Tsuzuki, S.; Hayamizu, K.; Watanabe, M. Physicochemical properties and structures of room temperature ionic liquids. Part 3. — Variation of cationic structures. *Journal of Physical Chemistry B* **2006**, *110*, 2833–2839.

(19) MacFarlane, D. R.; Forsyth, M.; Izgorodina, E. I.; Abbott, A. P.; Annat, G.; Fraser, K. On the concept of ionicity in ionic liquids. *Physical Chemistry Chemical Physics* **2009**, *11*, 4962–4967.

(20) Harris, K. R.; Kanakubo, M.; Tsuchihashi, N.; Ibuki, K.; Ueno, M. Effect of pressure on the transport properties of ionic liquids: 1-alkyl-3-methylimidazolium salts. *Journal of Physical Chemistry B* **2008**, *112*, 9830–9840.

(21) Harris, K. R. Relations between the fractional Stokes–Einstein and Nernst–Einstein equations and velocity correlation coefficients in ionic liquids and molten salts. *Journal of Physical Chemistry B* **2010**, *114*, 9572–9577.

(22) Harris, K. R.; Makino, T.; Kanakubo, M. Viscosity scaling of the self-diffusion and velocity cross-correlation coefficients of two functionalised ionic liquids and of their non-functionalized analogues. *Physical Chemistry Chemical Physics* **2014**, *16*, 9161–9170.

(23) Hatazawa, Ts.; Terrill, R. H.; Murray, R. W. Microelectrode voltammetry and electron transport in an undiluted room temperature melt of an oligo(ethylene glycol)-tailed viologen. *Analytical Chemistry* **1996**, *68*, 597–603.

(24) Harper, A. S.; Leone, A. M.; Lee, D.; Wang, W.; Ranganathan, S.; Williams, M. E.; Murray, R. W. Ion atmosphere relaxation controlled electron transfers in cobaltocenium polyether molten salts. *Journal of Physical Chemistry B* **2005**, *109*, 18852–18859.

(25) Wang, W.; Lee, D.; Leone, A. M.; Murray, R. W. Counterion diffusivity measurements support ion atmosphere relaxation control of electron transfer rates in a semi-solid ruthenium complex molten salt. *Chemical Physics* **2005**, *319*, 126–135.

(26) Balasubramanian, R.; Wang, W.; Murray, R. W. Redox ionic liquid phases: Ferrocenated imidazoliums. *Journal of the American Chemical Society* **2006**, *128*, 9994–9995.

(27) Wang, W.; Balasubramanian, R.; Murray, R. W. Electron transport and counterion relaxation dynamics in neat ferrocenated imidazolium ionic liquids. *Journal of Physical Chemistry C* **2008**, *112*, 18207–18216.

(28) Weaver, J. E. F.; Breadner, D.; Deng, F.; Ramjee, B.; Ragogna, P. J.; Murray, R. W. Electrochemistry of ferrocene-functionalized phosphonium ionic liquids. *Journal of Physical Chemistry C* **2011**, *115*, 19379–19385.

(29) Bonhôte, P.; Dias, A.-P.; Papageorgiou, N.; Kalyanasundaram, K.; Grätzel, M. Hydrophobic, highly conductive ambient-temperature molten salts. *Inorganic Chemistry* **1996**, *35*, 1168–1178.

(30) Abbott, A. P. Application of hole theory to the viscosity of ionic and molecular liquids. *ChemPhysChem* **2004**, *5*, 1242–1246.

(31) Abbott, A. P. Model for the conductivity of ionic liquids based on an infinite dilution of holes. *ChemPhysChem* **2005**, *6*, 2502–2505.

(32) Stejskal, E. O.; Tanner, J. E. Diffusion measurements: Spin echoes in the presence of a time-dependent field gradient. *Journal of Chemical Physics* **1965**, *42*, 288–292.

(33) Hansen, J.-P.; McDonald, I. R. Self-diffusion and electrical conductance in a simple molten salt. *Journal of Physics C: Solid State Physics* **1974**, *7*, 384–386.

(34) LeClaire, A. D. In *Physical Chemistry – An Advanced Treatise Vol. 10*; Henderson, D., Jost, W., Eyring, H., Eds.; Academic Press, 1970; Vol. 10.

(35) Dahms, H. Electronic conduction in aqueous solution. *Journal of Physical Chemistry* **1968**, *72*, 362–364.

(36) Ruff, I.; Friedrich, V. Transfer diffusion. Part 1. — Theoretical. *Journal of Physical Chemistry* **1971**, *75*, 3297–3302.

(37) Ruff, I.; Friedrich, V.; Demeter, K.; Csillag, K. Transfer diffusion. Part 2. — Kinetics of electron exchange reaction between ferrocene and ferricinium ion in alcohols. *Journal of Physical Chemistry* **1971**, *75*, 3303–3309.

(38) Vogel, H. Das Temperaturabhängigkeitsgesetz der Viskosität von Flüssigkeiten. *Physikalische Zeitschrift* **1921**, *22*, 645–646.

(39) Fulcher, G. S. Analysis of recent measurements of the viscosity of glasses. *Journal of the American Ceramic Society* **1925**, *8*, 339–355.

(40) Tammann, G.; Hesse, W. Die Abhängigkeit der Viscosität von der Temperatur bei unterkühlten Flüssigkeiten. *Zeitschrift für anorganische und allgemeine Chemie* **1926**, *156*, 245–257.

(41) Bruckenstein, S. Ohmic potential drop at electrodes exhibiting steady-state diffusion currents. *Analytical Chemistry* **1987**, *59*, 2098–2101.

(42) Tanner, J. E. Use of the stimulated echo in NMR diffusion studies. *Journal of Chemical Physics* **1970**, *52*, 2523–2526.

(43) Jerschow, A.; Müller, N. 3D diffusion-ordered TOCSY for slowly diffusing molecules. *Journal of Magnetic Resonance A* **1996**, *123*, 222–225.

(44) Sørland, G. H.; Anthonsen, H. W.; Zick, K.; Sjöblom, J.; Simon, S. A spoiler recovery method for rapid diffusion measurements. *Diffusion Fundamentals* **2011**, *15*, 1–9.

(45) Stewart, J. J. P. General Description of MOPAC. Stewart Computational Chemistry: 15210 Paddington Circle, Colorado Springs, CO 90821 USA, 2007.

(46) Redel, E.; Thomann, R.; Janiak, Ch. Use of ionic liquids (ILs) for the IL-anion size-dependent formation of Cr, Mo and W nanoparticles from metal carbonyl $M(CO)_6$ precursors. *Chemical Communications* **2008**, *15*, 1789–1791.

(47) Bird, C. L.; Kuhn, A. T. Electrochemistry of the viologens. *Chemical Society Reviews* **1981**, *10*, 49–82.

(48) Monk, P. M. S. *The Viologens: Physicochemical Properties, Synthesis and Applications of the Salts of 4,4'-Bipyridine*; Wiley: New York, 1998.

(49) Breuer, S.; Pham, D.-T.; Huemann, S.; Gentz, K.; Zörlein, C.; Hunger, R.; Wandelt, K.; Broekmann, P. Organic layers at metal/electrolyte interfaces: molecular structure and reactivity of viologen monolayers. *New Journal of Physics* **2008**, *10*, 125033.

(50) Norton, J. D.; White, H. S. Effect of comproportionation on the voltammetric reduction of methyl viologen in low ionic strength solutions. *Journal of Electroanalytical Chemistry* **1992**, *325*, 341–350.

(51) Simon, M. S.; Moore, P. T. Novel polyviologens: photochromic redox polymers with film-forming properties. *Journal of Polymer Science: Polymer Chemistry Edition* **1975**, *13*, 1–16.

(52) Pham, D.-T.; Gentz, K.; Zörlein, C.; Hai, N. T. M.; Tsay, S.-L.; Kirchner, B.; Kossmann, S.; Wandelt, K.; Broekmann, P. Surface redox chemistry of adsorbed viologens on Cu(100). *New Journal of Chemistry* **2006**, *30*, 1439–1451.

(53) Pham, D.-T.; Tsay, S.-L.; Gentz, K.; Zörlein, C.; Kossmann, S.; Tsay, J.-S.; Kirchner, B.; Wandelt, K.; Broekmann, P. Quasi-reversible chloride adsorption/desorption through a polycationic organic film on Cu(100). *Journal of Physical Chemistry C* **2007**, *111*, 16428–16436.

(54) Sagara, T.; Fujihara, Y.; Tada, T. Molecular structure dependence of the phase transition spike response of viologens at an HOPG electrode using bisviologen and carboxylated viologen. *Journal of The Electrochemical Society* **2005**, *152*, 239–246.

(55) Shoup, D.; Szabó, A. Chronoamperometric current at finite disk electrodes. *Journal of Electroanalytical Chemistry and Interfacial Electrochemistry* **1982**, *140*, 237–245.

(56) Levenberg, K. A method for the solution of certain non-linear problems in least squares. *Quarterly of Applied Mathematics* **1944**, *2*, 164–168.

(57) Marquardt, D. An algorithm for least-squares estimation of nonlinear parameters. *SIAM Journal of Applied Mathematics* **1963**, *11*, 431–441.

(58) Sutherland, W. Ionization, ionic velocities, and atomic sizes. *Philosophical Magazine* **1902**, *3*, 161–177.

(59) Einstein, A. Über die von der molekularkinetischen Theorie der Wärme geforderte Bewegung von in ruhenden Flüssigkeiten suspendierten Teilchen. *Annalen der Physik* **1905**, *322*, 549–560.

# 4.4 First results on Stabilization of Monolayer Protected Silver Clusters ("Ag₉MSA₇") and their Electrochemical and ESI-MS investigations

This chapter presents first experiments on the stabilization of monolayer protected Ag clusters and their electrochemical and ESI-MS investigations. It is considered an initial base for further more detailed studies in view of a publication.

The work presented here has been carried out by the following people:

Nataraju Bodappa, Department of Chemistry and Biochemistry, University of Bern:
Cluster synthesis and phase transfer, Size exclusion chromatography (SEC), UV-VIS-NIR spectroscopy, Differential Pulse Voltammetry (DPV).

Elina Kalenius, Department of Chemistry, University of Jyväskylä, Finland:
Electrospray Ionization Mass Spectroscopy (ESI-MS).

Nataraju Bodappa, Department of Chemistry and Biochemistry, University of Berne, and
Herbert Schaffer, Institute for Anatomy, University of Bern:
TransmissionElectron Microscopy

## 1. INTRODUCTION

Synthesis, characterization and applications of monolayer protected clusters (MPC) of gold have been the subject of a wide range of detailed studies in the last decade[1-3]. Au MPCs comprise a large variety of applications including drug delivery[4, 5], sensors, catalysis[6], photonics and electronic elements[7], and also the crystal structures of MPCs of Au25[8, 9], Au28[10], Au36[11], Au38[12], Au102[13], of MPCs have been reported. All these studies have significantly enhanced the understanding of the chemical, physical and electronic properties of Au MPCs, and recent investigations by electrochemical techniques[2,3][14] and by scanning tunneling spectroscopy[14] have further elucidated their electronic and conduction properties in electrolytic environment, both in electrolyte bulk solution and immobilized at single–crystal electrode substrates.

In contrast to the well-established synthesis techniques of stable Au MPCs, the preparation and characterization of analogous stable silver MPCs containing a "magic number" of atoms is still rather challenging due to the facile oxidation of silver. Although a substantial effort has been made by many groups in synthesizing such stable silver clusters, there exist to date only few reports on "well defined" silver MPCs with a stable and intact composition confirmed by mass spectroscopy, such as $Ag_7$[15] , $Ag_{32}$[16], $Ag_{44}$[17, 18], $Ag_{152}$[19] and $Ag_{280}$[20].

Recently, the groups of Zheng[20] and Bigioni[21] determined independently the crystal structure of $Ag_{44}$(p-MBA)$_{30}$ (p-MBA = para mercapto benzoic acid). These results were communicated as a major breakthrough opening substantial new insights into the structure and composition of ligand-stabilized silver MPCs. Interestingly, it was found that, the surface protecting motif involved in $Ag_{44}$(p-MBA)$_{30}$ clusters is completely different from $Au_{102}$(p-MBA)$_{44}$ clusters. Such crystallization experiments are considered to be relevant to clarify the existence of sulphur-based bonds to two-dimensional large Ag surfaces. In addition, the synthesis of water soluble silver clusters such as $Ag_7$(DMSA)$_4$[15] (DMSA=Dimercaptosuccinic acid), $Ag_n$(NALC)$_m$[21] (NALC=N-acetyl-L-cysteine), $Ag_n$(GSH)$_m$[22-26] (GSH=glutathione), $Ag_{25}$(capt)$_{18}$ (capt=captopril), $Ag_{44}$(NMBA)$_{30}$[18] (NMBA=5-mercapto 2-nitrobenzoic acid) were reported, as well as silver mercaptosuccinic acid (thiomalic acid) homoleptic type complexes ($Ag_7MSA_7$, $Ag_8MSA_8$)[27] and [Na[Ag(H$_2$MSA)].0.5H$_2$O)]$_{24-34}$ [28]. Also first electrochemical studies on Ag MPCs have been reported by several groups[29-31].

In a recent publication, we have reported the synthesis of water soluble silver clusters, whose composition has been assigned to the formula "$Ag_9$(H$_2$MSA)$_7$" (H$_2$MSA = mercaptosuccinic acid)[33] based on its fragmentation products. These clusters decompose slowly in water within one day to silver(I) thiolate, but they can be stabilized in aqueous solvent mixtures with acetonitrile, methanol or ethanol, and they are very stable in pure ethanol, or in solid state under an inert gas atmosphere. A detailed further investigation of up to now unknown properties of these clusters is an exciting and challenging topic, involving for example their further structural characterization by techniques such as Transmission Electron Spectroscopy (TEM) or Scanning Probe methods, but also their photoluminescence and electrochemical properties. As shown in our previous investigation of Au MPCs[14], especially Differential Pulse Voltammetry (DPV) is a powerful tool to probe the size dispersity and to extract energy level information of such clusters

in an electrolytic environment. However, an important requirement for DPV investigations of the above mentioned Ag MPCs is their sufficient long-time stability in solubilized form.

In this work, we focus therefore mainly on the further stabilization of the "$Ag_9MSA_7$" clusters in solution by considering the influence of electronic and steric factors, by changing the pH in the aqueous cluster solution, as well as by phase transfer of the clusters into an organic medium using sterically bulky counterions. The obtained stable clusters were then purified and size – fractionized by size-exclusion chromatography. The stability and properties of the clusters before and during phase transfer, and after size-fractionization were monitored by UV-Vis spectroscopy and Transmission Electron Microscopy (TEM), and the size-discriminated fractions were additionally investigated by Electrospray Ionization Mass Spectroscopy (ESI-MS). Finally, preliminary electrochemical DPV experiments were carried out in a dichloromethane electrolyte solution.

## 2. EXPERIMENTAL SECTION

### 2.1 Materials and Chemicals

Silver nitrate $AgNO_3$ (>99%), Tetraoctyl ammonium bromide $[CH_3(CH_2)_7]NBr$ (TOABr) (>98%), Sodium borohydride $NaBH_4$ (99.99%), Toluene ($\geq$99.7%, GC grade) and Dichloromethane $CH_2Cl_2$ ($\geq$99.9 %) were purchased from Sigma-Aldrich. $CH_2Cl_2$ was further dried in contact with molecular sieves to remove any trace amount of water. Tetrabutyl ammonium hexafluorophosphate ($TBAPF_6$) ($\geq$99.0%) was purchased from Fluka and dried overnight in an oven at 60°C to remove any presence of moisture. Mercaptosuccinic acid $HOOC-CH_2-CHSH-COOH$ ($H_2MSA$) (97%) was purchased from Aldrich. The 0.1M ammonium acetate buffer solution was prepared by using ammonium hydroxide (25%, Aldrich) and acetic acid (100%, Merck) solution. Tetrahydrofuran (THF) (HPLC grade) from Sigma-Aldrich was used. All water used for the preparation procedures was purified by Milli-Q system (18.2 MΩ-cm, 2-3 ppb TOC value).

## 2.2 Synthesis of H₂MSA monolayer protected silver clusters "Ag₉MSA₇"

The H$_2$MSA monolayer protected silver clusters "Ag$_9$MSA$_7$" were synthesized as reported in our previous paper[32] and shown in **Scheme 1**: Briefly, AgNO$_3$ and mercaptosuccinic acid H$_2$MSA were mixed in 1: 5 molar ratios and were ground during 15 min in the solid state at room temperature by a pestle in a mortar. We observed that the presence of moisture plays a crucial
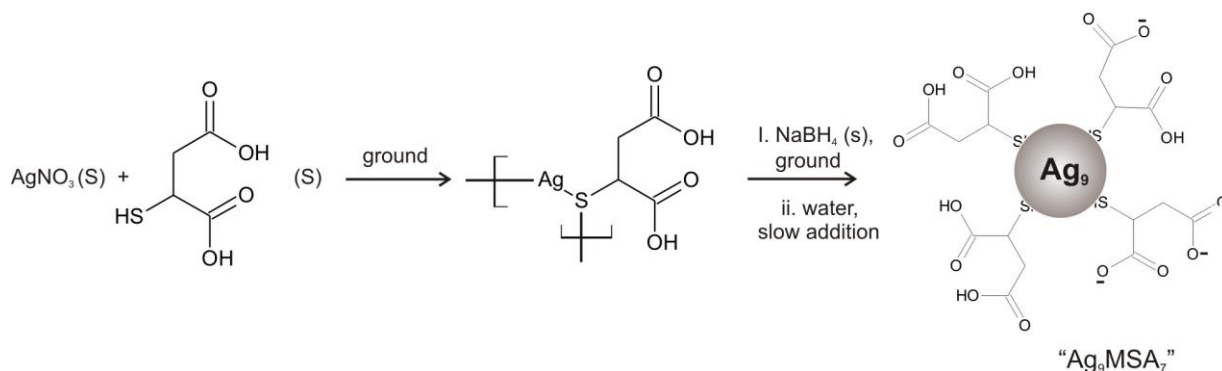


**Scheme 1.** Solid-state synthesis of mercaptosuccinic acid protected silver monolayer protected clusters. [33]

role in forming the Ag(I)MSA complex. NaBH$_4$ (in solid form) was then added to the above mixture in five-fold amount with respect to AgNO$_3$, and the mixture was then further ground for 15 min. 15 ml of water was then gradually added over a time scale of 1 min.

## 2.3 Size exclusion chromatography (SEC)

Size exclusion chromatography was performed according to the reported literature procedure[33]. The Bio beads S-X1 (pore size 30-40 μm with an exclusion limit of 600-14000 Da) were soaked overnight in THF solvent. The swollen beads were transferred into the column (diameter ~2 cm, with a glass frit) and packed using several bed volumes of solvent under a gentle stream of argon until the constant height reaches ~90 cm. The phase transferred clusters were dissolved in a minimum amount of THF solvent and transferred into the column, eluted at a rate of 0.5 to 0.7 ml/min. The eluted fractions were further passed over a PTFE syringe filter (0.25 μm). Each fraction (1 ml) was collected in small vials and tested by absorption spectroscopy. The procedure was repeated for the further fractionations.

## 2.4. UV-Visible absorption spectroscopy

UV/VIS/NIR spectroscopy was measured with a Perkin Elmer λ900 spectrophotometer, and a quartz cell with 1 cm path length was used. All spectra (for phase transferred clusters) were recorded either in toluene or in tetrahydrofuran.

## 2.5 Transmission Electron Microscopy (TEM)

For the preparation of samples, a dilute solution of the synthesized and SEC fractionated clusters in THF was dropcast on a carbon coated copper grid with 300 mesh size (PLANO GmbH, Germany) and dried in air. A FEI Tecnai F20 (Eindhoven, The Netherlands) instrument equipped with a Gatan GIF energy filter (Gatan, Munich, Germany) with an acceleration voltage 200 kV was used for recording the images.

## 2.6 Electrospray Ionization Mass Spectrometry (ESI-MS)

Mass spectrometric experiments were performed with a QSTAR Elite ESI-Q-TOF mass spectrometer equipped with an API 200 TurboIonSpray ESI source from AB Sciex (former MDS Sciex) in Concord, Ontario (Canada). The parameters of the ion source, ion optics and quadrupole were optimized to get maximum abundance of the ions under study.

## 2.7 Electrochemistry

The electrochemical Differential Pulse Voltammetry (DPV) investigations were performed using an Autolab PGSTAT302 N potentiostat (Eco Chemie) and a single compartment three-electrode cell with a working volume of 0.25 cm$^3$. Both a home-made macroscopic Pt electrode with diameter of 2.93 mm) and a Pt microelectrode with diameter of 12.5 μm (Bioanalytical Systems) were used as working electrodes. The surface area of the microelectrode was calibrated in a 0.001 M solution of $Ru(NH_3)_6Cl_3$ in 0.1 M KCl from measuring the steady state current in a linear potential sweep experiment. All DPV investigations of the "$Ag_9MSA_7(TOA^+)_x$" clusters were performed at room temperature in an argon-deaerated supporting electrolyte of 0.1 M $TBAPF_6$ in dichloromethane with a cluster concentration of 2-3 mg/ml. A Pt wire served as counter electrode and a Ag wire was used as pseudo-reference electrode as applied in previous publications.[34, 35] Blank DPV experiments were carried out in the supporting electrolyte without

MPCs to confirm the absence of other faradaic or charging peaks. Pulse width: 60 ms, pulse height: 50 mV, period: 200 ms. The scan-rate in all experiments was 20 mVs$^{-1}$.

## 3. RESULTS AND DISCUSSION

### 3.1. Stability of "Ag$_9$MSA$_7$" in water

The stability of the aqueous solutions with the originally synthesized clusters solutions were tested with absorption spectroscopy at pH values of 3, 4, 6, 10 by using 1 M acetic acid, 1 M ammonium hydroxide and 100 mM ammonium acetate buffer solution, as shown in **Figure 1**. At all pH values, the absorption signals diminish over the entire wavelength range between 400 and 1000 nm, but the stability of the clusters is significantly higher (several hours) in the low pH range of 2-4 than at very alkaline pH values. Simultaneously with the decrease of the absorption, a change in the absorption spectra occurs that is also noticed by a change of the colour of the solution from brownish black to yellow and is associated with the degradation of the clusters into a silver(I) thiol complex. The pronounced pH dependence of the cluster stability could be due to the strong nucleophilic nature of the OH$^-$ species that reacts with the surface Ag atoms of the cluster core resulting in the formation of Ag(I) thiolate and Ag$_2$O species.
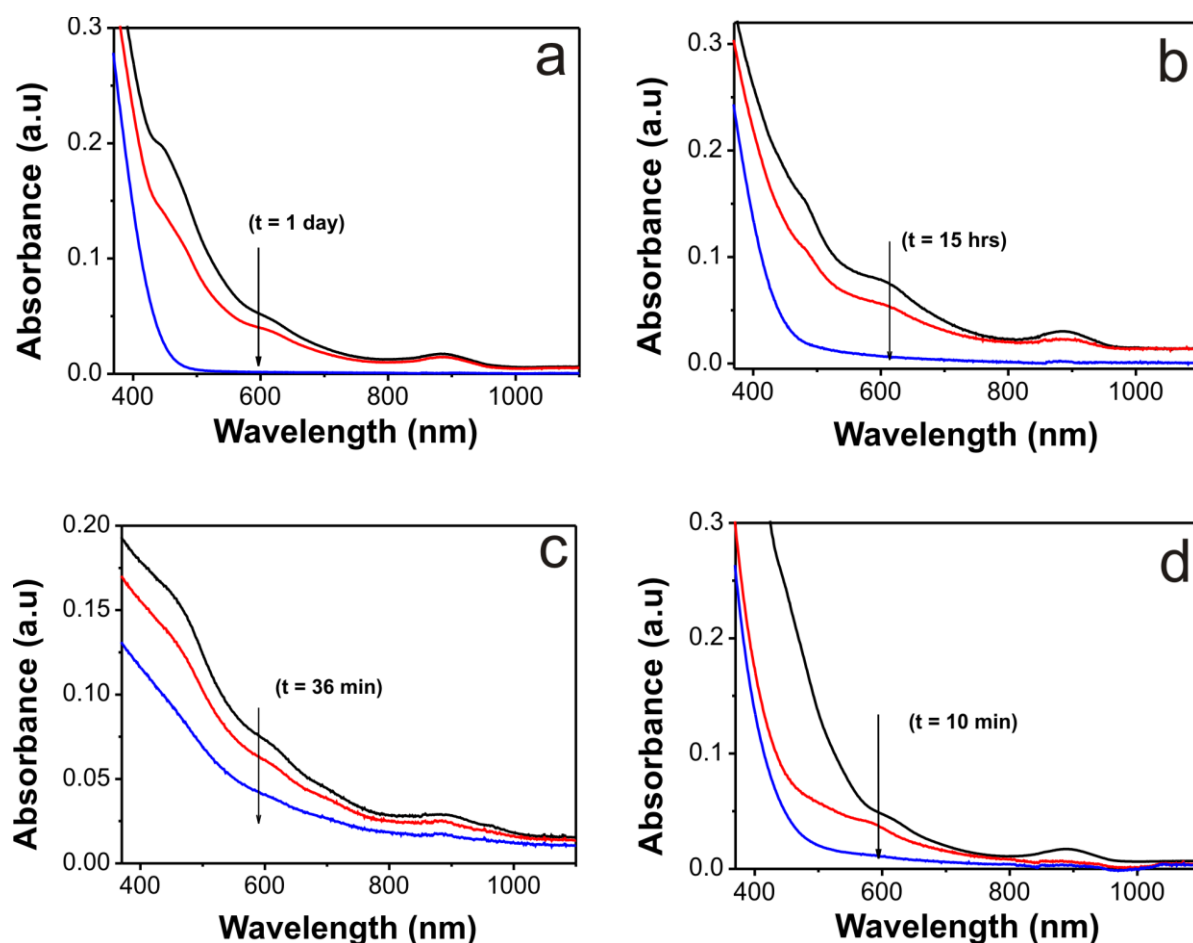
**Figure 1.** Time dependent stability of the UV-VIS-NIR absorption spectrum of the aqueous solutions of the originally synthesized (crude) "$Ag_9(H_2MSA)_7$"clusters at pH 3(a), 4(b), 6(c) and 10(d),  at room temperature. The time sequence follows from the black curve through the red curve to the blue curve within a time range indicated in the figures with the time information assigned to the different curves.

### 3.2. Phase transfer and stability in toluene

The phase transfer of MPCs was carried out by using toluene as a water-immiscible phase. First, 0.25 mmol (132 mg of tetraoctylammonium bromide (TOABr) was dissolved in toluene. The aqueous solution of the crude Ag MPCs in water was added to the toluene phase, and the resulting emulsion was stirred for ca 2 hours. The phase transfer process was monitored by the color change in the organic phase from colorless to black color, **Scheme 2**. Afterwards, by using a separating funnel the water layer was removed. The remaining toluene layer was washed with excess of water to remove any water soluble impurities. The phase transfer of the Ag MPCs is facilitated by the interactions between the hydrophilic carboxylate anion (MSA⁻) located on the Ag MPCs and the hydrophobic tetraoctylammonium cation (TOA⁺) in the toluene phase.

Interestingly, the phase transfer process was not successful using tetraphenyl phosphonium bromide and tetrabutyl ammonium bromide. After completing the reaction, the clusters were washed with milli-Q water 5-6 times and filtered using 0.2 μm PTFE syringe filter paper to remove the excess $H_2MSA$, TOABr and disulphides. The eluted cluster solution in toluene was then passed through anhydrous $Na_2SO_4$ to remove trace amounts of water. Afterwards, the clusters were centrifuged to remove any insoluble Ag(I) thiolates present in the product, leaving the Ag clusters in the toluene solution.
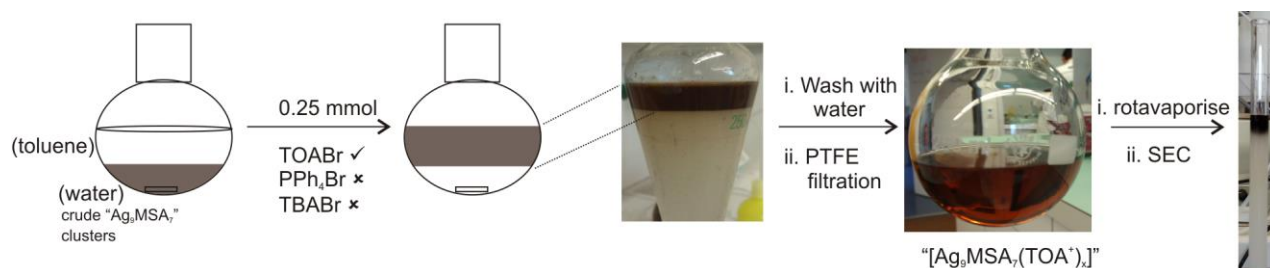


**Scheme 2.** Schematic for the phase transfer and purification process of "$Ag_9MSA_7$" MPCs.

**Figure 2a** shows the UV-VIS-NIR spectrum of the crude Ag MPCs in water immediately after the synthesis (black trace), and in toluene immediately after the phase transfer (red trace).
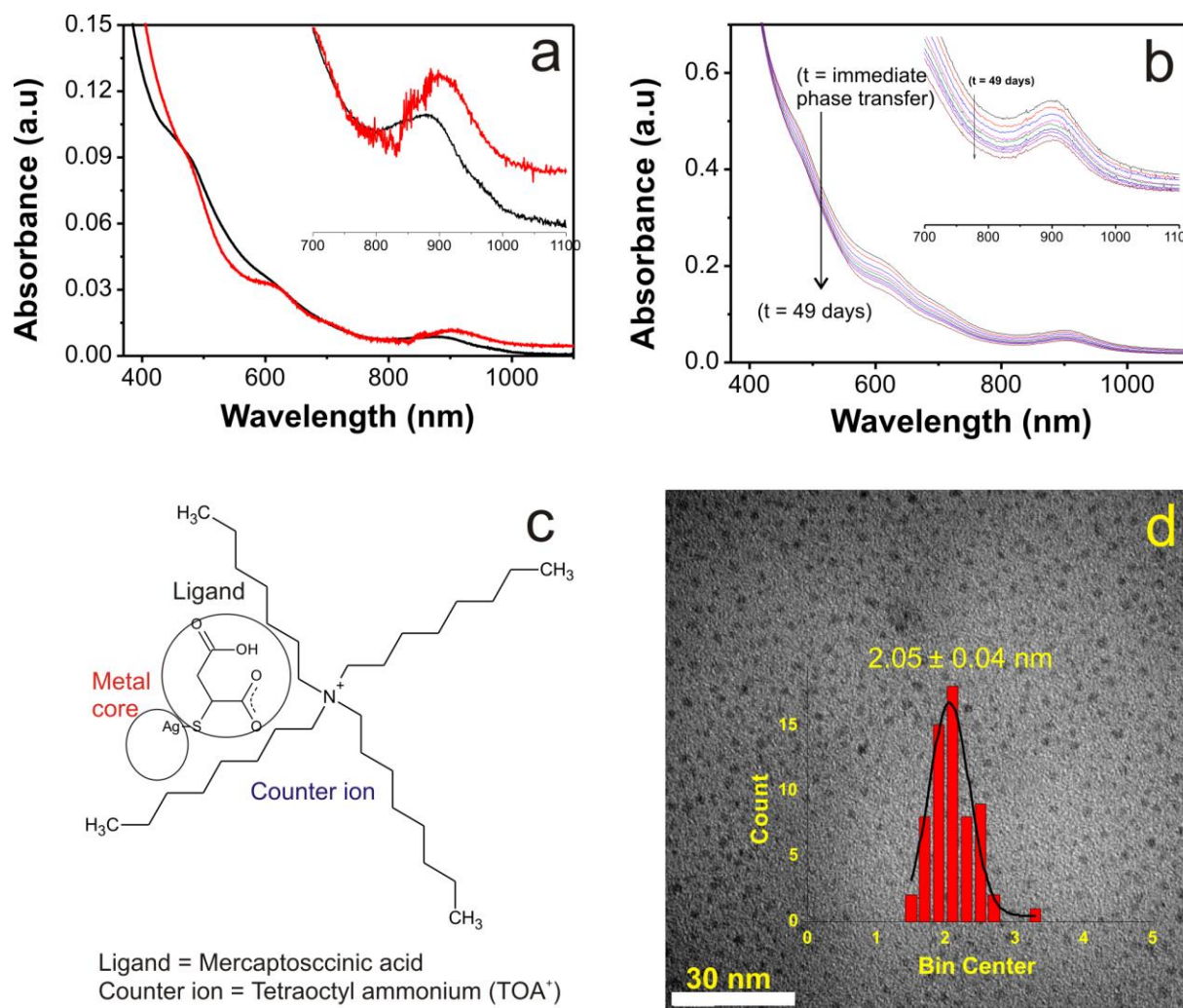
**Figure 2.** (a) UV-VIS-NIR absorption spectrum of the crude ("as synthesized") "Ag$_9$(H$_2$MSA)$_7$" clusters in water immediately after synthesis (black trace), and immediately after phase transfer in toluene (red trace). The inset shows an enlarged part of the spectra in the near-infrared range (b) Time dependence of the UV-VIS-NIR absorption spectra for the phase transferred "Ag$_9$(H$_2$MSA)$_7$(TOA$^+$)$_x$" MPCs in toluene. The inset shows an enlarged part of the spectra in the near-infrared range. The different curves show the time dependence of the spectra within the time range indicated by the time information of the first and of the last recorded spectrum. (c) Transmission electron microscopy (TEM) image and size distribution histogram of the crude "Ag$_9$(H$_2$MSA)$_7$(TOA$^+$)$_x$" MPCs after phase transfer in toluene and drop-casting on the TEM grid. (d) Assumed primary structure of the "Ag$_9$(H$_2$MSA)$_7$(TOA$^+$)$_x$" MPCs.

It confirms that the entire cluster core structure is maintained in the organic phase, where the Ag MPCs show absorption features at 898 nm (1.38 eV), 711 nm (1.74 eV), 618 nm (2.0 eV) and 470 nm (2.64 eV) that are related with the quantum size effect. The absorption features in toluene are more pronounced than those in the aqueous phase (see inset in **Fig 2a**). It is also clearly seen that the absorption band observed in water (centered at 880 nm) is positively shifted in toluene (898 nm). This red shift is attributed to the presence of TOA$^+$ cations bound to the

terminal carboxylate anions of the cluster ligands in the organic phase[36]. The investigation of the stability of the phase transferred clusters by absorption spectroscopy is shown in **Fig. 2b.,** where it is evident that the clusters are fairly stable in toluene at room temperature over a time scale of more than a month. The absorption peak intensities decrease only very slightly (see inset of **Fig 2b**). It is assumed that the high stability of the clusters after the phase transfer is due to the protection of the cluster shell by the large counterion (TOA$^+$), as shown in **Fig. 2c** and by the net total charge on the cluster molecule. As shown in **Fig. 2d**, the TEM images of these clusters show a relatively narrow size distribution with an average core diameter of ~ 2.1 nm.

### 3.3. Purification of the phase transferred clusters by SEC

One of our key goals of this work aims at preparing pure clusters and finding the intact molecular composition with an atomic-level precision. This was done by submitting the phase transferred clusters to Size Exclusion Chromatography (SEC) to remove any excess TOA$^+$ ions and to separate clusters with an other size than "Ag$_9$(H$_2$MSA)$_7$". A similar SEC procedure was chosen as applied previously by Bürgi et al.[33] who separated Au$_{40}$ clusters from Au$_{38}$ clusters:
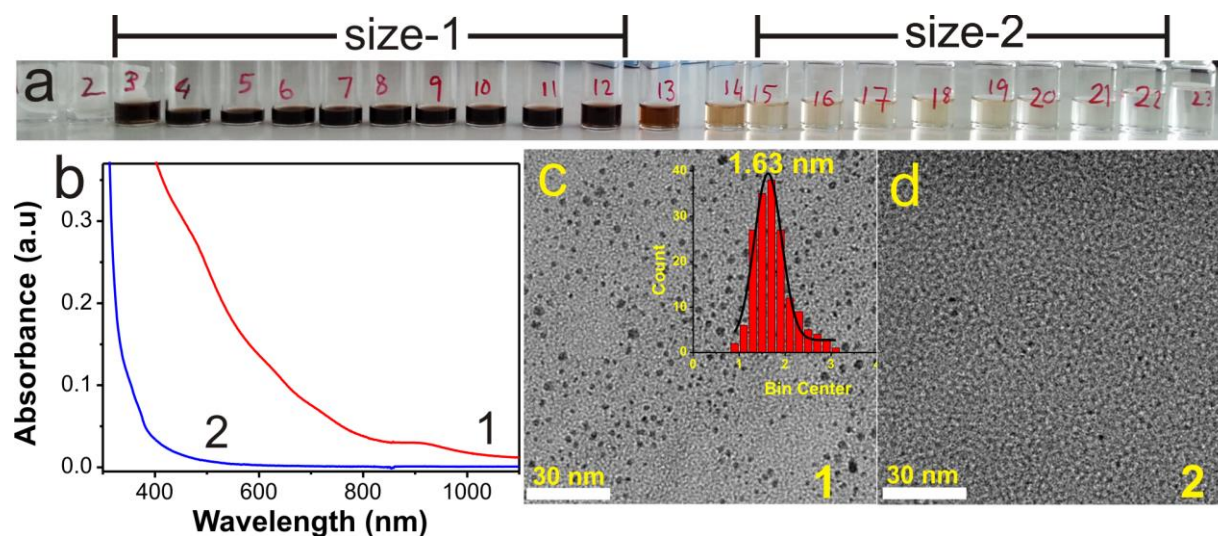


**Figure 3.** Spectroscopic and TEM investigation of phase-transferred clusters after Size Exclusion Chromatography (SCE). (a) Picture of the SEC eluted fractions. (b) UV-VIS-NIR absorption spectra of size-fractionated "Ag$_9$(H$_2$MSA)$_7$(TOA)$_x^+$" clusters. Curve 1: Fraction 7 (range size-1). Curve 2: Fraction 18 (range size-2). (c,d) TEM images of fraction 7 (c) and fraction 18 (d) as examples of size ranges 1 and 2, respectively.

The toluene in the phase transferred clusters was completely removed by rotaevaporization. The dried form of the clusters (200 mg), were re-dissolved in a minimum amount of THF solvent,

injected into the SEC packed column and eluted slowly with a flow rate of 0.5 to 0.7 ml/min. In total 22 fractions were collected separately in small vials (**Fig. 3a**). By comparing the absorption features in the UV-VIS-NIR spectra of these fractions they could be divided into 2 ranges: "Size-1 range" with fractions 3-12 and "size-2" range with fractions 15-22. Within each of these two size ranges the UV-VIS-NIR spectra were identical. Most clusters are within the size-1dimensional range, whereas only a small number is in the size-2 dimensional range. **Fig. 3b** shows a comparison of the UV-VIS-NIR spectra of clusters of fraction 7 (red line), as an example from the size-1 cluster range, with clusters of fraction 18 (blue curve) as an example from the size-2 cluster range. The absorption spectrum of the fraction 7 clusters from size-1 range is similar to the spectrum of the water soluble crude "$Ag_9(H_2MSA)_7$" cluster shown in the black curve of Figure 2a, and the spectral features indicate absorption bands at 898, 711, 618, 470 and 242 nm. In contrast, the spectrum of the fraction 18 clusters from size-2 range indicates only 2 absorption bands at 370 and 355 nm. **Fig. 3c** shows a TEM image and the size distribution histogram of the fraction 7 clusters from size-1 range, with an average size of 1.63 nm. This is slightly less than the value of 2.05nm shown in Fig. 2d for the crude phase transferred clusters before applying the SEC procedure. This decrease in size might be due to the partial removal of $TOA^+$ ions from the cluster surface while running the SEC column purification. **Fig. 3d** shows a TEM image of the fraction 18 clusters from size-2 range. Due to the small yield of this product the only scattered distribution on the TEM grid did not allow to derive a statistical histogram. An average size value of approximately 1.55 nm was estimated directly from the TEM patterns.

### 3.4. Voltammetry of phase transferred Ag MPCs

The phase transfer of the water soluble clusters enables us to perform electrochemical DPV investigations of the "$Ag_9(H_2MSA)_7$" clusters. Fig. 4 shows DPV measurements of phase transferred "$Ag_9(H_2MSA)_7(TOA^+)_x$" clusters recorded between -2.0V to +3.0V vs. Ag after drying and dissolution in 0.1M $TBAPF_6$ in $CH_2Cl_2$. **Fig. 4a** shows two independent voltammograms of the crude phase-transferred "$Ag_9(H_2MSA)_7(TOA^+)_x$" clusters before SEC treatment, recorded for two separately synthesized batches. The first batch (black curve) was recorded with a macroscopic Pt electrode between -2.0 and +1.3V vs. Ag. We then repeated the measurements for the second batch of the crude phase-transferred clusters between -2.0 and +3V vs. Ag by using a Pt microelectrode (blue trace). In both batches one oxidation doublet (O1-O2) and one

reduction doublet (R1-R2) with a large peak-to-peak spacing between O1 and R1 are seen (see labels on the black curve). The first oxidation (O1) and first reduction (R1) process take place at +0.32 V and -0.87 V, respectively. The corresponding energy gap for these MPCs amounts therefore to 1.19 eV (electrochemical band gap). After correcting for the charging energy, as estimated by the difference between the position of R2 and R1, the HOMO-LUMO gap of the cluster is estimated to be 0.82 eV. To the best of our knowledge, this is the first observation of molecule-like voltammetric results in case of Ag MPCs. The voltammogram of the second batch shows additionally 2 peaks at 2.3 and 2.8V vs. Ag.
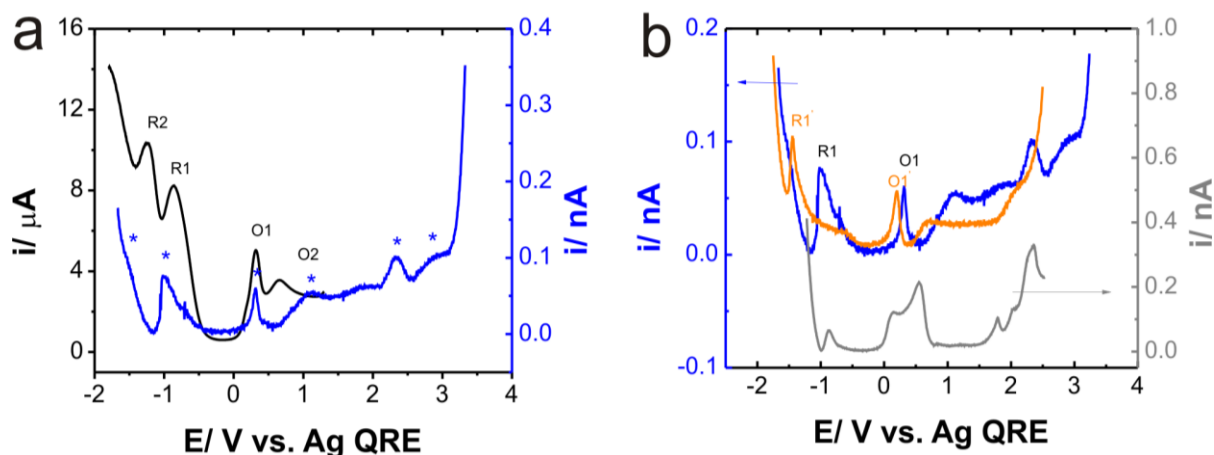


**Figure 4.** DPV measurements of phase-transferred "$Ag_9MSA_7(TOA^+)_x$" clusters in 0.1M $TBAPF_6$ in $CH_2Cl_2$. (a) DPV curves of crude phase-transferred "$Ag_9MSA_7(TOA^+)_x$" clusters prepared in two different synthesis batches. Black curve: DPV of batch 1, recorded with macroscopic Pt electrode. Blue curve: Batch 2, recorded with Pt microelectrode. (b) Comparison of DPV curves of phase-transferred crude clusters (blue curve) with SEC processed clusters of fraction 7 size-1 range (orange curve) and fraction 18 size-2 range (gray curve), recorded with a Pt microelectrode.

**Figure 4b** shows a comparison of DPV curves for phase-transferred crude and size fractionated clusters recorded with the Pt microelectrode. The blue trace shows the result for the crude clusters (same curve as blue curve in Fig. 4a). The orange curve is obtained after SEC from fraction 7 of the size-1 range. It shows similar results as the crude clusters, but the electrochemical band gap increases by 50 mV. This could be due to the partial removal of $TOA^+$ ions from the ligand shell of the phase transferred cluster during the SEC separation. Similar ligand shell effects were observed recently in the case of electrochemical investigations of phase transferred water soluble $Au_{25}(3\text{-}MPS)_{18}$ clusters[37], a very similar system to the present case, where MPS = (3-mercaptopropyl)sulfonate. Therefore, the exact HOMO-LUMO gap of the

native cluster, "$Ag_9MSA_7$" (wihout $TOA^+$ counter ion) is higher than the value of 0.87 eV. In the case of clusters from fraction 18 of the size-2 range (gray curve), the pronounced variations in the intensities of the current peaks strongly suggest the presence of other sizes. However, due to the very limited yield of size-2 fractions, a further SEC fractionation was not possible.

**3.5. Electrospray Ionisation Mass Spectrometry (ESI-MS) of size fractionated silver MPCs**

**Figure 5** shows a typical ESI-MS spectrum as obtained in both cases of size-1and of size-2 fractions, and **Table 1** lists the most significant observed fragmented experimental and theoretical m/z values of both the size-1 and the size-2 fractions. The spectrum shows a stable molecular ion peak at an m/z value of 2425.13 which corresponds to the *cyclic* tetrameric silver motif, $[Ag_4(HMSA)_4(TOA)_3]^-$. This kind of tetrameric stable motif units were also observed in the ESI-MS of oligomeric homoleptic thiolate silver(I) complexes [27, 38]. In fact, $RS(Au-SR)_n$ subunits, are the most stable protecting motifs in many gold MPCs.[39] We have also identified the $[Ag_7MSA_7(TOA)]^{2-}$ at m/z = 2063.41 and $[Ag_8MSA_8(TOA)]^{2-}$ at m/z = 2191.37, higher range molecular compositions with a charge of -2. The analysis of the fragmented peaks indicates that the AgMSA is attached to the $TOA^+$ ions. In addition to this, the isotopic distribution of the fragmented peaks without $TOA^+$ ions such as, $[Ag_4(MSA)_3]^-$, $[Ag_3(MSA)_3]^{2-}$ were also observed and shown in **Table 1**.
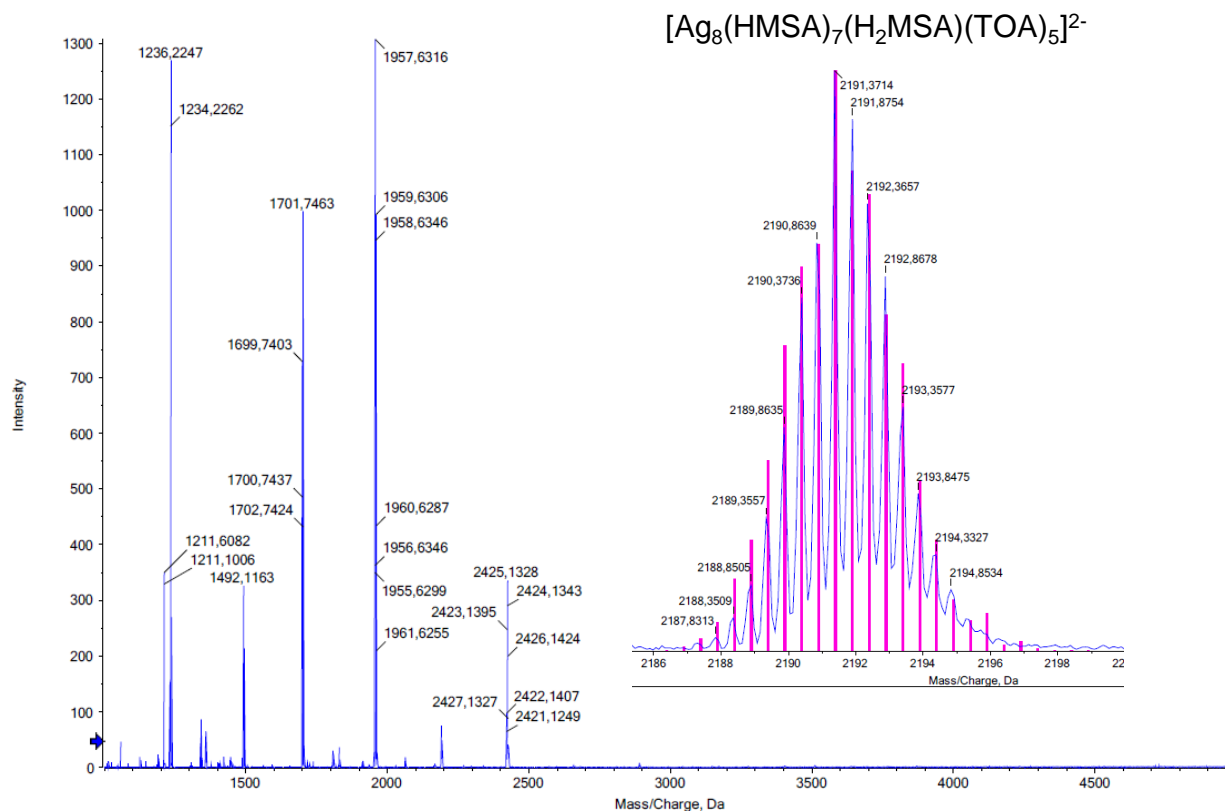
**Figure 5.** Typical negative mode ESI-MS spectrum of Ag clusters as obtained for both size-1 and size-2 fractions. The Inset shows the experimental (blue) and calculated (pink) mass spectra of the isotopic distribution peaks for $[Ag_8(HMSA)_7(H_2MSA)(TOA)_5]^{2-}$.

**Table 1.** ESI–MS mass-to-charge ratios values for measured vs. calculated values of size-1 and size-2 clusters.

| Ion | charge | *m/z* (theor ma) | *m/z* (exp ma) | mass accuracy (m/z) |
|---|---|---|---|---|
| | | **ESI-MS -size-1** | | |
| $[Ag_3(HMSA)_3]^{2-}$ | 2- | 384.3322 | 384.8818 | -0.55 |
| $[Ag_4(HMSA)_3]^{2-}$ | 2- | 437.7848 | 437.8293 | -0.04 |
| $[Ag_4(HMSA)_2(H_2MSA)_2]^{2-}$ | 2- | 512.7841 | 512.8245 | -0.04 |
| $[Ag_3(HMSA)_2]^-$ | 1- | 618.6815 | 618.7155 | -0.03 |
| $[Ag_3(HMSA)_3(TOA)]^{2-}$ | 2- | 617.6002 | 617.60 | 0.00 |
| $[Ag_4(HMSA)_3(H_2MSA)(TOA)]^{2-}$ | 2- | 745.5481 | 745.5906 | -0.04 |
| $[Ag_4(HMSA)_2(H_2MSA)]^-$ | 1- | 876.5769 | 876.6124 | -0.04 |
| $[Ag_4(HMSA)_4(TOA)]^{2-}$ | 2- | 978.3122 | 978.3485 | -0.04 |
| $[Ag_3(HMSA)_2(H_2MSA)(TOA)]^-$ | 1- | 1236.2076 | 1236.2244 | -0.02 |
| $[Ag_4(HMSA)_3(TOA)]^-$ | 1- | 1342.1048 | 1342.1197 | -0.01 |
| $[Ag_4(HMSA)_2(H_2MSA)_2(TOA)]^-$ | 1- | 1492.1035 | 1492.099 | 0.005 |
| $[Ag_3(MSA)_3(TOA)_2]^-$ | 1- | 1701,73 | 1701.74 | -0.01 |

| | | | | |
|---|---|---|---|---|
| [Ag$_4$(HMSA)(MSA)$_3$(TOA)$_2$]$^-$ | 1- | 1957.63 | 1957.63 | 0.00 |
| **ESI-MS -size-2** | | | | |
| [Ag$_3$(HMSA)$_3$(TOA)]$^{2-}$ | 2- | 617,6002 | 617,6386 | -0,04 |
| [Ag$_4$(HMSA)$_4$(TOA)$_2$]$^{2-}$ | 2- | 978,3122 | 978,3472 | -0,04 |
| [Ag$_4$(HMSA)$_3$(MSA)(TOA)$_3$]$^{2-}$ | 2- | 1211,5773 | 1211,608 | -0,03 |
| [Ag$_3$(HMSA)$_2$(H$_2$MSA)(TOA)]$^-$ | | 1236,2076 | 1236,2229 | -0,02 |
| [Ag$_4$(HMSA)$_3$(TOA)]$^-$ | 1- | 1342,1048 | 1342,1209 | -0.02 |
| [Ag$_4$(HMSA)$_3$(MSA)$_3$(TOA)$_3$]$^{2-}$ | 2- | 1359,0521 | 1358,9823 | 0,06 |
| [Ag$_4$(HMSA)$_2$(H$_2$MSA)$_2$(TOA)]$^-$ | 1- | 1492,1035 | 1492,1163 | -0,01 |
| [Ag$_3$(HMSA)$_3$(TOA)$_2$]$^-$ | 1- | 1701,7362 | 1701,7463 | -0,01 |
| [Ag$_7$(HMSA)$_6$(H$_2$MSA)(TOA)$_4$]$^{2-}$ | 2- | 1830,1851 | 1830,1747 | 0,01 |
| [Ag$_4$(HMSA)$_3$(H$_2$MSA)(TOA)$_2$]$^-$ | 1- | 1957,6318 | 1957,6316 | 0,00 |
| [Ag$_7$(HMSA)$_7$(TOA)$_5$]$^{2-}$ | 2- | 2063.4532 | 2063.4196 | 0.03 |
| [Ag$_8$(HMSA)$_7$(H$_2$MSA)(TOA)$_5$]$^{2-}$ | 2- | 2191,3914 | 2191,3714 | 0,02 |
| [Ag$_4$(HMSA)$_4$(TOA)$_3$]$^-$ | 1- | 2425,1611 | 2425.1328 | 0.02 |

The charging energies (voltammetric) and the size (mass spectrometric) for previously reported silver clusters are comparable with the values of Au MPCs. Therefore, we consider it worthwhile to also compare our obtained values with the well established values of AuMPCs. If we compare the HOMO-LUMO gap of the size fractionated size-1 clusters (orange curve in **Figure 4b**), we observe a good match with the HOMO-LUMO gap of Au$_{38}$(PET)$_{24}$ (PET=Phenylethane-1-thiol) clusters. Therefore the above observed mass spectrometric peaks could be assigned to fragmented peaks of a larger sized Ag(approximately 25-38) cluster. This result suggests strongly that, the "Ag$_9$MSA$_7$" assignment in our previous publication[32] and also our cluster formulas used in the previous part of this work (and put in quotation marks) represent in reality a fragmented peak. It has to be clearly pointed out here that, such mismatching assignments of the molecular formulas have happened also with the very well studied Au$_{25}$(PET)$_{18}$ cluster[40] that had previously been assigned with a molecular formula of "Au$_{38}$(PET)$_{24}$" in a series of publications[41-46]. Only after the application of both very high accuracy mass spectrometry and the crystallization of this compound, the revised formula Au$_{25}$(PET)$_{18}$ was secured.

The above observations and remarks suggest therefore, the SEC-processed clusters in both size ranges size-1 and size-2 are indeed protected with a motif of cyclic oligomers, [Ag(MSA)]$_n$ (or) the clusters might belong to a larger core size than "Ag$_9$MSA$_7$" and could be a family of homoleptic type.

## 4. CONCLUSIONS

In conclusion, we have enhanced the stability of "$Ag_9MSA_7$" MPCs by submitting them to phase transfer them into an organic solvent in the presence of sterically bulky counterions. The resulting phase transferred clusters, "$Ag_9MSA_7(TOA)_x$" shows a very high stability in ambient conditions that as enabled for the first time to perform DPV investigations.. Size exclusion chromatography reveals also a minor yield of clusterswith a smaller size during the synthesis of "$Ag_9MSA_7$" clusters. The electrochemical studies of the "$Ag_9MSA_7(TOA^+)_x$" (1.63 nm) clusters show an electrochemical gap of 1.19 V with a HOMO-LUMO gap of 0.87 eV.

As an important result, the combination of the MS investigations with the electrochemically determined HOMO-LUMO gap strongly suggest that the real cluster sizes are larger than the empirically used formula "$Ag_9MSA_7(TOA^+)_x$". Further studies, involving for example also crystallization, are necessary to confirm these assumptions and to get more detailed insight into the real size and composition of the clusters, as a challenging subject of research.

## Acknowledgments

## REFERENCES

[1]     H. Qian, M. Zhu, Z. Wu, R. Jin, *Acc. Chem. Res.* **2012**, *45*, 1470.
[2]     R. W. Murray, *Chemical Reviews (Washington, DC, United States)* **2008**, *108*, 2688.
[3]     T. Laaksonen, V. Ruiz, P. Liljeroth, B. M. Quinn, *Chem. Soc. Rev.* **2008**, *37*, 1836.
[4]     A. Verma, O. Uzun, Y. Hu, Y. Hu, H.-S. Han, N. Watson, S. Chen, D. J. Irvine, F. Stellacci, *Nat. Mater.* **2008**, *7*, 588.
[5]     R. R. Arvizo, S. Bhattacharyya, R. A. Kudgus, K. Giri, R. Bhattacharya, P. Mukherjee, *Chem. Soc. Rev.* **2012**, *41*, 2943.
[6]     G. Li, R. Jin, *Acc. Chem. Res.* **2013**, *46*, 1749.
[7]     S. W. Boettcher, N. C. Strandwitz, M. Schierhorn, N. Lock, M. C. Lonergan, G. D. Stucky, *Nat. Mater.* **2007**, *6*, 592.
[8]     M. W. Heaven, A. Dass, P. S. White, K. M. Holt, R. W. Murray, *J. Am. Chem. Soc.* **2008**, *130*, 3754.
[9]     M. Zhu, C. M. Aikens, F. J. Hollander, G. C. Schatz, R. Jin, *J. Am. Chem. Soc.* **2008**, *130*, 5883.

[10]   C. Zeng, T. Li, A. Das, N. L. Rosi, R. Jin, *J. Am. Chem. Soc.* **2013**, *135*, 10011.
[11]   C. Zeng, H. Qian, T. Li, G. Li, N. L. Rosi, B. Yoon, R. N. Barnett, R. L. Whetten, U. Landman, R. Jin, *Angewandte Chemie-International Edition* **2012**, *51*, 13114.
[12]   H. Qian, W. T. Eckenhoff, Y. Zhu, T. Pintauer, R. Jin, *J. Am. Chem. Soc.* **2010**, *132*, 8280.
[13]   P. D. Jadzinsky, G. Calero, C. J. Ackerson, D. A. Bushnell, R. D. Kornberg, *Science* **2007**, *318*, 430.
[14]   Nataraju Bodappa, Ulrike Fluch, Yongchun Fu, Marcel Mayor, Pavel Moreno-García, Hans Siegenthaler, T. Wandlowski, *Nanoscale* **2014**, *in press*.
[15]   Z. Wu, E. Lanni, W. Chen, M. E. Bier, D. Ly, R. Jin, *J. Am. Chem. Soc.* **2009**, *131*, 16672.
[16]   J. Guo, S. Kumar, M. Bolan, A. Desireddy, T. P. Bigioni, W. P. Griffith, *Anal. Chem.* **2012**, *84*, 5304.
[17]   K. M. Harkness, Y. Tang, A. Dass, J. Pan, N. Kothalawala, V. J. Reddy, D. E. Cliffel, B. Demeler, F. Stellacci, O. M. Bakr, J. A. McLean, *Nanoscale* **2012**, *4*, 4269.
[18]   L. G. AbdulHalim, S. Ashraf, K. Katsiev, A. R. Kirmani, N. Kothalawala, D. H. Anjum, S. Abbas, A. Amassian, F. Stellacci, A. Dass, I. Hussain, O. M. Bakr, *Journal of Materials Chemistry A* **2013**.
[19]   I. Chakraborty, A. Govindarajan, J. Erusappan, A. Ghosh, T. Pradeep, B. Yoon, R. L. Whetten, U. Landman, *Nano Lett.* **2012**, *12*, 5861.
[20]   Y. Negishi, R. Arai, Y. Niihori, T. Tsukuda, *Chem. Commun.* **2011**, *47*, 5693.
[21]   M. Farrag, M. Tschurl, U. Heiz, *Chem. Mater.* **2013**, *25*, 862.
[22]   S. Kumar, M. D. Bolan, T. P. Bigioni, *J. Am. Chem. Soc.* **2010**, *132*, 13141.
[23]   X. Yuan, M. I. Setyawati, A. S. Tan, C. N. Ong, D. T. Leong, J. Xie, *NPG Asia Mater* **2013**, *5*, e39.
[24]   T. Udayabhaskararao, M. S. Bootharaju, T. Pradeep, *Nanoscale* **2013**, *5*, 9404.
[25]   A. Desireddy, S. Kumar, J. Guo, M. D. Bolan, W. P. Griffith, T. P. Bigioni, *Nanoscale* **2013**, *5*, 2036.
[26]   F. Bertorelle, R. Hamouda, D. Rayane, M. Broyer, R. Antoine, P. Dugourd, L. Gell, A. Kulesza, R. Mitrić, V. Bonačić-Koutecký, *Nanoscale* **2013**, *5*, 5637.
[27]   T. Udaya Bhaskara Rao, T. Pradeep, *Angew. Chem. Int. Ed.* **2010**, *49*, 3925.
[28]   K. Nomiya, K.-I. Onoue, Y. Kondoh, N. C. Kasuga, H. Nagano, M. Oda, S. Sakuma, *Polyhedron* **1995**, *14*, 1359.
[29]   M. R. Branham, A. D. Douglas, A. J. Mills, J. B. Tracy, P. S. White, R. W. Murray, *Langmuir* **2006**, *22*, 11376.
[30]   W. Cheng, S. Dong, E. Wang, *Electrochem. Commun.* **2002**, *4*, 412.
[31]   V. R. Chaudhari, P. A. Hassan, S. K. Haram, *New J. Chem.* **2014**, *38*, 1761.
[32]   T. U. B. Rao, B. Nataraju, T. Pradeep, *J. Am. Chem. Soc.* **2010**, *132*, 16304.
[33]   S. Knoppe, J. Boudon, I. Dolamic, A. Dass, T. Bürgi, *Anal. Chem.* **2011**, *83*, 5056.
[34]   J. F. Hicks, D. T. Miles, R. W. Murray, *J. Am. Chem. Soc.* **2002**, *124*, 13322.
[35]   O. Toikkanen, V. Ruiz, G. Rönnholm, N. Kalkkinen, P. Liljeroth, B. M. Quinn, *J. Am. Chem. Soc.* **2008**, *130*, 11049.
[36]   M. A. Habeeb Muhammed, T. Pradeep, *J. Cluster Sci.* **2009**, *20*, 365.
[37]   K. Kwak, D. Lee, *The Journal of Physical Chemistry Letters* **2012**, *3*, 2476.
[38]   K. Nomiya, Y. Kondoh, H. Nagano, M. Oda, *Journal of the Chemical Society, Chemical Communications* **1995**, 1679.
[39]   H. Hakkinen, *Nat Chem* **2012**, *4*, 443.
[40]   D. Lee, R. L. Donkers, G. Wang, A. S. Harper, R. W. Murray, *J. Am. Chem. Soc.* **2004**, *126*, 6193.
[41]   D. G. Georganopoulou, M. V. Mirkin, R. W. Murray, *Nano Lett.* **2004**, *4*, 1763.
[42]   W. Wang, R. W. Murray, *Langmuir* **2005**, *21*, 7015.
[43]   R. Guo, R. W. Murray, *J. Am. Chem. Soc.* **2005**, *127*, 12140.
[44]   W. Wang, D. Lee, R. W. Murray, *The Journal of Physical Chemistry B* **2006**, *110*, 10258.

[45]    J. P. Choi, R. W. Murray, *J. Am. Chem. Soc.* **2006**, *128*, 10496.

[46]    S. Antonello, G. Arrigoni, T. Dainese, M. De Nardi, G. Parisio, L. Perotti, A. René, A. Venzo, F. Maran, *ACS Nano* **2014**.

# 5. Conclusions and Outlook

## 5.1 Conclusions

In this thesis, it has been demonstrated that Au(hkl) and Pt(hkl) surfaces modified with a submonolayer of "as-prepared" Au(55nm)@SiO$_2$ Shell-Isolated Nanoparticles(SHINPs), show *distorted* voltammetric and spectroscopic (*in-situ* Raman) responses **(Chapter 4.1)**. This was found to be due to the blocking of the electrode surfaces with surfactants originating from the synthesis of the Au(55 nm)@SiO$_2$ NPs, which gives rise to *additional* current and spectroscopic features, and therefore causes *disturbances* in the data interpretation and assignment. An efficient strategy has been introduced to overcome the problem: The approach is based on hydrogen-evolution treatment of the surfaces modified with SHINPs by polarizing them in the potential region of hydrogen evolution in 0.1 M aqueous NaClO$_4$. The efficiency of this method has been demonstrated for Me(111)-(1 × 1) and Me(100)-(1 × 1) substrates (Me = Au, Pt) by choosing the pyridine adsorption and phase formation on these electrode substrates. High-quality Raman spectra were obtained on these well-defined and structurally characterized Au(hkl) and Pt(hkl) single-crystal surfaces, where the analysis of the characteristic A1 vibrational modes were in good agreement with the interpretation of voltammetric and chronoamperometric experiments.

Furthermore, an increased control has been demonstrated **(Chapter 4.2)** over both, the assembly and the electronic coupling of Au MPCs on an atomically flat electrode. By choosing Pt(111) as substrate and by synthesizing Au MPCs that expose a few pyridyl-groups coordinating to the substrate, the stability of the immobilized clusters could be considerably improved. By varying the deposition conditions, samples coated with stacked layers consisting of closely packed Au MPCs or samples decorated with laterally separated individual Au MPCs were obtained. Electrochemical experiments were performed with samples ranging from dissolved Au MPCs in bulk solution, over stacked layers of Au MPCs down to single laterally separated Au MPCs. In all electrochemical experiments discrete charging events could be resolved that corroborate the narrow dispersity of the Au MPCs and demonstrate their potential as single electron switches. The spacing of the electrochemically addressed energy levels, and thus also the capacitance of the Au MPCs, however, depends on the surrounding electrolyte. The tunneling spectroscopy

studies also demonstrate that the energy level mapping of single Au MPCs depends on the proximity of the neighboring clusters. The tunneling conductance increases and the HOMO-LUMO gap appears in the case of the *isolated* $Au_{144}$ clusters, compared to a stacked array of clusters.

In addition **(Chapter 4.3),** the conductivity and viscosity of the redox-active ionic liquid (IL) [1-butyl-1'-heptyl-4,4'-bipyridinium bis(trifluoromethanesulfonyl)imide], as well as the diffusion coefficients of its components have been studied over a 50 °C wide temperature range. Both the PGSE–NMR technique and voltammetric measurements have been used for the diffusivity studies. It was found that the diffusion coefficients determined by means of NMR and voltammteric measurements are, within the range of experimental error, equal — and they are (in accordance with other IL studies) higher than what the conductivity or viscosity measurements would indicate. Based on the fact that both the electrochemical and the NMR measurements yield practically the same diffusion coefficients, there is no experimental evidence that interpretations based in earlier studies of other redox-Il systems by *Murray et al.* on the assumption of a "homogeneous electron exchange" apply to the viologen IL investigated in this thesis.

The measured diffusion coefficients and bulk conductivities can be well interrelated based on the "ionicity" concept introduced previously by *Watanabe et al.* (that is, by treating the IL as a weak electrolyte). In agreement with the empirical Walden rule, a direct comparison between the measured conductivities and viscosities was also possible, for which a hole conduction model presented by *Abbott* has been utilized. The equality of diffusion coefficients resulting from the NMR and the electrochemical studies, combined with the fact that the time-scale of these two measurement techniques differ by nearly 4 orders of magnitude, can further be interpreted as an independent evidence supporting the validity of the "ionicity" concept over a "velocity cross-correlation" based explanation of deviations in the Nernst–Einstein equation suggested by *Harris*.

Finally, it has been shown **(Chapter 4.4)** that an enhanced stability of "$Ag_9MSA_7$" MPCs can be achieved by submitting them to phase transfer into an organic solvent in the presence of sterically bulky counterions. The resulting phase transferred clusters, "$Ag_9MSA_7(TOA)_x$" show a

very high stability in ambient conditions that has enabled for the first time to perform voltammetric investigations. Size exclusion chromatography reveals also a minor yield of clusters with a smaller size during the synthesis of "$Ag_9MSA_7$" clusters. The electrochemical studies of the "$Ag_9MSA_7(TOA^+)_x$" (1.63 nm) clusters show an electrochemical gap of 1.19 V with a HOMO-LUMO gap of 0.87 eV. However, as an important result, the combination of the MS investigations with the electrochemically determined HOMO-LUMO gap strongly suggest that the real cluster sizes are larger than the empirically used formula "$Ag_9MSA_7(TOA^+)_x$".

## 5.2 Outlook

The above introduced hydrogen evolution based protocol can be used for cleaning polycrystalline and single crystal electrode surfaces modified with SHINPs. As a result, *in-situ* Shell Isolated Nanoparticle Raman Spectroscopy (SHINERS) can be used as a promising technique to resolve the unsolved spectral interpretation in various cases. In other words, using the developed strategy of the SHINERS technique, it is easier to interpret the Raman spectra of various fields ranging from chemistry to biology.

The introduced controlled assembly technique of nanoparticles protected with an organic shell monolayer onto the electrode surface can be extended to assemble other types of MPCs, since it represents a versatile approach to control the MPCs on the electrode surfaces. The multistate charging observed in the investigated MPCs could be taken as an advantage to build multistate single-electron based switches which are operable at room temperature. It would be an interesting and challenging topic to build such a large scale tunneling device that is operable at *single electron/particle* level. Caution should be applied, however, to use already well established electrochemical data for gold MPCs, since it has been shown in this thesis (Chapter 4.2) that the data differ in their capacitance values at the single particle level. It is therefore better to re-calibrate the established energy scales of all existing MPCs at the single particle level. This information is crucial when the device is operated at the single particle level. As the charging features are also sensitive to the electrolyte, also a variation of the electrolyte can be used to tune the switching states of the given particle.

In the case of ILs, an extended study of checking the validity of the "ionicity" concept with molecular dynamics simulations is needed to get a deeper insight into the nature of mass, charge and momentum transport mechanisms in redox-active ILs. The investigation of the electrochemical behaviour (e.g. a transfer from radical cation to neutral state) for the $[C_4VC_7]$ $[Tf_2N]_2$ IL studied in this thesis is also an interesting topic. This is planned in our research group with further studies by means of impedance spectroscopy and surface imaging techniques (in-situ STM and AFM). By changing the type of the counter anions, the effect of the counter anion in the electrochemical behaviour can also be investigated.

In case of "$Ag_9MSA_7$" clusters, further studies involving for example also crystallization and High performance Liquid Chromatography (HPLC) are necessary to confirm the assumptions on the chemical formula and to get more detailed insight into the real size and composition of the clusters, as a challenging subject of research. This work is anticipated for the next months.

In summary, the results of this thesis involved in a frame work of interdisciplinary topics, together with the above mentioned outlook are considered a valuable base for the fundamental insight into various fields such as nanoparticle synthesis, nanoscale electronics, spectroscopy, biology and ionic liquids.

# Appendix

## Publications

1. Thumu Udaya B. Rao, **Nataraju Bodappa**, and Pradeep Thalappil. "$Ag_9$ Quantum Cluster through a Solid-State Route". *J. Am. Chem. Soc.*, 2010, *132* (46), pp 16304–16307

2. Jian-Feng Li, Alexander Rudnev, Yongchun Fu**, Nataraju Bodappa**, and Thomas Wandlowski. *"In Situ* SHINERS at Electrochemical Single-Crystal Electrode/Electrolyte Interfaces: Tuning Preparation Strategies and Selected Applications". *ACS Nano*, 2013, *7* (10), pp 8940–8952

3. **Nataraju Bodappa**, Ulrike Fluch, Yongchun Fu, Marcel Mayor, Pavel Moreno-García, Hans Siegenthaler, and Thomas Wandlowski. "Controlled assembly and single electron charging of monolayer protected $Au_{144}$ clusters: electrochemistry and scanning tunneling spectroscopy study". *Nanoscale* 2014, accepted.

4. **Nataraju Bodappa**, Peter Broekmann, Yong-Chun Fu, Julien Furrer, Yutaro Furue, Takamasa Sagara, Hans Siegenthaler, Hironobu Tahara, Soma Vesztergom, Klaus Zick and Thomas Wandlowski. "Temperature dependent transport Properties of a redox-active ioic liquid with a Viologen group". Submitted to *Journal of physical chemistry C,* 2014.

5. **Nataraju Bodappa**, Sagarna Leyre, Pradeep Thalappil, Hans Siegenthaler and Thomas Wandlowski . "Stability and Electrochemistry of Molecule like "$Ag_9MSA_7(TOA^+)_x$" Monolayer Protected Clusters". In preparation to Analytical chemistry

## Presentations on conferences and meetings

1. **Nataraju Bodappa**, Thomas Wandlowski; *1st year PhD graduate symposium, Bern, Switzerland,* September 1 3, 2011; Gold nanoparticles: Quantized charging and multistate electronic switching in ionic liquid at room temperature. (Oral)

2. **Nataraju Bodappa**, Ulrike Fluch, Marcel Mayor, Thomas Wandlowski. *National research Progamme-62, Annual meeting; Fribourg, Switzerland*, September 1 5, 2011; Integrated Gold Nanoparticles: An approach towards the realization of single electron charging and memory concepts. (Oral)

3. **<u>Nataraju Bodappa</u>**, Artem Mishchenko, Stijn F.L. Mertens, Thomas Wandlowski. *CUSO Postgraduate school in electrochemistry-SECM as a tool for surface activity characterization and modification; Lausanne, Switzerland*, June 21-23, 2011; Quantized charging observation of immobilized gold nanoclusters on Pt and HOPG in HMIm-FEP ionic liquid using EC-STS at room temperature. (Poster)

4. **<u>Nataraju Bodappa</u>**, Ulrike Fluch, Yongchun Fu, Pavel Moreno-García, Marcel Mayor and Thomas Wandlowski; *Swiss Working Group for Surface and Interface Science (SAOG - 2013);* Probing Electronic Functions of Single Gold Nanocluster ($Au_{144}$) An Electrochemical Scanning Tunneling Spectroscopy Approach. (Poster)

5. **<u>Nataraju Bodappa</u>**, Ulrike Fluch, Yongchun Fu, Pavel Moreno-García, Marcel Mayor, Hans Siegenthaler and Thomas Wandlowski; *Surface electrochemistry: towards energy research 25.08-29.08-2014;* Controlled assembly and single electron charging of monolayer protected $Au_{144}$ clusters. (Poster)

6. Alexander Rudnev, Viktoriya Nikitina, Yongchun Fu, Thu-Hien Vu, **<u>Nataraju Bodappa</u>**, Viliam  Kolivoska and Thomas Wandlowski; *Metrohm 2013;* Electrochemistry in Ionic Liquids: Practical Hints and Selected Applications.

# Acknowledgements

# **Erklärung**

gemäss Art. 28 Abs. 2 RSL 05

Name/Vorname: .............................. Bodappa Nataraju ..............................

Matrikelnummer: .............................. 10-129-302 ..............................

Studiengang: .............................. Chemistry ..............................

Bachelor ☐     Master ☐     Dissertation ☒

Titel der Arbeit: Charge transport in monolayer protected Au and Ag clusters in electrolyte environment and transport properties of a redox–active ionic liquid

LeiterIn der Arbeit: Prof. Thomas Wandlowski,

Prof. Hans Siegenthaler (temporary replacement)

Ich erkläre hiermit, dass ich diese Arbeit selbständig verfasst und keine anderen als die angegebenen Quellen benutzt habe. Alle Stellen, die wörtlich oder sinngemäss aus Quellen entnommen wurden, habe ich als solche gekennzeichnet. Mir ist bekannt, dass andernfalls der Senat gemäss Artikel 36 Absatz 1 Buchstabe r des Gesetztes vom 5. September 1996 über die Universität zum Entzug des auf Grund dieser Arbeit verliehenen Titels berechtigt ist.

Ich gewähre hiermit Einsicht in diese Arbeit.

Bern | 17·09·2014
..............................
Ort/Datum

B·Nataraju
..............................
Unterschrift